Imperial College London

PhD Thesis

Bioactive nanoparticle incorporation into inorganic/organic hybrids

Zhenlun Li

October 2018

Department of Materials

Imperial College London

Declarations

Declaration of originality

I hereby declare all work in this thesis, unless otherwise referenced or acknowledged, is the result of my own research carried out at Imperial College London during the period from October 2014 to September 2018.

Zhenlun Li

October 2018

Copyright

The copyright of this thesis rests with the author and is made available under a Creative Commons Attribution Non-Commercial No Derivatives licence. Researchers are free to copy, distribute or transmit the thesis on the condition that they attribute it, that they do not use it for commercial purposes and that they do not alter, transform or build upon it. For any reuse or redistribution, researchers must make clear to others the licence terms of this work.

Acknowledgements

Having been being a part of JRJ family for 5 years, I'd like to express my first thanks and appreciation to Prof. Julian R. Jones. A brilliant supervisor who has helped and guided me through this Ph.D life and thanks again for the pints he bought me during the pub times.

I'd like to thank every past and current member from JRJ group. It is a warm family with laugh and joy, I'm pretty sure I can't have a such Ph.D experience anywhere else. Thanks to Maria Nelson, my co-supervisor when I was a master student in the group 5 years ago, you are amazing and always encourage me even I had the worst result at that time; Award winning Italian woman scientist Francesca, you are more like my 'real' co-supervisor during this research work and I would be so pointless without you; Paul and Justin, a cool guy and a very cool guy, cheers; Tian and Ali, I deeply hope you two can have a talk show on TV; Gloria, Lizzie and Ale, you girls are amazing and thanks for organizing every activities for the lazy boys. For the rest of the team, I thank you all, every one of you is special to me.

I would also like to acknowledge Dr. Siwei Li and Dr. Parichart Naruphontjirakul for helping me carry out the cytotoxicity tests; Dr Mahmoud Ardakani for being a superhero taught me everything on TEM and SEM; Nicole Kelly at Warwick University for helping me run solid-state NMR.

I'd like to thank Luna Xu who accompanied me all the time when I was writing this thesis. And finally, my special thanks to my parents who have been selflessly supported me for the past 10 years, you guys are the best.

十年旅英，献给我的父母。

Abstract

Mesoporous silica nanoparticles have a great therapeutic potential as they can deliver active ions and they also have been made to nanocomposites with polymers for bone regeneration. Hybrids are co-networks of inorganic and organic components that can be produced with interconnected pores, matching mechanical properties to the host tissue and controlled biodegradability. Both silica nanoparticles and hybrids can be made from the sol–gel process. Calcium incorporated mesoporous silica nanoparticles (MCE) have been developed as a bioactive cation carrier. In this thesis, a PTHF/PCL/MCE/SiO_2 nano-hybrid network was achieved. For the first time, (3-Glycidyloxypropyl)trimethoxysilane (GPTMS) functionalized MCEs were incorporated into a hybrid and covalently bonded to the silicate network. Dense calcium containing silica nanoparticles were found not to be suitable for GPTMS grafting because of the low concentration of hydroxyl groups on the particle surface. Calcium incorporated mesoporous silica nanoparticles proved themselves to be a better choice for the functionalization as they had larger surface area and higher -OH surface density. In a Tris buffer dissolution study, the existence of covalent bonds between MCEs and the polymer network made them to release calcium at a slightly slower rate compared with unfunctionalized samples. In SBF dissolution, only a small amount of HCA formation was captured on specific samples after 3 weeks. This suggested the amount of calcium incorporated into particles were too low. Because of the suspected release of remained BF_3OEt_2, which caused a significant pH drop in solution, samples failed to pass cytotoxicity tests unless they were washed in water for 24 h prior to the test. Finally, porous scaffolds were fabricated by using 3D extrusion printing and the ink rheology profile showed a shear thinning behaviour.

The concept of using nanoparticles as a bioactive cation carrier covalently bonded to the hybrid network was proven to be feasible. This nano-hybrid system also has potential for incorporating other cations for different applications, such as lithium for cartilage and strontium for bone regeneration.

Contents

Declarations **2**

Acknowledgements **3**

Abstract **4**

Contents **5**

List of abbreviation **9**

List of Figures **13**

List of Tables **18**

List of Schemes **19**

Chapter 1 Introduction **20**

Chapter 2 Literature Review **23**

2.1 HUMAN BONE **23**

2.1.1 Bone structure 23

2.1.2 Clinical treatments for bone defects 24

2.2 Articular cartilage **25**

2.2.1 Cartilage structure 25

2.2.2 Clinical treatments for articular cartilage 26

2.3 Scaffolds for tissue regeneration **27**

2.4 Bioactive glasses and sol-gel process **28**

2.4.1 Melt-derived bioactive glasses 28

2.4.2 The sol-gel process 29

2.5 The mechanism of bioactivity for bioactive glasses **31**

2.5.1 HCA formation 31

2.5.2 Intracellular interaction between HCA and the bone. 31

2.6 Sol-gel hybrids **32**

2.6.1 Class II (IV) hybrids 33

2.6.2 Calcium incorporated hybrids 34

2.7 PCL hybrids **36**

2.7.1 PCL in tissue engineering 36

2.7.2 PCL Class II hybrids 37

2.7.3 Poly(tetrahydrofuran)/PCL/SiO_2 Hybrids 38

2.8 Sol-gel derived silica nanoparticles **41**

2.8.1 Dense nanoparticles 41

2.8.2 Mesoporous silica nanoparticles 43

2.8.3 Cation incorporation 45
2.8.4 Nanocomposites 46
2.8.5 Nanoparticles grafted with GPTMS 46
2.9 Additive manufacturing 48
2.9.1 3D extrusion printing 50
2.9.2 3D extrusion printing for hybrids 51
2.8 Research objectives 53
Chapter 3 Characterisation 54
3.1 Silica nanoparticles characterisation 54
3.1.1 Dynamic light scattering (DLS) 54
3.1.2 Zeta potential 54
3.1.3 Transmission electron microscopy (TEM) 55
3.1.4 Nitrogen adsorption 56
3.2 Sample composition characterisation 57
3.2.1 Fourier transform infrared spectroscopy (FTIR) 57
3.2.2 NUCLEAR MAGNETIC RESONANCE (NMR) SPECTROSCOPY 57
3.2.3 Thermogravimetric analysis (TGA) and differential scanning calorimetry (DSC) 58
3.2.4 Inductively Coupled Plasma Optical Emission Spectroscopy (ICP-OES) 58
3.3 Hybrid characterisation 59
3.3.1 Compression and tension tests 59
3.3.2 Scanning electron microscope (SEM) 59
3.3.3 X-ray diffraction (XRD) 59
3.3.4 Simulated body fluid (SBF) dissolution study 60
Chapter 4 Synthesis and Functionalization of Calcium Incorporated Dense Silica-Nanoparticles 61
4.1 INTRODUCTION 61
4.2 MATERIALS AND METHODS 61
4.2.1 Dense silica-nanoparticle synthesis and calcium incorporation 61
4.2.2 Surface functionalization of silica-nanoparticles with GPTMS 63
4.2.3 Particle characterisation 64
4.3 RESULTS AND DISCUSSION 65
4.3.1 Calcium incorporated dense silica-nanoparticles (CaSNP) 65
4.3.2 Calcium incorporated silica-nanoparticles functionalization with GPTMS (CaESNP) 67
4.4 Conclusions 74
Chapter 5 Synthesis and Functionalization of Calcium Incorporated Mesoporous Silica-Nanoparticles 75
5.1 INTRODUCTION 75

5.2 MATERIALS AND METHODS **75**
5.2.1 Mesoporous silica-nanoparticle synthesis and calcium incorporation (CaMSN) 75
5.2.2 Surface functionalization of calcium incorporated mesoporous silica nanoparticles with GPTMS (CaMSN -> MCE) 77
5.2.3 Particle characterisation 77
5.3 RESULTS AND DISCUSSION **80**
5.3.1 Calcium incorporated mesoporous silica-nanoparticle (CaMSN) 80
5.3.2 The functionalisation of CaMSNs with GPTMS (CaMSNs -> MCE) 85
5.3.3 The effect of GPTMS on CaMSNs 92
5.4 Conclusions **101**
Chapter 6 Functionalized Bioactive Mesoporous Silica-Nanoparticles in Silica/PTHF/Polycaprolactone Hybrids **103**
6.1 INTRODUCTION **103**
6.2 MATERIALS AND METHODS **104**
6.2.1 Sol-gel synthesis of MCE containing hybrids 104
6.2.2 The making of cylindrical and disc bulk samples 108
6.2.3 3D printing of the MCE containing nano-hybrid 109
6.3 CHARACTERISATION **111**
6.3.1 Chemical reaction study 111
6.3.2 Chemical composition study 112
6.3.3 Bulk sample macro observation 112
6.3.4 Bulk sample micro observation and network investigation 112
6.3.5 Mechanical testing of bulk samples 112
6.3.6 Dissolution study 114
6.3.7 Cytotoxicity test 115
6.3.8 3D printing - ink and scaffold characterisation. 116
6.4 RESULTS AND DISCUSSION **117**
6.4.1 Oxidation of PCL diol (M_n= 530 Da) 117
6.4.2 Hybrid synthesis 118
6.4.3 Hybrid bulk samples – macro observations 121
6.4.4 Hybrid bulk samples – micro observations 122
6.4.5 Mechanical testing on bulk samples 125
6.4.6 Dissolution study 130
6.4.7 Cytotoxicity test 140
6.4.8 3D printing of nano-hybrid scaffolds 141
6.5 Conclusions **149**

Chapter 7 Summary and Future Works 151
7.1 Thesis summary 151
7.2 Future work 153
7.2.1 Nanoparticles 153
7.2.2 Hybrid scaffolds 153
References 154
Appendix 168
Permissions for using images from publications: 168

List of abbreviation

BET	Brunauer–Emmett–Teller
BF_3OEt_2	boron trifluoride diethyletherate
$Ca(NO_3)_2$	Calcium nitrate
$CaCl_2$	Calcium chloride
CAD	Computer assisted design
CaMSN	Calcium incorporated mesoporous silica nanoparticle
CaSNP	Calcium incorporated dense silica nanoparticle
$CDCl_3$	Deuterated chloroform
CH_3CN	acetonitrile
CMC	critical micelle concentration
CME	calcium methoxyethoxide
CTAB	hexadecyl trimethyl ammonium bromide
CTAB	cetyltrimethylammonium bromide
D_c	Degree of network condensation
DFT	Density functional theory
DLS	Dynamic light scattering
DSC	Differential scanning calorimetry
ECM	Extracellular matrix
EDC	1-Ethyl-3-(3-dimethylaminopropyl)-carbodiimide
EDX	Electron dispersive X-ray spectrometer
ESNP	GPTMS functionalized dense silica nanoparticle
FBC	fetal bovine chondrocytes

FCS	Foetal calf serum
FDA	Food and drug administration
FTIR	Fourier transform infrared spectroscopy
GPTMS	(3-Glycidyloxypropyl) trimethoxysilane
HA	Hydroxyapatite
HCA	Hydroxycarbonate apatite
HCl	Hydroxy chloride
HMDI	hexam-ethylene diisocyanate
ICP-OES	Inductively coupled plasma optical emission spectroscopy
ICPTES	3- isocyanatopropyltriethoxysilane
IR	Infrared
IUPAC	International Union of Applied Chemistry
K_2HPO_4 $3H_2O$	Potassium phosphate dibasic trihydrate
KCl	Potassium chloride
MAS	Magic angle spinning
MCE	GPTMS functionalized and calcium containing mesoporous silica nanoparticle
MEM	Minimum Essential Medium
$MgCl_2$ $6H_2O$	Magnesium chloride hexahydrate
Mn	Number average molecular weight
MSC	Mesenchymal stem cell
MSN	Mesoporous silica nanoparticles
MTT	3-(4,5-dimethylthiazol-2-yl)-2,5-diphenyltetrazolium bromide

Na_2SO_4	Sodium sulfate
NaCl	Sodium chloride
$NaHCO_3$	Sodium bicarbonate
NBO	Non briding oxygen
NHS	N-hydroxysuccinimide
NMR	Nuclear magnetic resonance
PBS	Phosphate buffered saline
PCL	Polycaprolactone
PDI	Polydispersity index
PDLLA	poly-DL-lactic acid
PDMS	Polydimethylsiloxane
PE	Polyethylene
PEG	Polyethylene glycol
PGLA	Poly(lactide-co-glycolide)
PLA	Polylactide
PLLA	poly(L-lactide)
PMMA	polymethylmethacrylate
PMP	Polymethylpentene
PPF	Poly(propylene fumarate)
PTFE	Polytetrafluoroethylene
PTHF/polyTHF	Polytetrahydrofuran
PU	Polyurethane
ROP	ring-opening polymerisation

rpm	revolutions per minute
SBF	Simulated body fluid
SEM	Scanning electron microscope
SNP	Bare dense silica nanoparticle
TEM	Transmission electron microscopy
TEMPO	2,2,6,6-Tetramethyl-1-piperidinyloxy
TEOS	Tetraethoxysilane
TGA	Thermogravimetric analysis
TGF-β1	Transforming growth factor beta 1
TMSPMA	3-(trimethoxysilyl)propylmethacrylate
Tris	Tris(hydroxymethyl)aminomethane
XPS	X-ray photoelectron spectroscopy
XRD	X-ray diffraction
ZDEC	diethyldithiocarbamate
β-TCP	β-Tricalcium phosphate
γ-PGA	poly(g-glutamic acid)

List of Figures

Figure 1.1 - Three main elements in the bone and cartilage regeneration field. Adapted from [1]. 20

Figure 2.1 Hierarchical structure of bone with different scale. Adapted from [8]. 23

Figure 2.2 - Cross section diagram of articular cartilage with A, cellular organization and B, collagen fibre architecture. Adapted from [25]. 25

Figure 2.3 - The formation of silica tetrahedra and nanoparticles at room temperature in the sol-gel process. Adapted from [4]. 29

Figure 2.4 - Scheme for ion exchange [44]. 31

Figure 2.5 - The simple scheme for the bone formation on HCA layer. Adapted from [189] 32

Figure 2.6 - Structure of a Class II (IV) hybrid with inorganic and organic components that are covalently bonded. Adapted from [42]. 33

Figure 2.7 - Scheme for synthesis poly(CL-co-GPTMS) using caprolactone and GPMTS. 37

Figure 2.8 - Proposed structural network of the PTHF/PCL/Silica hybrid. Adapted from [7]. 38

Figure 2.9 - Proposed mechanism of the ring opening polymerisation of polyTHF with PCL-diCOOH acting as the chain terminator. Adapted from [7]. 39

Figure 2.10 - Approaches for the synthesis of silica nanoparticles. Adapted from [81] 41

Figure 2.11 - Nucleation and aggregation mechanism for silica nanoparticles. Adapted from [163]. 42

Figure 2.12 TEM and DLS results on particle diameter with increasing ammonia concentration and [TEOS]=0.28M [84]. 43

Figure 2.13 - Scheme of showing MSNs in the bone regeneration. Adapted from [95]. 43

Figure 2.14 - a) Phase diagram of CTAB in water with increasing concentration. Adapted from [101]. b) scheme of synthesis MSNs by using CTAB as a template. Adapted from [190]. 44

Figure 2.15 - Schematic showing the change of Ca distribution during the incorporation process. Adapted from [102]. 45

Figure 2.16 - Reaction between silica gel and GPTMS molecule in an organic solvent. 47

Figure 2.17 - Reaction mechanism of grafting GPMTS. Adapted from [117]. 47

Figure 2.18 - Extrusion head generating a continuous filament. Adapted from [191]. 50

Figure 2.19 - Load versus time curves for inks through a standard metallic tip and a conical plastic tip [141]. _____ *51*
Figure 2.20 - Photo showing the 3D extrusion setup used by Nelson. Photo taken by the thesis author. _____ *52*
Figure 3.1 - Scheme showing TEM under imaging mode. Adapted from [192]. _____ *55*
Figure 3.2 - IUPAC classification of physisorption isotherms. Adapted from [148]. _____ *56*
Figure 4.1- TEM images of SNPs and CaSNPs with a diameter of 100 nm: a) & b) SNPs without calcium, c) calcium incorporated with a ratio of 1:8 washed 3 times by water, d) calcium incorporated SNPs washed 1 time by 2 M nitric acid and 2 times by water. _____ *65*
Figure 4.2 - DLS particle size distributions for calcium incorporated nanoparticles before (CaSNP) and after the functionalisation with GTPMS (CaESNP). _____ *66*
Figure 4.3 - FTIR (left 500-2500 cm^{-1} range and right 2500-4000 cm^{-1}) spectra from: a) SNP, b) CaSNP, c) ESNP, d) CaESNP and e) CaESNP with plasma treatment. _____ *67*
Figure 4.4 - Raman spectra of a) SNP, b) CaSNP, c) ESNP, d) CaESNP and e) CaESNP with plasma treatment. _____ *69*
Figure 4.5 - TGA on nanoparticle samples from 25 °C to 800 °C. _____ *70*
*Figure 4.7 - SEM images of a) CaSNPs and b) functionalized CaESNPs**b*** _____ *72*
Figure 4.7 - SEM images of a) CaSNPs and b) functionalized CaESNPs. _____ *72*
Figure 4.8 - Zeta potential for dense silica particles before (CaSNP) and after (CaESNP) the addition of GPTMS _____ *73*
Figure 5.1 - TEM images of MSNs synthesised with different stirring rate: a) 400 rpm, b) 500 rpm and c) 750 rpm. _____ *80*
Figure 5.2 - FTIR spectra of MSNs treated by two different methods of removing CTAB. ___ *81*
Figure 5.3 – TEM images of MSNs (no calcium): a) pore facing to the camera, b) channel view and c) pores that were blocked by CTAB. _____ *82*
Figure 5.4- TEM images of CaMSN: a) all particles lost porosity and b) some particles still showed visible pores. _____ *83*
Figure 5.5 - DLS size distribution for mesoporous particles before and after the functionalization with GPTMS. _____ *84*
Figure 5.6 - Zeta potential measurements for all particles before and after the functionalization with GPTMS. _____ *85*

Figure 5.7 - FTIR spectra of: a) CaMSN and b) MCE. Left: wavelength 500-2500 cm^{-1} Right: wavelength 2500-4000 cm^{-1}. _____ 86
Figure 5.8- Raman spectra of: a) CaMSN and b) MCE._____ 87
Figure 5.9 - TGA analysis on both dense and mesoporous nanoparticles before and after the functionalization with GPTMS. _____ 87
Figure 5.10 - TGA (top) and DSC (bottom) results of top: a)&c) particles without drying treatment and b)&d) particles treated with an extra drying process prior to the functionalization. _____ 89
Figure 5.11 - TEM images and corresponding EDS results for a) CaMSN and b) MCE. _____ 92
Figure 5.12 - Nitrogen adsorption of mesoporous particles with different amounts of GPTMS. _____ 93
Figure 5.13 - Pore size distribution calculated by using DFT. _____ 93
Figure 5.14 - Pore size distributions of mesoporous particles with different amounts of GPTMS. according to DFT calculations from the gas sorption isotherms. _____ 93
Figure 5.15- ^{29}Si single-pulse MAS NMR spectra (top line), ^{1}H MAS spectra (middle line) and the ^{13}C MAS (bottom line) of mesoporou silica nanoparticles._____ 98
Figure 5.16 – Elemental concentrations and pH in MEM following immersion of for mesoporous particles._____ 99
Figure 5.17 - TEM images of mesoporous particles 7 days after the dissolution study in MEM : a) CaMSNs, b) MCE1mmol/g, c)MCE2mmol/g, d)MCE4mmol/g and e)MCE8mmol/g. _____ 100
Figure 6.1 - Flowchart for making nanoparticles contained hybrids._____ 104
Figure 6.2 - The mechanism of Anelli's oxdiation (modified from [177]) _____ 105
Figure 6.3 - Schematic of the proposed ring opening polymerization mechanism between MCE and THF. _____ 107
Figure 6.4 - The set-up of the extrusion printing device. _____ 110
Figure 6.5 - Illustration of the scaffold design. The gap between filaments was 0.6x0.6 mm, length and width were both 12 mm and the height was 6.51 mm._____ 111
Figure 6.6 - The set-up of the tensile test on a Bose Electroforce machine._____ 114
Figure 6.7 - The rheometer used for testing the viscosity of the inks. The gap between the peltier plate and the substrate plate was set to 350 or 500 um depended on the ink. ____ 116
Figure 6.8 - FTIR spectra of PCL diol before and after oxidation. _____ 117

Figure 6.9 - Proton NMR spectra on PCL diol before and after the oxidiation. _____ *118*

Figure 6.10 - Proton NMR spectra in $CDCl_3$ of solution containing MCE+PCL+THF+GPTMS (bottom) and solution containing MCE+PCL+THF+GPTMS+BF_3OEt_2 mixed for an hour (top). _____ *119*

Figure 6.11- Thermal analysis on hybrid samples with different amounts of MCEs added during the synthesis. _____ *121*

Figure 6.12 - Photographs of 2 hybrid bulk samples containing 250 mg of MCEs each. ___ *121*

Figure 6.13 - Photo of hybrid cylindrical samples made with modified method. _____ *122*

Figure 6.14 - SEM images of cylindrical bulk samples. From the top and bottom regions of the cylinders. _____ *123*

Figure 6.15 - ^{29}Si MAS NMR spectra on samples with different amounts of MCEs added during the synthesis. _____ *124*

Figure 6.16 - Compression curves for samples containing MCEs from 0 mg to 250 mg. The final inorganic : organic weight ratio for all samples was around 23% : 77% and the variation was below 4%. _____ *126*

Figure 6.17 - Cyclic loading tests for hybrid samples with 0 mg, 50 mg, 150 mg and 250 mg of MCEs added during the synthesis. A total of 10 cycles were conducted. _____ *127*

Figure 6.18 - Samples prepared for the tension test. 10 mm x 45 mm strips were cut from hybrid discs with 0 mg, 50 mg, 150 mg and 250 mg of MCEs added during the synthesis. _ *128*

Figure 6.19 - Photographs showing samples fracturing during the tensile test at different positions : a) top, b) bottom and c) middle. _____ *129*

Figure 6.20 - Tensile curves for samples made with 0 mg, 50 mg, 150 mg and 250 mg of MCEs. _____ *129*

Figure 6.21 - Elemental concentration obtained from ICP-OES analysis following immersion of hybrids in Tris buffer a) calcium, b) calcium in the first 3 days, c) silicon d) the pH change. _____ *131*

Figure 6.22 - TEM images of dissolution products in Tris solution for hybrid samples across 4 weeks. All hybrid samples had the same organic : inorganic weight ratio and the same amounts of MCEs while the GPTMS added during the MCE synthesis were different:0 mmol/g, 1 mmol/g and 2 mmol/g. _____ *133*

Figure 6.24 - FTIR spectra for hybrids containing different amounts of MCEs following immersion in SBF for 3 days, 1 week and 4 weeks. _____ *136*

Figure 6.25 - XRD patterns of hybrid samples containing different amount of MCEs at different time points of the dissolution study in SBF. _____ *138*
Figure 6.26 - SEM images of hybrid samples following immersion in SBF at different time points. _____ *139*
Figure 6.27 - Cell viability of the dissolution products of hybrids with different amount of MCEs with a) ATDC5 and b) MC3T3-E1 cell lines. Samples were also soaked in water for 24 h and then used for the ATDC5 tests and shown in c). Samples soaked in water for 2 h, 6 h, 24 h and un-soaked samples were put in MEM containing phenol red indicator and the colour change is shown in d). _____ *140*
Figure 6.28 – Rheometery of the hybrid sol-gel ink with 0 mg, 100 mg and 250 mg of MCEs added during the synthesis tested using a rheometer, a), viscosities for all samples were recorded with an increase in shear rate from 1 s^{-1} to 120 s^{-1} in 60 s. In b), viscosities were recorded with a fixed shear rate of 80 s^{-1} over a time period up to 15 minutes. _____ *142*
Figure 6.29 - Printing windows for hybrid inks with 0 mg, 100 mg and 250 mg of MCEs added during the synthesis. _____ *144*
Figure 6.30 - Un-dried scaffolds printed from Hink_250mg at different printing times: a) before the printing window, b) at the beginning of the printing window, c) middle of the printing window and d) nearly the end of printing window. _____ *145*
Figure 6.31 - Photographs of dried scaffolds printed from Hink_0mg, 100mg and 250mg. *146*
Figure 6.32 - SEM images for scaffolds printed with and without nanoparticles. _____ *147*
Figure 6.33 - SEM images of scaffolds printed from Hink_250mg under different magnifications. MCEs are highlighted in red dotted circles. _____ *148*

List of Tables

Table 2.1 - Mechanical properties of bone _____ *24*

Table 2.2 - Mechanical properties for articular cartilage. Tensile values [28][29] are given from bovine articular cartilage and compressive values [30][31] are given from the human articular cartilage. _____ *26*

Table 2.3 - Criterion in bone and cartilage scaffolds _____ *27*

Table 2.4 - Techniques for Additive Manufacturing of scaffolds for tissue engineering. ____ *49*

Table 3.1 - Reagents used for making SBF _____ *60*

Table 4.1 - Weight percentage of GPTMS in NPs _____ *71*

Table 4.2 - Acid digestion results on CaESNPs that were plasma treated. _____ *71*

Table 5.1 - The amount of GPTMS grafted on the mesoporous particles surface calculated from TGA results. _____ *90*

Table 5.2 - Surface area and pore size calculated from nitrogen adsorption data _____ *94*

Table 5.3 - Chemical shifts and relative percentage abundance of silicon T and Q species obtained from ^{29}Si solid state NMR with resulted degree of condensation and total T fractions. _____ *96*

Table 6.1 - Time recorded for hybrids samples to gel. The time was counted from 1 h after the addition of BF_3OEt_2 _____ *120*

Table 6.2 - Chemical shifts and relative percentage abundance of silicon T and Q species obtained from ^{29}Si solid state NMR with resulted degree of condensation. _____ *124*

List of Schemes

Scheme 4.1 - Synthesis process of CaSNPs. _____ *62*

Scheme 4.2 - The reaction between GPTMS and CaSNP in toluene. _____ *63*

Scheme 4.3 - Schematics of three potential products from the functionalization of silica nanoparticles with GPTMS. _____ ***Error! Bookmark not defined.***

Scheme 5.1 - Scheme of synthesis of MSN with CTAB as surfactant for templating. _____ *76*

Scheme 5.2 - The apparatus for mesoporous particle functionalization. _____ *77*

Scheme 5.3 - Experimental setup for nanoparticle dissolution studies. _____ *79*

Scheme 5.4 - The sketch of how GPTMS blocks the mesopores within a nanoparticle. _____ *95*

Scheme 5.5 - The proposed change of Q species at the surface of a nanoparticles during functionalization with GPTMS. _____ *97*

Scheme 5.6 - The plot of functionalized nanoparticles. _____ *97*

Scheme 6.1 - A proposed drawing of of nano-PCL hybrid network. _____ *108*

Scheme 6.2 - Scheme for showing the cylindrical bulk hybrid samples when they were under compression. _____ *126*

Scheme 6.3 – Scheme showing how samples (a) with and (b) without MCEs behaved under tension. _____ *130*

Chapter 1 Introduction

Patient demand and clinical needs have driven developments in biomaterials. Focus has changed from inert materials for replacing living tissues towards bioactive and biodegradable materials for tissue regeneration [1].

In bone and cartilage regeneration, three elements play important roles: cells, signals and scaffolds (Figure 1.1)[2][3]. Scaffolds are 3D templates for cell and tissue to grow, which means they should be bioactive and biodegradable. Significant achievements have been made in scaffold design, especially in the bone regeneration. A remarkable milestone was made by Prof. Larry Hench in the invention of bioactive glasses in 1969 [4], which was the first synthetic material to be found to bond with human tissue.

One of the most well-known bioglass composition invented by Prof. Hench is 45S5 (46.1 mol.% SiO_2, 24.4 mol.% Na_2O, 26.9 mol.% CaO and 2.6 mol.% P_2O_5) it can bond with bone in a very

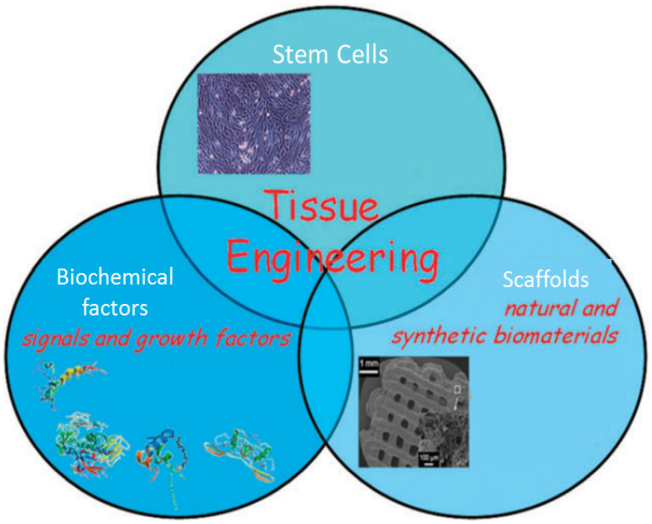


Figure 1.1 - Three main elements in the bone and cartilage regeneration field. Adapted from [1].

short time and initiate bone growth away from the bone-implant interface. NovaBone is one of the most successful commercial products made from 45S5 particles and surgeon can make them into putty by mixing with blood and use it for autograft and securing metal screws and hooks [5]. BonAlive is another commercial product made from bioglass by using a different composition S54P4 (53.8 mol.% SiO_2, 21.8 mol.% CaO, 22.7 mol.% Na_2O, 1.7 mol.% P_2O_5) and

has similar clinical results with 45S5 but a slower degradation rate [4]. Apart from these, Bioglass 13-93 with 7.7 mol.% MgO (54.6 mol.% SiO_2, 6 mol.% Na_2O, 22.1 mol.% CaO, 1.7 mol.% P_2O_5, 7.9 mol.% K2O, 7.7 mol.% MgO) was also invented to avoid the crystallization on sintering, however it has lower bioactivity compares with BonAlive because of the presence of magnesium [6].

Still, there are no commercial scaffolds (temporary templates for bone regeneration) made from bioactive glass as it is a great challenge to fulfil all the criteria of a scaffold. Scaffolds need to maintain the bioactive properties of the bioactive glass, be mechanically compatible with the host tissue and be porous to allow cell migration and proliferation and vascularisation if is needed (for bone). It is also important to ensure they can degrade away after the new tissue is formed and the degradation rate should be under control [4]. In recent years, the use of organic-inorganic hybrid materials as scaffolds are becoming more popular. The concept of hybrid is a homogenous system with inorganic-organic components interacting at the molecular level [7]. The presence of hybrid scaffolds has solved the mechanical problem with bioactive glass scaffolds, which are too brittle and no flexibility, and compared with composite scaffolds hybrids they can degrade congruently [4].

Although scaffolds made using hybrid systems are attractive, making them bioactive is still a challenge. For bone regeneration as an example, the incorporation of calcium into hybrid system is either restricted by the high temperature required during the heat treatment or incorporated calcium ion has a burst release [8]. Even if an appropriate calcium precursor is found for the hybrid system, the system has to be modified again if cations other than calcium is preferred to be incorporated into (e.g. lithium for cartilage as lithium protects cartilage from cytokine-mediated degradation by reducing collagen-degrading matrix metalloproteinase prodcution via inhibition of the p38 mitogen-activated protein kinase pathway [9]).

Here, the aim of this thesis is to develop a ‘cation carrier’ for hybrid scaffolds by using (3-glycidyloxypropyl)trimethoxysilane (GPTMS) functionalized silica nanoparticles. Calcium was chosen as the sample cation to incorporate into silica nanoparticles. The original double organic network PCL/PTFH/silica hybrid system developed by Tallia *et. al.*[10] was chosen as

the hybrid system to modify with the nanoparticles. The final goal was to prove feasibility of producing a 3D printed, PCL/PTHF/silica/nanoparticle double organic and double inorganic network nano-hybrid system with calcium that can induce the apatite formation. The objectives were to:

1. Synthesis calcium incorporated dense silica nanoparticles (CaSNP) and then functionalize with GPTMS (CaESNP). (Chapter 4)
2. Synthesis calcium incorporated mesoporous silica nanoparticles (CaMSN) and then functionalize with GTPMS (MCE). Investigate the effects of grafting GPMTS on silicate network and calcium release. (Chapter 5)
3. Introduce MCE into the PTHF/PCL/SiO_2 hybrid system. Investigate the effect of MCEs on nano-hybrid bulk samples' mechanical properties, hybrid network and bioactivities. Investigate the feasibility of using 3D extrusion print to fabricate nano-hybrid scaffolds. (Chapter 6)

Chapter 2 Literature Review

2.1 HUMAN BONE

2.1.1 Bone structure

Bone has varied functions in human body such as structural support, protection and storing of healing cells [11] and its functions are determined by the arrangement of the material structures. As shown in Figure 2.1, long bones consist of: cancellous bone (or trabecular bone) and cortical bone (or compact bone) and these two bone types can be distinguished by their difference in porosity [12]. Cortical bones are at the outer layer of a bone and has a higher density compared with cancellous bones. At the microstructure level, osteon is found and it's the primary functional unit of cortical bone which is in a cylindrical shape with size about 250 μm [13]. Osteon is formed from concentrically wrapped lamella sheets. By looking into the nanoscale, collagen fibres are found and they are surrounded by mineral. At the sub-nano scale, plate-like apatite crystals were found in the space between collagen fibrils [14].

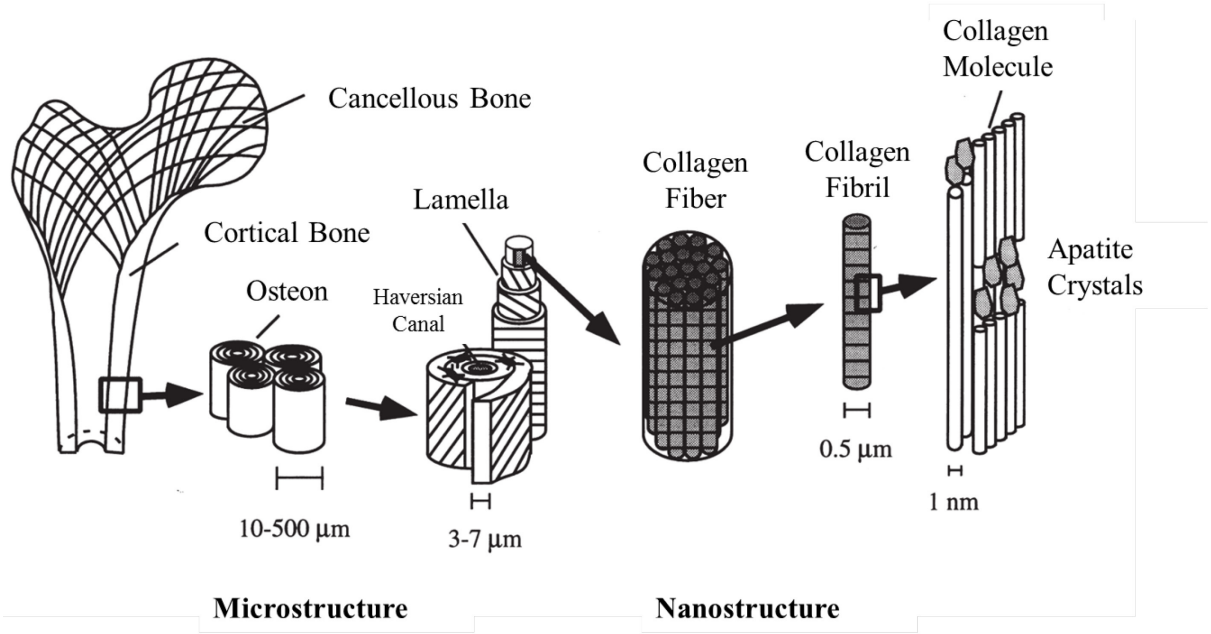


Figure 2.1 Hierarchical structure of bone with different scale. Adapted from [11].

There are three major cell types in bone: osteocytes, osteoclasts and osteoblasts. Osteocytes are responsible for recycling calcium salts in the bone matrix and support the bone structure. Osteoclasts break down bone tissue by triggering the bone resorption process. In this process,

osteoclasts secret acid and a collagenase which then decomposes the hydrated protein composite and bone matrix. Osteoblasts are differentiated from mesenchymal stem cells and are responsible for the bone formation. They can produce hydroxycarbonate apatite (HCA) which then forms a mineralized matrix. At the end of bone formation process, osteoblasts turn into osteocytes when they are buried in the matrix and then continue to maintain bone structure [15][16].

Mechanical properties for bone are different depending on the position in the human body and also are correlated with person's age and gender [17]. Table 2.1 has summarised sets of mechanical properties for cortical and cancellous bone and this is useful for the bone scaffold design.

Table 2.1 - Mechanical properties of bone

	Cortical bone [2][8][9][20]	Cancellous bone [21][22][23]
Compressive strength (MPa)	100-150	2-12
Tensile strength (MPa)	50-151	1-5
Modulus (GPa)	10-20	0.1-5
Fracture toughness (MPa $m^{1/2}$)	2-12	0.1-0.8
Compressive strain (%)	1-3	5-7
Porosity (%)	5-10	50-90

2.1.2 Clinical treatments for bone defects

Autologous and allografts bone transplantations are the two most seen methods used for repairing patient bone when the bone defect size is too large for self-healing [16]. Autologous bone transplantation means bone is sourced from the same patient and this gives great osteoconductive and osteoinductive properties [24]. However, this method needs healthy bones from patient and causes donor site morbidity and also this process is painful with long recovery time. Allograft transplantation is the process that bone is donated from another individual (bone bank) but the mechanical properties of irradiated bone are poor [25]. With defects size becomes even larger, synthetic bone graft materials are needed. Materials like

calcium phosphate and bioactive glasses granules are mixed with blood to form a putty which is then put into the defect [4].

2.2 Articular cartilage

2.2.1 Cartilage structure

Articular cartilage has a thickness about 2 to 4 mm and it has no blood vessels, nerves or lymphatics [26]. The function of articular cartilage is to provide a low frictional coefficient surface for joint movements. The structure of articular cartilage can be separated into serval zones as shown in Figure 2.2. The superficial tangential zone has the duty to protect rest of cartilage regions from shear stress and also because of its function, chondrocytes in this zone are flattened. The layer under the superficial zone is the middle zone where spherical chondrocytes, proteoglycans and thick collagen fibrils are found. This zone makes up to 60% of the cartilage volume. The function of this zone is to provide a bridge between superficial zone and deep zone and also it resists the compressive force. One layer deeper is the deep zone. Collagen fibrils here are vertically oriented which makes deep zone can resist the greatest compressive force compared with other zones. Calcified zone, where calcified cartilage is found, is under the deep zone and these two zones are separated by the tidemark [27][28][29].

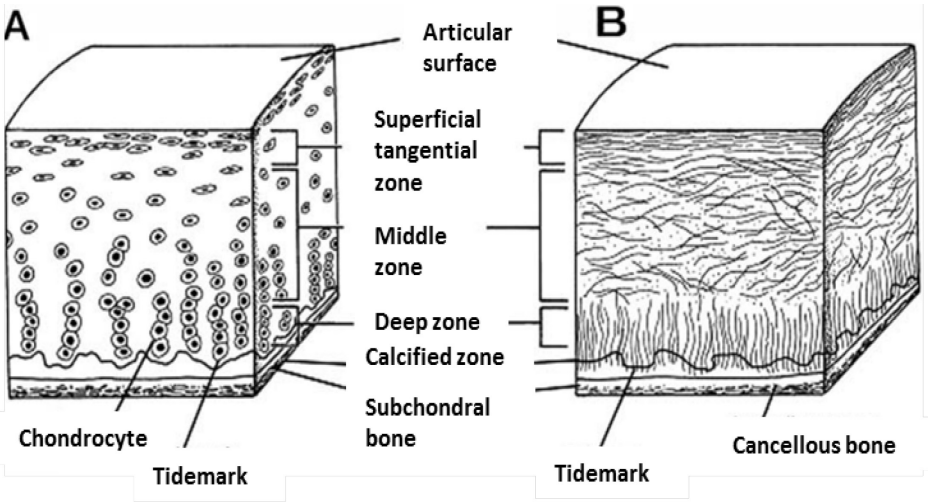


Figure 2.2 - Cross section diagram of articular cartilage with A, cellular organization and B, collagen fibre architecture. Adapted from [28]**.**

The determination of articular cartilage's mechanical properties is a complicated topic because it is difficult to mimic the environment with cartilage fluid and ECM *in vivo* [30]. Range values are summarized in Table 2.2.

Table 2.2 - Mechanical properties for human articular cartilage. Tensile values: [31][32]**, compressive values:** [33][34][35]**.**

	Articular Cartilage
Tensile strength (MPa)	0.8-25
Tensile strain (%)	10-40
Tensile modulus (MPa)	5-25
Compressive strength (MPa)	6.4-14.6
Compressive strain (%)	5-20
Compressive modulus (MPa)	6.1-13.3

2.2.2 Clinical treatments for articular cartilage

The self-regeneration ability of cartilage is limited by the absence of blood flow and consequently nutrients can only be delivered by diffusion. Total knee replacement is a very invasive but effective method to replace damaged cartilage and the life span for a replaced knee is about 20 years [36]. However, this treatment is not idea for young patient as they need revision surgery over the life time. Microfracture is a less invasive method in which holes are punched into subchondral bone and the bone marrow that contains stem cell will flush out and stimulates the healing process, but fibrocartilage is likely to be formed instead of healthy hyaline cartilage [37]. Another way to help repair the cartilage is mosaicplasty. This method is to harvest osteochondral tissue from non-load bearing site of the same patient and then transplant to the defect site. This method is limited by the defect size and cause pain to the donor site [38].

2.3 Scaffolds for tissue regeneration

With the disadvantages and limitations in methods and materials used in clinical treatments, engineered scaffolds are widely used in bone and cartilage regeneration [39].

As summarized in Table 2.3, the design criteria for an idea scaffold are different for bone and cartilage, but in general, it should be porous and interconnected for cell ingrowth and it should be biocompatible, bioactive and biodegradable, which means no fibrous capsule should be formed when it enters the human body and the scaffold is able to stimulate cell's differentiation and produce ECM. By the end of the application, material should degrade away and the dissolution product can be excreted by the body. The mechanical properties of this scaffold should be similar to the local tissue and it is important to make the degradation rate matches the rate of local tissue regeneration so the host tissue will not lose support [4]. In addition, the shape of designed scaffold should match with defect shape to fix it in position so this means scaffold requires a customized manufacture method [40].

Table 2.3 - Criterion in bone and cartilage scaffolds

Scaffold Property	Bone	Cartilage
Biocompatibility	No inflammation and immunorejections.	
Bioactivity	Promote cell attachment and proliferation	Stimulate cell for ECM production and remodelling
Biodegradability	Degradation rate is at the same speed as the local tissue regenerated and no cytotoxic dissolution products	
Architecture	Interconnected porous structure	
Mechanical properties	Same as the host tissue and remain unchanged during the degradation	
Manufacture	Customization and up-scalable	

2.4 Bioactive glasses and sol-gel process

Invented by Prof. Larry Hench in 1969, bioactive glass is the first synthetic material found that could bond to bone [41]. Melt-derived bioactive glass is a degradable glass composed of Na_2O, CaO, P_2O_5 and SiO_2. The molar ratio between these components determine the final bioactivity and the most successful composition discovered, termed as 45S5 or Bioglass®, contains 2.6 mol% P_2O_5, 46.1 mol% SiO_2, 26.9 mol% CaO and 24.4 mol% Na_2O and it can form a strong bonding with the bone [42]. Bioglass not only bonds with bone but also induces the bone growth and this is contributed by the formation of an HCA layer on the glass surface. The detail of HCA formation will be discussed in *Section 2.5*.

2.4.1 Melt-derived bioactive glasses

The traditional way to make bioactive glasses is using a melt quench process. In this process, all chemical compounds are firstly well mixed and then melt at a high temperature, usually above 1300°C, and then molten glass is quenched in a graphite mould or water depend on the shape of wanted product (monolith or frit) [4].

There are several disadvantages found by using the melt-quenching method. One of them is that it is difficult to make porous scaffolds as bioactive compositions, 45S5 as an example, have a very narrow sintering window, which means crystallisation will happen during processing, which reduces the bioactivity [43]. Another limitation for melt-derived bioactive glasses is it is difficult to reach high purity. This is because components used in bioactive glasses are very reactive which can easily pick up other cations as impurity, e.g. from the crucible the reagents are melted in. Also, bioactive glass powders prepared before melting are exposed to the environment and can be easily contaminated [44].

2.4.2 The sol-gel process

To overcome the disadvantages in the melt-quenching process, a chemistry-based bottom-up synthesis process, called sol-gel process, is applied to make bioactive glasses.

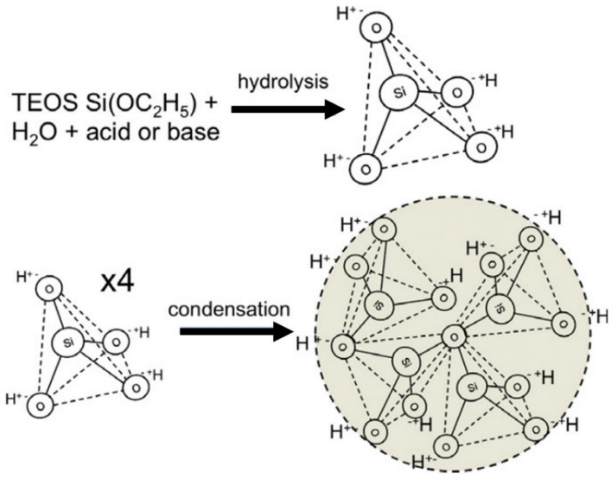


Figure 2.3 - The formation of silica tetrahedra and nanoparticles at room temperature in the sol-gel process. Adapted from [4]**.**

As shown in Figure 2.3, in the sol-gel process starts from a compositional precursor, TEOS as an example, which is hydrolysed and then condensed into nanoparticles at room temperature, which are then assembled into a gel through polymerisation-type reactions [45]. Either acidic or basic based catalyst can be used for this gel formation reaction. The process for using acidic based sol-gel process includes hydrolysis of precursors and condensation to form a gel that contains excess solvent, water and ethanol. Aging and drying processes are then carried out. Aging is carried out in a sealed container to let the condensation reaction continue and liquid is then removed during the drying process. Nanopores are formed because liquid has left the structure. After the gel is dried, heat treatment is needed, normally at 600-800°C, to stabilize the particles. Both drying and stabilization processes need to be carried out slowly to avoid the sample cracking [46]. The base catalysed sol-gel process will give spherical nanoparticles and the synthesis route is known as Stöber process which will be discussed in more detail in *Section 2.7.*

Sol-gel derived bioactive glasses can have up to 90 mol% SiO_2 compared with melt-derived bioactive glasses which will lose bioactivity when the SiO_2 content goes over approximately

60 mol% and this is attributed to the nanoporosity and low network connectivity of sol-gel glasses [47]. The sol-gel process has also simplified the glass composition needed for synthesis compared with the melt-quenching process, which needs the presence of Na_2O to lower the glass melting point. With the sol-gel process, sodium is no longer needed as no melting is required [4].

Table 2.3 – Advantages& disadvantages of 'Melt-derived' vs 'Sol-gel' process.

	Melt-derived	Sol-gel
Available bioactive composition	Few	Wide range to choose
Temperature needed	High	Low
Made into porous scaffolds	Hard	Easy
Synthesis time	Short	Long aging & drying process
Product purity	Hard to achieve high	High

2.5 The mechanism of bioactivity for bioactive glasses

The bioactive mechanism can be identified as two stages, stage 1: the formation of HCA layer and stage 2: the intracellular interaction between HCA and host bone surface.

2.5.1 HCA formation

The reaction between bioactive glasses and the host tissue to form a HCA layer can be summarized into 5 steps. (1) At beginning, Na^+ or Ca^{2+} cations exchange with H^+ from solution (Figure 2.4) and the pH of surrounding solution increases [48].

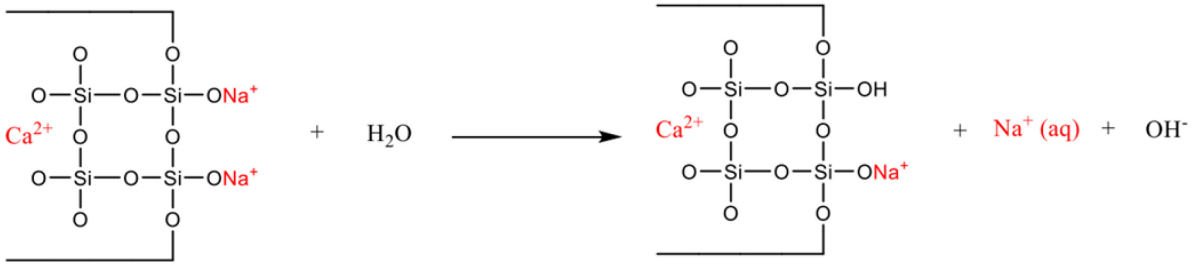


Figure 2.4 - Scheme for ion exchange [48].

Due to the pH change in step 1, Si-O-Si bonds are attacked by OH^- and hydrolysed (2). Soluble silica SiO_4^{4-} is then released into the solution, leaving Si-OH at the glass surface. (3) Silanol groups left in step 2 condense and a silica rich layer if left. (4) Calcium ions and phosphate ions from the bioactive glass network and the fluid migrate to the silica rich layer, forming an amorphous $CaO\text{-}P_2O_5$ rich film. (5) Hydroxyls and carbonate from the surrounding solution are then incorporated into the film, leading to the crystallization of $CaO\text{-}P_2O_5$ and then HCA forms [49][50].

2.5.2 Intracellular interaction between HCA and the bone.

When the HCA layer is formed, fibronectin, an extracellular protein, attracts macrophages, mesenchymal stem cells and osteoprogenitor cells to the HCA surface [51]. The osteoprogenitor cells then differentiate into osteoblasts which form an organic matrix. Guided by the osteoblastic cells, this organic matrix is then mineralized (Figure 2.5)[52].

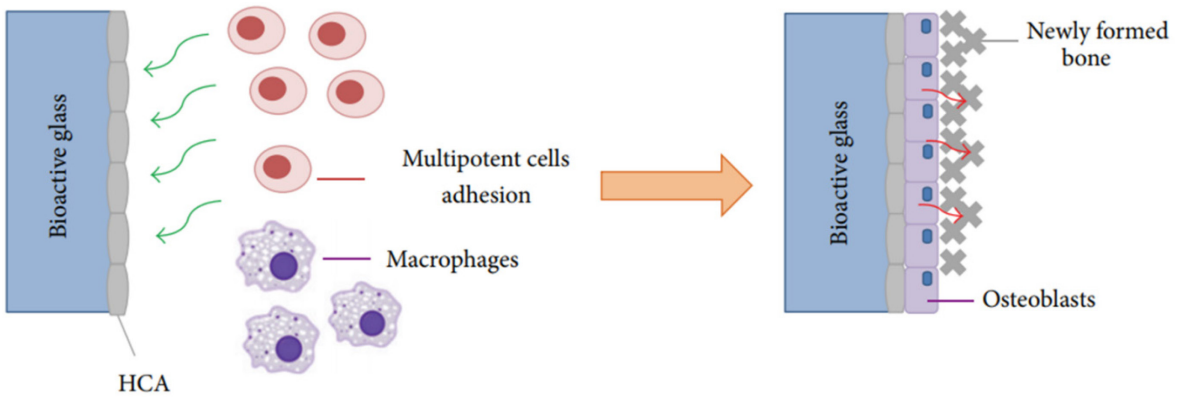


Figure 2.5 - The simple scheme for the bone formation on HCA layer. Adapted from [193]

2.6 Sol-gel hybrids

Hybrid materials are composed of inorganic and organic components which are interacting at molecular level and they are indistinguishable at the microscale [53]. The synthesis of hybrid materials uses the sol-gel process, but a polymer is introduced after the inorganic sol is prepared. Therefore, the inorganic network forms around polymer chains [46].

Compared with sol-gel derived bioactive glasses, the synthesis for hybrid materials needs a lower temperature around 60°C for aging and 130°C for drying. The process of stabilization and sintering is not needed [4].

Depend on the interaction between inorganic and organic components, hybrids can be classified as four types. Components interact using hydrogen bonding or molecular entanglements are identified as Class I hybrids while components in Class II hybrids are covalently bonded and the covalent bonds are formed due to the polymer having been pre-functionalised to have groups that can covalently couple to the inorganic component. Class III and Class IV hybrids are similar to the previous two classes but their organic and inorganic components are polymerized/formed *in situ.* Class III hybrids are corresponding to Class I which have non-covalent weak bonds and Class IV hybrids are corresponding to Class II with covalent bonds between components [53].

2.6.1 Class II (IV) hybrids

With the presence of covalent bonds, Class II hybrids have better mechanical properties compared with Class I hybrids. Their behaviour in water is also more stable. The covalent bonding also helps material to achieve a better homogenisation and tailorability [4].

The structure of a typical Class II hybrid is shown in Figure 2.6, a molecule is found between the polymer and silica network. This bridge between two components is called 'coupling agent'. The coupling agent is a molecule, or a short chain polymer, contains organic moiety on one side and three alkoxysilane groups on the other side. The organic part can be functionalized and bonds to the polymer network while the inorganic part can be hydrolysed and then condense with the silica network [46]

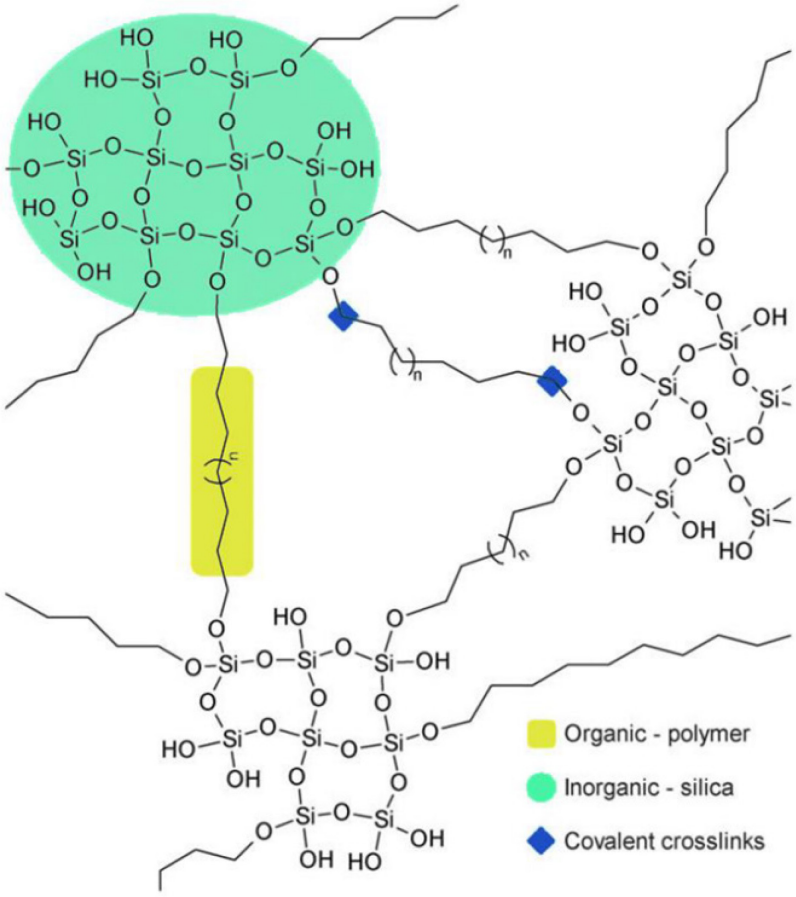


Figure 2.6 - Structure of a Class II (IV) hybrid with inorganic and organic components that are covalently bonded. Adapted from [46].

There are a range of polymer choices to be used as the organic components in a Class II hybrid. For example, polydimethylsiloxane (PDMS) [54] gives a hybrid with great mechanical properties but it is hydrophobic; 3-(trimethoxysilyl)propylmethacrylate (TMSPMA) and polymethylmethacrylate (PMMA) [55][56] have been made into hybrids which have great strength and ductile behaviour but they are not biodegradable; natural polymers like gelatin [57] have also been used to make hybrids, however, compared with synthetic polymers natural polymers have a lack of reproducibility.

The choice of coupling agent depends on the polymer's functional groups. 3-(glycidyloxypropyl)trimethoxysilane (GPTMS) is used with polymers contain carboxylic groups, e.g. gelatin, where the epoxide ring from GPTMS is opened by the nucleaophilic carboxylic group [57]. Polymers containing hydroxyl functional groups can use 3-isocyanatopropyltriethoxysilane (ICPTES) as the coupling agent [58]. Coupling agents are normally added before the sol-gel process to functionalize the polymer.

2.6.2 Calcium incorporated hybrids

Undoubtedly, the role of calcium in bone formation is important. In bioactive glasses, calcium ions not only participate in HCA formation but also induce osteoblast proliferation [59]. As a result, the incorporation of calcium into hybrid materials to make them bioactive for applications is needed.

The most common calcium precursor used in sol-gel bioactive glasses is calcium nitrate, which needs heat treatment at 400 °C to remove the by-product, nitrate, which is toxic [60]. This process is impossible to carry out for hybrid materials as the high temperature will burn off the polymers.

Poologasundarampillai *et al*. demonstrated using calcium chloride as the calcium precursor in a poly(g-glutamic acid) (γ-PGA) hybrids [61]. Although there is no toxic by-product released during the synthesis, the calcium was not incorporated into the silicate network and the crystallization of $CaCl_2$ was found on material surface and this is also because of the temperature using is limited at 60°C [62].

Another calcium precursor commonly used in sol-gel bioactive glasses is calcium methoxyethoxide (CME). It is found to provoke improved glass homogeneity compared with

calcium nitrate [63]. This raises the interest of using CME as the calcium precursor in hybrid systems. Poologasundarampillai *et al.* [8] used CME in γ-PGA hybrids and calcium is successfully incorporated into the silica network at low temperature. They also reported an increase in compressive strength due to the ionic crosslinking of γ-PGA caused by calcium. However, CME is sensitive to water as it gelled very quickly with the presence of water which has limited the choices of hybrid systems that it can be incorporated into [64][65].

Ting [66]demonstrated using CME in the PTHF/PCL/Silica hybrid system and successfully 3D printed scaffolds containing CME. However, it is found that the gelation time and the printing window was dramatically shortened by introducing CME.

2.7 PCL hybrids

2.7.1 PCL in tissue engineering

Polycaprolactone (PCL) biocompatible and biodegradable material for FDA approved implants. It also has great rheological and viscoelastic properties compared with other polyesters and this means PCL is easy to handle, modify and manufacture into implants [67].

In bone applications, PCL has been well studied and manufactured into different products. Electrospinning is one of the popular techniques to fabricate PCL bone scaffolds. Thomas *et al.* have studied the effects of PCL nanofibre's alignment on mechanical properties [68]; Choi *et al.* has manufactured PCL/collagen scaffolds by electrospinning and human skeletal muscles cells were cultured on this nanofibre matrix [69]. Bioactive scaffolds have also been fabricated by using medical grade PCL (mPCL) and 20% beta-tricalcium phosphate are incorporated into the mPCL [70][71]. This combination has been further by Abbah *et al.* [72] and showed capability of inducing porcine bone ingrowth to scaffolds but the mechanical testings showed scaffolds had a limited range of motion.

PCL also plays an important role in cartilage scaffolds design. A biphasic implant using PCL and fibrin glue loaded with TGF-β1 was manufactured by Huang *et al.* and the study showed that the scaffold successfully recruited mesenchymal cells and when the scaffold was implanted in the sub-periosteum, chondrogenesis occurred [73]. By using electrospinning, Li *et al.* produced 3D nanofibrous PCL scaffolds seeded with fetal bovine chondrocytes (FBCs) and the results suggested that 3D substrate, compared with the flat specimen, was better environment for proliferation and chondrocytic phenotype maintenance [74]. Furthermore, a novel hyaluronic acid/PCL scaffold was developed then tested in animals and implanted scaffolds showed excellent capsular in-growth [75]. However, for all these studies mechanical properties were either not reported or did not match cartilage's mechanical properties.

2.7.2 PCL Class II hybrids

Although PCL has been widely used in tissue engineering, it is difficult made into hybrid materials as it is not soluble in water and it does not have many functional groups to bond with inorganic molecules [76].

Developed by Tian *et al.* [77], a PCL containing Class II hybrid was made for the first time. In his hybrid system, TEOS was used as precursor for inorganic component, PCL diol was used as organic component and ICPTES was chosen as the coupling agent which formed a urethane linkage between -NCO and -OH. This hybrid system was biodegradable when tested in porcine esterase solution and biocompatibility was tested in fibroblast cells but no mechanical properties were reported and the hybrid gelation time was considerably long (4 days) [78].

Rhee *et al.* has also manufactured SiO_2/PCL hybrids with similar method by using ICPTES as the coupling agent [79]. Their research reported hybrids degraded slower with higher PCL molecular weight and the mechanical properties of PCL hybrids were also reported for the first time with a Young's Modulus of 582 ± 179 MPa, tensile strength of 20.8 ± 0.7 MPa and a tensile strain of 48 ± 8 % which did not match the ideal requirements for bone (too weak) nor cartilage (too strong)[80].

Another interesting PCL/SiO_2 hybrid system was developed by Sang *et al.* [81]. This Class II hybrid system contained a copolymer, poly(CL-*co*-GPTMS), and silica inorganic component. The synthetic copolymer was designed with a GPMTS unit as the side chain so there is no need for coupling agent in the hybrid synthesis. The synthesis strategy for this copolymer was one pot ring-opening polymerisation (ROP) (Figure 2.7). The advantage of using this method is the amount of methoxysilane groups and caprolactone (CL) repeating units are precisely controlled. The mechanical properties can be tuned by changing the ratio between GPMTS and CL repeating units.

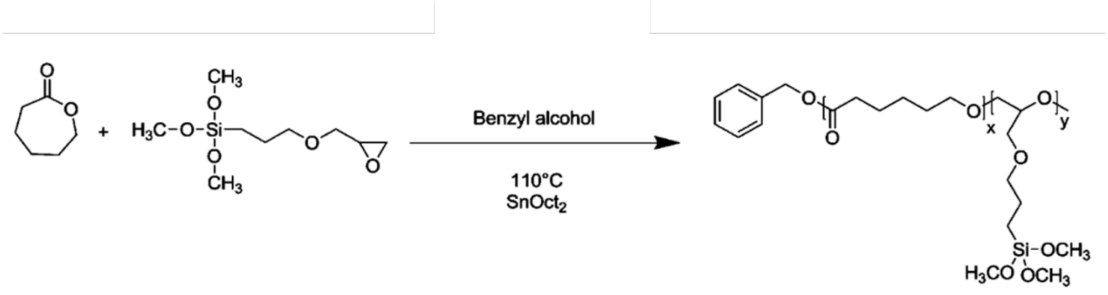


Figure 2.7 - Scheme for synthesis poly(CL-co-GPTMS) using caprolactone and GPMTS.

2.7.3 Poly(tetrahydrofuran)/PCL/SiO_2 Hybrids

Conventional PCL hybrid systems described above are only composed of one organic component and an inorganic component, However, recently Tallia *et al.* [10] established a PCL hybrid system that not only has PCL as its organic component, but also poly(tetrahydrofuran) (PTHF) (Figure 2.8). In this double network system, PCL-diCOOH is covalently bonded with silica network via GPTMS and this gives the first network. In the second network, PTHF is also covalently bonded with silica via GPMTS and at the end of PTHF chain PCL-COOH. Interestingly, between the long PTHF polymer chains, non-covalent bond interaction are proposed because the made material show a self-healing ability [10]..

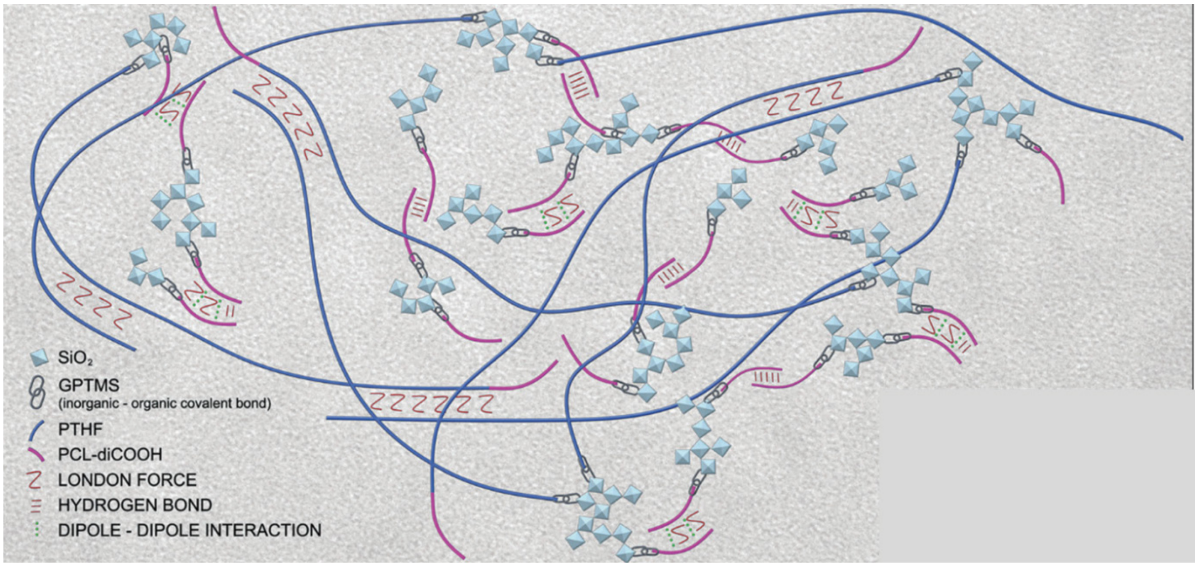


Figure 2.8 - Proposed structural network of the PTHF/PCL/Silica hybrid. Adapted from [10]**.**

The reaction mechanism proposed for this hybrid system is an *in situ* cationic ring opening polymerisation (CROP) by using boron trifluoride diethyletherate, which is a common Lewis acid and is a source of boron trifluoride (BF_3) which can be further hydrolyzed with water into fluoroboric acid and has a high acidity and will give potential cytotoxicity if they are not removed/reacted completely [82]. (Figure 2.9). GPTMS acts as an initiator: the high ring strain of epoxide ring attracts boron trifluoride diethyletherate (BF_3OEt_2) which then attacked by THF through nucleophilic attack and at this stage CROP is initialised. As the chain keeps growing, the presence of PCL-diCOOH may terminate the polymerisation as carboxylic groups may attack the oxonium ion [83][84][85].

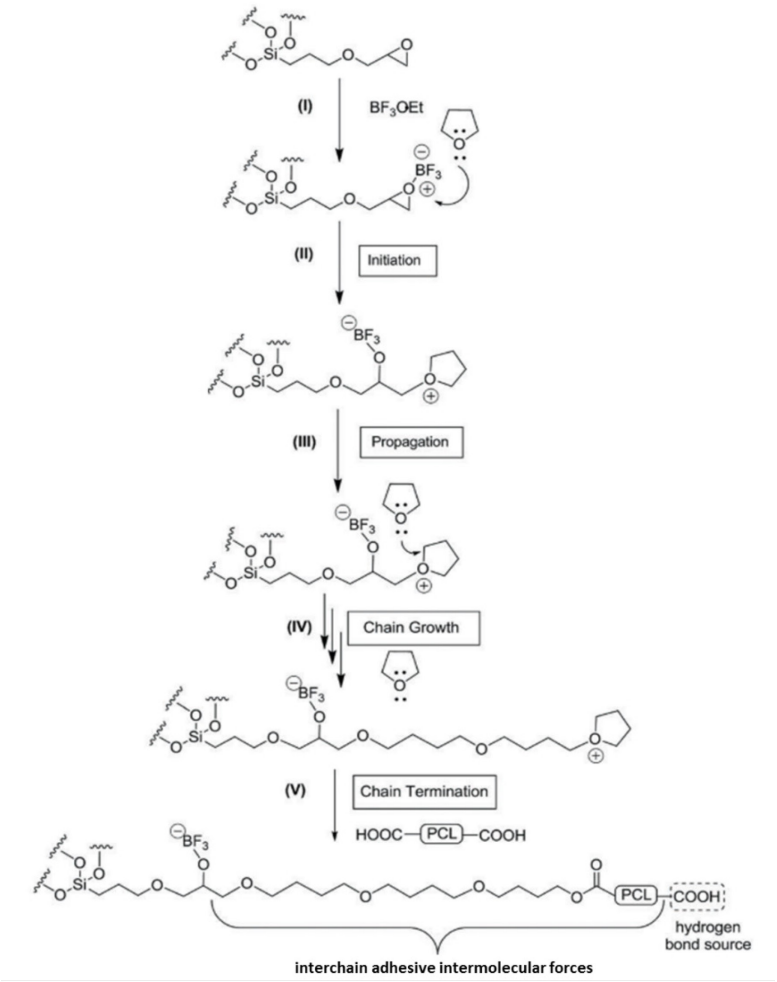


Figure 2.9 - Proposed mechanism of the ring opening polymerisation of polyTHF with PCL-diCOOH acting as the chain terminator. Adapted from [10]**.**

The resulted bulk samples and scaffolds fabricated by 3D printing showed a 'bouncy' behaviour and capable to self-heal without any trigger. The mechanical properties were tuneable by changing the ratio between organic and inorganic components: by increasing the inorganic weight percentage from 2.5 wt% to 39 wt%, tension tests showed true strain to failure decreased from 25.5±3.3% to 2.4±1.5% and true stress to failure increased from 0.12±0.05 MPa to 1.42±0.47 MPa [10]. However, until now, bioactivity is still a challenge to achieve in this system.

2.8 Sol-gel derived silica nanoparticles

Over decades, great efforts were made to investigate novel methods to synthesise silica nanoparticles (SNPs), resulting in precise control on the morphology [86]. Because of the tailorable morphology, SNPs show a various number of potential applications such as intracellular delivery of molecules and cell tracking [87]. The ability of cation incorporation such as strontium [88] and calcium [89] has also broadened their therapeutic application potential.

The synthesis strategy of silica nanoparticles depends on the morphology of the wanted nanoparticles. The general strategy can either be a top-down method or a bottom-up method (Figure 2.10)[86]. Top-down methods involve grinding bulk materials into fine size particles while bottom-up methods involve assemble atoms or molecule constituents into nanoparticles. This project focused on using the sol-gel process, a bottom-up approach, to synthesise silica dense nanoparticles (SNPs) and mesoporous nanoparticles (MSNs).

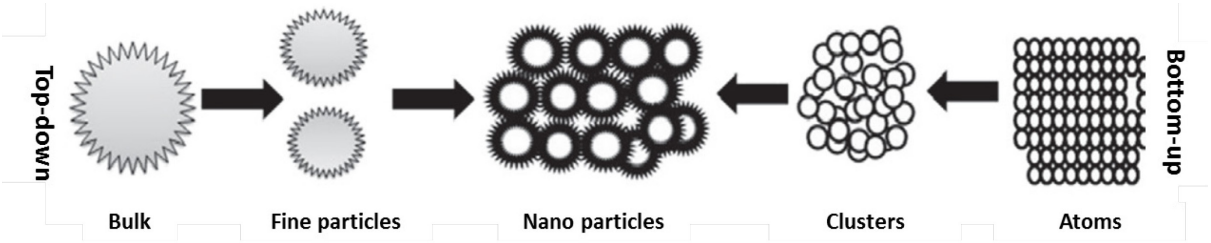


Figure 2.10 - Approaches for the synthesis of silica nanoparticles. Adapted from [86]

2.8.1 Dense nanoparticles

A well-known method for preparing dense silica nanoparticles is the Stöber process, established by Stöber *et al.* in 1968 [90]. In this ammonium hydroxide catalysed basic sol-gel process, SNPs were synthesised with diameter ranged from 10 nm up to 1 µm. In the Stöber process, the particle size, morphology, and distribution can be controlled by varying reaction parameters [91].

The reaction for silica spheres is similar to the acidic sol-gel process that TEOS is hydrolysed and then condensed [92]. However, the mechanism of particle growth is complicated. Reported by Lee *et al*. [93] and Bogush *et al.* [94], the growth of silica nanoparticles followed

a nucleation and aggregation mechanism (Figure 2.11). First, LaMer and Dinegar's theory of monomer addition [95] occurs and gives primary particles. The high pH value then causes repulsion between these primary particles and gives individual particles. Meanwhile, the polycondensation reaction also occurs, resulting in the formation of secondary particles [47].

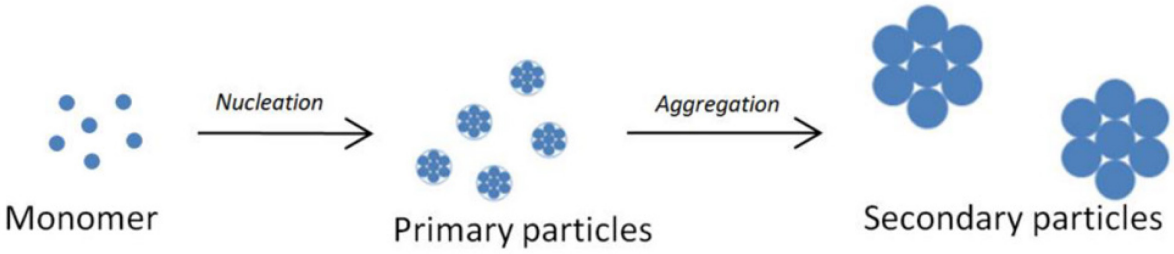


Figure 2.11 - Nucleation and aggregation mechanism for silica nanoparticles. Adapted from [168].

The Stöber process has been modified many times in literature. For example, Park *et al.* [96] used a semi-batch process with a feed pump. They fed a solution containing water, ethanol and ammonia with another solution containing TEOS and ethanol. Bogush *et al.* [94] synthesised more uniform particles with a seeded growth technique. However, most of those adaptions have made Stöber process more complicated with no obvious advantages.

Greasley *et al.* [89] demonstrated using a simple version of Stöber process to synthesise size controlled SNPs reproducibly. They reported increasing the concentration of ammonia also increased the particle size (Figure 2.12). They also found increasing the TEOS concentration resulted in a higher SNPs yields but the polydispersity also changed from monodisperse to heterodisperse.

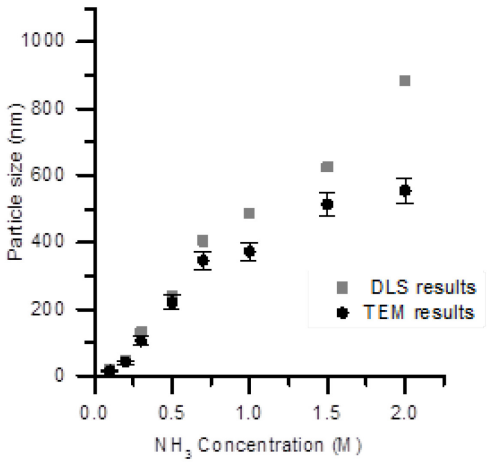


Figure 2.12 TEM and DLS results on particle diameter with increasing ammonia concentration and [TEOS]=0.28M [89].

2.8.2 Mesoporous silica nanoparticles

Interest in mesoporous silica nanoparticles (MSN) have grown incredibly after the MCM-41 ,spherical hexagonal mesoporous silica nanoparticles, were used in drug delivery in 2001 for the first time [97]. With the porous structure and high surface area, MSNs have proved themselves to be a better drug delivery carrier over SNPs in many cases [98]. In addition, depending on the content incorporated in or functionalized on MSNs, drug delivery systems can be designed not only for cancer treatments [99][87], but also for bone and tissue

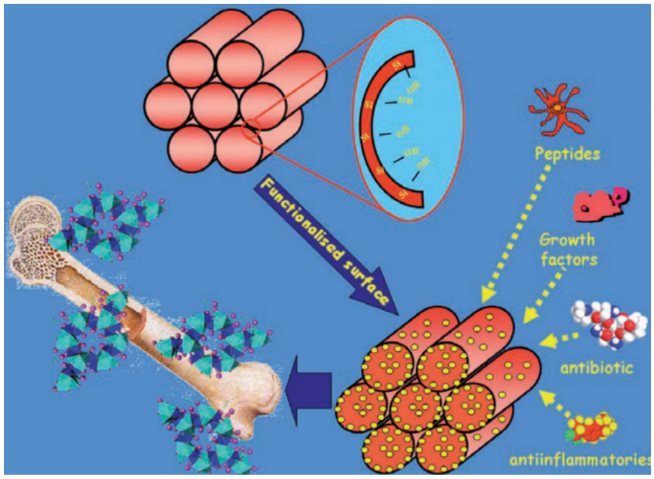


Figure 2.13 - Scheme of showing MSNs in the bone regeneration. Adapted from [100].

engineering [100][101].

The synthesis methods of MSNs have been developed and investigated by huge number of groups in past decades and most of them are adapted from the Stöber process by introducing a surfactant, used as a micelle template, in the synthesis [102][103][104][105]. Among these studies, cetyltrimethylammonium bromide (CTAB) is found to be one of the most used surfactant micelles for silica. The concentration of surfactants in the solution is important and the term 'critical micelle concentration' (CMC) is established and meaning the concentration threshold for surfactants start to self-assemble and form micelle and shield the hydrophobic parts (Figure. 2.14 a). If surfactant concentration keeps increasing, cylindrical structures, periodic hexagonal, cubic and lamellar mesophases will be given [106]. When silica precursors are added into the solution, they are hydrolysed and condense at the surfactant surface and form a silica wall around micelle surface. Hollow meso-channels are formed after removing the surfactant.

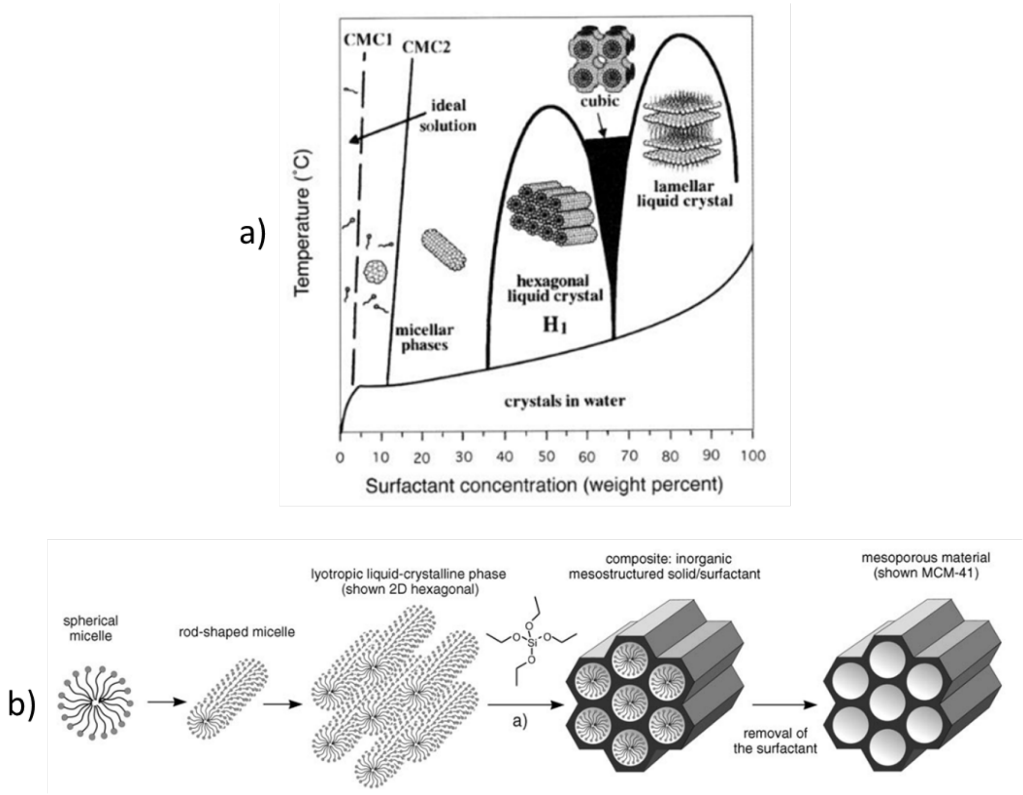


Figure 2.14 - a) Phase diagram of CTAB in water with increasing concentration. Adapted from [106]**. b) scheme of synthesis MSNs by using CTAB as a template. Adapted from** [194]**.**

2.8.3 Cation incorporation

To make silica nanoparticles bioactive, it is essential to incorporate cations. In the case of bone regeneration, calcium (Ca) is focused on. The traditional precursor for calcium is calcium nitrate and it can only be incorporated into the network when the calcination temperature is above 400˚C [107]. As shown in Figure 2.15, when calcium nitrate is added into the nanoparticle solution it is dissolved. After the mixture is dried, calcium nitrate precipitates at the surface of nanoparticles. Calcium diffuses into the silica network when 400˚C is applied but a heating above 600˚C is required as this will finally remove the nitrates [107][108]. When an excess amount of calcium is added into the solution before heating, aggregation will be caused as calcium ions on the particles surface change the surface charge [109].

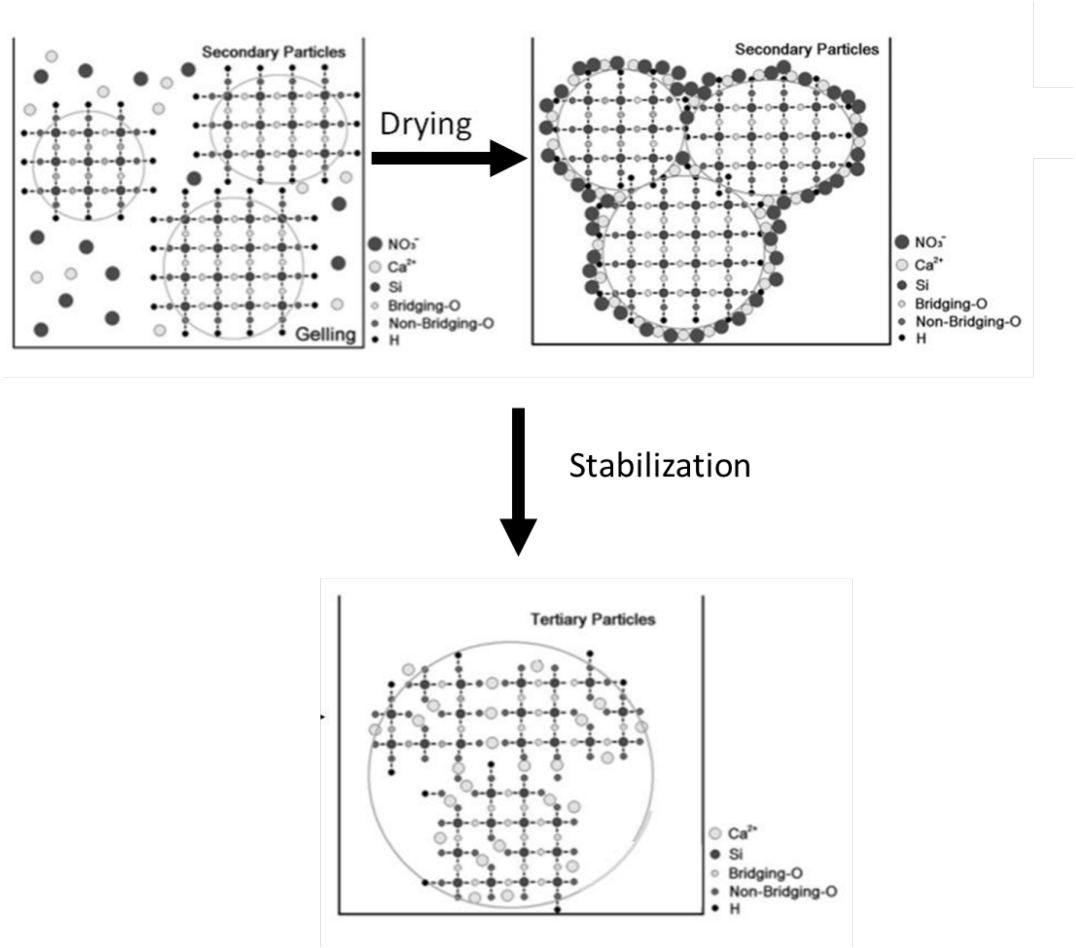


Figure 2.15 - Schematic showing the change of Ca distribution during the incorporation process. Adapted from [107].

2.8.4 Nanocomposites

The term 'nanocomposite' refers to a combination of different phases with at least one of the constituents under 100 nm [110]. The inorganic part of a silica nanocomposite can either be a precursor (TEOS) or silica nanoparticles. For silica nanoparticles, solution blending is one of the most used methods to make nanocomposites which just mixes nanoparticles into the polymer [111]. Many groups have demonstrated making nanocomposites with bioactive silica nanoparticles by using solution blending [112][113][114][115]. The introduction of bioactive silica nanoparticles in these nanocomposites were all reported with apatite forming ability and Loher *et al.* [116] also reported an increasing in Young's modulus of original Poly(lactide-co-glycolide) (PGLA) polymer and faster polymer degradation rate was observed.

However, only few bioactive nanoparticles are covalently bonded to the polymer matrix are found in literature. Liu *et al.*[117] used hexam-ethylene diisocyanate (HMDI) as a coupling agent between poly(L-lactide) (PLLA, 9700 Da) and bioactive nanoparticles and found the tensile strength increased from 56.7 to 69.2 MPa. The in vitro study showed the capability of formation an apatite layer on nanocomposite surface, compared to pure PLLA scaffolds. El-Fiqi *et al.*[118] functionalized particle surfaces with amine groups which were then used to bond with the carboxylic groups from collagen. The resulting nanocomposite hydrogel was found shrink less and had improved mechanical properties.

Although most of nanocomposites are reported better mechanical properties have been achieved, they are still high dependent on the mechanical properties of the original polymer matrix used and this has limited the applications of these materials such as in bone regeneration.

2.8.5 Nanoparticles grafted with GPTMS

The functionalization method of silica nanoparticles with GPTMS is termed as liquid phase process [119]. The reaction can happen in aqueous solution or organic solvent. With the presence of water, methoxylsilane groups are hydrolysed to Si-OH groups which are then condensed with the silanol groups on the particles surface. However, this condensation may

also happen between GPTMS molecules and forms irregular multi molecular layers [120]. In organic solvents, a simple one step reaction occurs between GPTMS and the silica surface as shown in Figure 2.16.

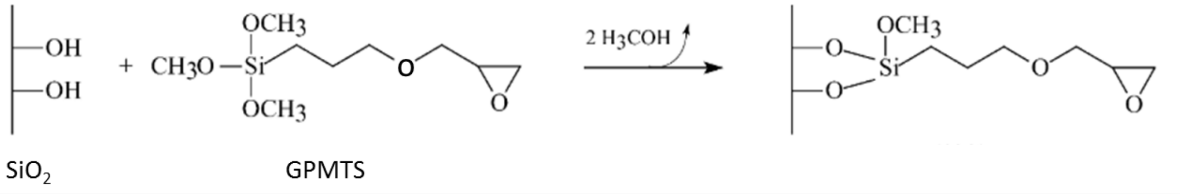


Figure 2.16 - Reaction between silica gel and GPTMS molecule in an organic solvent.

Theoretically, the absence of water should result in monolayer of GPMTS, but Allen *et al.*[121] reported that there were still some multi-layer regions found due to the difficulty in eliminating all the water molecules in the reaction. He *et al.*[122] suggested the use of acidic silica sol with pH = 2.6 in organic solvent can give proposed monolayer structure, however, the low pH may leads to the opening of epoxide ring if the water molecule is not fully eliminated (Figure 2.17).

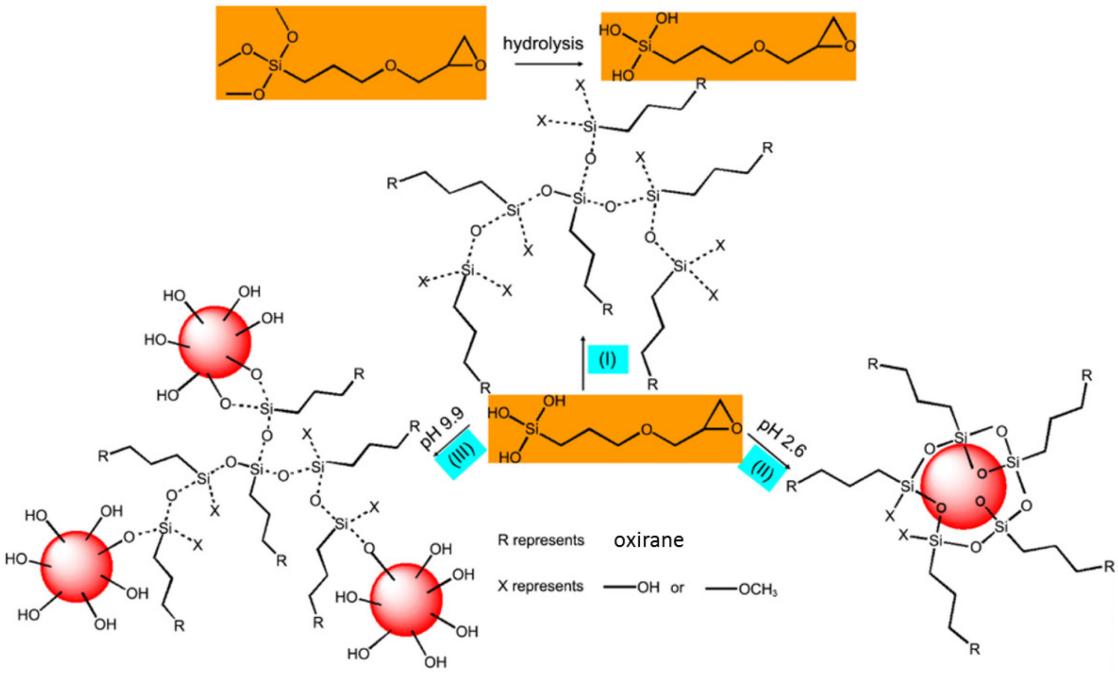


Figure 2.17 - Reaction mechanism of grafting GPMTS. Adapted from [122].

The characterisation method of GPTMS-SiO_2 can be Fourier transform infrared spectroscopy (FTIR) [123], X-ray photoelectron spectroscopy (XPS) [124], solid-state NMR [125], Raman spectra [126] and thermogravimetry (TGA) can also be utilized to quantify the organic components [125].

2.9 Additive manufacturing

The criteria of an ideal scaffold for bone/cartilage regeneration as mentioned in previous section need a custom-made fabrication method in order to generate scaffolds with different morphology to fit in different defects. It is also important to have porous scaffolds with designed pore size which is an important parameter in scaffolds to determine the permeability of nutrients and scaffolds' mechanical properties. Studied by Mitsak *et al.*[127], PCL scaffolds fabricated with a higher porosity and permeability lead into better bone regeneration, blood vessel infiltration and compressive strength.

The development of additive manufacturing (AM) has made the fabrication of ideal scaffolds easier and handier. It is a fabrication process normally starts with a computer-aided design (CAD) file with a 3D model of the wanted scaffold and the AM machine manufacture the scaffold layer by layer [128]. There are many AM techniques used in generating scaffolds for bone regeneration and they are summarized in Table 2.4.

Table 2.4 - Techniques for Additive Manufacturing of scaffolds for tissue engineering.

Technique	Process	Processed materials	Advantages/Disadvantages
Laser-assisted bioprinting [129][130][131]	-Deposition control by laser pulse energy -Resolution control by distance between ribbon/substrate, spot size and stage movement	-HA -HA osteoblast-like cell -Nano HA -Human osteoprogenitor cell -Human umbilical vein endothelial cell	Adv: -Applicable for organic, inorganic materials and cells -Quantitatively controlled Disadv: -Homogeneous ribbons needed
Selective Laser Sintering[132][133][134]	-Preparing the powder bed -Layer by layer addition of powder -Sintering each layer according to the CAD file, using laser source	-PCL -Nano HA -Calcium phosphate -Carbonated hydroxyapatite -PLLA	Adv: -No post processing is needed Disadv -Feature resolution depends on laser beam diameter
Stereolithography [135][136][137]	-Immersion of platform in a photopolymer liquid -Exposure to focused light according to desired design -Polymer solidifying at focal point, non-exposed polymer remains liquid -Layer by layer fabrication by platform moving downward	-Poly(propylene fumarate)(PPF) -HA -PDLLA/HA	Adv: -Complex internal features can be obtained -Growth factors, proteins and cell patterning are possible Disadv: -Only applicable for photopolymer
Robocasting [138][139][140][141][142][143][144]	-filaments of viscous material extrusion based on the predesigned structure -Layer by layer deposition of filaments at constant rate under specific pressure -Disruption of filaments according to the tear of speed	-PCL -HA -Bioactive glasses -Mesoporous bioactive glass/alginate composite -Polyactic acid -PLA/PEG/G5 glass -Bioactive 6P53B glass	Adv: -Mild condition of process allows drug and biomolecules plotting -Independent 3D nozzle movement -Precise control on thickness Disadv: -Heating/post-processing needed for some materials

2.9.1 3D extrusion printing

3D extrusion printing or so-called robocasting, is one of the many techniques used in AM. Compared with other techniques, materials can be chosen as the printing ink is more flexible and the overall cost is low [145].

A typical extrusion printing system consists of an ink reservoir (or syringe) which can move in x, y and z directions to control the position of extruded filament, a printing platform that can fix the substrate and a nozzle with a printing tip that can squeeze viscous ink into filaments. An ink reservoir can be a syringe cartridge and pistol in the cartridge is pressed down to squeeze the paste like ink out of the tip. Continuous filament is generated and 3D structure can be constructed layer by layer (Figure 2.18).

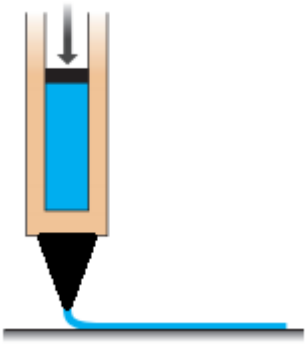


Figure 2.18 - Extrusion head generating a continuous filament. Adapted from [195]**.**

The general rheological properties required of the ink should be shear thinning which means they should be able to flow through the nozzle under load but hold the shape when in contact with the substrate and no longer under load [145]. The geometry of printing tip has a great effect on the extrusion load [146] – a standard metallic tip has almost 7 times extrusion load than a conical plastic tip (Figure 2.19). As a result, a cone tip is preferred for materials with high viscosity. Viscosity also determines the nozzle size, inks that are less viscous should use nozzle tips with smaller nozzle diameter to give fine struts and reduce the minimum separation between struts.

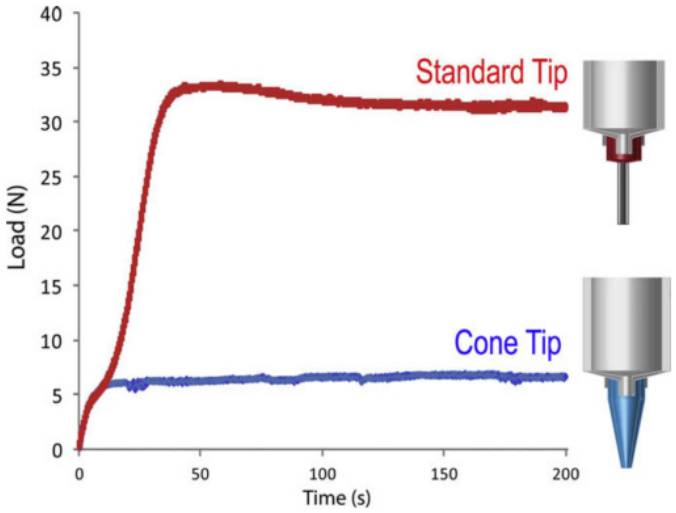


Figure 2.19 - Load versus time curves for inks through a standard metallic tip and a conical plastic tip [146].

2.9.2 3D extrusion printing for hybrids

Hybrid materials using polymer/silica network are synthesised with sol-gel process which provide a chance they can be directly 3D extrusion printed from sol, utilising the gelation process, although very little studies are found from literature.

A Class I gelatin/silica hybrid was first printed by Gao *et al.* [147]. Prior to the printing, a hybrid ink was aged at 37°C to achieve the printable viscosity and shear thinning behaviour. While the silica network was condensing, gelatin was also cooling down and gelled at room temperature after being extruded on the substrate. Printed scaffolds were then treated with a NHS-EDC crosslinking protocol, however only gelatin crosslinked with itself around the silica network instead of having an organic-inorganic bonded Class II network. Mechanical tests showed a dramatic drop in compression strength when printed scaffolds were soaked in aqueous solution due as the water separate the gelatin from the silica.

Nelson demonstrated 3D extrusion printing of a Class II gelatin/silica hybrid scaffold [148]. The hybrid system was first developed by Mahony *et al.* [57] which uses GPTMS as the coupling agent to bond gelatin to the silica network. Hybrid was prepared as sol and they optimised the sol viscosity. Inks were then loaded in a 5 mL syringe that connected to the printing tip via a clear tubing. A syringe heater was used to apply a heat at 40°C to ensure the ink could smoothly flow through the tube (Figure 2.20). Printed scaffolds were immediately

transferred to a 40°C oven for aging. Critical point drying was applied after aging and scaffolds with 200 µm pore size were made. The tested compressive strength was 1.3 MPa, compared with scaffolds made by foaming which were 0.06 MPa[57], a significant improvement was achieved by using 3D extrusion printing.

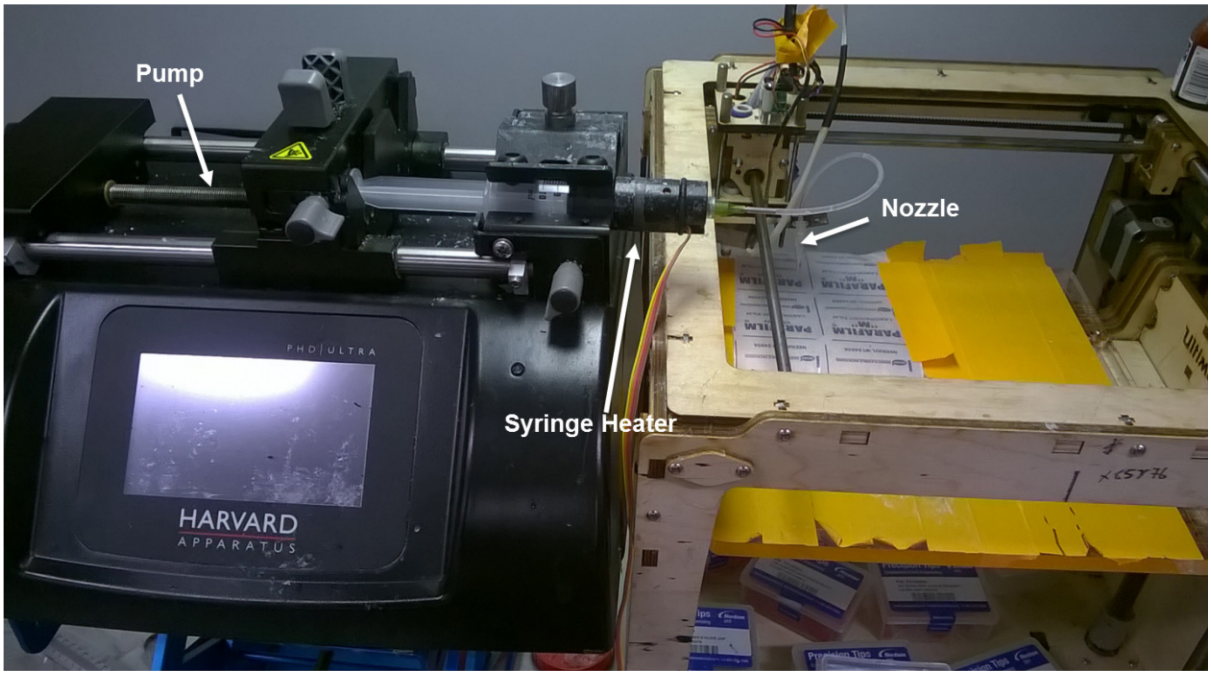


Figure 2.20 - Photo showing the 3D extrusion setup used by Nelson. Photo taken by the thesis author.

Recently, Tallia *et al.*[10] successfully printed the PTHF/PCL/Silica Class IV hybrid scaffolds, discussed in *Section 2.7.3*, by using 3D extrusion printing. Scaffolds with pore sizes 120 – 140 µm were produced. They have showed excellent mechanical properties, for cartilage applications, with a compressive strength of 1.67 MPa in dry conditions and 1.49 MPa after soaking in PBS for 7 days. However, the allowed printing time (printing window) was limited as the network condensed very quick resulted the ink gelled and blocked the printing nozzle, also this hybrid system was synthesised in organic solvent so the solvent evaporated much quicker during the printing compared with gelatin hybrids which were made in aqueous solution and printed scaffolds were not bioactive due the absence of calcium in the hybrid network.

2.8 Research objectives

Having reviewed the development and knowledge in silica nanoparticles, hybrids and 3D printing, the overall objective of this thesis was to develop a new PTHF/PCL/Silica hybrid system that contained calcium incorporated and GPMTS functionalized silica nanoparticles and to fabricate scaffolds of the new material using 3D extrusion printing.

Current calcium precursors for hybrid system all have disadvantages. Silica nanoparticles can incorporate cations. The potential solution can be introducing calcium incorporated silica nanoparticles into the hybrid system and make it bioactive. Unlike conventional nanocomposites, the chosen system here already has a silica network and nanoparticles will be functionalized with GPTMS before adding into the system so they will covalently bond with the polymer network and have better mechanical properties.

In addition, with calcium incorporated nanoparticle surface is grafted with GPTMS, a slower release of calcium ions from the hybrid is expected. Compared with non-bonded particles, bonded particles should take longer to leave the hybrid network and dissolve in solution.

The reason for choosing PTHF/PCL/Silica hybrid system is because this system has already shown excellent mechanical properties both in dry and wet condition, its mechanical property is also tailorable and it is feasible for printing. It is also interesting to have a double organic component – double inorganic component network with the introduction of silica nanoparticles.

The thesis will first look at the possibility of functionalizing calcium incorporated dense silica nanoparticles and mesoporous nanoparticles. Although literature has demonstrated the functionalization between GPTMS and silica nanoparticles or silica gel, no one has done any research on calcium incorporated nanoparticles. It is challenge because the high temperature used during the particle calcination will burnout hydroxyl groups on the particle surface which are needed for reacting with GPTMS molecules. Considering the amount of GPTMS grafted on the particle surface will be low, it will also be a challenge to quantify and qualify the presence of GPTMS.

The thesis will then look at the making of this bioactive double inorganic double organic network hybrid system and 3D print it into scaffolds. The expectation is to have a controlled release on calcium and improve the 3D printing process by prolonging the printing time.

Chapter 3 Characterisation

The following characterisation techniques were used throughout Chapters 4-6.

3.1 Silica nanoparticles characterisation

3.1.1 Dynamic light scattering (DLS)

DLS is a powerful technique to determine the particle size and distribution in solution. It measures the hydrodynamic radius of particles by detecting the random Brownian motion of particles and the Brownian motion is given by the interaction between particles and solution molecules [149].

During the measurement, a monochromatic beam is applied at the sample and the beam light is scattered by sample particles. The scattering information is collected by a detector set with an angle θ with respect to the transmitted beam light. Particles with larger diameter tend to give small angled scattered bean compared with smaller particles.

It is important to maintain the test environment temperature during the measurement because temperature will change particles' Brownian motion which then affects the accuracy of the final reading [150].

The instrument used was a Zetasizer Nano ZS (Malvern Panalytical Ltd). Test temperature was set at 20°C. Samples were dispersed in 1.5 mL of deionized water by sonicating for 10 minutes.

3.1.2 Zeta potential

Zeta potential gives the information about a colloidal dispersions' stability by showing the degree of electrostatic repulsion between particles [151]. The surface charge calculated can also give information about particle surface modification.

The surface charge on particles surface attracts ions and forms a Stern layer, the internal layer of the electric double layer. The existence of a Stern layer attracts more counter ions and forms a second layer. This double layer allows ions move freely and the electro-kinetic potential between this double layer is known as zeta potential. By applying an electric field to the sample, movement between particles and the dispersant occurs, known as electrophoresis. Electrophoresis is then measured by using Doppler velocimetry. The Henry

equation is then applied to calculate the zeta potential, with known values of dispersant viscosity, electric filed strength and dielectric constant [152].

The instrument used was a Zetasizer Nano ZS (Malvern Panalytical Ltd) with a test temperature set at 20°C. Samples were dispersed in 3 mL of ethanol by sonicating for 10 minutes and then 1 mL of the particle sol was transferred into the measurement cuvette.

3.1.3 Transmission electron microscopy (TEM)

High resolution images of nanoparticles can be obtained by using TEM. As shown in Figure 3.1, a tungsten filament emits electrons at high temperature and the electrons pass through and are focused by condenser lenses. Adjustment of the condenser lenses can control the beam current density and the image 'brightness'. Electrons then are focused by an objective lens, which allows the control on 'focus' in practice. Objective apertures allow the adjustment of image contrast at mass-thickness dominated regions. Intermediate lenses are used to toggle between image and diffraction pattern. Finally, the projection lens is for the final viewing screen imaging.

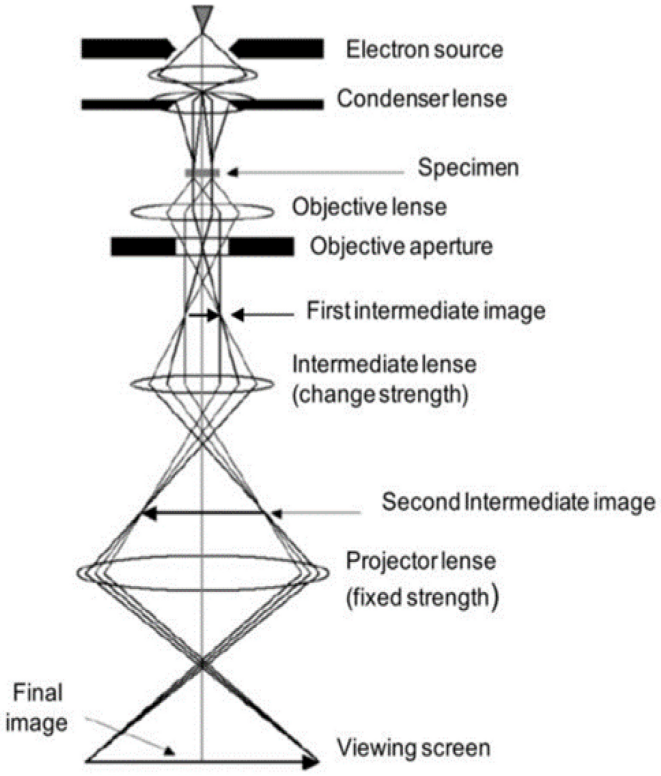


Figure 3.1 - Scheme showing TEM under imaging mode. Adapted from [196].

The instrument used was a JEM-2100Plus TEM (JEOL, USA) at 200 kV operating voltage. Samples were dispersed in ethanol and sonicated for 10 minutes before they were spread/dropped onto a 400-mesh copper TEM gird (Agar Scientific, UK).

3.1.4 Nitrogen adsorption

Information about particle nanoporosity and surface area can be obtained by using nitrogen adsorption. An isotherm plot can be obtained which shows the amount of gas absorbed at different relative pressure (P/P_0). Depending on the behaviour of the material, isotherm are classified into 8 types by International Union of Applied Chemistry (IUPAC) (Figure 3.2) [153].

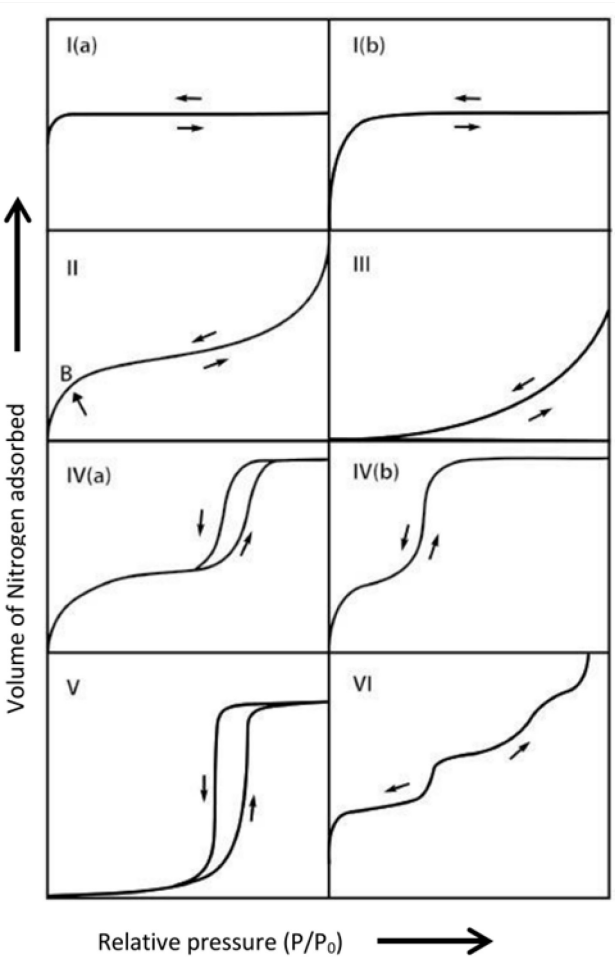


Figure 3.2 - IUPAC classification of physisorption isotherms. Adapted from [153].

The Brunauer–Emmett–Teller (BET) equation was used to calculate the surface area at the linear region of the adsorption isotherm [154]. Density functional theory (DFT) was suggested by literature to be used as the model for calculating pore size distribution of the nanoparticles as it is the most appropriate equilibrium model for pores under 4 nm compared[155][156].

The instrument used was an Autosorb- iQ-MP (Quantachrome). 100 mg of fine ground nanoparticles were loaded in a 9 mm samples cell. Samples were degassed for 24 h at 60°C.

3.2 Sample composition characterisation

3.2.1 Fourier transform infrared spectroscopy (FTIR)

The use of FTIR can help identifying specific bonds in the sample. When IR with a wavelength range 4000 – 400 cm^{-1} is applied to the sample, dipolar covalent bonds in the sample will absorb the energy at a specific wavenumber in this range. This energy will cause the excitation which leads to covalent bond vibration including stretching and bending. A detector is used to receive the reflected IR beam from the sample and create an IR spectrum against absorbance plot [157].

The Instrument used was Nicolet iS10 (Thermo Scientific). 64 scans at a full wavelength range were applied.

3.2.2 NUCLEAR MAGNETIC RESONANCE (NMR) SPECTROSCOPY

Solution-state NMR. Proton NMR (^{1}H-NMR) is the most common NMR analysis. In a proton NMR spectrum, chemical shift of peaks can give information about atoms bonded directly to protons which can be used to identify the functional groups containing hydrogen. The integration of the area under the peak can tell the proportion of protons from different functional groups and finally, the multiplicity of the peak gives the number of non-equivalent hydrogen neighbours [158]. The instrument used for solution-state NMR was a 400 MHz Bruker spectrometer. Samples were prepared in deuterated chloroform ($CDCl_3$).

Solid-state NMR. ^{29}Si MAS solid-state NMR is the technique to investigate the structure of solids, including the quantification of Q^n and T^n species in a silicate network. A Q^n structure correspond to $Si(O\text{-}Si)_n(OH)_{4-n}$, one Si atom bonded with four oxygen atoms. A T^n structure

means one Si atom bonded with one carbon and three oxygen atoms, and gives C-Si(O-Si)$_n$(OH)$_{3-n}$ in structure. By obtaining the relative abundance of Q^n and T^n species, the silica network condensation degree (D_c) can be calculated (Equation 3.1) [61].

$$D_C = \left(\left[\frac{4Q^4+3Q^3+2Q^2+Q^1}{4}\right] + \left[\frac{3T^3+2T^2+T^1}{3}\right]\right) \times 100\% \quad \textbf{Equation 3.1}$$

Solid-state measurements were conducted by Nicole Kelly from Dr. John Hanna group at Warwick University using a 7.0 T Varian/Chemagnetics InfinityPlus spectrometer.

3.2.3 Thermogravimetric analysis (TGA) and differential scanning calorimetry (DSC)

TGA and DSC are techniques to determine the thermal properties of a material. TGA evaluates the mass change of a sample under heating over the time. This method can tell the weight ratio between inorganic and organic components in a hybrid due to the weight loss from combustion of the polymers. DSC measures concurrently while TGA is running. It gives the difference in heat energy needed for a sample to increase to a certain temperature and a reference sample.

The instrument used was STA-449C Jupiter (NETZSCH). 20 -25 mg of samples were loaded in a platinum crucible. The upper temperature for all experiments was 800°C.

3.2.4 Inductively Coupled Plasma Optical Emission Spectroscopy (ICP-OES)

ICP-OES gives the accurate element concentration in a solution. Precise amount of solution is feed into a nebuliser and solution droplets from the nebuliser are then transferred to the plasma flame, created by argon gas and electromagnetic field. Samples in the plasma flame become to atoms due to the collision with electrons and charged particles in the plasma. Electrons around sample atoms are continuously excited and emit a radiation with a specific wavelength corresponding to sample's element, as electrons fall back into their valence band, and this is detected by the optical emission spectroscopy. Sample element intensities measured in OES are then compared with intensities measured from standard solutions with known element concentration, therefore, the final concentration readings can be plotted [159].

The instrument used was iCAP 6300 ICP-OES (Thermo Scientific). Standards were prepared from 0 to 40 ppm. Samples were diluted 10 times prior to the measurement.

3.3 Hybrid characterisation

3.3.1 Compression and tension tests

The mechanical properties of the hybrid materials are crucial to their application. Compressive and cyclic compressive tests were carried out on Z010 mechanical test machine (Zwic/Roell); Tensile testing were also tested on a Bose Electroforce Series III machine. Details for specific mechanical testing experiments will be stated in Section 6.3.5.

3.3.2 Scanning electron microscope (SEM)

The surface morphology of hybrid materials can be imaged using SEM. In SEM, a non-destructive electron beam is used to scan over the sample. When electrons from the beam arrived at the sample surface, they interact with atoms at the surface and cause secondary electrons to be emitted from the surface. The detection of secondary electrons can give information about the topography of the surface and forms a high-resolution image. Coating of samples is necessary to make samples conductive, otherwise electron beam will charge the sample surface and distort the image.

The instrument used was a Gemini 1525 FEG-SEM (Zeiss). Samples were coated with a 10 – 15 nm layer of chromium.

3.3.3 X-ray diffraction (XRD)

The information about crystalized compounds in the sample can be obtained by using XRD. The theory of how XRD analysis works is developed from X-ray beam electron scattering when hit with the sample. Bragg's law (Equation 3.2)[160] can be used to describe the diffraction pattern of crystalline structures.

$$n\lambda = 2d \sin\theta \qquad \textbf{Equation 3.2}$$

λ stands for the wavelength of the X-ray, d stands for the distance between atomic planes, θ refers to the angle of incidence and n is a positive integer.

The instrument used was D2 PHASER (Bruker). Samples were prepared as powder. Incidence angle was set from 6° to 70° with a 2θ step size of 0.0305° and a count rate of 0.5 s per step.

3.3.4 Simulated body fluid (SBF) dissolution study

Although SBF cannot fully and mimic the *in vivo* environment [161], it does provide a similar pH and ion concentrations to natural blood plasma. For bone regeneration applications, it can be used to investigate the HCA formation on the scaffold surface. Dissolution studies with SBF in this thesis followed the method established by Macon *et al.*[162] on International Commission on Glass TC04. They modified the ISO standard protocol, which was using sample surface area to liquid ratio, by using samples mass to liquid ratio and they proposed the modified method was more appropriate for bioactive glasses because of their high surface area.

The sample mass to SBF volume ratio used here was 75 mg of hybrids to 50 mL of SBF. SBF was prepared by using Kokubo's protocol [163] and details of reagents used are listed in Table 3.1. The dissolution study was designed to be 4 weeks long with time points at 0.5, 1, 2, 4, 8, 24, 72, 168, 336 and 752 h. At each time point, 1 mL of SBF supernatant was taken for the later analysis on ICP-OES and then refilled the dissolution pot with 1 mL fresh SBF. pH values were recorded at each time point.

Table 3.1 - Reagents used for making SBF

Chemicals	Amount (g L^{-1})
NaCl	8.035
$NaHCO_3$	0.355
KCl	0.225
K_2HPO_4 $3H_2O$	0.231
$MgCl_2$ $6H_2O$	0.311
HCl 1M	38 mL
$CaCl_2$ $2H_2O$	0.386
Na_2SO_4	0.072
Tris	6.118

Chapter 4 Synthesis and Functionalization of Calcium Incorporated Dense Silica-Nanoparticles

4.1 INTRODUCTION

Silica-nanoparticles possess great potential for medical applications [109] and the incorporation of cations has broadened this application. For example, the incorporation of calcium makes particles into bioactive materials that release silica and calcium ions, which can stimulate osteogenic cells to produce bone matrix [164]. The application of silica-nanoparticles is greatly dependent on their size, morphology and surface groups. For example, size has a great effect on the toxicity and cell uptake mechanism [165], while surface modification can reduce aggregation [166] and can even be used to target specific cell types.

GPTMS is an important silane coupling agent and it can bond to organic and inorganic compounds at the same time by using its methoxysilane groups and epoxy ring. This provides a chance that GPTMS can covalent bonds between bioactive silica nanoparticles and a polymer network to give a nano-silica hybrid.

In this chapter, calcium incorporated dense-silica nanoparticles (CaSNP) were produced with a diameter of ~100nm and then functionalized with GPTMS (CaESNP). The focus of this chapter is on characterising the GPTMS on CaSNP surfaces. Previous work showed GPTMS grafted on bare SNPs [167], but functionalising calcium incorporated CaSNPs with GTPMS was more challenging because of the need to take the particles through a high temperature calcination process to enable calcium incorporation into the silicate network.

4.2 MATERIALS AND METHODS

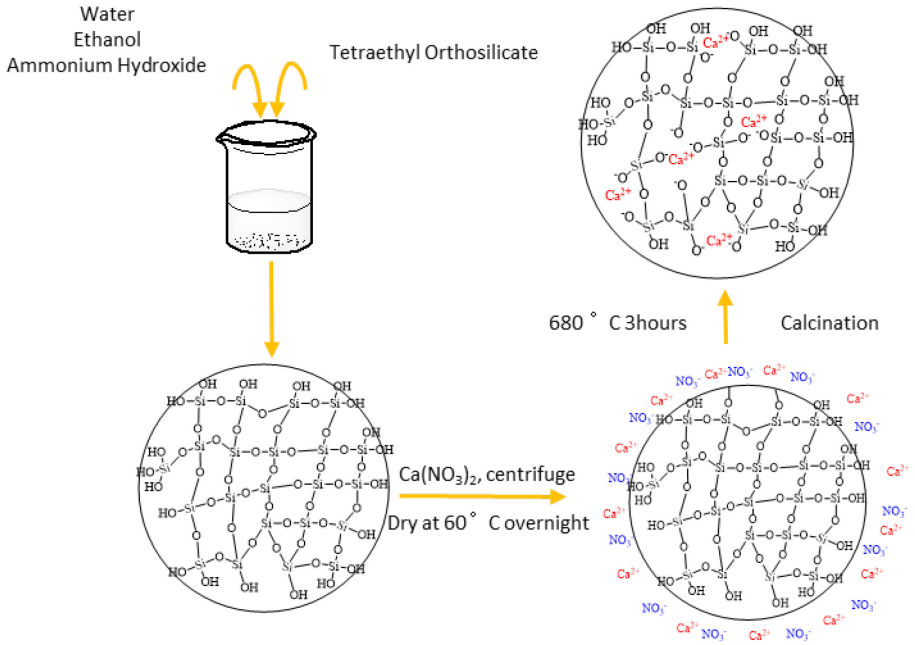
4.2.1 Dense silica-nanoparticle synthesis and calcium incorporation

The synthesis of NPs followed the Stöber process that was modified by Greasley *et al.* [89]. This method was reported to give a good reproducibility and monodispersity while procedures of this method is also simpler compared to literature [89].

All reagents were purchased from Sigma-Aldrich. NPs were made with diameters ranged from 80-120 nm. Water (4.19 mL) and ethanol (33.00 mL) were firstly mixed in a 100 mL conical

flask followed by adding ammonium hydroxide (0.27 mL). The mixed solution was then treated in the ultrasonication bath at room temperature for 10 minutes. After 10 minutes, TEOS (2.50 mL) was added into the solution and left over night on a magnetic stirring plate, at room temperature, with a stirring rate of 500 rpm to let hydrolysis and condensation reaction of TEOS to occur. The next day, particles were collected by centrifugation under 7830 rpm for 40 minutes. Particles were then washed 2 times by ethanol and 1 time by water to remove the unreacted chemicals and avoid the agglomeration [99]. Particles were transferred to 60°C oven to dry overnight.

For calcium incorporation (CaSNP), SNPs were re-dispersed with water in a Falcon tube and then calcium nitrate tetrahydrate ($Ca(NO_3)_2 \cdot 4H_2O$) was dissolved in water and added into the same tube and mixed, using an ultrasonicator, for 5 minutes. According to literature, the amount of $Ca(NO_3)_2$ added was kept in a molar ratio of silica : calcium of 1:8 in order to obtained the optimal calcium incorporation (maximum calcium incorporation with minimal excess) [168]. SNPs were then collected by centrifugation and dried at 60°C. Heat treatment was carried out (680°C for 3 hours with ramp of 3°C/min) after SNPs were dried in order to stabilize the network. After calcination, particles were washed again with ethanol for 3 times to remove any calcium that was not incorporated and then dried again in 60°C oven overnight.

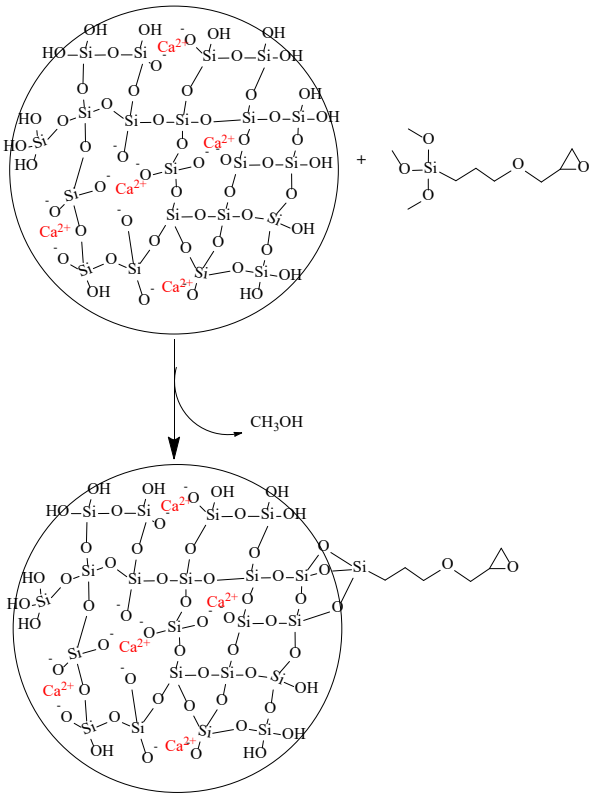


Scheme 4.1 - Synthesis process of CaSNPs.

4.2.2 Surface functionalization of silica-nanoparticles with GPTMS

The method used to make (ESNP & CaESNP) was modified from that reported by Sales *et al*. [125] wherein alcohol condensation occurs in an organic solvent with no water present. Two types of calcium incorporated SNPs were functionalized. The first type of SNPs was the particles prepared by the method described in *Section 4.2.1* and the second type was the same particle but treated with plasma (H_2+O_2) for 5 minutes in order to activate the particle surface by recreating the hydroxyl groups which were burnt out during the calcination.

All reagents were purchased from Sigma-Aldrich. Prepared particles (250 mg) were re-dispersed in anhydrous toluene (99.8%, 25 mL) in an ultrasonication bath for 10 minutes. The solution was then degassed for 15 minutes before transferring to a hot plate. The reaction was performed at 70°C under argon reflux with a stirring rate of 750 rpm. After the solution was stirred for 1 hour, GPTMS (1mL) was added in and stirred for another 6 hours to let the functionalization occur. Reacted particles were collected by centrifugation and washed by THF 2 times to remove any unreacted GPTMS and then dried at 60°C oven.



Scheme 4.2 - The reaction between GPTMS and CaSNP in toluene.

4.2.3 Particle characterisation

Acid digestion composition analysis. This analysis is to determine the elemental composition of calcium incorporated particles before and after the functionalization reaction to study if there is any calcium loss during the reaction. The method used was from Hench *et al.* [169]. Sample particles (50 mg) were ground and mixed with lithium metaborate (250 mg) in a small platinum crucible. The mixture was treated at 1050°C for 40 minutes to enable fusion. After cooling, the fused mixture was dissolved in nitric acid (2 M) and the solution was then diluted 10 times in nitric acid (2 M) for ready to use by ICP-OES (Thermo Scientific ICap 6000series) to give the concentration of each element.

TEM, SEM and DLS analysis. As described I Chapter 3, these techniques were used to characterise the particle morphology. The results from DLS were affected by the clusters of particles so TEM is essential for having an accurate result of particle size. Particles for TEM were prepared on 400 mesh copper grids coated with holey carbon film and the operating voltage was 200 kV.

FTIR, Raman spectra, Zeta potential and TGA analysis. Particles that functionalized by GPTMS were analysed by these techniques to determine the chemistry change on the particle surface. FTIR and Raman spectra were performed to find the signature vibration bands from GPTMS and the weight loss given from the TGA results can quantify the amount of GPTMS grafted on the particle surface.

4.3 RESULTS AND DISCUSSION

4.3.1 Calcium incorporated dense silica-nanoparticles (CaSNP)

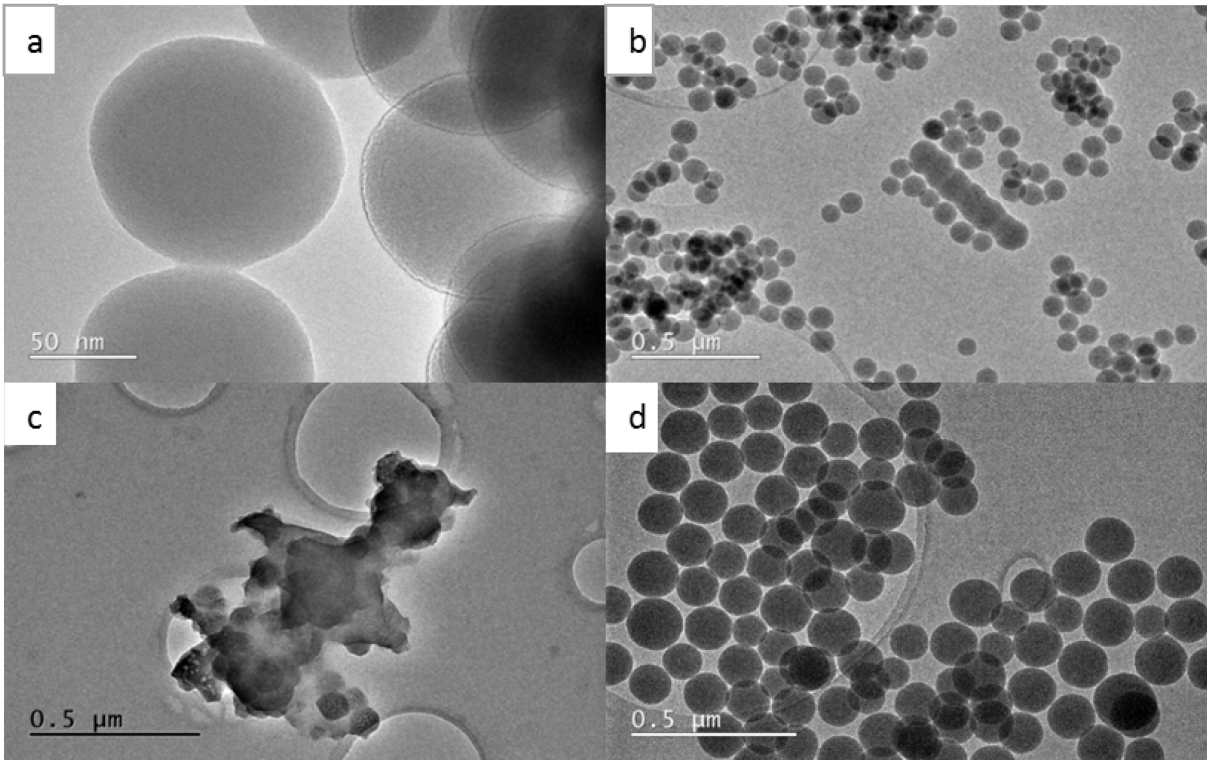


Figure 4.1- TEM images of SNPs and CaSNPs with a diameter of 100 nm: a) & b) SNPs without calcium, c) calcium incorporated with a ratio of 1:8 washed 3 times by water, d) calcium incorporated SNPs washed 1 time by 2 M nitric acid and 2 times by water.

SNPs were successfully synthesised with the Stöber process improved by Greasley *et al.* The particle size targeted in this project is 100 nm and the TEM images (Figure 4.1 a & b) showed an average size of 104.8±9.2 nm with n=50, although the DLS result (Figure 4.2 CaSNP) give an average diameter of 154 nm (PDI=0.732) due to some particle aggregation happened. During the process of calcium incorporation, it was found that washing the SNPs after calcination 3 times with water was not enough to remove the excess calcium since the molar ratio Si:Ca used was 1:8 which left a lot of calcium on the particles (Figure 4.1 c). To solve the problem, the first wash was changed to use 2 M nitric acid instead of using water and the rest remained same and the final result showed by TEM image was clean and well dispersed (Figure 4.1 d).

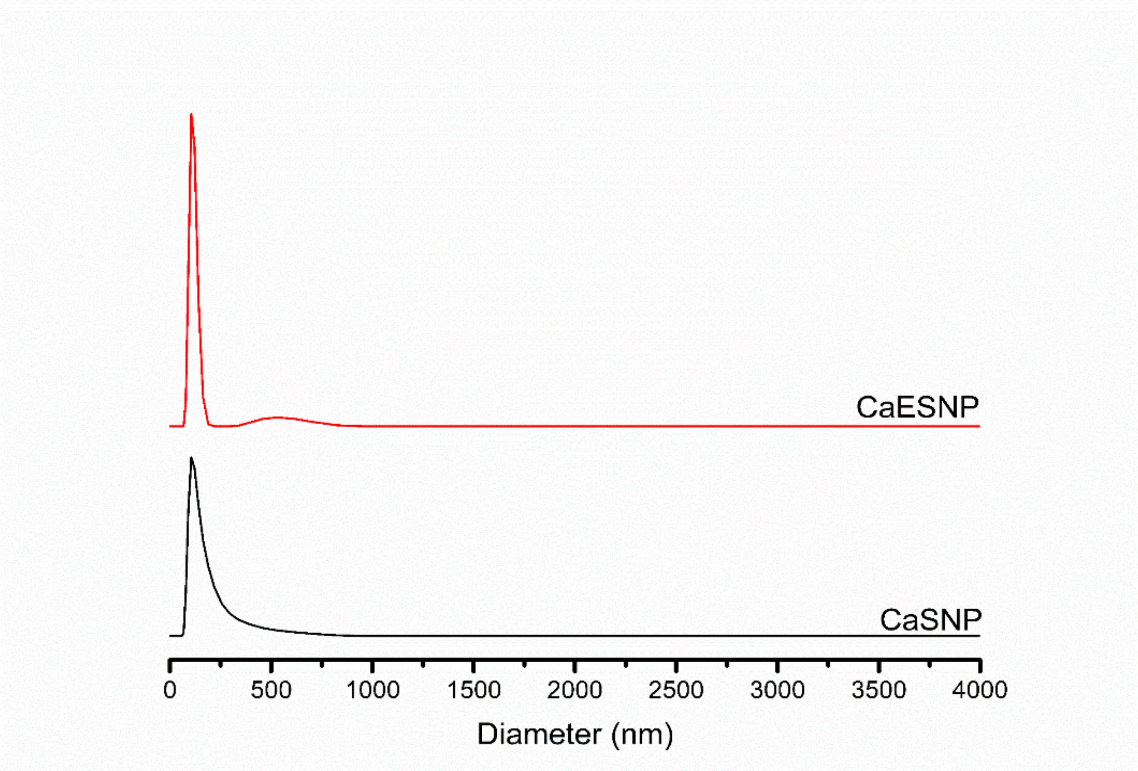


Figure 4.2 - DLS particle size distributions for calcium incorporated nanoparticles before (CaSNP) and after the functionalisation with GTPMS (CaESNP).

4.3.2 Calcium incorporated silica-nanoparticles functionalization with GPTMS (CaESNP)

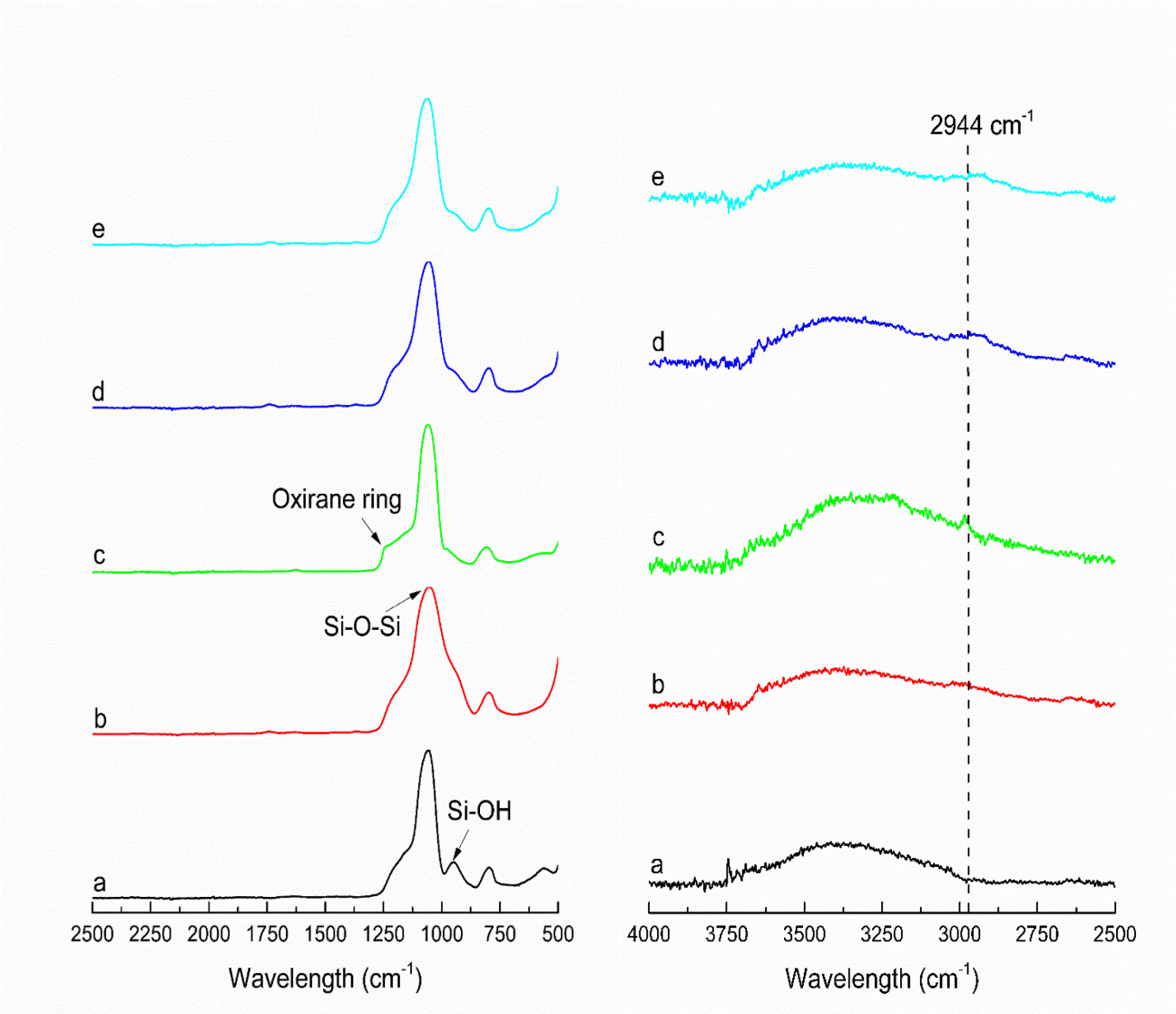


Figure 4.3 - FTIR (left 500-2500 cm^{-1} range and right 2500-4000 cm^{-1}) spectra from: a) SNP, b) CaSNP, c) ESNP, d) CaESNP and e) CaESNP with plasma treatment.

The reaction between GPTMS and hydroxyl groups on the particle surface is a simple reaction, but it was a challenge to validate successful GPTMS grafting and to determine the amount of GPTMS on the particle surface.

FTIR was the first technique used to analyse the chemical composition of the functionalized nanoparticles (Figure 4.3). The result shows SNPs and CaSNPs have similar spectra despite SNPs show a higher Si-OH absorbance at 990 cm^{-1}. This is because SNPs were not treated by calcination and they were dried at 60°C, so compared to CaSNPs treated at 680°C there were

more hydroxyl groups left on the particle surface (Figure 4.3 a and b). By comparing the FTIR spectra on particles before and after the functionalization, a sharper shoulder appeared for ESNP at 1100-1245 cm^{-1} and a peak at 2984 cm^{-1} also appeared. For CaESNP samples, FTIR spectra from both plasma treated and untreated particles showed no significant change compared to the un-functionalized CaSNP (Figure 4.2 c, d and e).

Zhang *et al.* reported that FTIR of GPTMS functionalized silica surface had changes in bands at 2944 cm^{-1} and 1343-1465 cm^{-1}, which are attributed to the alkyl C-H stretching and bending of GPTMS, but the signature band from the epoxy ring at 1150 cm^{-1} was missing and overlapped with the strong silica band [167]. However, O-H stretching bands from water or alcohol (2500-3300 cm^{-1}) may overlap with the alkyl C-H band, so the result is not strong enough to prove the GPTMS was attached to the particles. In order to get a better resolution and more accurate result in the 2500-3300 cm^{-1} wavelength range from the FTIR, Raman spectra was deployed.

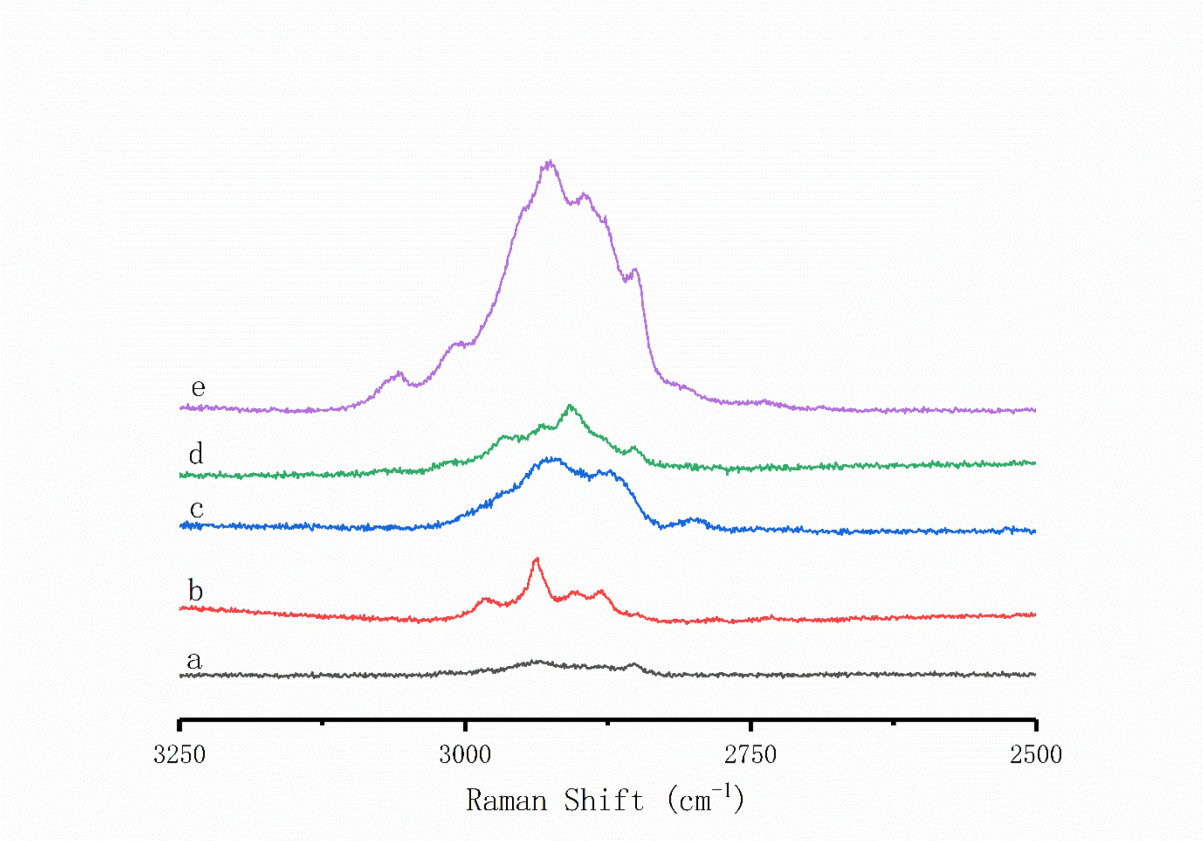


Figure 4.4 - Raman spectra of a) SNP, b) CaSNP, c) ESNP, d) CaESNP and e) CaESNP with plasma treatment.

Raman spectra from plasma treated CaESNPs and untreated CaESNPs show different peaks in this range after the functionalization. CaESNPs that were not pre-treated by plasma showed no change compared to the CaSNP (Figure 4.4 b and d), suggesting that calcium CaSNPs lost most of its hydroxyl groups due to the 3 hours of heat treatment at 680°C and as a consequence there were not enough sites for GPTMS grafting. On the other hand, plasma pre-treated CaESNPs (Figure 4.4 e) produced similar Raman spectra to that from ESNP (Figure 4.4 c), showing a collection of peaks in the range 2790-2850 cm^{-1}, corresponding to O-CH_3 and 2810-2960 cm^{-1} C-CH_3 of the opened epoxide ring. There are also small peaks at 2970-3100 cm^{-1} and 2980-3020 cm^{-1} that referred to aromatic C-H and CH=CH bonds, which are possibly contributed by remaining organic solvent (Toluene). As all the functionalized particles were

dried in a conventional 60°C oven without vacuum overnight, before transferring to the desiccator, it was not surprising to find C-CH_3 and O-CH_3 bonds in the composition as the ring opening reaction is possible with water in the atmosphere [170].

The Raman spectra suggested that CaSNPs was not a good nanoparticle source to be functionalized with GPTMS unless they are treated by plasma to re-activate the surface with hydroxyl groups. After the confirmation of existence of GPTMS on the particle surface, TGA was used to quantify the amount of GPTMS.

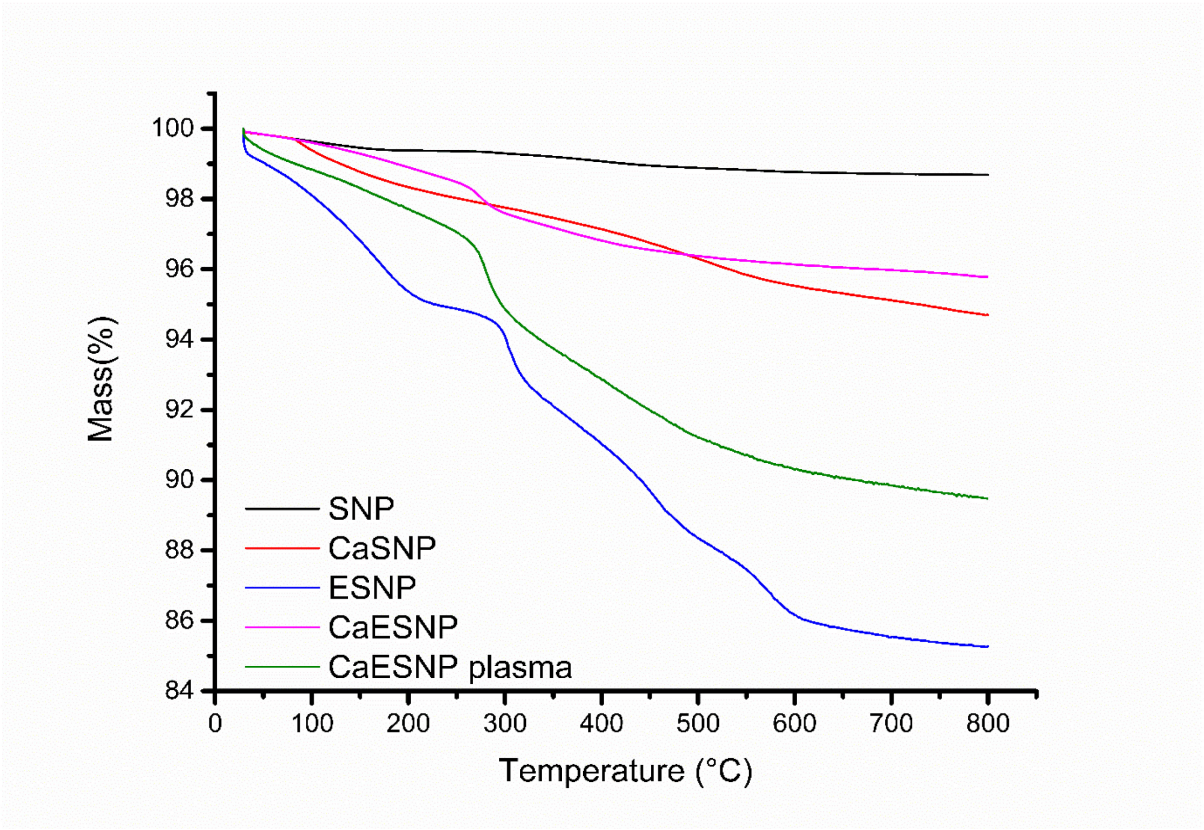


Figure 4.5 - TGA on nanoparticle samples from 25 °C to 800 °C. Representative values were chosen for this graph.

TGA results (Figure 4.5) showed clear differences between all samples. SNPs only lost 1.32% of their weight at the end of the measurement, while CaSNPs lost 5.31%. The reason for the difference is because calcium acted as a network modifier and made the silica network less interconnected, so when the sample was under high temperature like up to 800°C, hydroxyl groups from Si-OH were removed, condensation was promoted, and the network became more connected. By looking at functionalized samples: ESNP, CaESNP and CaESNP plasma, a significant weight loss occurred on all samples, which started around 255°C. This indicates the

starting of burning of the organic part of the GPTMS and with this information GPTMS can be quantified by using the Equation 4.1:

$$\boldsymbol{wt\%_{GPTMS}} = \boldsymbol{M\%_{ENP}} - \boldsymbol{M\%_{NP}} \quad \text{Equation 4.1}$$

This formula calculates the weight percentage of GPTMS in the nanoparticle network ($wt\%_{GPTMS}$) where $M\%_{ENP}$ is the weight loss of functionalized nanoparticles between the temperature of 250°C to 800°C and $M\%_{NP}$ means the weight loss of related un-functionalized nanoparticles from 250°C to 800°C.

Table 4.1 - Weight percentage of GPTMS in NPs

SAMPLE ID	ESNP	CAESNP	CAESNP PLASMA
$wt\%_{GPTMS}$	7.82 ± 1.22	-0.88 ± 0.49	4.05 ± 1.87

From Table 4.1, the calculated result shows ESNP gives a GPTMS concentration of 33.14 µmol/g and CaESNP plasma treated gives 17.12 µmol/g, while untreated CaESNP gives a negative result, meaning no GPTMS was present.

Table 4.2 - Acid digestion results on CaESNPs that were plasma treated.

Si:Ca molar ratio	After Calcination	Si (%At)	Ca (%At)	After functionalization	Si (%At)	Ca (%At)
CaESNP 1:6		81.08	18.89		85.51	14.49
CaESNP 1:8		80.11	19.89		83.62	16.38

Acid digestion was then carried out on two CaESNP samples with different Si:Ca theoretical composition (1:6 and 1:8). The purpose of this analysis was to ensure there was no calcium loss during the overnight functionalization synthesis in the toluene. Both samples showed that only 3-4% of the calcium content was released , which means the Ca is not released in large amounts into the organic solvent.

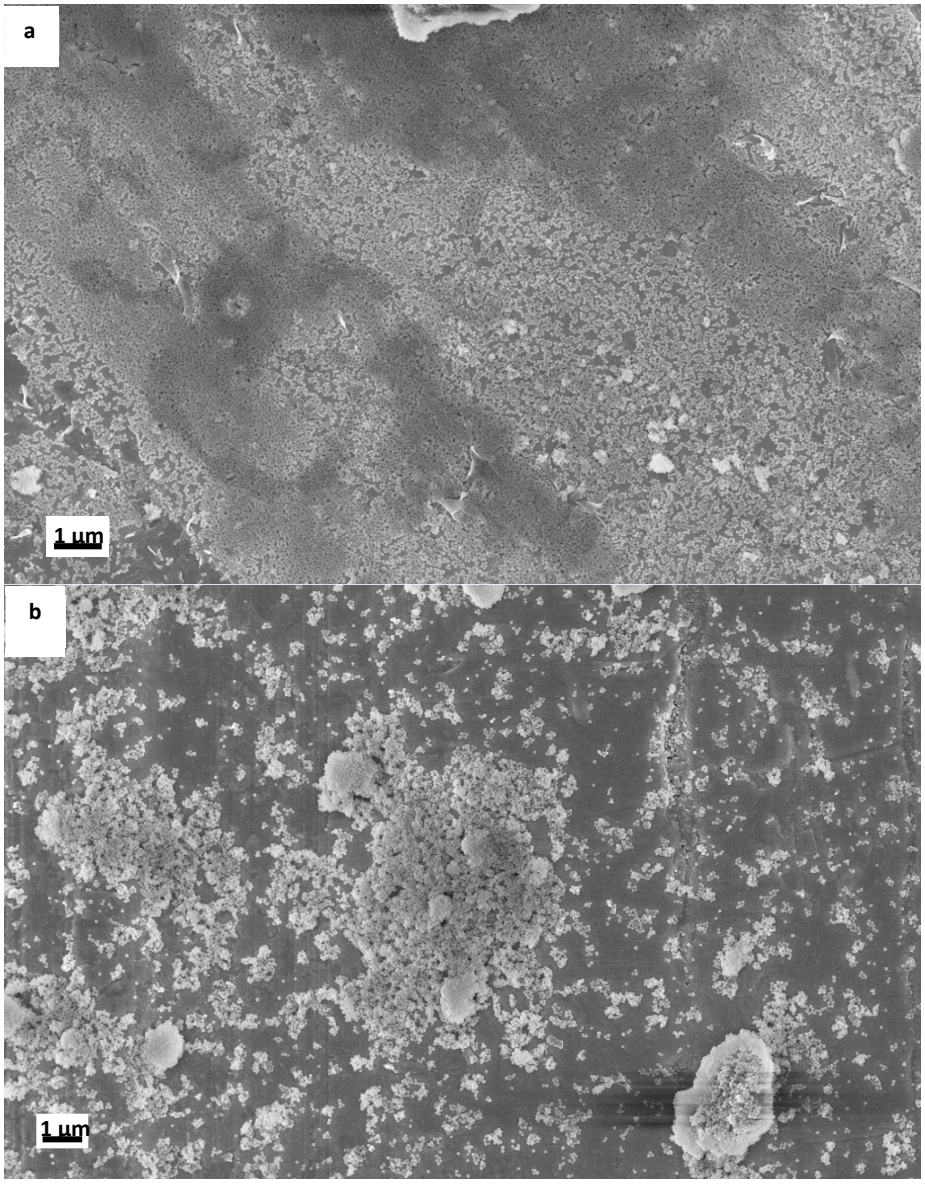


Figure 4.7 - SEM images of a) CaSNPs and b) functionalized CaESNPs.

The effect of GPTMS on particle distribution was also studied using SEM. Before the adding of GPTMS, CaSNPs were distributed evenly in the ethanol (Figure 4.7 a). When GPTMS was grafted on the surface, particles showed a more aggregated distribution (Figure 4.7 b).

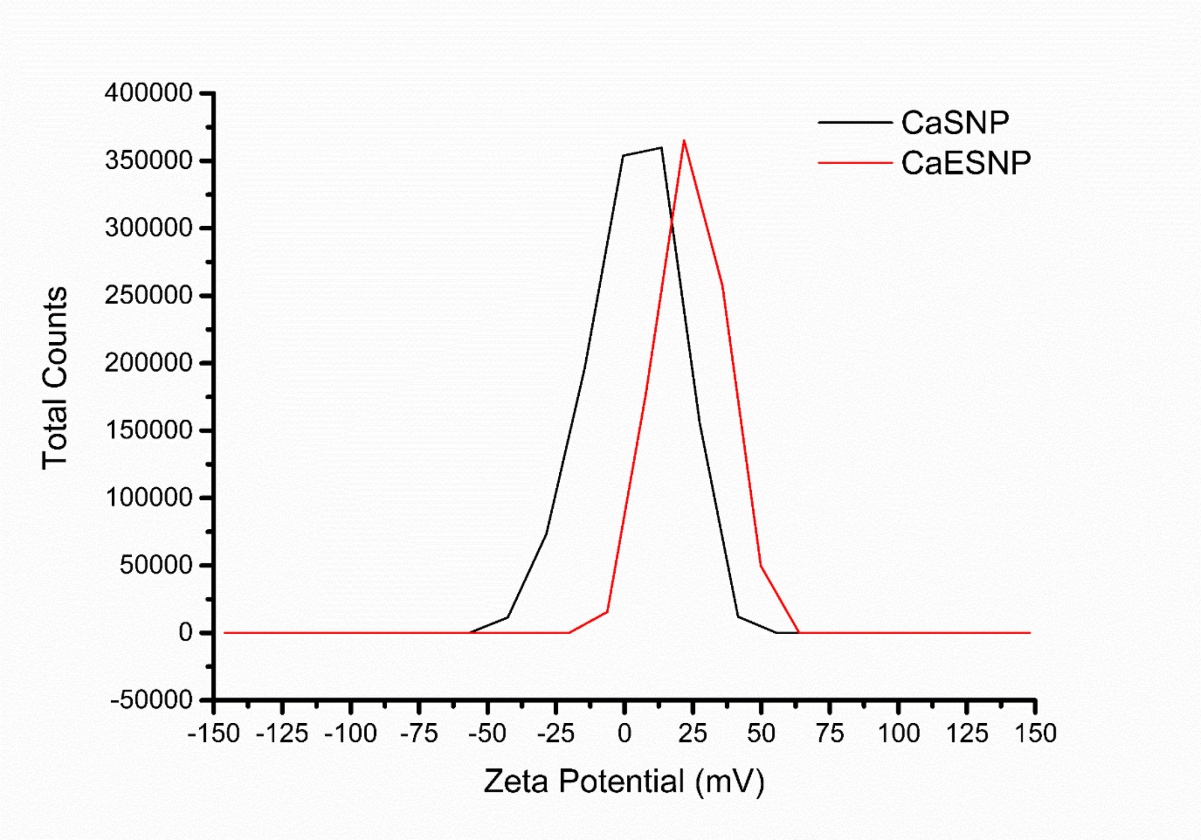


Figure 4.8 - Zeta potential for dense silica particles before (CaSNP) and after (CaESNP) the addition of GPTMS. Representative values were chosen for this graph.

Finally, DLS and Zeta potential were performed on the dense particles before and after the functionalization (Figure 4.2 and Figure 4.8). There was no significant change in size distribution of particles after the functionalization (average d=129.6 nm PDI=0.756), despite a secondary small peak was found at 531 nm (Figure 4.2) and this was possibly caused by the one GPTMS molecule attached with more than one nanoparticles, as described in Scheme 4.3c.

Zhang *et al.* reported the zeta potential for bare silica particles before and after the functionalization changed from -26.27 mV to +38.07 mV, indicating hydroxyl groups were converted into GPTMS molecules. Results from Figure 4.7 showed an increase from -0.52 mV to 21.80 mV and this proved the success grafting of GTPMS. However, compared with bare silica nanoparticles (-26.27 mV), calcium incorporated particles here showed a zeta potential of -0.52 mV. The reason for having a less negative result on CaSNPs was because samples were calcium incorporated and treated by high temperature so the OH groups left on the surface and the presence of Ca^{2+} ions also brought more positive charges.

4.4 Conclusions

Monodispersed CaSNPs of 100 nm diameter that contained 16.38 %mol CaO were produced consistently by using the modified version of Stöber process. The functionalization of CaSNPs with GPTMS did not give a same result as for silica SNPs from the literature. FTIR was not sensitive enough to determine the existence of GPTMS on the particle surface since the amount of attached GPTMS were too small. Raman spectra and TGA were reliable techniques for characterizing the alkyl group from GPTMS and it showed that CaSNPs were more difficult to graft with GPTMS compared with SNPs as they have lost majority of hydroxyl groups on the surface during the 3 hours of calcination process. In addition, plasma treated CaSNPs have shown a chance that hydroxyl groups could be re-activated on the surface and then react with GPTMS, although the final amount of grafted molecules, as calculated from TGA results, was still lower than for SNPs. The overnight reaction between GPMTS and the particle only lost 3.51%-4.40% of calcium from particles. By showing aggregated clusters, SEM images provided a hypothesis on how GPTMS contacted with particle surface that one GPTMS molecule may has attached with two or three nanoparticles instead of one. Aggregation was confirmed by the DLS results on CaESNPs with the appearance of a second peak at a higher diameter. Zeta potential showed a less negative charge on CaSNPs, compared to SNPs because of the loss of hydroxyl groups during calcination and the presence of positive charged Ca^{2+} ions. The zeta potential for CaESNPs increased to +21.80 mV by grafting GPTMS molecules on the particle surfaces.

Chapter 5 Synthesis and Functionalization of Calcium Incorporated Mesoporous Silica-Nanoparticles

5.1 INTRODUCTION

Given their ordered meso-structure and biocompatibility, mesoporous silica nanoparticles (MSNs) are candidates for host matrices of bioactive molecules [171]. The mesoporous structure with pore size 2-50 nm gives MSNs a high surface area and also a high pore volume resulting in high loading capacity for drugs and the particles are potentially vehicles for controlled delivery of therapeutic cations [172].

Having successfully functionalized calcium incorporated dense silica-nanoparticles by using plasma, mesoporous silica-nanoparticles were expected to be able to host a higher yield of grafted GPTMS molecules as they have a larger surface area and therefore higher quantity of hydroxyl groups on the surface is higher, making the plasma treatment unnecessary.

In this chapter, the synthesis method of MSNs and calcium incorporated mesoporous particles (CaMSNs) will firstly be reviewed. The functionalization method was revisited, as MSN morphology is different from SNPs. The characterization on GPMTS was carried out in more detail with solid-state NMR, for the first time, to look at how GPTMS attached to the particle surface. The calcium release profile was also studied i to see if the presence of GPTMS on particle surface affects the ion release.

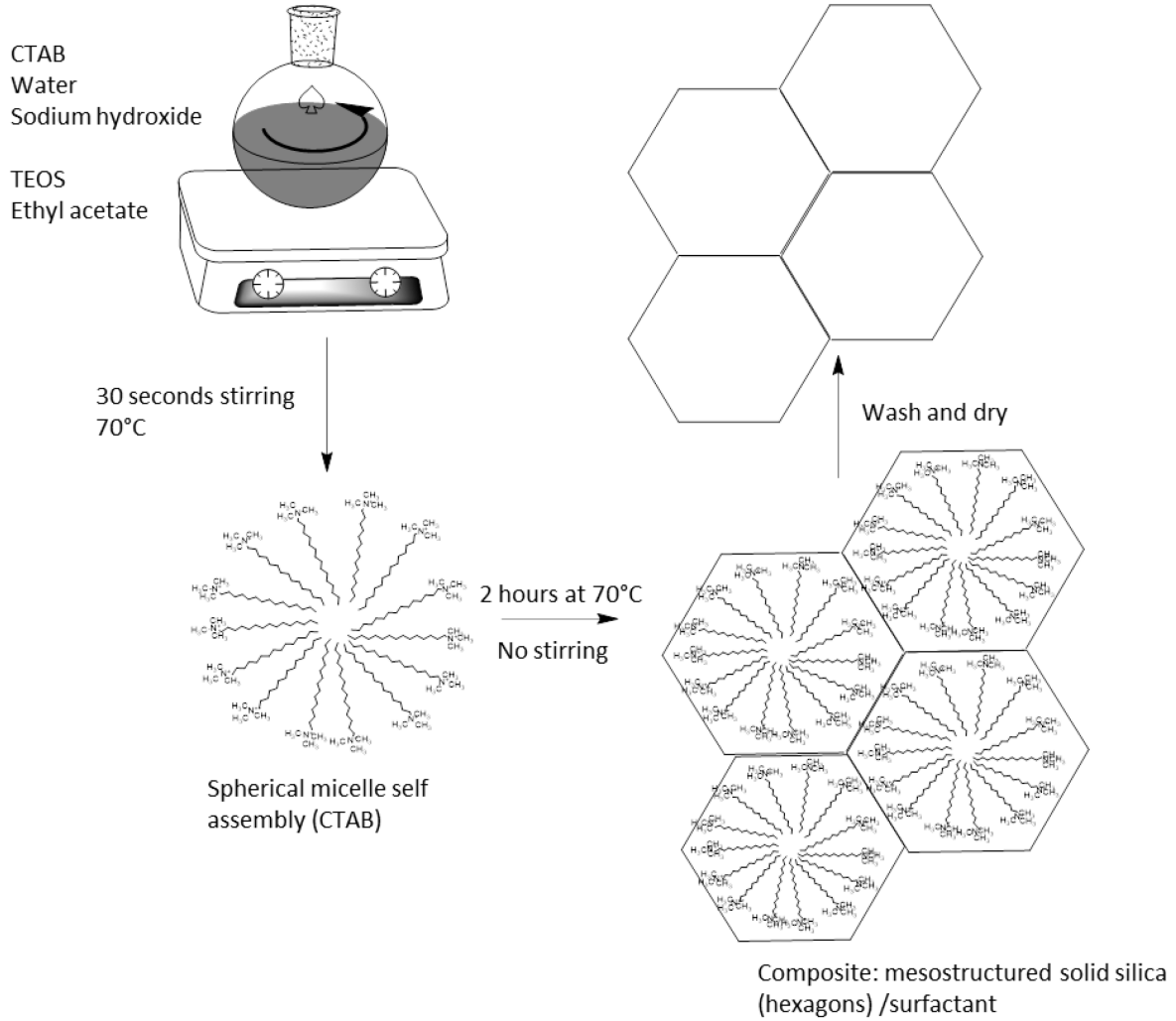
5.2 MATERIALS AND METHODS

5.2.1 Mesoporous silica-nanoparticle synthesis and calcium incorporation (CaMSN)

The synthesis method was modified from Chang *et al.* [102] and all reagents were purchased from Sigma-Aldrich.

As shown in Scheme 5.1, the modified method mixed H_2O (500mL), CTAB (1g) and NaOH (2M, 3mL) on a hot plate at 70°C for 10 minutes. After that, TEOS (5 mL) was added dropwise and stirred for one minute before adding ethyl acetate (5 mL) and stirred for 30 seconds. The stirring was turned off and solution was left on the hot plate for two hours before centrifugation. After this, washing process was carried out two times with ethanol and water

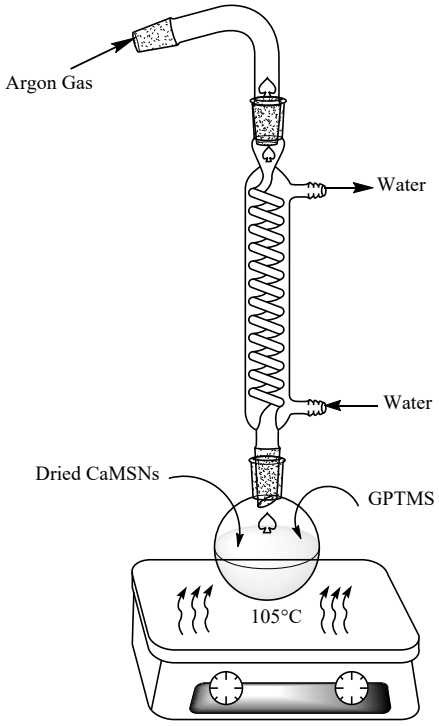
by cycles in ultrasonication bath to remove any unreacted substances. The particles were then re-dispersed in the 200 mL solution prepared with acetic acid and ethanol (95:5 v/v) and stirred at 70°C for one hour to remove the surfactant CTAB. Acetic acid was removed by using centrifugation and washing cycles three times with water and $Ca(NO_3)_2 \cdot 4H_2O$ (6.88 g) was added into the solution during the last wash cycle. The particles were transferred to the 60°C oven for drying overnight. Finally, calcination was carried out at 680°C for three hours at the heating rate of 3°C/min and particles were washed three times with ethanol to remove any excess calcium before drying again at 60°C.



Scheme 5.1 - Scheme of synthesis of MSN with CTAB as surfactant for templating.

5.2.2 Surface functionalization of calcium incorporated mesoporous silica nanoparticles with GPTMS (CaMSN -> MCE)

The method used for producing MCEs was the same as the one for making CaESNPs described in *Section 4.2.2* except that the reaction temperature was increased to 105°C instead of 70°C (Scheme 5.2). Although mesoporous particles did not need plasma treatment for regaining the hydroxyl groups, they need extra pre-treatments to remove all the water molecules trapped in the mesopore channels by using Schlenk line vacuum drying at 70°C for 30 minutes and then degassing with toluene for 30 minutes. Theoretically, functionalized nanoparticles should be dried and stored in the vacuum oven but due to the limitation of the lab equipment MCEs were dried in the 60°C conventional oven and stored at the desiccator [167].



Scheme 5.2 - The apparatus for mesoporous particle functionalization.

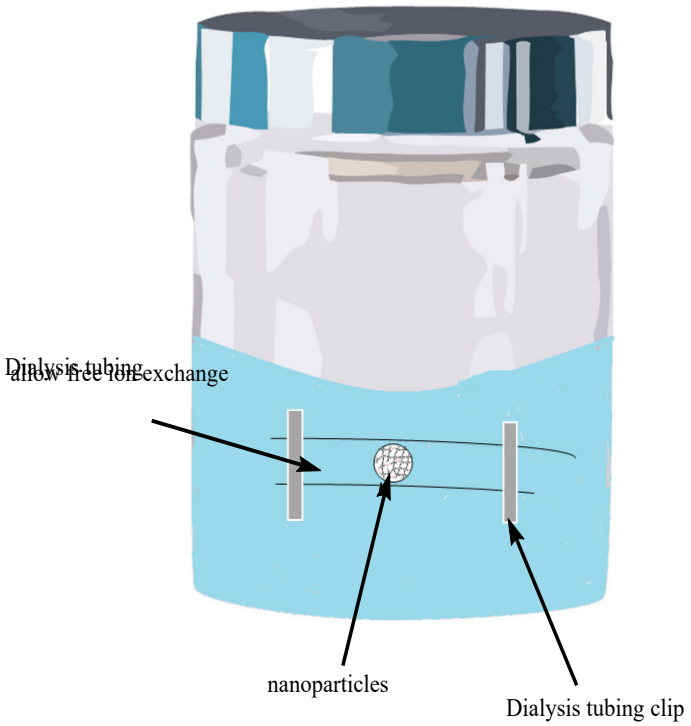
5.2.3 Particle characterisation

The same characterisation methods for dense nanoparticles described in *Section 4.2.4* were also used here. TEM for analysing the particle morphology, DLS for particle size distribution and FTIR, Raman, Zeta potential along with TGA/DSC for characterisation of grafted GPTMS. In addition, nitrogen adsorption, solid-state NMR and dissolution studies were also conducted to give a more solid understanding on the interaction between GTPMS and CaMSNs.

Nitrogen adsorption BET analysis. This analysis was used to show how GPTMS changed the particle size and the pore sizes. A 40 point adsorption/ 40 point desorption isotherm was obtained and BET analysis from 0.1 to 0.25 $cc.g^{-1}$ performed. DFT was used as the equilibrium model to determine the pore size distribution in the relative pressure range form $1x10^{-7}$ to 0.5.

Solid-state NMR analysis. ^{29}Si solid-state MAS-NMR analysis was performed by Nicole Kelly at Warwick University. Considering the amount of GPTMS attached to the particle surface might be very small, this technique can accurately show the presence of T^n species that is given form the GPTMS to prove the GPTMS is successfully grafted on the particle surface. CaMSNs samples made with 0 mmol/g, 1 mmol/g and 4 mmol/g of GPTMS were sent for characterisation.

Dissolution study. The study was done in Minimum Essential Medium (Gibco® MEM no calcium, ThermoFisher Scientific) with antibiotics (1% v/v) added. 37.5 mg of each sample was re-dispersed with 3 mL of MEM and pipetted into SnakeSkin Dialysis Tubing (3.5K MWCO, 16 mm dry I.D), which was sealed with dialysis tubing clips (Spectra/Por®) and put into a pot with a total MEM volume of 25 mL (Scheme 5.3) [162]. All samples were then incubated at 37°C in an orbital shaker (IKA 3940001 KS 3000 i Control Incubating Shaker) at 120 rpm. At each time point: 1 h, 2 h, 4 h, 8 h, 24 h, 48 h, 72 h and 168 h, 1 mL of solution was taken from the pot and refilled with fresh MEM. The taken solution was diluted 10 times with 2 M nitric acid and analysed by using ICP-OES. When the study was finished, particle samples in the pot were collected, dried and washed by ethanol as they were then prepared for TEM bright field imaging.



Scheme 5.3 - Experimental setup for nanoparticle dissolution studies.

5.3 RESULTS AND DISCUSSION

5.3.1 Calcium incorporated mesoporous silica-nanoparticle (CaMSN)

With the method established by Chang *et al.,* CaMSN (SiO_2-CaO) particles synthesised had a random shape and larger size than expected as shown in the TEM image (Figure 5.1). As the author did not specify the stirring rate during the synthesis, three different experiments were done with a stirring rate of 400 rpm, 500 rpm and 750 rpm to see if it can affect the particle shape. TEM images showed that as stirring rate increased, the particles became more spherical and a more uniform size distribution were achieved. Lin *et al.* suggested that mesoporous particles synthesis were highly affected by the concentration of silica-surfactant micelles and in order to achieve a smaller particle size it is important to keep a high stirring rate to reduce the micelle concentration which can finally suppress the particle growth [173].

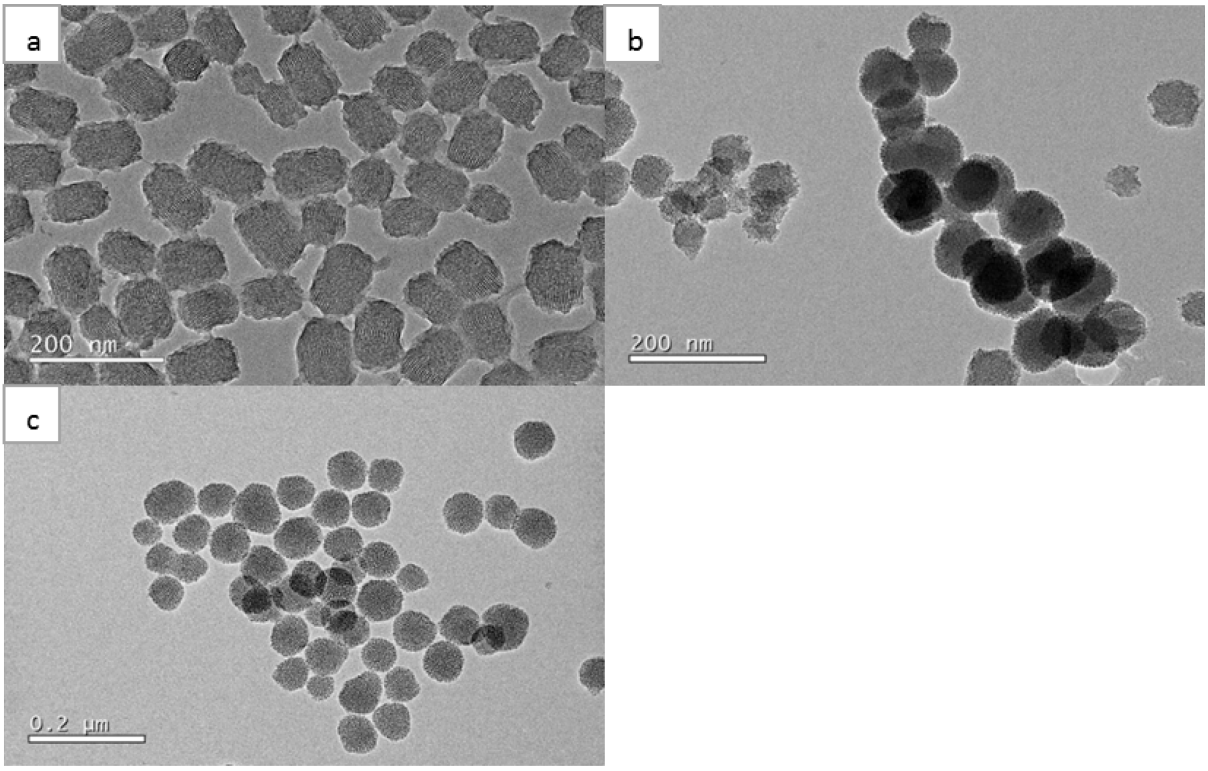


Figure 5.1 - TEM images of MSNs synthesised with different stirring rate: a) 400 rpm, b) 500 rpm and c) 750 rpm.

After MSNs can consistently produce by using a stirring rate of 750 rpm, the method of surfactant removal was also modified. The original method from the literature was to treat particles at 550°C for 16 hours to burnout all the CTAB. However, Niinisto *et al.* reported

there is a significant loss on the hydroxyl group from silica at the temperature of 550°C [174]. Hydroxyl groups were needed for the reaction between particles and GPTMS and more hydroxyl groups means a higher yield of grafted GPTMS might be achieved, so a new method to remove the surfactant CTAB was introduced. Following the method reported by Aime *et al.,* acetic acid was used to extract the CTAB by using CH_3COO^- bound with CTA^+ and washed out by water two times [175].

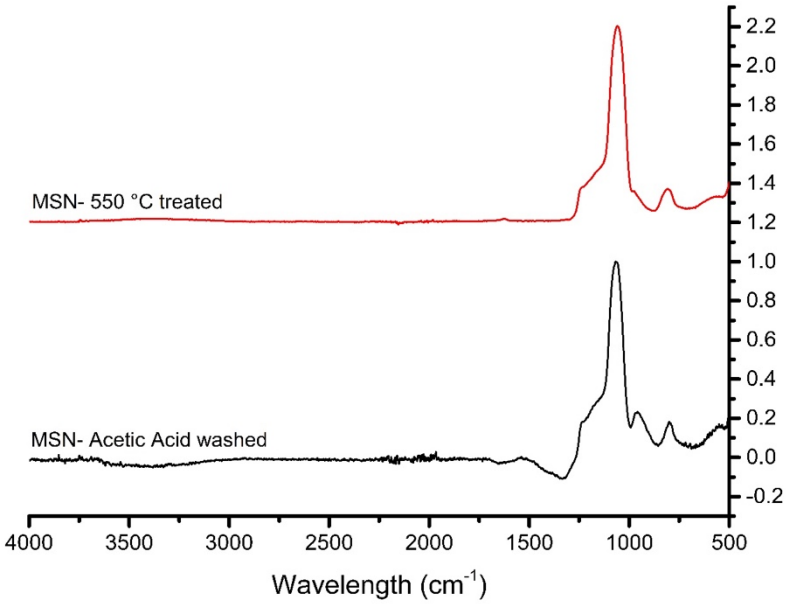


Figure 5.2 - FTIR spectra of MSNs treated by two different methods of removing CTAB.

FTIR analysis was also performed on washed sample and the result shows there was only a small amount of acetic acid left, causing the noisy vibration bands at 2000 cm^{-1} and 3600 cm^{-1} (Figure 5.2). Also, by comparing the Si-OH band at 990 cm^{-1}, the acetic acid washed sample clearly possessed more hydroxyl groups compared to the sample treated at 550 °C, which confirmed this modified method was an effective way to produce CaMSNs while preserving hydroxyl groups.

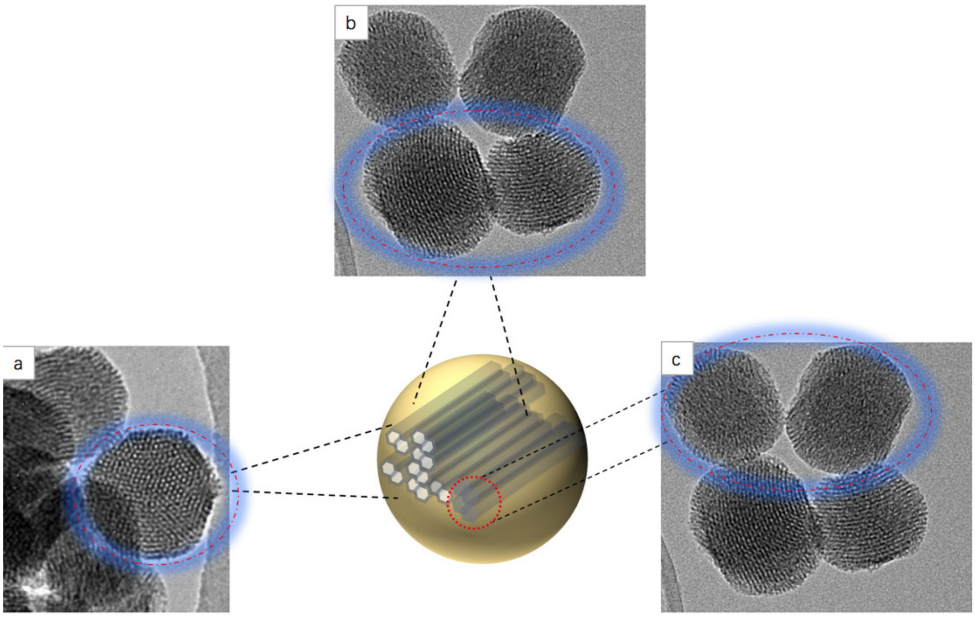


Figure 5.3 – TEM images of MSNs (no calcium): a) pore facing to the camera, b) channel view and c) pores that were blocked by CTAB. Particles shown here all have a diameter of 82nm ± 5nm

Figure 5.3 illustrates the view on a MSN (no calcium) from three different orientations under the TEM and ordered pores were seen by looking through from the pore channel (Figure 5.3a) and a stripe pattern was seen by looking at the channels (Figure 5.3b). However, the TEM image also showed that there was still a small number of particles with CTAB left blocked pores (Figure 5.3c) but this should not be a concern because the heat treatment at 680°C for CaMSN sample would remove the any CTAB remained.

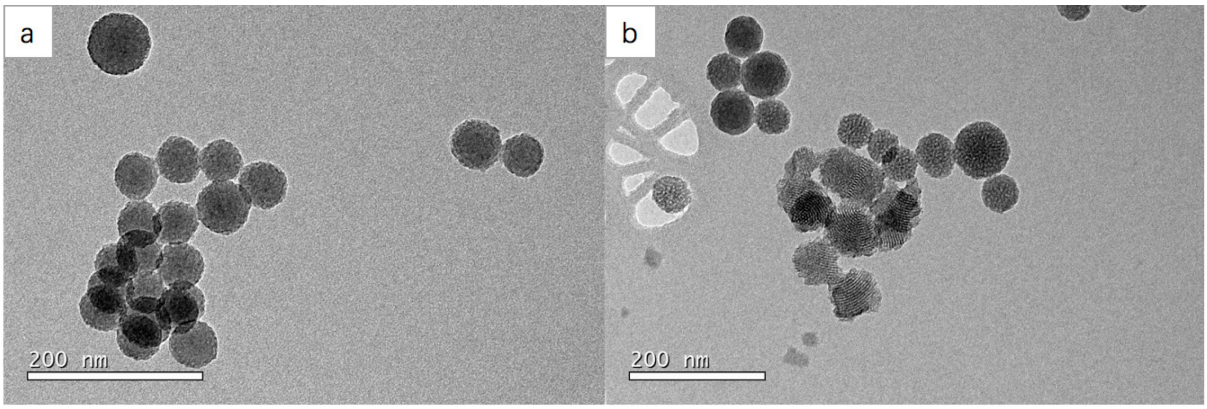


Figure 5.4- TEM images of CaMSN: a) all particles lost porosity and b) some particles still showed visible pores.

TEM images (Figure 5.4) also revealed the change of MSNs after the addition of calcium (CaMSN). The general morphology and particle size remained unchanged but many particles lost their porosity. There were still some particles with visible pores (Figure 5.4 b) which means not all the particles were fully loaded by calcium and adding a higher calcium concentration into particles is suggested in the future.

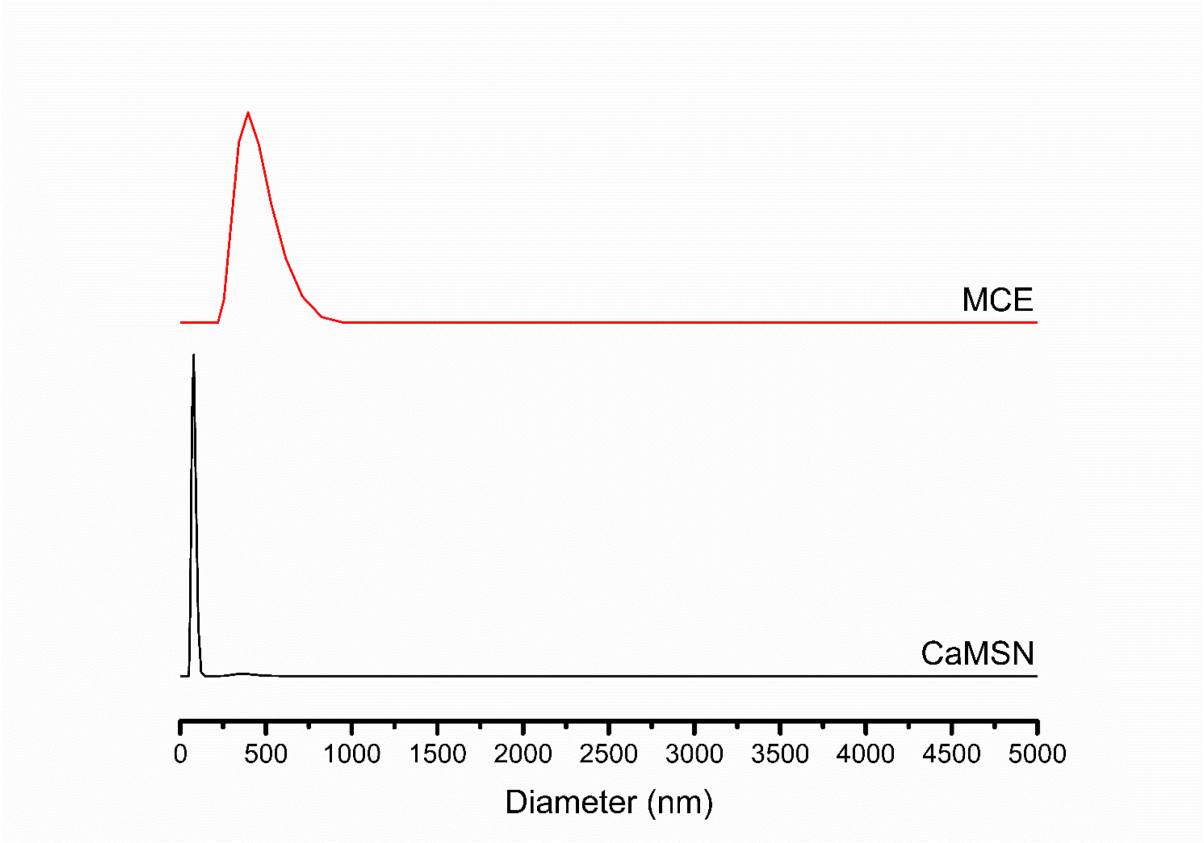


Figure 5.5 - DLS size distribution for mesoporous particles before and after the functionalization with GPTMS. Representative values were chosen for this graph.

DLS was also performed on mesoporous particles and gave an average diameter of 80.4 nm (PDI=1), which was similar to the literature. The results for GTPMS functionalized mesoporous nanoparticles MCE was also shown in Figure 5.5 and it showed a broad peak at 428.7 nm (PDI 0.174). The reason for having a larger diameter value and broader peak was the same for what happened on CaESNPs: a single GPTMS molecule attached to more than one nanoparticle and also GPTMS molecules may had changed the zeta potential of the particles in the solutions.

5.3.2 The functionalisation of CaMSNs with GPTMS (CaMSNs -> MCE)

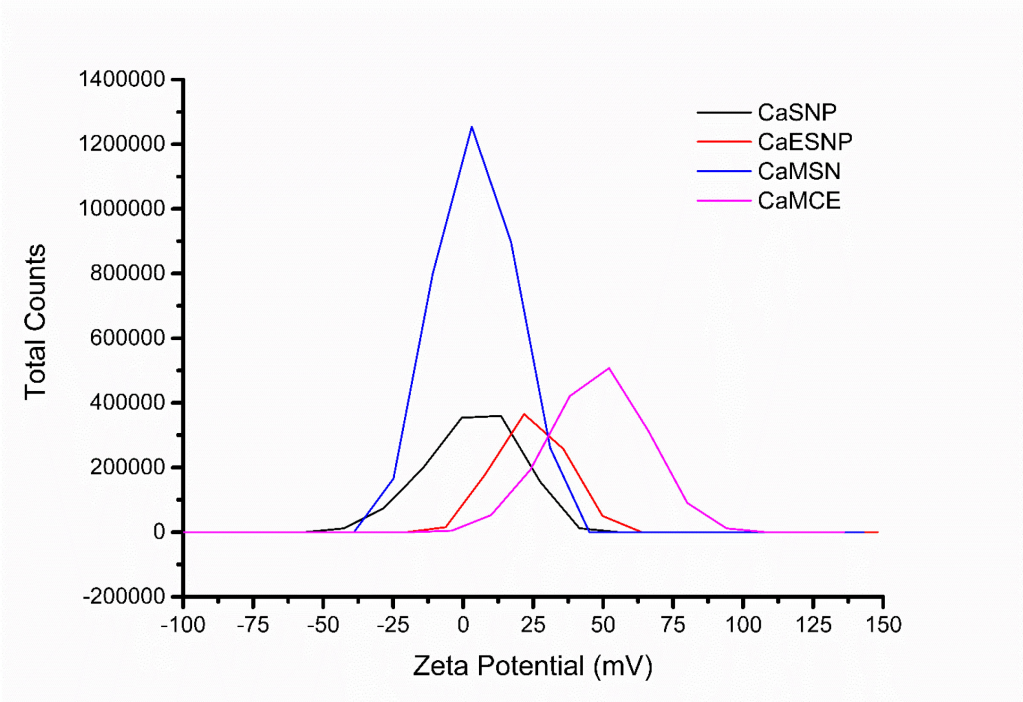


Figure 5.6 - Zeta potential measurements for all particles before and after the functionalization with GPTMS. Representative values were chosen for this graph.

Zeta potential measurements of the mesoporous nanoparticles are shown in Figure 5.6, which also includes the zeta potential data for dense particles from Chapter 4 to allow comparison. Both un-functionalized CaSNPs and CaMSNs fell in the same region, while the values for both functionalized particles shifted to more positive values. The reason for this shift was explained in *Section 4.3.2* and is due the GPTMS grafted on the particles surface replacing hydroxyl groups. The zeta potential value for CaMCEs (+52.1 mV) was more positive compared with CaESNPs (21.8 mV), which provided an evidence that calcium incorporated mesoporous nanoparticles were grafted with more GPTMS compared with dense particles.

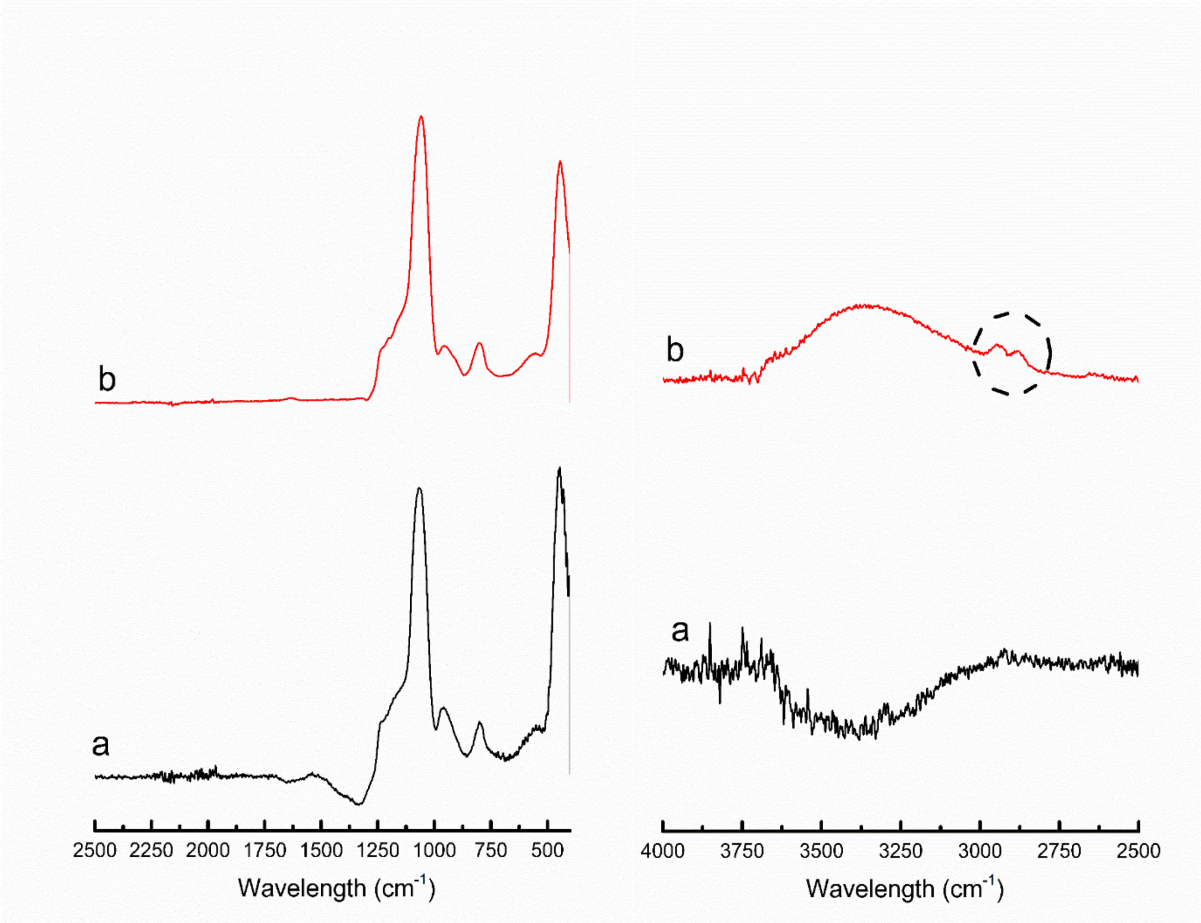


Figure 5.7 - FTIR spectra of: a) CaMSN and b) MCE. Left: wavelength 500-2500 cm^{-1} Right: wavelength 2500-4000 cm^{-1}.

FTIR was also performed on mesoporous particles before (Figure 5.7a) and after (Figure 5.7b) the functionalization. Spectra from both CaMSNs and MCEs showed distinctive peaks similar to dense silica nanoparticles, with bands at 1055 cm^{-1} and 800 cm^{-1} corresponding to Si-O-Si and Si-O stretching [176]. At the wavelength range of 2500-4000 cm^{-1}, a dual band was found at 2884 cm^{-1} and 2947 cm^{-1} on functionalized MCE samples, representative of alkyl C-H stretching [167], which were not present in the spectra of dense nanoparticles samples. Although the relative absorbance for the alkyl bands are low compared with main peaks on the range 500-2500 cm^{-1}, they do indicate the presence of GPTMS in the MCEs.

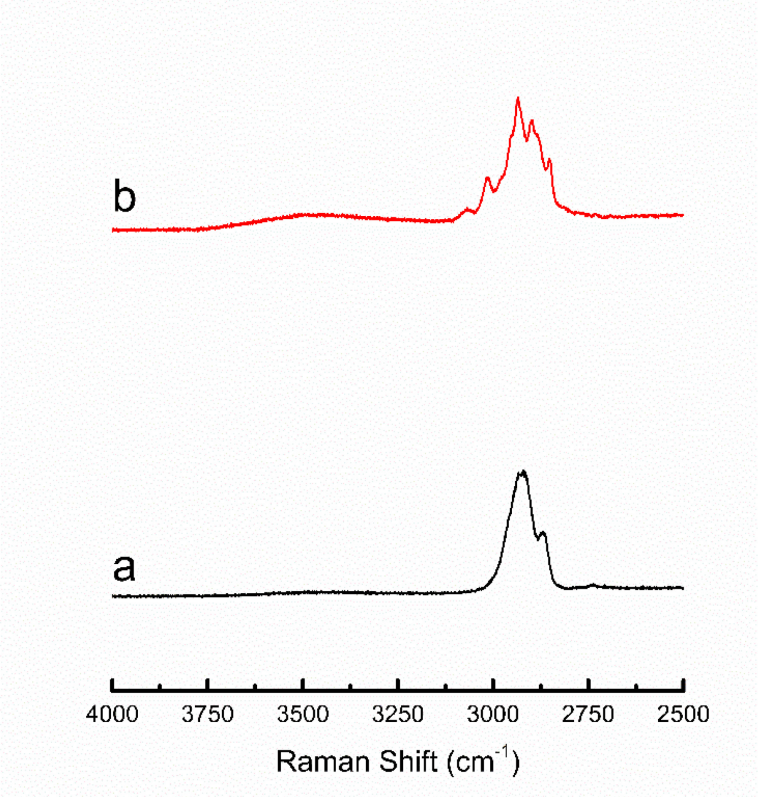


Figure 5.9- Raman spectra of: a) CaMSN and b) MCE.

Raman spectroscopy was also performed. CaMSNs (Figure 5.8 a) showed a strong signal at 2880 cm^{-1}, which represented OH groups. At this point, the Raman spectrum did suggest that

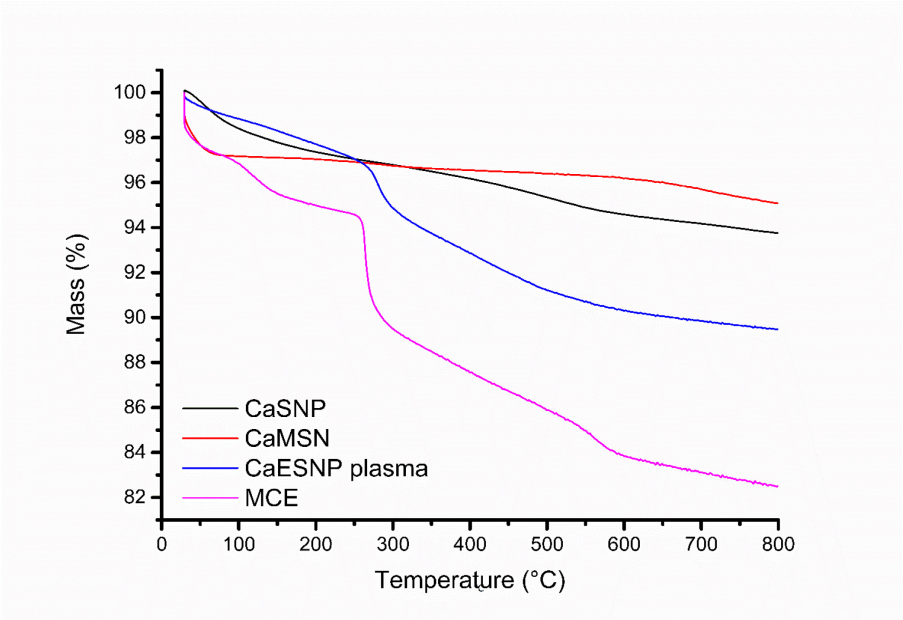


Figure 5.8 - TGA analysis on both dense and mesoporous nanoparticles before and after the functionalization with GPTMS.

after the calcination, CaMSNs contained a higher quantity of hydroxyl groups than dense

nanoparticles (CaSNPs). Spectra of the functionalized particles (MCEs), on the other hand, showed multiple peaks at 2790 cm^{-1}, 3010 cm^{-1} and 3065 cm^{-1}. As discussed already in *Section 4.3.2*, these were peaks from CH_2, O-CH and CH=CH bonds are contributed by GPTMS and toluene. FTIR and Raman spectra suggested that calcium incorporated mesoporous silica-nanoparticles were feasible for grafting with GPTMS without plasma treatment.

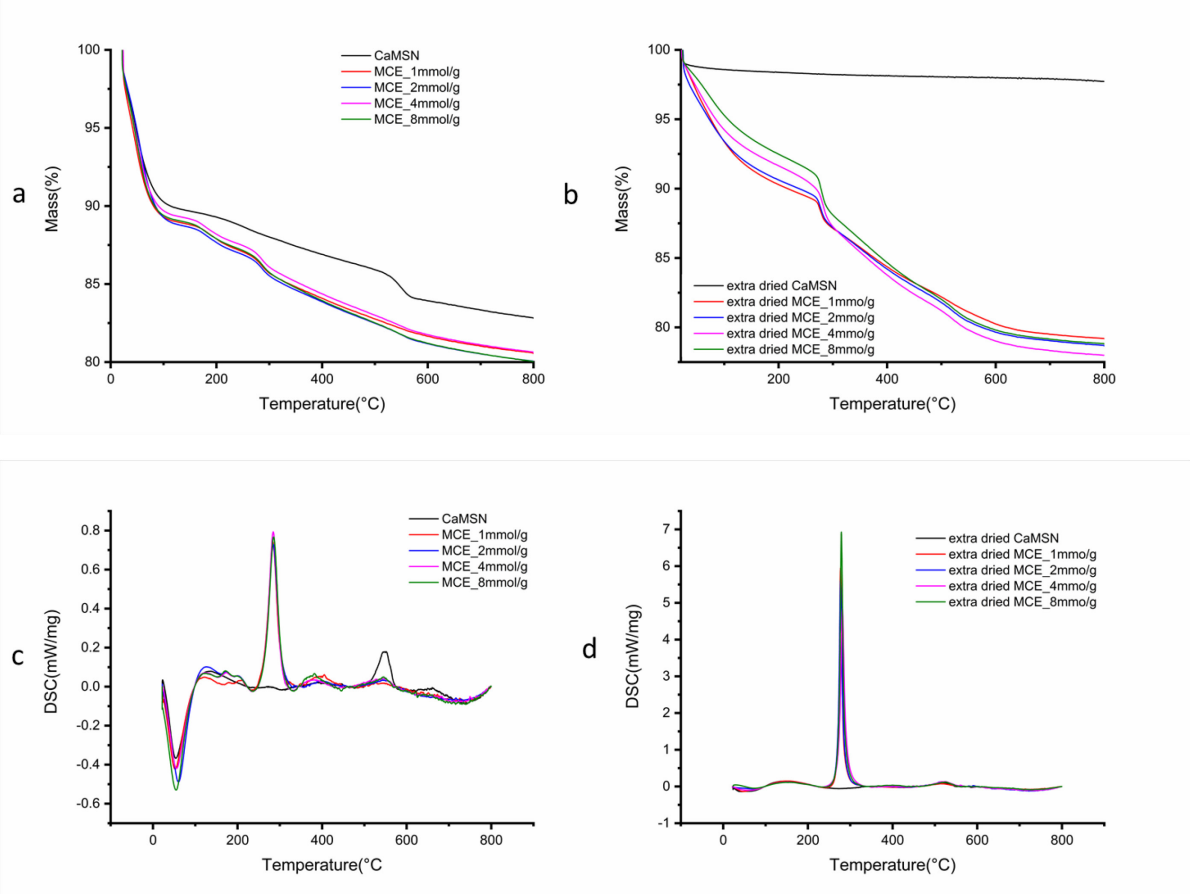


Figure 5.10 - TGA (top) and DSC (bottom) results of top: a)&c) particles without drying treatment and b)&d) particles treated with an extra drying process prior to the functionalization.

TGA analysis was also used to compare the amount of GPTMS attached on MCEs with those attached on CaESNPs (Figure 5.9). By using the Equation 4.1, it was found that CaESPN plasma treated samples had 4.05 wt% (17.12 μmol/g) of GPTMS while mesoporous MCEs had 10.19 wt% (43.22 μmol/g) when both samples were exposed to 1 mL of GPTMS during synthesis. A significant weight loss for CaMSNs and MCEs occurred before 100°C which did not happen to the dense particles and this was contributed by the evaporation of water molecules trapped in the pores.

Having known the fact that the amount of GPMTS can be grafted onto mesoporous nanoparticles were more than 2 times higher than plasma treated dense nanoparticles, it was interesting to investigate the maximum capacity of CaMSNs when grafting with GPTMS. GPMTS with concentration of 1 mmol/g, 2 mmol/g, 4 mmol/g and 8 mmol/g were added into the CaMSN solution during the synthesis and analysed by TGA/DSC. The results (Figure 5.10 a & c) showed an unexpectedly low yield of grafted GPTMS. In addition, the mass percentage of all samples dropped to ~90% before reaching 100 °C. This mass loss was from the water molecules trapped in the pores. After reviewing the synthesis method, the reason for having this huge mass loss from water and low GPTMS yield was attributed to the samples were stored in a 60 °C oven prior to the functionalization, which was not dry enough to get rid of all the water molecules and these water molecules interrupted the alcohol condensation reaction by hydrolysing the methoxysilane groups from GPTMS. The method was modified by drying CaMSNs under vacuum at 70 °C for 30 minutes and then degassing in toluene for another 30 minutes and also, the reaction temperature was increased from 70 °C to 105 °C. Extra-dried MCE samples made by the modified method were then also been analysed by TGA/DSC (Figure 5.10 b & d) and result showed a significant increase in GPTMS yield. Calculated values for extra-dried samples and un-dried samples were listed in Table 5.1.

Table 5.1 - The amount of GPTMS grafted on the mesoporous particles surface calculated from TGA results.

GPTMS feed in / Sample	1 mmol/g	2 mmol/g	4 mmol/g	8 mmol/g

Un-dried, GPTMS wt%	1.02	0.65	1.18	1.09
Extra-dried, GPTMS wt%	9.33	10.09	11.57	11.73
Un-dried, GPTMS µmol/g	4.32	2.71	4.99	4.61
Extra-dried, GPTMS µmol/g	39.48	42.69	48.95	49.63

5.3.3 The effect of GPTMS on CaMSNs

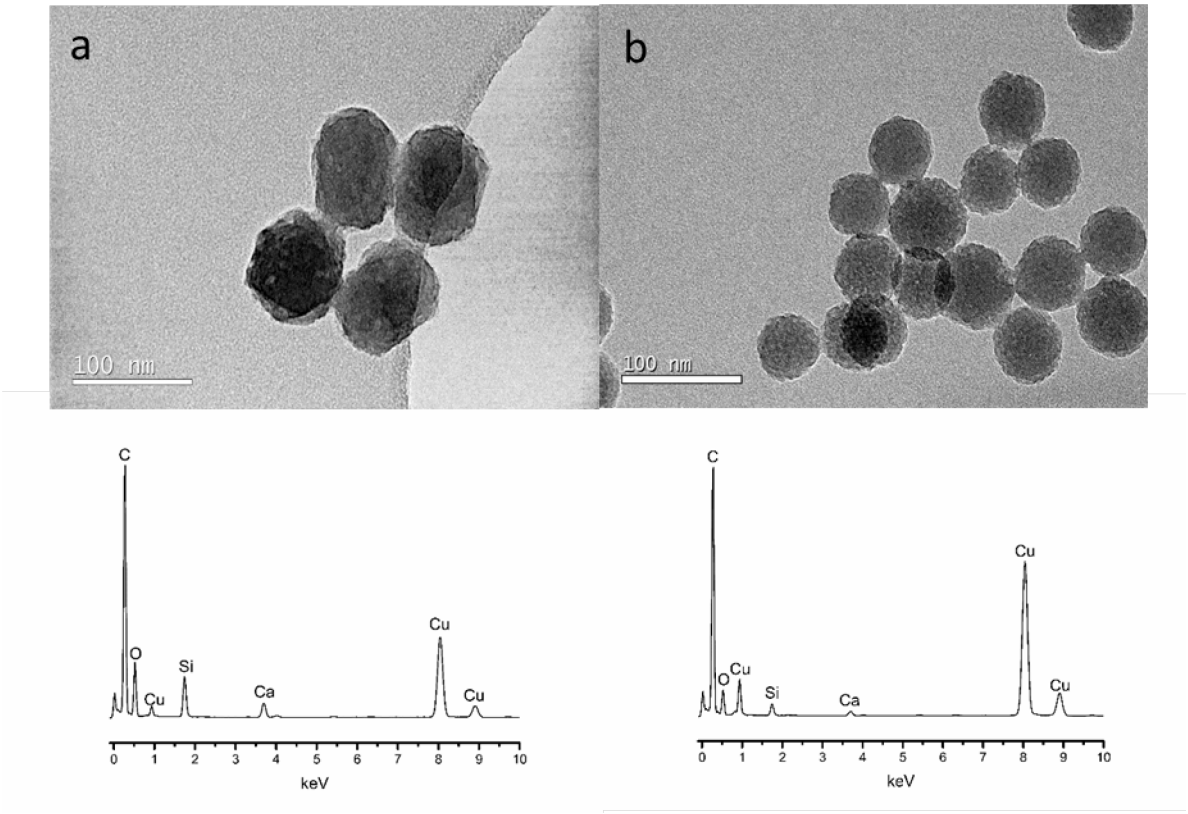


Figure 5.11 - TEM images and corresponding EDS results for a) CaMSN and b) MCE.

After MCEs could be made consistently, it was important to understand how GPMTS molecules affect the morphology of mesoporous nanoparticles on the surface and also the inner-surface of pore channels. He *et al.* reported that [122] the particle size increased after the addition of GPMTS and Luzinov *et al.*[177] reported that the monolayer of GPMTS formed on silica surface was about 1 nm. However, the size change reported from literature was unable to be captured by using TEM (Figure 5.11b) or DLS accurately. In order to carry on the study, nitrogen adsorption BET analysis was then performed.

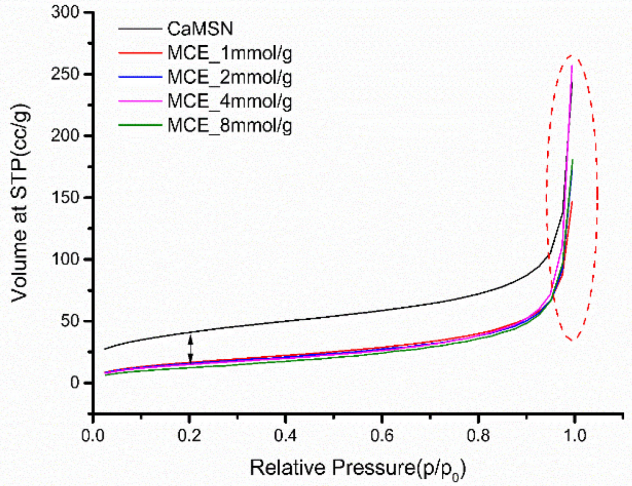


Figure 5.12 - Nitrogen adsorption of mesoporous particle with different amounts of GPTMS.

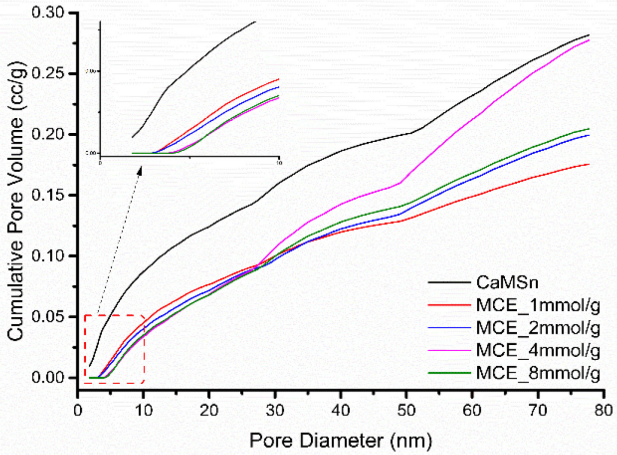


Figure 5.13 - Pore size distribution calculated by using DFT.

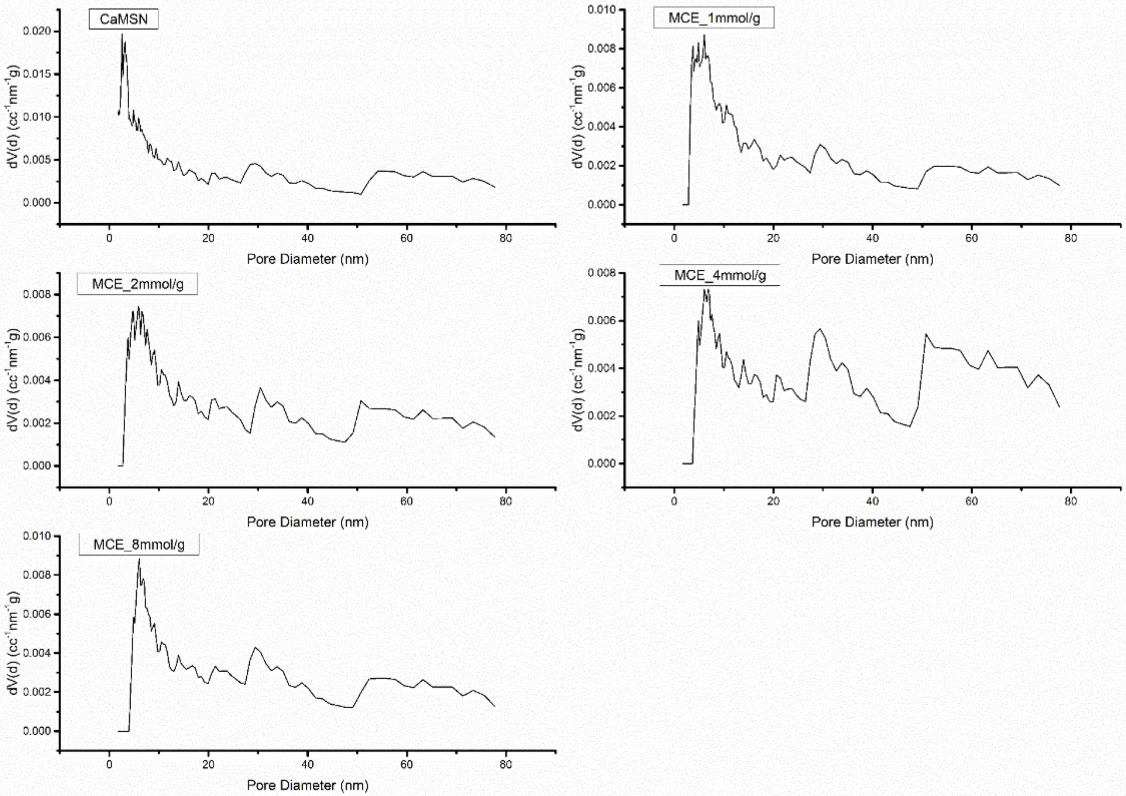


Figure 5.14 - Pore size distributions of mesoporous particles with different amounts of GPTMS. according to DFT calculations from the gas sorption isotherms.

Figure 5.12 showed gas sorption isotherms of the functionalised mesoporous particles. All samples produced type IV isotherms, which are typical of mesoporous adsorbents [153]. The circled region represents the capillary condensation phase and they were all still rising steeply, indicating that some large pores are present, which was possibly caused by pores the aggregation between particles after the incorporation of calcium. Also, this steep slope might also be caused by the fact that pores are highly connected. By comparing the samples before and after adding the GPTMS, functionalized MCEs have a much lower gas uptake in the monolayer region (difference illustrated by the black arrow). This indicated a significant lowering of the surface area on MCE samples. The beginning value of CaMSN samples was much higher than for MCEs, which indicated that some of the surface and possibly mesopores were blocked by the treatment, lowering the overall surface area.

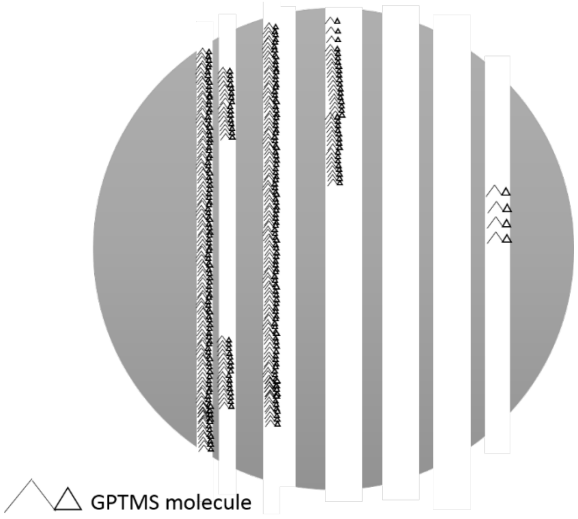
Table 5.2 - Surface area and pore size calculated from nitrogen adsorption data

	Specific surface area (BET) [m^2/ g]	**Modal pore diameter (DFT) [nm]**	**Pore volume (DFT) [cc/g]**
CaMSN	144.52	2.583	0.079
MCE_1mmol/g	62.50	2.941	0.046
MCE_2mmol/g	58.55	3.179	0.036
MCE_4mmol/g	56.78	3.537	0.033
MCE_8mmol/g	47.81	3.775	0.029

As shown in Table 5.2, surface area of all samples was calculated using 4-point BET and the surface area for CaMSN (144.52 m^2/g) was much lower than the surface area of MSNs (700 – 1500 m^2/g) reported in literature [98][178]. This was caused by the effect of adding calcium into the silica network as calcium ions acted as a network modifier which means they expanded the silica network because of their large ionic radius [179][180].

There was a significant drop in surface area when GPTMS was introduced and the more GPTMS added into the system, the smaller surface area was. In addition, the DFT plot (Figure 5.13) showed that at the pore size region 0-10 nm, MCE pores smaller than 8 nm gave very little contribution to the cumulative pore volume (the region highlighted by red rectangle), compared with un-functionalized CaMSNs. By looking at the pore diameter and pore volume calculated form the DFT graph (Table 5.2), it was discovered that with more GPTMS added into the particle system, a larger diameter and smaller pore volume were achieved. The

reason for pore diameter calculated from DFT graph is increasing instead of decreasing can be explained by using Figure 5.14. In these graphs, the higher the peak was, the more volume was contributed by corresponding diameter on the x-axis. The highest peak for CaMSN was 0.0196 cc/nm/g while the other 4 figures for MCEs were 0.0073-0.0088 cc/nm/g which were significantly smaller and this was caused by the closing of small pores. Since small pores were all closed, only larger pores were counted and as a consequence the average diameter of these MCE samples were bigger.



Scheme 5.4 - The sketch of how GPTMS blocks the mesopores within a nanoparticle.

The information obtained from nitrogen adsorption results suggested that GPTMS molecules did not only attach to the outer surface of mesoporous particles, but they had also been grafted on the inner surface of meso-channels and finally blocked pores (Scheme 5.4). Heat treating the samples at 680 °C for 3 hours for calcium incorporation removed some hydroxyl groups on the outer surface but hydroxyl groups on the inner surface (channel surface) were likely to remain in a higher density even after the calcination.Therefore, GPMTS molecules could be grafted on hydroxyl groups within the pore channels instead of on the surface, which can also explain why there was no significant MCE particle size change observed by TEM.

The interaction between GPMTS and mesoporous nanoparticles has been understood on a macro view by using nitrogen adsorption. Solid-state NMR was then performed to give an understanding on the micro view of how GPTMS affects the mesoporous network structure.

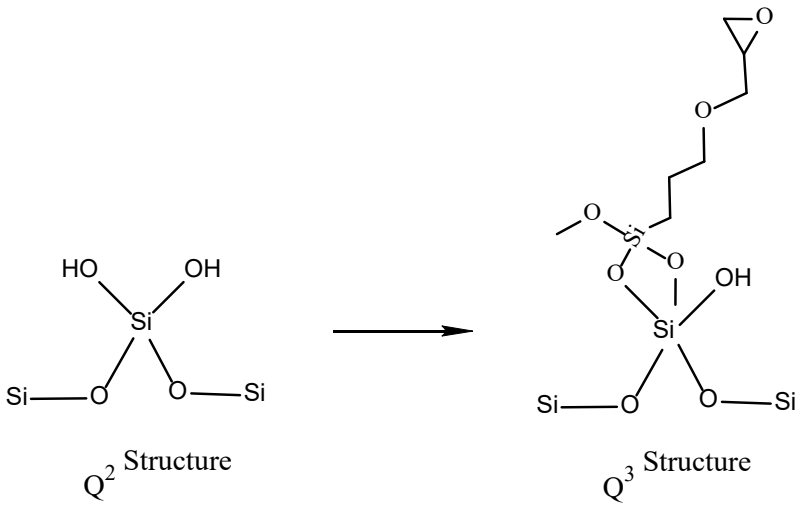
Table 5.3 - Chemical shifts and relative percentage abundance of silicon T and Q species obtained from ^{29}Si solid state NMR with resulted degree of condensation and total T fractions.

Q Species	Q^1		Q^2		Q^3		Q^4	
	δ_{iso} [ppm]	*I* [%]	δ_{iso} [ppm]	*I* [%]	δ_{iso} [ppm]	*I* [%]	δ_{iso} [ppm]	*I* [%]
CaMSNs	-83.6	9.7	-92.2	21.9	-98.6	16.8	-106.8	51.5
MCE_1	-80.2	4	-88	9.4	-98.3	42.2	-108.8	39.1
MCE_4	-80.6	13.4	-88	8.4	-96.5	36.6	-107.5	33.3

T Species	T^1		T^2		T^3		D_c	T/(Q+T)
	δ_{iso} [ppm]	*I* [%]	δ_{iso} [ppm]	*I* [%]	δ_{iso} [ppm]	*I* [%]	[%]	[%]
CaMSNs	N/A	N/A	N/A	N/A	N/A	N/A	75.05	0
MCE_1	-47.7	1.8	-54.6	2.5	-63	1	77.90	5.3
MCE_4	-49.3	3	-56.3	2.9	-64.5	2.4	68.95	8.3

Samples prepared with no GPMTS (CaMSNs) and those functionalized with 1 mmol/g (MCE_1) and 4 mmol/g (MCE_4) of GPTMS were sent for solid-state NMR analysis. A summary of data is shown in Figure 5.15 (page 95) and the corresponding quantitative results are calculated in Table 5.3. By comparing the samples before and after the functionalization, the appearance of peaks for T^n species ($C\text{-}Si(O\text{-}Si)_nNBO_n$) at range -47.7 ppm to -64.5 ppm on MCE samples indicates the success of GPTMS grafting. For ^1H MAS spectra, the broad peak from CaMSN samples became sharper when they were functionalized to MCEs and this is also given by the GPTMS.

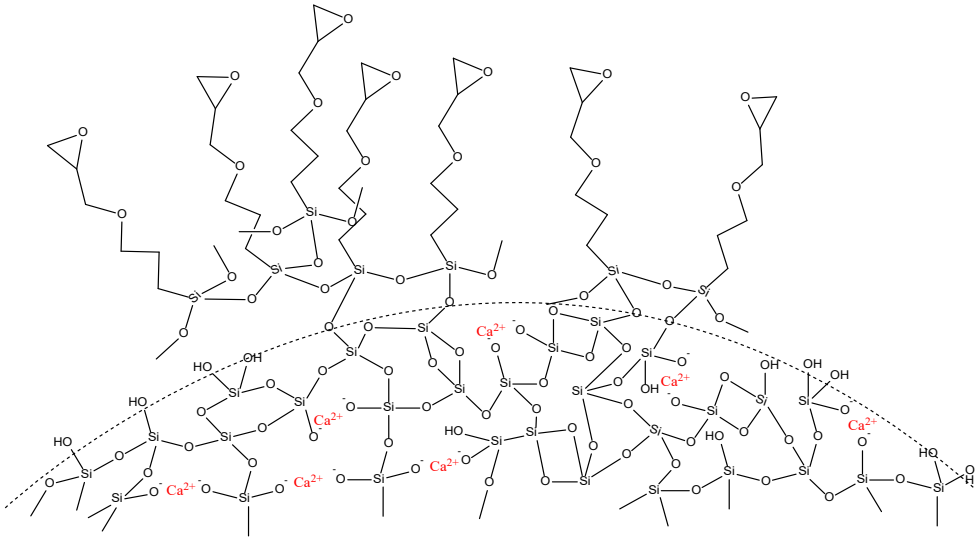
Considering the Q^n species from Table 5.3, MCE samples showed a large relative decrease in both Q^2 and Q^1 units compared to unfunctionalizes CaMSNs. Q^2 was contributed by the $(OH)_2Si(O\text{-}Si)_2$ combination at the surface of particles, when GPTMS molecules were introduced the reaction between them took over the OH bonds. However, after GPTMS molecules reacted with hydroxyl groups on the surface and formed Si-O-Si bridges, only Q^3 showed an increase while Q^4 decreased. This suggested that not both of the OH groups from Q^2 units were used by GPTMS, but in the most cases only one of the hydroxyl groups was used and left a Q^3 structure.



Scheme 5.5 - The proposed change of Q species at the surface of a nanoparticles during functionalization with GPTMS.

Considering the T^n species from the table, a T^3 structure indicated the total condensation of a GPTMS molecule. Comparing the T fraction (T/(T+Q)) of both MCE samples, MCE_4 (8.3%) shows a larger value than MCE_1 (5.3%) which means there were more GPTMS molecules attached when a higher amount of GPMTS was introduced during the synthesis and this result confirmed the data from TGA. In addition, the appearance of T^1 and T^2 on both MCE_1 and MCE_4 indicated that not all the methoxysilane groups were condensed so the product sketched in Scheme 4.3 was inaccurate and it was re-drawn in Scheme 5.6 below.

^{13}C MAS spectra (Figure 5.15) were also performed but because of the amount of GPTMS attached were relatively low, no noticeable signal was given from the analysis.



Scheme 5.6 - The plot of functionalized nanoparticles.

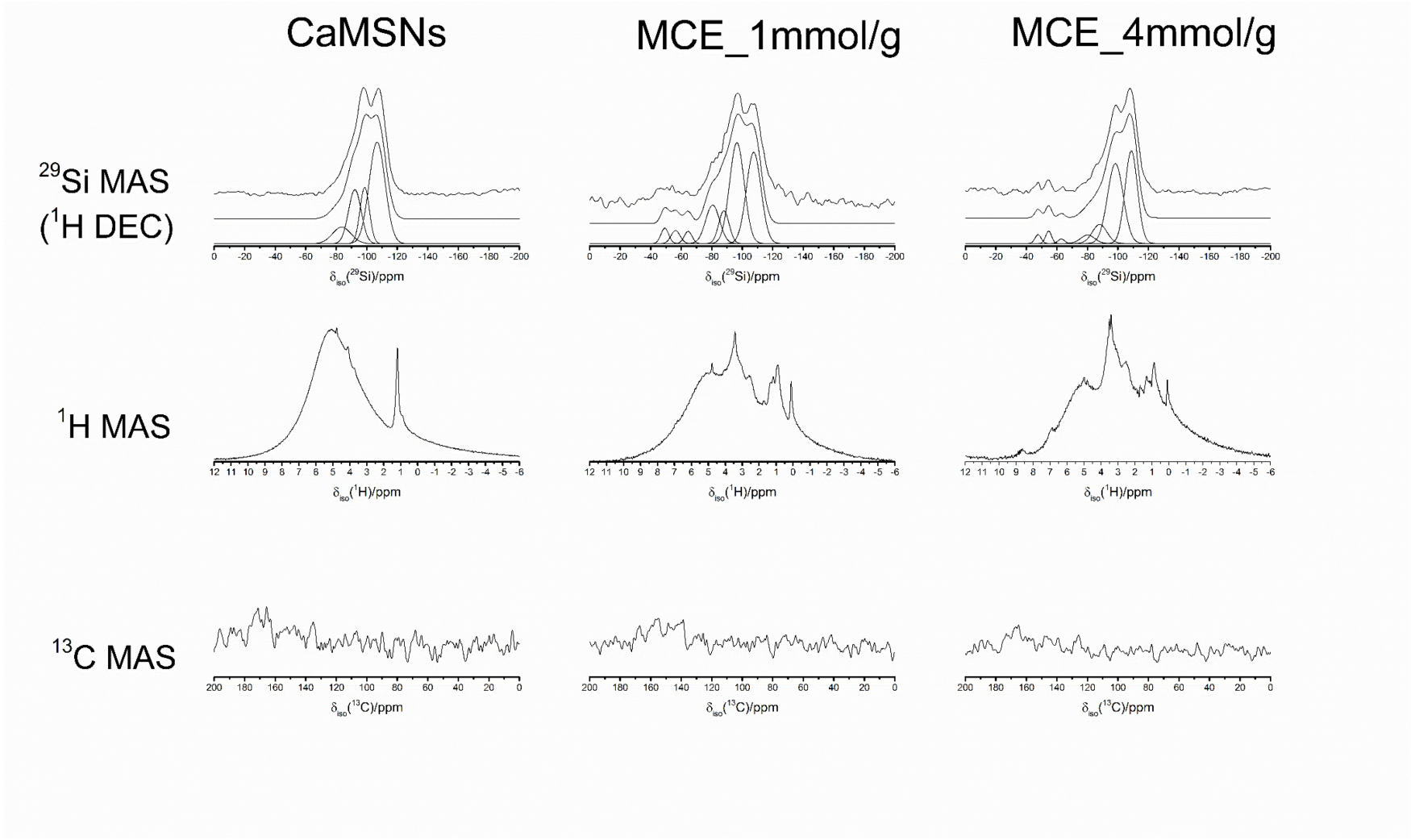


Figure 5.15- ^{29}Si single-pulse MAS NMR spectra (top line), ^{1}H MAS spectra (middle line) and the ^{13}C MAS (bottom line) of mesoporou silica nanoparticles.

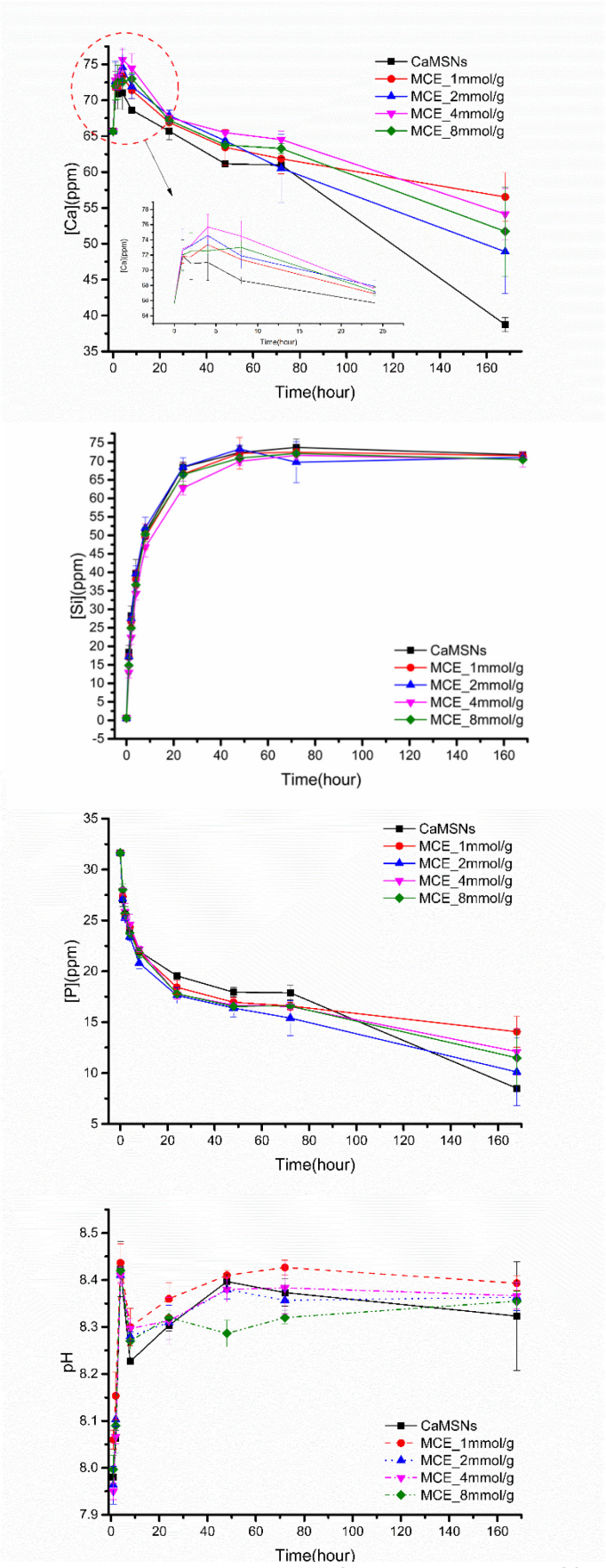


Figure 5.16 – Elemental concentrations and pH in MEM following immersion of for mesoporous particles.

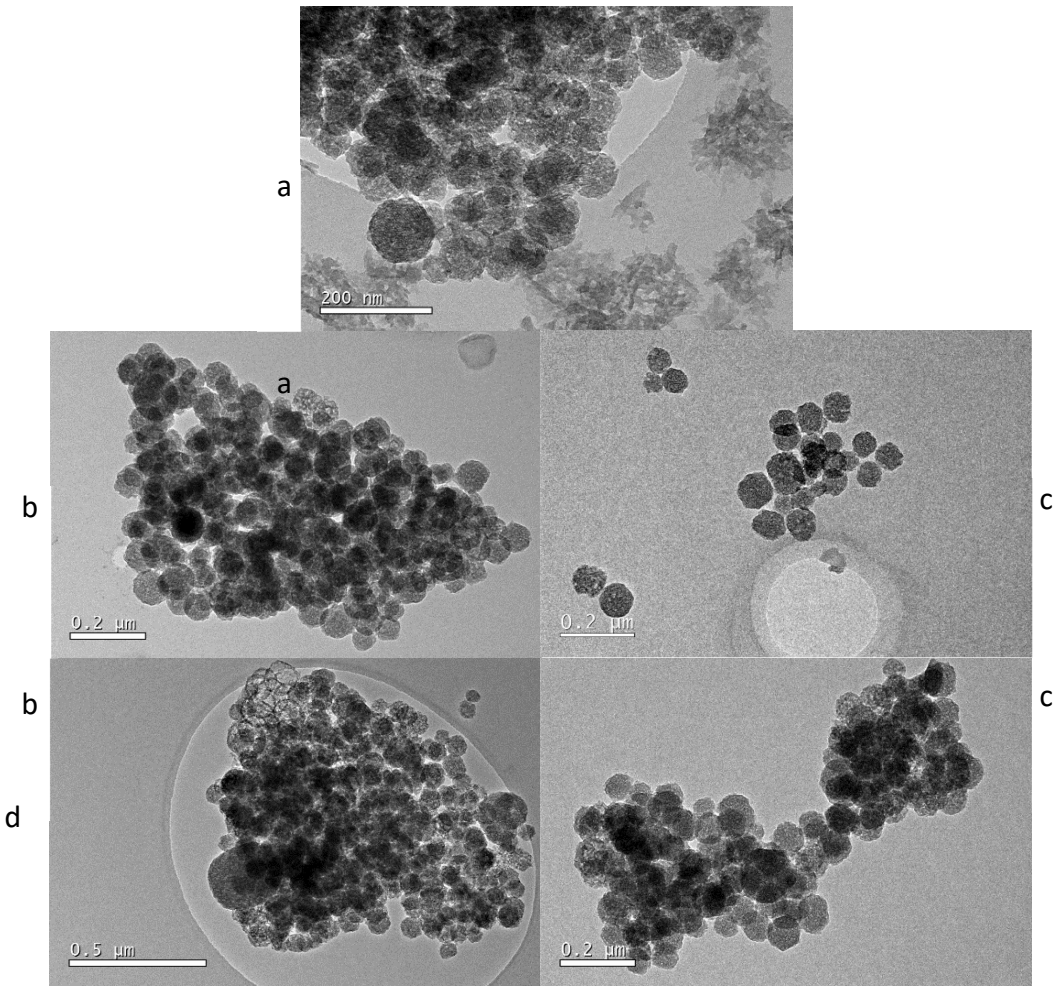


Figure 5.17 - TEM images of mesoporous particles 7 days after the dissolution study in MEM : a) CaMSNs, b) MCE1mmol/g, c)MCE2mmol/g, d)MCE4mmol/g and e)MCE8mmol/g.

The dissolution studies (Figure 5.16) were performed on CaMSNs and MCEs with 1 mmol/g, 2 mmol/g, 4 mmol/g and 8 mmol/g of GPTMS fed during the synthesis to understand the effect of GPMTS on ion release and MEM (pH 7.6) was chosen to mimic the extracellular environment for nanoparticles. After 7 days of study, TEM images (Figure 5.17) were taken on washed samples to investigate the morphological changes.

The Ca^{2+} release profile showed all samples had a burst release in the first 24 hours and then the total concentration went down till the end of the study. By focusing on the first 24 hours, MCE samples had a continuous release of calcium for the first 4 hours while calcium released from CaMSN samples has reached its peak value in the first hour. This suggested that GPTMS

on the particles surface had slightly slowed the calcium release by forming layers around particles.

The reason for the decreasing of calcium concentration in MEM after 4 hours for all samples can be explained by also considering the result of phosphorous profile. Phosphorus content in the MEM decreased which indicated that released calcium ions formed calcium phosphate with phosphate ions before they escaped the dialysis tubing and then precipitated back on the particle surface. In both calcium and phosphorous profile, meida containing CaMSNs had the lowest concentration of P by the end of the study, which could be the indicative of GPMTS interrupting the precipitation of calcium phosphate on the MCE particles, which was supported by comparing the TEM images. From TEM images, hollow particles were found in MCE samples (figure 5.17d) but precipitates observed were less compared to CaMSNs (figure 5.17a).

The Si release profiles look similar for all samples. They all showed a quick release on the first day, which followed a similar trend to the calcium ions, and then entered to a plateau after 48 hours. This can be explained by checking the pH values during the degradation. The quick released Ca^{2+} exchanged with H^{+} ions in the MEM, causing an increased in the solution pH in a short time which can promote the breaking of Si-O-Si bonds.

5.4 Conclusions

In this chapter, monodispersed spherical calcium incorporated mesoporous nanoparticles were made with the size 80-100 nm and the method was modified in order maintain a higher hydroxyl group density on the particle surface and a shorter total preparation time (from 4 days to 3 days).

Functionalized MCE particles showed consistent behaviour compared to dense particles in terms of DLS/zeta potential, FTIR, Raman and TGA results. In addition, TGA results showed mesoporous silica-nanoparticles can provide a better silica surface for grafting GPTMS compared to dense nanoparticles. However, results also showed that the yield of GPTMS grafting did not increase linearly with the amount of GPTMS added in during the synthesis. Although CaMSNs can functionalize with GPTMS without plasms treatment, in order to reach a higher yield in the future application, plasma treatment is recommended.

Nitrogen adsorption analysis was applied on MCE samples to investigate how GPTMS molecules distributed on the particles surface and the results suggested that small pores were likely blocked by the addition of GPTMS. The use of solid-state NMR confirmed the success of grafting GPTMS on the particles surface and confirmed the result from TGA that GPTMS concentration on particle surface increased with the amount added during the synthesis, however, not all the methoxylsilane groups were condensed.

Finally, the dissolution profile showed GPTMS molecules on the particle surface did slow down the release of calcium and the formation of calcium phosphate has also been slowed down consequently.

Chapter 6 Functionalized Bioactive Mesoporous Silica-Nanoparticles in Silica/PTHF/Polycaprolactone Hybrids

6.1 INTRODUCTION

Inorganic-organic hybrid sol-gel materials have indistinguishable components above the nanoscale and this nano-scale interaction enables them to degrade congruently and have tailorable mechanical properties [53]. However, the majority of hybrid materials do not have bioactive cations incorporated, like calcium for example, and this was because the conventional way to incorporate cations needs high temperature treatment (>450°C) [4].

To address this problem, MCEs were introduced into a class IV PCL based hybrid system in this chapter. As MCEs can be prefabricated to contain cations, the role of MCEs is the carrier of cations to help the PCL hybrids become bioactive. Calcium was chosen as the bioactive cation. The reason for choosing this PTHF/PCL/SiO_2 hybrid system invented by Tallia *et al.* [10] was because this hybrid system used GPTMS as a coupling agent, as well as a polymerization initiator. MCEs have GPTMS on both inter- and outer surface which were expected to covalently bond to this hybrid system. Also, the mechanical properties of this hybrid system were tailorable, which means with different cations incorporated into the GPTMS functionalized mesoporous nanoparticles, the hybrid material's application range could become wider.

This chapter first reports on the synthesis of the hybrid system with nanoparticle incorporation and how the original method was modified for MCEs incorporation. After bulk samples were made consistently, the hybrid silicate network, mechanical properties, morphology, dissolution profiles and material cytotoxicity were investigated. Hybrid sols were then prepared for extrusion 3D printing. Inter-connected porous scaffolds were printed and the impact of MCEs on 3D printing feasibility was studied by using rheometry.

6.2 MATERIALS AND METHODS

All reagents were purchased from Sigma-Aldrich and VWR and used as received unless otherwise stated.

6.2.1 Sol-gel synthesis of MCE containing hybrids

The silica/PTHF/PCL synthesis method was modified from Tallia *et al*. [10]. The general procedure can be divided into 3 steps as shown in the flow chart.

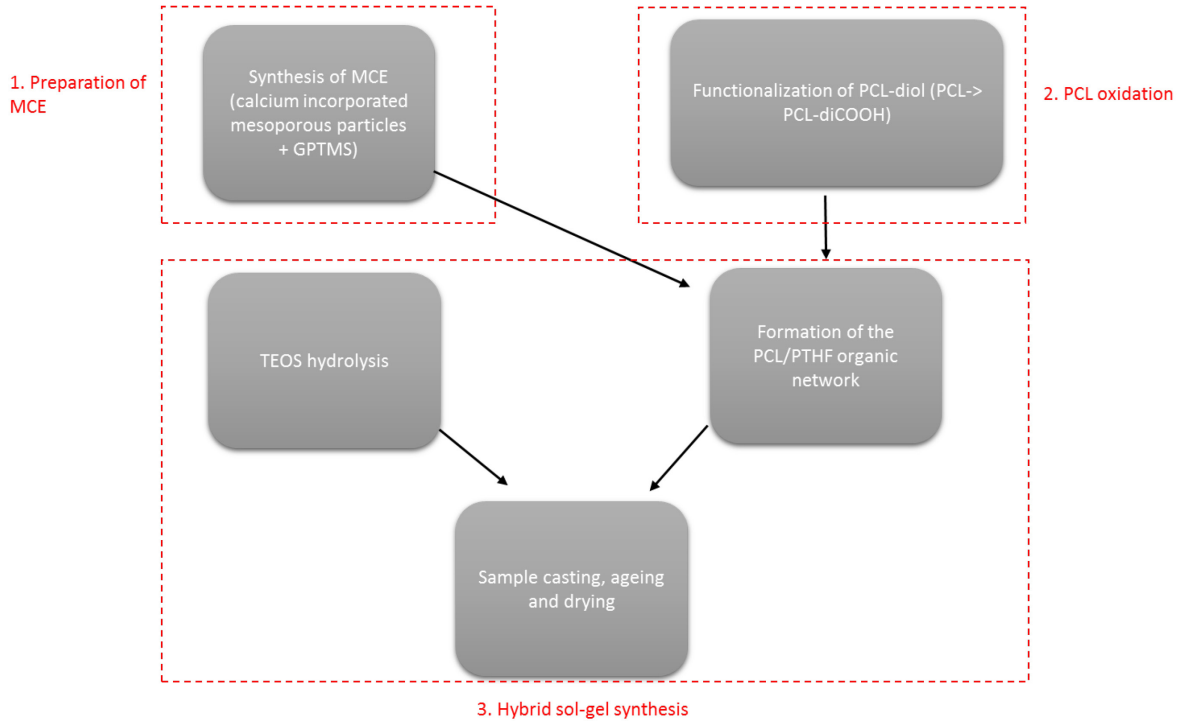


Figure 6.1 - Flowchart for making nanoparticles contained hybrids.

Preparation of MCEs. GPTMS functionalized MCEs were produced by using the method described in Chapter 5 with the last drying process modified. Particles were reacted with GPMTS molecules overnight then washed twice with THF and then re-dispersed in 5 mL of THF by using ultrasonication bath. The THF solution containing MCEs was then kept for later use. The reason for not drying MCEs and using them directly in THF is to avoid the ring opening reaction of epoxide rings on GPTMS molecules in the 60°C oven.

Oxidation of polycaprolactone diol (M_n = 530 Da). PCL diol were oxidized so that the OH end groups became carboxylic groups. This was done by using Anelli's oxidation reaction [181]. 2,2,6,6-tetramethyl-1-piperidinyloxy (TEMPO) was used as the catalyst in a biphasic system

containing acetonitrile and water [182]. As illustrated in Figure 6.2, the overall oxidation reaction can be divided into 2 stages. In the first stage, bleach (NaOCl) worked as the stoichiometric oxidant that reacted with KBr giving HOBr. The existence of HOBr then converted the TEMPO radical into oxoammonium salt, which is a catalytic primary oxidant that then converted the primary alcohol into aldehyde. At the end of stage one, the oxoammonium salt was transferred into hydroxylamine. The hydroxylamine was oxidized and converted by HOBr to a TEMPO radical at the beginning of the stage 2, at which point a second catalytic cycle was done to give the final product. In order to boost the reaction, sodium bicarbonate ($NaHCO_3$) was used to provide a less basic environment (pH=8.6).

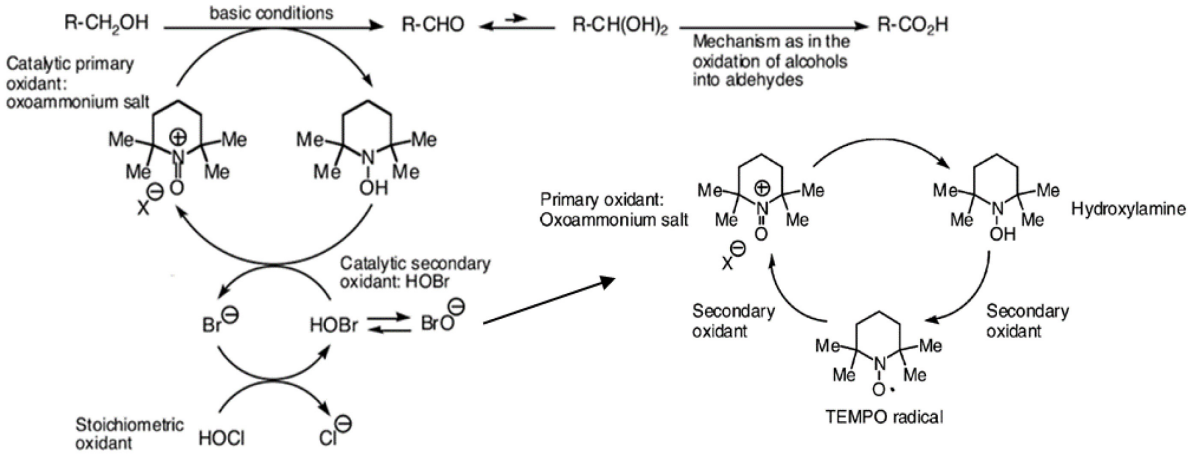


Figure 6.2 - The mechanism of Anelli's oxdiation (modified from [182]**)**

In this oxidation procedure, 3 g of PCL diol (5.66 mmol) were dissolved in 45.70 mL of acetonitrile (CH_3CN, anhydrous 99.8%). While stirring at 400 rpm continuously, 12.30 mL of saturated $NaHCO_3$ was firstly added followed by 4.53 mL of KBr (2.26 mmol in water) and 11.32 mL of TEMPO (1.13 mmol in acetonitrile). The solution was then left mixing for 1 h in a sealed glass round bottom flask. After the solution was perfectly mixed, a total amount of 74.04 mL of bleach (NaOCl, 5 vol.%) was added at 4 time points. The first time point was 1 h after mixing everything with v_1 = 29.02 mL, the second time point was 4 h after the mixing with $v_2 = v_1 = 29.02$ mL, the third time point was at 7.5 h after the mixing with v_3 = 8.0 mL and the last adding time point was 24 h after the mixing with $v_4 = v_3 = 8.0$ mL. After all the addition of the bleach, the solution was left mixing for another 3.5 h and then HCl (37 vol.%) was added to adjust the solution pH from 8 to ≤ 3 to convert anion ($-COO^-$) into carboxyl group (-COOH).

The solution was then stirred for another 2 h and CH_3CN was removed by using the Rotavapor (Büchi Labortechnik AG) at 40 °C and 226 mbar. The residue solution was mixed with ethyl acetate so the oxidised PCL diol polymers were extracted via solvent exchange and this was repeated 3 times. Na_2SO_4 was added into the ethyl acetate solution containing ox-PCL to remove any water remained and then the solution was transferred to the Rotavapor again to remove the ethyl acetate at 40°C and 240 mbar. The final ox-PCL diol product was stored at desiccator for at least 12 h before use.

Preparation of the hybrid sol. Hybrid materials containing MCEs synthesised in this project were at a target organic : inorganic weight ratio of 80:20, by modifying the method established by Tallia *et al.* [10].

To successfully synthesise the hybrid sol, both inorganic and organic sols had to be prepared separately. The synthesis of inorganic sol followed the TEOS hydrolysis and condensation reaction described in *Section 2.4.2*. Here, 4.29 mL (4 g) of TEOS was hydrolysed with 1.59 mL of water and 0.53 mL of HCL (2 M) by mixing together at 800 rpm and stirring for 1 h. The hydrolysed sol was then ready to mix with the organic-MCE sol.

The mechanism of synthesis of organic-MCE sol was similar to the original method described in *Section 2.7.3*. A schematic of the proposed reaction is shown in Figure 6.3, the epoxide ring on the particle surface was hypothesized to be activated by boron trifluoride etherate (BF_3OET_2), which then would progress to the intermediate stage I. The presence of THF should trigger nucleophilic attack to take the compound to intermediate stage II. The ring opening polymerization at this moment would then be triggered for chain growth.

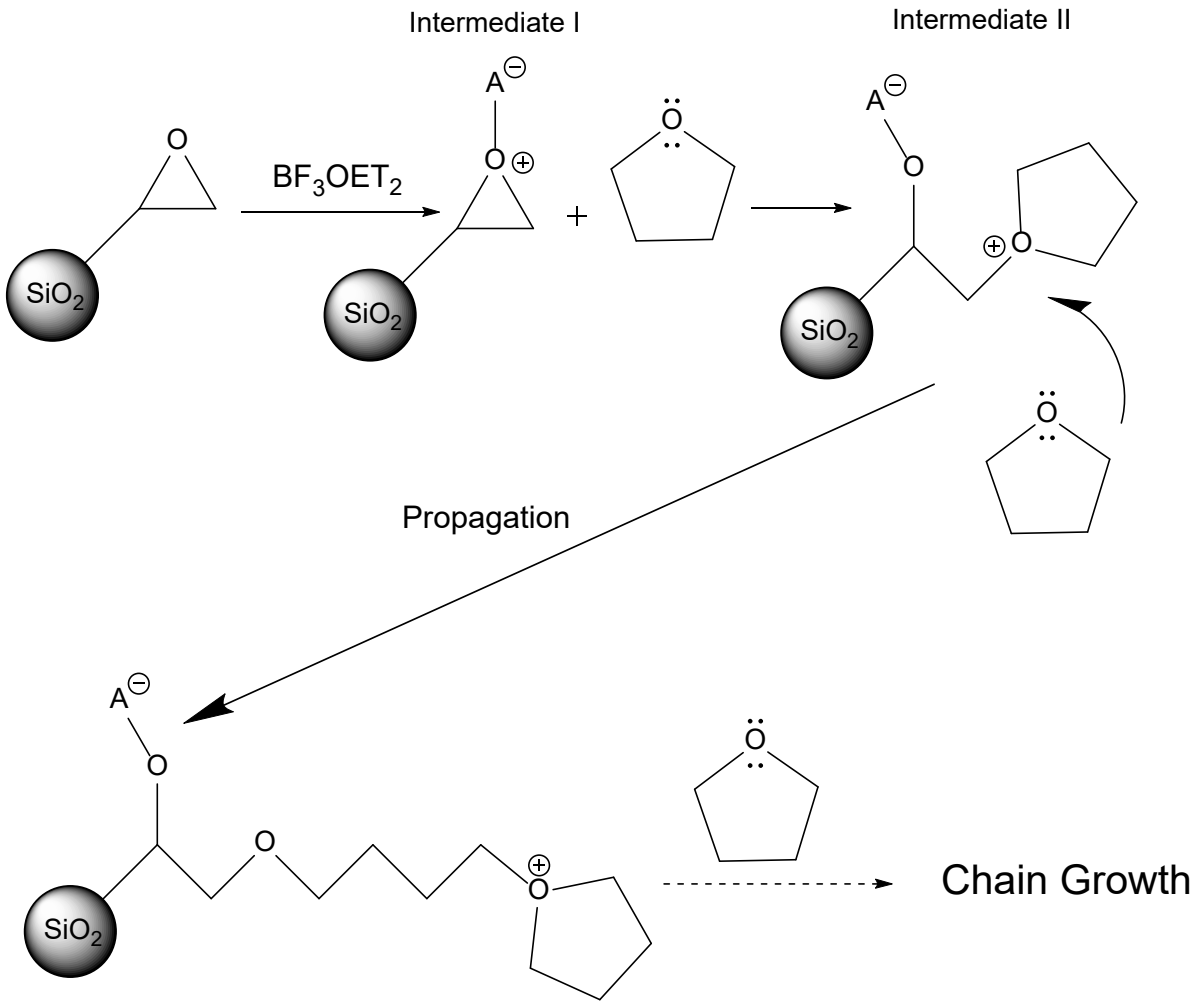
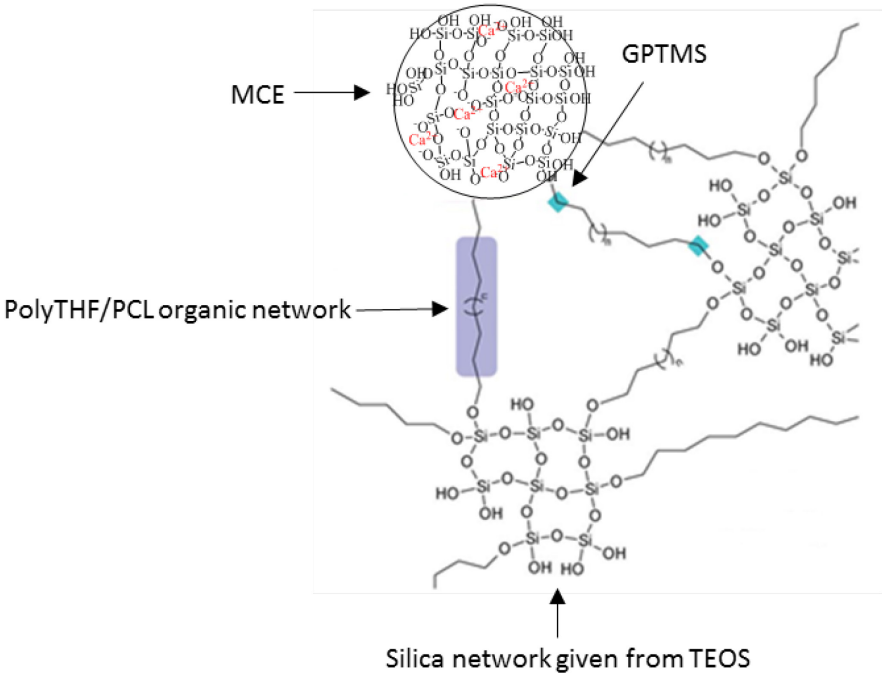


Figure 6.3 - Schematic of the proposed ring opening polymerization mechanism between MCE and THF.

In this synthesis, 1 g of oxidised PCL-COOH diol was dissolved in 5 mL of THF (anhydrous, 99.9%) and stirred for 15 minutes. MCEs (0 mg – 250 mg) in the THF, prepared by following the method described above, were added into the PCL solution which then made up a 10 mL solution. The PCL concentration in THF was 1 g/mL. The solution was then treated in the ultrasonication bath for 10 minutes and then stirred for 10 minutes at 800 rpm before the addition of 833 µL of GPTMS. After another 15 minutes of mixing, 116.4 µL of BF_3OET_2 was added into the solution and then mixed for 1 h to let the ring opening polymerization occur. The polyTHF-PCl polymer network was also formed during this time and the reaction mechanism was described in the *Section 2.7.3*. Finally, the hydrolysed TEOS inorganic sol was added into this organic-MCE sol dropwise which then mixed to give the hybrid sol (Scheme 6.1).



Scheme 6.1 - A proposed drawing of of nano-PCL hybrid network.

6.2.2 The making of cylindrical and disc bulk samples

After hybrid sols were made, they needed to be casted into solid bulk samples for the further characterisation. Cylindrical shaped and disc shaped samples were made with Sample IDs starting with HMC_ followed by the amounts of MCEs added during the synthesis.

For casting cylindrical shaped samples, hybrid sol prepared was further mixed for another 15 minutes to make sure the sol was getting more viscous before pouring into the moulds. The cylindrical moulds were PTFE with an internal diameter of 15 mm and height of 25 mm. Moulds were placed in the PMP containers (Nalgene) and then hybrid sols were transferred into the moulds carefully by pipetting. The PMP containers were then sealed (screw tops) and placed in the 40 °C oven for 7 days in order to let the sol aging, further polymerized and gelled. After 7 days, sealed PMP container lids were slightly loosened day by day to let the sample fully dry. After 20 days, samples were removed from the oven and ready for characterisation.

For casting disc samples, a similar manufacture route was followed. The moulds used for making disc samples had a diameter of 130 mm with a height of 40 mm and PMP containers were not needed. After samples were transferred into the moulds, aluminium foil was used to wrap over and seal the moulds (4 layers). After 7 days of aging, the first layer of aluminium foil was removed and the other layers were removed every 4 days. Samples were ready to use when all the aluminium foil layers were removed.

6.2.3 3D printing of the MCE containing nano-hybrid

The advantage of the sol-gel process is that the hybrids could be potentially capable of being printed directly from sols by using extrusion printing.

Hybrid ink preparation. Following the process of making hybrid sols described (*Section 6.2.1*), the sol was left stirring for 15 minutes with the reaction container lid on. After 15 minutes, the lid was removed and the solution was stirred for another 15 minutes to make the sol more viscous. The time taken at this step differed from sample to sample and was dependent on the amount of MCEs put in the solution. Details will be discussed in the results section. When an optimal viscosity of the sol was achieved, it was then transferred into 3 mL luer-lock syringes (VWR International, UK). Syringes containing the hybrid ink were then capped with stoppers and wrapped with aluminium foil. They were finally transferred into a -80°C freezer. The polymerisation reaction stopped due the low temperature and the ink was frozen. Syringes were stored there and ready to use on the day of printing.

3D extrusion printing. The set up for 3D printing is shown in Figure 6.4. The 3D printer used in this project is a robotic deposition device (A3200 Robocaster, 3D Inks LLC, USA) while the scaffold design and printer control used the same software RoboCAD 4.1 (3D Inks LLC, USA). Conical extruder tips with diameter of 0.20 mm (SmoothFlow™ Tapered Tips, Nordson EFD, UK) were chosen to connect to the ink syringes. The printing substrate was paraffin paper which provided a surface that printed filament firmly attached on and when the scaffold was dried they did not stick to each other.

Before printing, the ink syringe was taken from the -80°C freezer and it took 10 minutes for the syringe to return to the room temperature. Inks at this stage were still not gelled enough for printing as the polymerisation reaction stopped during the ink making. An extra time, ranging from 15 minutes to 70 minutes, was needed to wait at room temperature for inks in

the syringe to reach the printable viscosity. Time needed at this stage was variable and was dependent on the amount of MCEs put in and also the room temperature. When the ink sol was gelled enough to make thread when pushing the syringe, it was ready to print. The printing time was limited due to the ink becoming over gelled (too viscous). The actual viscosity and printing window were determined by visual observation as well as trial and error.

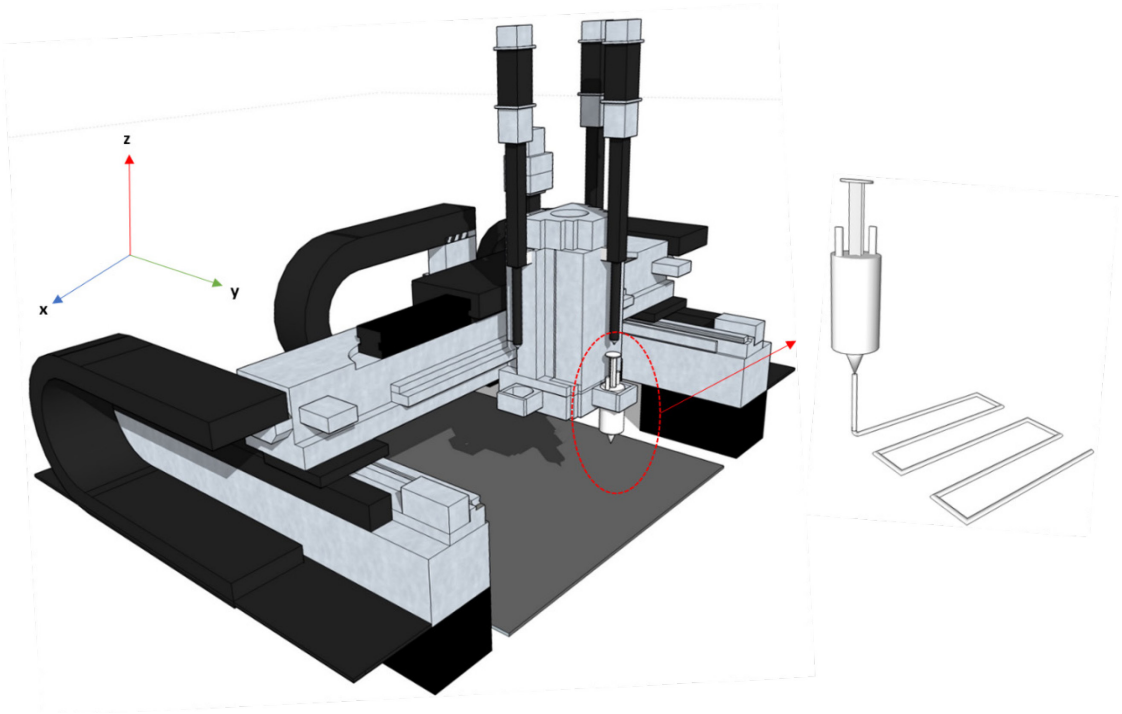


Figure 6.4 - The set-up of the extrusion printing device.

Scaffold design and making. The hybrid sol was extruded from the syringe continuously with a constant force at a speed of 10 mm/s ,which produced a continuous filament The same design pattern printed by Gao *et al.*[147] and Tallia *et al.*[10] was followed, a layer by layer 90° mesh aligned structure (Figure 6.5). The distance between each parallel filament was set at 0.60 mm and the z-spacing, i.e. the height of each layer, was set to 0.21 mm. A total of 32 layers were fabricated, producing a final dimension of designed cubic scaffold of 12 mm x 12 mm x 6.51 mm. After the scaffold was successfully fabricated, it was immediately transferred into a PMP container and sealed to avoid the quick evaporation of the sol solvent. It was then transferred into the 40°C oven, aged and dried by using the same method as described for the cylindrical bulk samples.

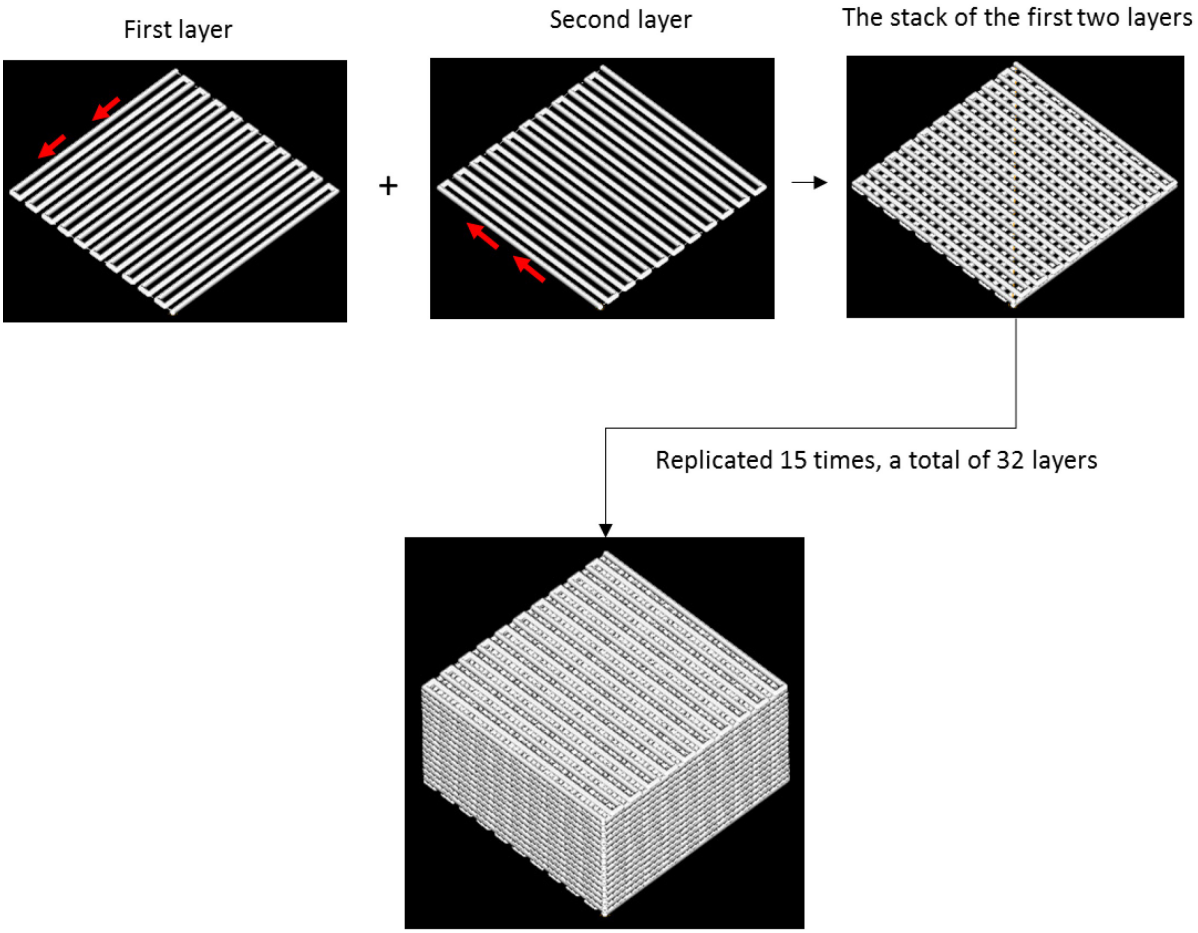


Figure 6.5 - Illustration of the scaffold design. The gap between filaments was 0.6x0.6 mm, length and width were both 12 mm and the height was 6.51 mm.

6.3 CHARACTERISATION

6.3.1 Chemical reaction study

The oxidised PCL diol and the final hybrid underwent chemical composition analysis to ensure the correct product was made. FTIR was used to investigate changes in signature bands from PCL before and after oxidation and also to assess the BF_3OET_2 catalysed polymerization, which was proposed to open the epoxide ring and formed polyTHF. Although FTIR is an easy tool to determine the chemical structure, it is restricted by its resolution and band overlap. NMR was then used to help validate the FTIR results. Proton NMR analysis using $CDCl_3$ was carried out on both PCL di-OH and PCL di-COOH samples and also on the polyTHF/PCL organic sol.

6.3.2 Chemical composition study

The MCE-containing hybrid samples were made targeting at an organic : inorganic ratio of 80:20. TGA/DSC thermal analysis was used to assess if they achieved this ratio. All samples were made with a fixed PCL-diCOOH : TEOS weight ratio and the only difference was the amount of MCEs introduced : 0 mg, 50 mg, 150 mg and 250 mg and they were all ground to powders before the measurement. It was expected that with more MCEs added into the system, the final weight ratio should shift more to the inorganic part.

6.3.3 Bulk sample macro observation

Both cylindrical and disc samples were made with a fixed PCL-diCOOH : TEOS weight ratio and the amount of MCEs introduced into the hybrid network was 0 mg, 50 mg, 150 mg and 250 mg. All MCEs were synthesised with similar particle size and the amount of GPMTS added was 4 mmol/g. All samples were compared visually as increasing MCE content was expected to decrease transparency. In addition, the reaction time for the final hybrid sol becoming viscous, i.e. the time for polyTHF/PCL/silica/MCE network to start condensing, was also recorded to investigate if the presence of MCEs affects the reaction.

6.3.4 Bulk sample micro observation and network investigation

Scanning electron microscopy (SEM) was deployed to investigate the morphology of bulk samples and also the information on MCE distribution in the network. Samples were prepared in two orientations: top facing and bottom facing, to compare and determine if MCEs had sunk to the bottom during the synthesis and aging due to the gravity.

With the help from Nicole Kelly at Warwick University, Solid-State NMR was carried out on samples containing 0 mg, 100 mg and 200 mg MCEs and all MCEs were synthesised with 4 mmol/g of GPTMS fed. The ^{29}Si single-pulse MAS spectra were obtained and analysed to calculate the relative amount of Q^n and T^n species. The degree of condensation was then calculated and to see how MCEs affect the original hybrid network.

6.3.5 Mechanical testing of bulk samples

Compression tests on cylindrical samples. The mechanical properties of cylindrical nano-hybrid samples were firstly investigated by uni-axial compressive tests. The machine used was a Z010 mechanical test machine (Zwic/Roell) with a 10 kN load cell. The compression

displacement rate was set to 0.5 mm/min. Two sets of samples were prepared for the compression tests. While all samples were made with a fixed PCL : TEOS weight ratio of 1 : 4, the first set had a same amount of MCEs added into the system however, the GPTMS added during the MCEs synthesis were different: 0 mmol/g, 1 mmol/g and 4 mmol/g. In the second set, all MCEs were prepared with the same amount of GPTMS added (4 mmol/g) but the amount of MCEs introduced to the hybrid system was different: 0 mg, 50 mg, 150 mg and 250 mg. All samples were polished by using sand paper to have a flat surface. The dimensions for all samples were 10.26±0.11 mm in diameter and 14.39±0.71 mm in height. Tests were repeated by 3-5 times depend on the number of available samples.

Cyclic (compressive) loading test. Cylindrical samples with different amount of MCEs (0 mg, 50 mg, 150 mg and 250 mg) were tested with the loading cycle with a speed of 0.5 mm/min. The total cycle was 10 and with a 2 N pre-load while the maximum deformation was set individually according to each sample's behaviour. All samples were polished by using the sand paper and had a dimension of 10.27±0.18 mm in diameter and 13.23±0.87 mm in height.

Tensile test. For disc shaped samples, the Bose Electroforce Series III machine was used to test investigate the behaviour in tension. Rectangular samples with a dimension of 45 mm x 10 mm x 2.11±0.35 mm was cut from the hybrid discs. At both sides of strips, a 10 mm long length was marked and these spaces were left for gripping (Figure 6.6). The tensile tests up to failure were carried out with a 220 N load cell and a displacement rate of 1 mm/min.

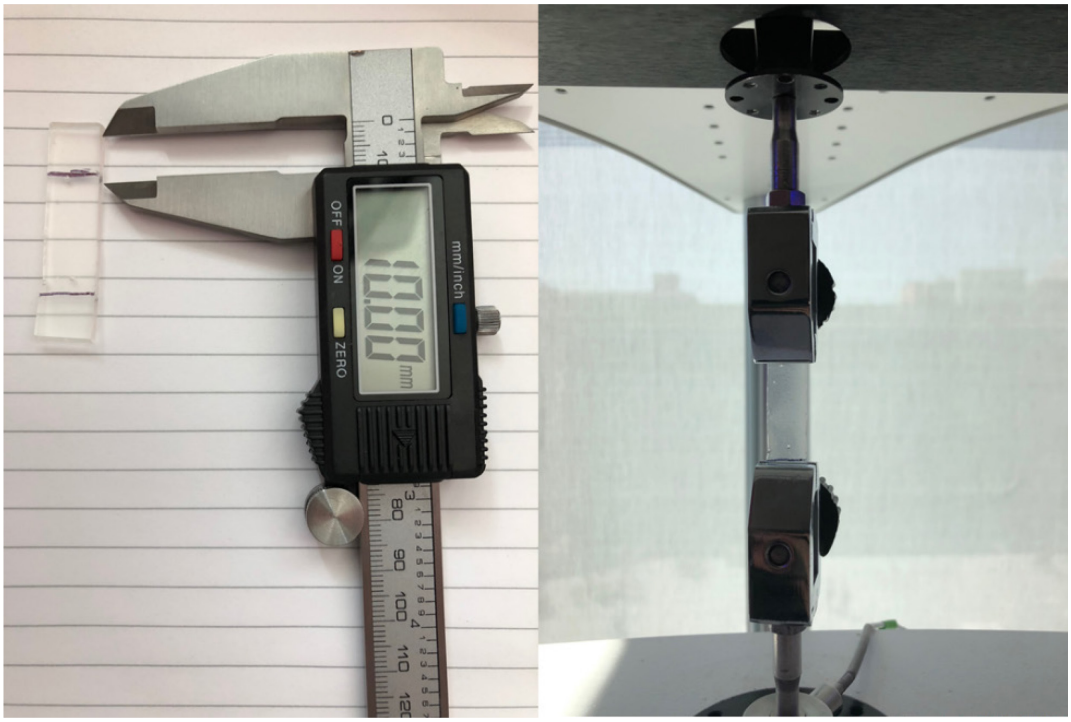


Figure 6.6 - The set-up of the tensile test on a Bose Electroforce machine.

6.3.6 Dissolution study

Dissolution study in SBF. Hybrid samples contained different amount of MCEs were prepared (0 mg, 50 mg, 150 mg and 250 mg). The priority of this study was to investigate the apatite formation on the sample surface. More MCEs present in the sample means more calcium concentration available for HCA formation, while all the 0 mg samples had no calcium. Samples used for this study were ground to powders with 75 mg per 50 mL of SBF.

Dissolution study in Tris. Different from the SBF study, hybrid samples prepared for Tris buffer studies had same amount of MCEs (250 mg) but different amount of GPTMS fed during the MCE synthesis (0 mmol/g, 1 mmol/g and 2 mmol/g). This study was designed to investigate how the covalent bonding between MCEs to the polymer network affected the release of the ions. The reason for choosing Tris was because, unlike SBF, the solution had no calcium source and it did not affect the final calcium release reading. Samples used for this study were prepared as bulk samples with 75 mg per 50 mL of Tris.

6.3.7 Cytotoxicity test

The cell study work was carried out by Dr Siwei Li and Dr. Parichart Naruphontjirakul using MC3T3-E1 preosteoblast and ATDC5 chondrogenic cells.

In vitro cell culture. ATDC5 chondrogenic cell line and MC3T3-E1 preosteoblast cell line (ATCC, UK) were expanded in basal α-MEM supplemented with 10% (v/v) foetal calf serum (FCS), 100 unit/mL penicillin and 100 μg/mL streptomycin. Cultures were maintained in humidified atmosphere at 37°C, 5% CO_2 and 21% O_2. Cells were passaged upon confluence using 500 μg/ml trypsin-EDTA (ethylene diamine tetra-acetic acid).

Cytotoxicity. Cylindrical shaped hybrid samples were ground into powders whether and they were cytotoxic to the chondrogenic cell/preosteoblast cell was assessed according to ISO 10993-5 [183]and ISO 10993-12 [184]. Conditioned media containing the dssolution products of the hybrids were prepared by soaking the particles in the media for 72 at a concentration of 0.2 g/mL in α-MEM at 37°C. Medical grade polyethylene (PE) was used as negative control (non-cytotoxic) and polyurethane (PU) containing 0.1% (w/w) zinc diethyldithiocarbamate (ZDEC) was used as positive control (reproducible cytotoxic response). Diluted solutions (25%, 50%, 75% and 100%) were prepared from the dissolution product and 10% (v/v) FCS was added before the cell viability assessment.

A calorimetric cell metabolic activity assay was used to determine the cell viability based on the conversion of 3-(4,5-dimethylthiazol-2-yl)-2,5-diphenyltetrazolium bromide (MTT) into formazan. On a 96-well plate, MC3T3-E1 cells were seeded with $1x10^4$ cells per well. Cells were left to grow in basal α-MEM for 24 h. After 24 h, the media was removed, dissolution products or controls were added together with fresh basal α-MEM incubated for another 24 h (100 μl/well). The culture media was then replaced by MTT, which was diluted in serum-free α-MEM at a concentration of 1 mg/ml. After the plate was incubated for another 2 h, the MTT solution was replaced with 100 μl of isopropanol each plate and shaken briefly to dissolve the formazan derivatives. The optical density was measured spectrophotometrically at 570 nm using a microplate reader (SpectraMax M5).

6.3.8 3D printing - ink and scaffold characterisation.

Rheology test. The effect of MCEs on the hybrid sol gelation time was assessed by using the rheometer. Hybrid ink samples with different amount of MCEs were prepared for the test (0 mg, 50 mg, 150 mg and 250 mg). Each sample was taken from the freezer and left at room temperature for 10 minutes to defrost and then tested the shear stress over a shear rate from 1 s^{-1} to 120 s^{-1} in a 60 s period. Viscosity change was measured over a period of 10 minutes at a shear rate of 80 s^{-1}. The machine used was the Discovery Hybrid Rheometer HR-1 (TA Instruments, UK) with a Peltier plate (diameter = 8 mm) and the set-up was shown in the Figure 6.7.

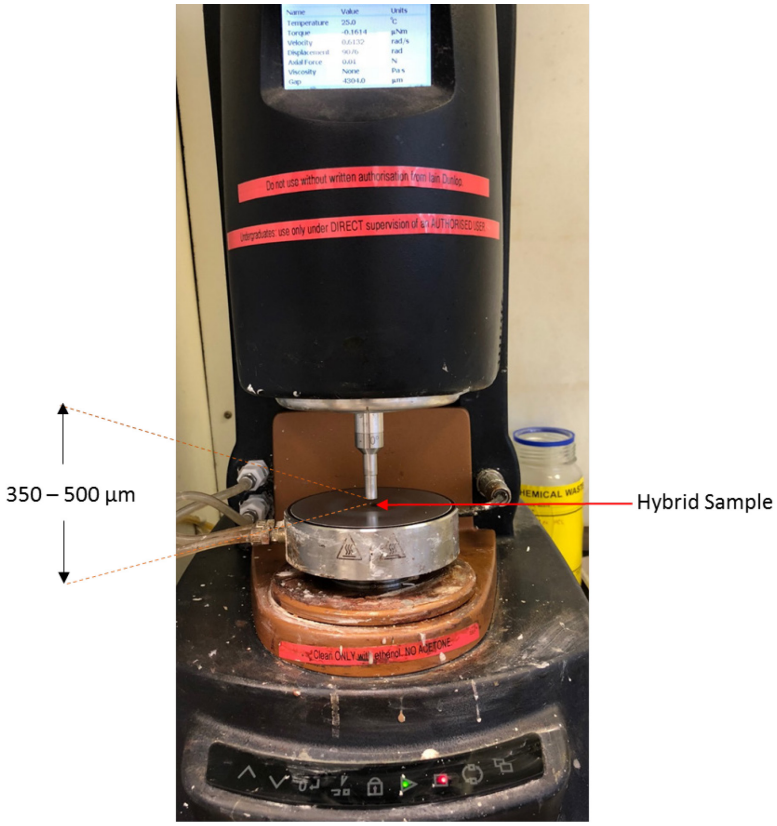


Figure 6.7 - The rheometer used for testing the viscosity of the inks. The gap between the peltier plate and the substrate plate was set to 350 or 500 um depended on the ink.

SEM imaging. Dried 3D printed scaffolds were imaged by using SEM. The morphology of the scaffold was studied and also the effect of shrinkage on the scaffold structure was assessed. Also, the scaffolds printed in the different printing window were compared under SEM.

6.4 RESULTS AND DISCUSSION

6.4.1 Oxidation of PCL diol (M_n= 530 Da)

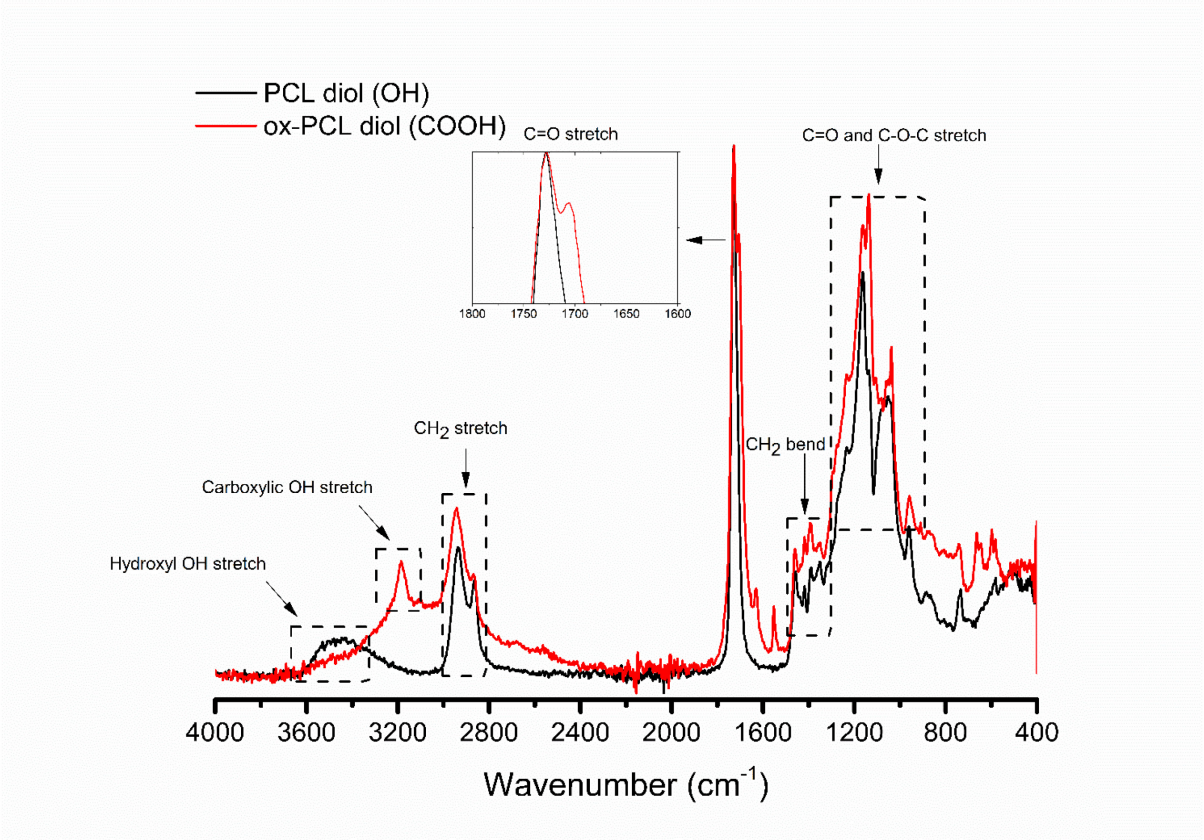


Figure 6.8 - FTIR spectra of PCL diol before and after oxidation.

The FTIR spectra for both PCL-diOH and PCL-diCOOH were obtained (Figure 6.8). The PCL-diOH was used as a control sample to evaluate the variations after the oxidation process. From the results, 3 signature bands were shown from the PCL-diOH sample: CH_2 stretching at 2900-3000 cm^{-1}, carbonyl group C=O stretching at 1720 cm^{-1} and a broad band for hydroxyl OH stretching at 3500 cm^{-1}. For oxidised PCL-diCOOH samples, differences were observed. The hydroxyl OH stretch band disappeared and instead, carboxylic OH stretch was detected at 3190 cm^{-1}. At 1720 cm^{-1}, the sharp C=O peak became to a dual peak and this is because the carboxylic group brought a second species of C=O bond. There were also various peaks observed in the range of 1200-1450 cm^{-1} corresponding to the CH_2 bend and 930-1160 cm^{-1} contributed by the C=O and C-O-C stretch.

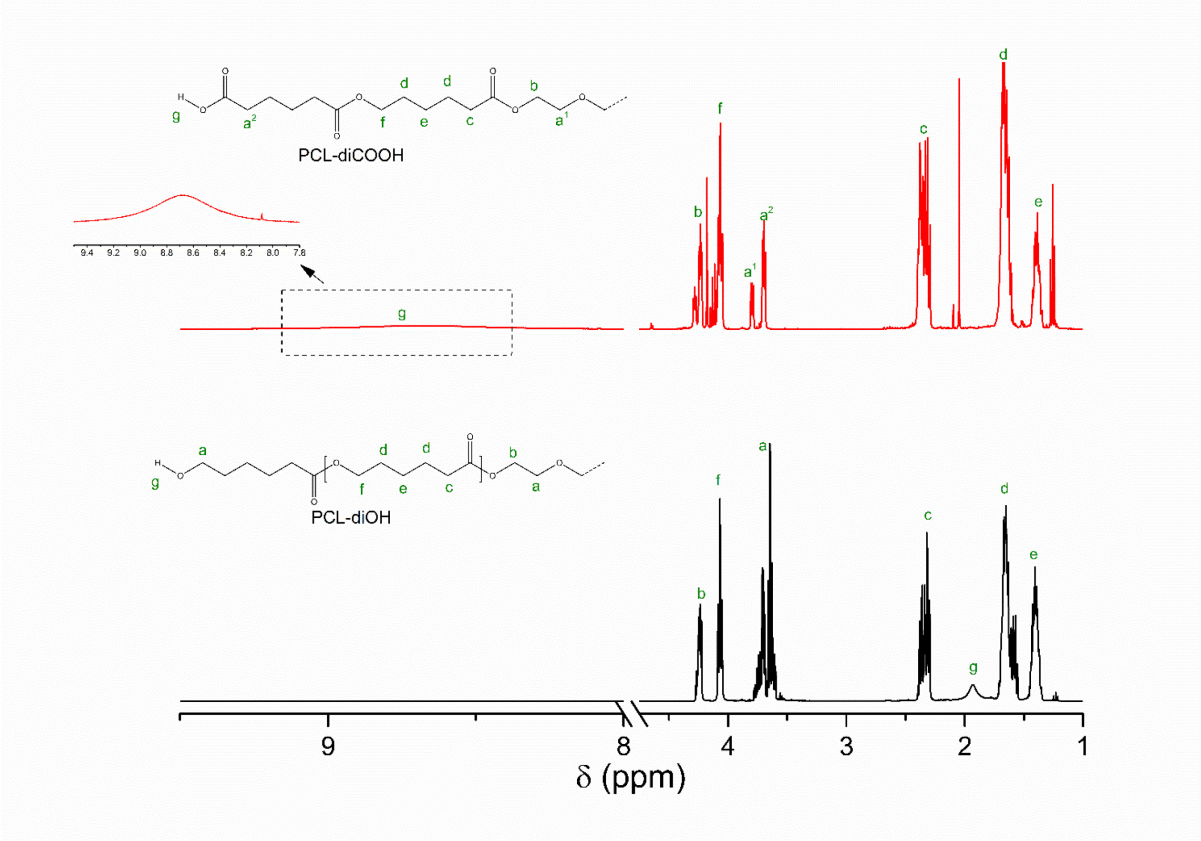


Figure 6.9 - Proton NMR spectra on PCL diol before and after the oxidiation.

^{1}H NMR analysis on PCL-diOH and PCL-diCOOH was also carried out. All peaks from PCL-diOH were labelled with the correspondent protons and matched with the literature findings [77] and the OH groups was detected with a clear signal at peak ‘g’ at 1.93 ppm. The same procedure was repeated on the PCL-diCOOH samples, the OH peak disappeared meaning there were no hydroxyl groups present. Instead, a new broad band was detected at 9.78 ppm which represents the proton involved in carboxylic groups. In addition, peak ‘a’ from PCL-diOH was split into two peaks in the oxidised samples, which was also the evidence of the existence of the carboxylic group that affected the adjacent protons.

6.4.2 Hybrid synthesis

The reaction mechanism of forming a polyTHF/PCL polymer network was described in the literature review chapter, the addition of MCEs was expected to have no effect on this network formation and this was justified by using the proton NMR.

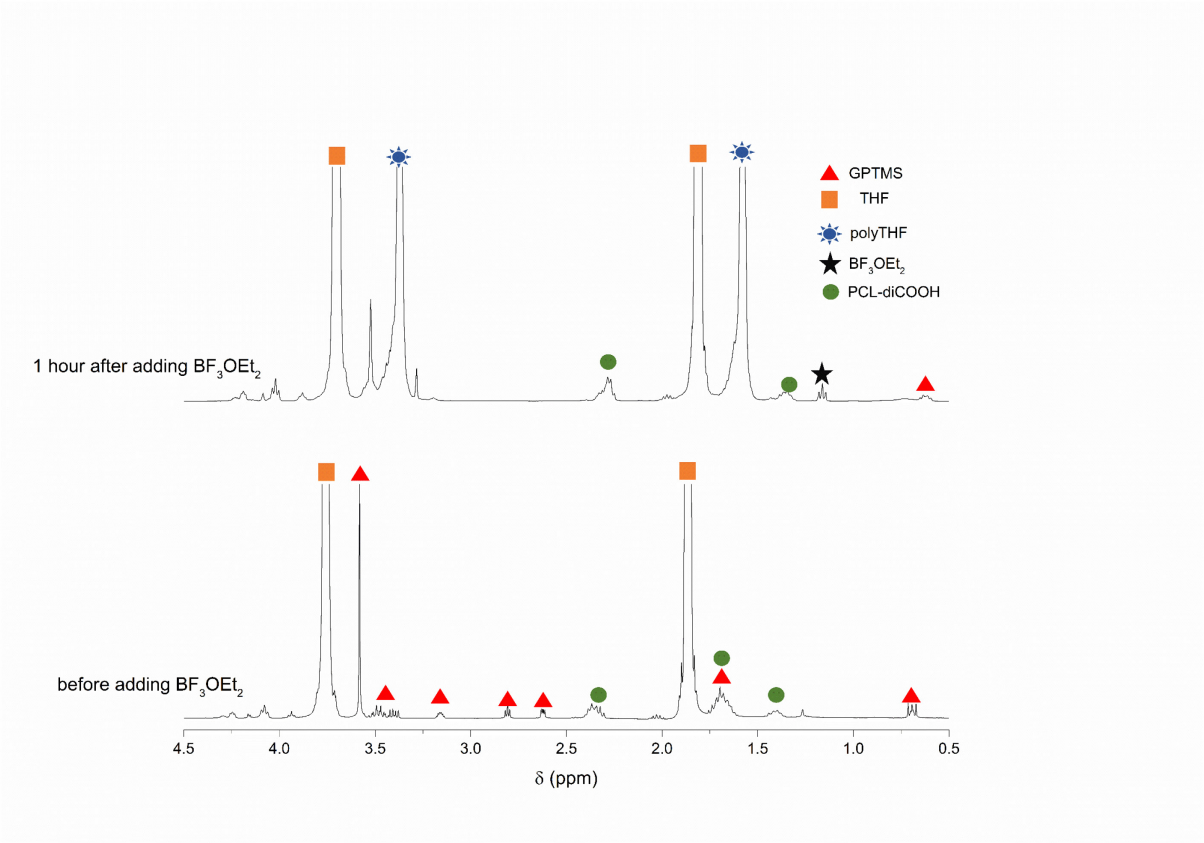


Figure 6.10 - Proton NMR spectra in $CDCl_3$ of solution containing MCE+PCL+THF+GPTMS (bottom) and solution containing MCE+PCL+THF+GPTMS+BF_3OEt_2 mixed for an hour (top).

According to literature [10], the polymerisation reaction would not happen unless the Lewis acid, BF_3OEt_2, is present. NMR spectra were obtained on the solution before and after the addition of BF_3OEt_2 (Figure 6.10). Signature peaks for the epoxide ring from GPTMS were observed at 2.60 ppm, 2.77 ppm and 3.13 ppm [83] on samples before adding the BF_3OEt_2. Then, 1 hafter the addition, these three peaks disappeared and instead, peaks for polyTHF at 1.58 ppm and 3.37 ppm were observed and this was confirmation of the ring opening polymerisation.

Although the NMR results show MCEs did not affect the polymerisation, it was found that with more MCEs introduced, the time taken for the hybrid sol to gel was longer. Samples shown in Table 6.1 were made with fixed PCL : TEOS (1:4) weight ratio and the hybrid sol volumes were the same. 1 h after the addition of BF_3OEt_2, hybrid samples without any nanoparticles were gelled after 40 minutes regardless of the room temperature while samples containing 250 mg of MCEs needed more than 70 minutes. To further investigate the

problem, an extra batch of samples with 500 mg MCEs was prepared and it took 3 days to gel. The reason for why and how MCEs slowed down the reaction was yet unknown at this stage.

Table 6.1 - Time recorded for hybrids samples to gel. The time was counted from 1 h after the addition of BF_3OEt_2

MCEs added to the sol (mg)	Time taken for sol became viscous	Time taken for sol fully set (gelled)
0 mg	~20 minutes	>40 minutes
50 mg	~20 minutes	>50 minutes
150 mg	~30 minutes	>60 minutes
250 mg	~45 minutes	>70 minutes
500 mg	N/A	>3 days

TGA analysis (Figure 6.11) was conducted on hybrid samples. According to literature [185], synthesis protocol used should give organic : inorganic composition ratio of 80 : 20 on hybrids without MCEs. The TGA results showed HMC_0mg had left 23.18% of its weight at 800°C, which was 3.18% higher than the theoretical value, but by considering there was also a small amount of weight loss before 180°C, which might be caused by the water and remaining solvent THF, samples were consistent with the literature.

By introducing the MCEs during the synthesis, TGA results showed the inorganic component weight percentage for samples with 150 mg and 250 mg MCEs increased by3.28% and 4.22%, due to the silica network of the particles. However, samples made with 50 mg MCEs showed a similar weight percentage inorganic as the original hybrid. This can be explained that the ring opening polymerisation in this synthesis was not a controlled polymerisation and it varied with room temperature, drying method and solvent evaporation rate, as a result, the final organic weight ratio in the product might had a minor variation.

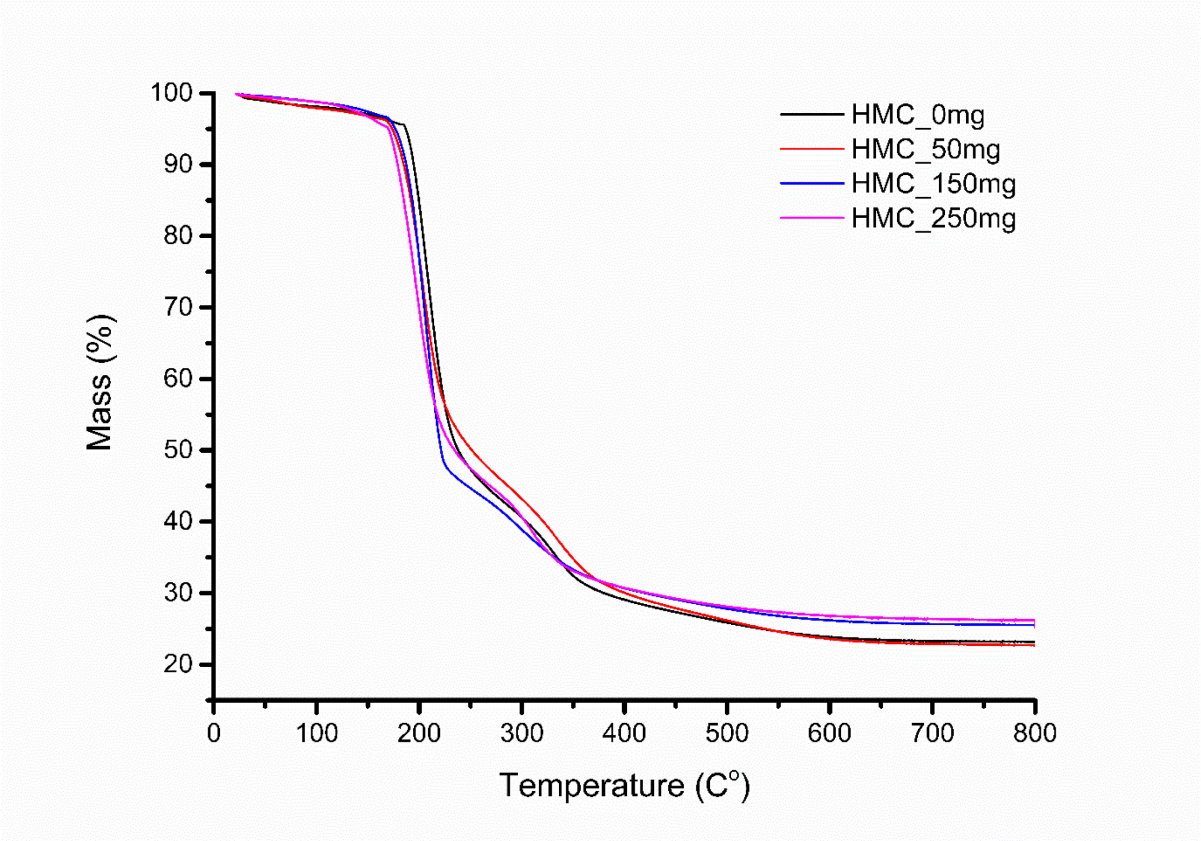


Figure 6.11- Thermal analysis on hybrid samples with different amounts of MCEs added during the synthesis. Sample HMC were cylindrical hybrid samples contained different amount of MCEs.

6.4.3 Hybrid bulk samples – macro observations

According to the synthesis method established by Tallia *et al.* [10], hybrid sols were poured into the moulds immediately after the solution became more viscous. However, samples with MCEs made in this project showed un-even distributions of MCEs by visual observation (Figure 6.12).

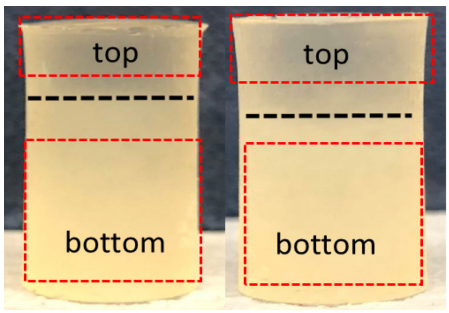


Figure 6.12 - Photographs of 2 hybrid bulk samples containing 250 mg of MCEs each.

When the hybrids were poured into moulds and placed in the oven, they were viscous but not gelled. Therefore, particles started to sink to the bottom slowly when there was no stirring. In order to avoid these un-even distributions of MCEs, moulds containing hybrid sols were placed on an orbital shaker at 120 rpm in a 37 °C oven for 24 h. After hybrid sols were fully set, they were then transferred to the 40 °C oven and the same age/dry procedure was carried out.



Figure 6.13 - Photo of hybrid cylindrical samples made with modified method.

As can be seen from the Figure 6.13, samples made with the new method using orbital shaker showed an evenly distributed MCEs in the hybrid. However, Samples made with 500 mg of MCEs, which took 3 days to gel, had a white bottom surface which means majority of MCEs were still sunk to the bottom even with the help from the orbital shaker. This phenomenon suggested that the sol-gel reaction did not occur until all particles were sunk. This was because the high number of MCEs took over a large surface area so the reaction between other components were physically interrupted. As a conclusion, with a total sol-gel reaction volume of 15.50 mL, the maximum amounts of MCEs can be added was 250 mg.

6.4.4 Hybrid bulk samples – micro observations

SEM was used to image the sample synthesised with 250 mg MCEs on its top and bottom section to compare the nanoparticle distribution in a micro view (Figure 6.14). For MCEs in

the top section, they were more mono dispersed compared with the bottom section, where an area of agglomeration was observed. Although by visual observation, MCEs were distributed better by using the orbital shaker during the aging period, SEM images suggest that there were still more particles sitting at the bottom of cylindrical bulk samples.

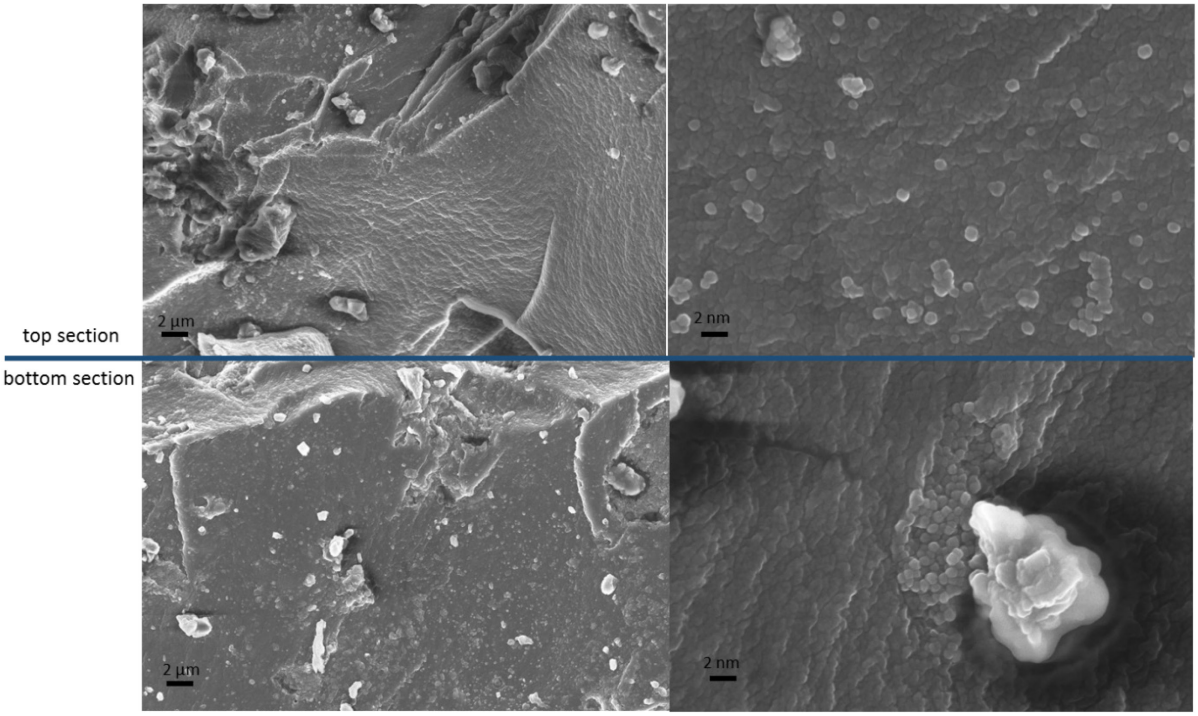


Figure 6.14 - SEM images of cylindrical bulk samples. From the top and bottom regions of the cylinders.

Silica network's connectivity was then assessed by using ^{29}Si MAS NMR on hybrid samples made with 0 mg (original hybrid from the literature), 100 mg and 250 mg of MCEs (Figure 6.15). In addition, the percentage abundance of T^n and Q^n species was calculated according to the spectra and listed in the Table 6.2.

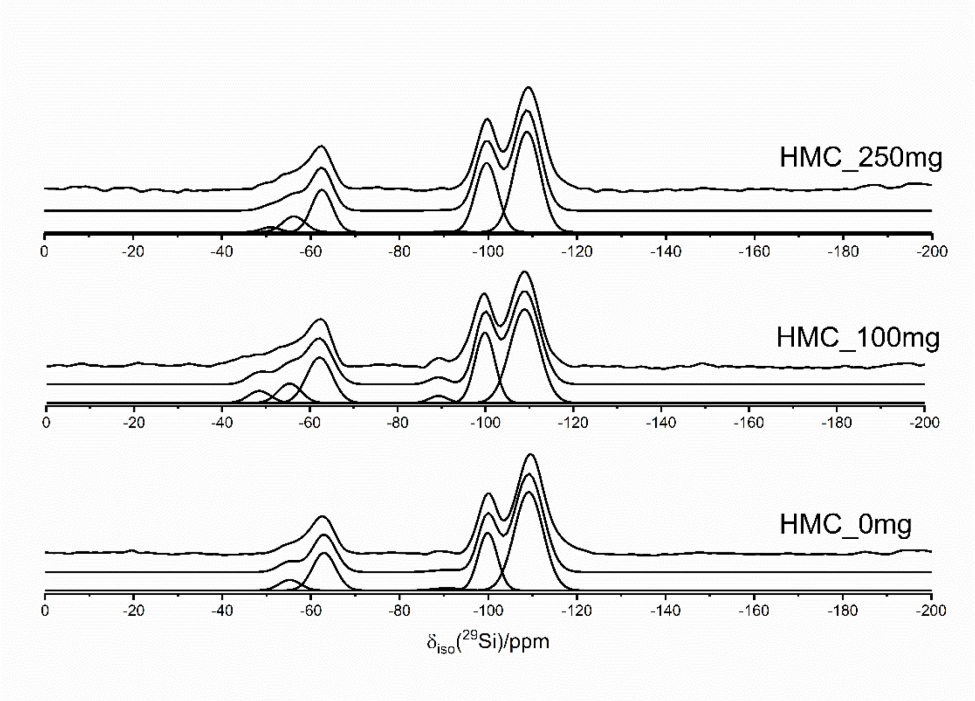


Figure 6.15 - ^{29}Si MAS NMR spectra on samples with different amounts of MCEs added during the synthesis.

Table 6.2 - Chemical shifts and relative percentage abundance of silicon T and Q species obtained from ^{29}Si solid state NMR with resulted degree of condensation.

Samples	Q^2		Q^3		Q^4		
	δ_{iso} [ppm]	*I* [%]	δ_{iso} [ppm]	*I* [%]	δ_{iso} [ppm]	*I* [%]	
HMC_0mg	-90.7	1.2	-99.9	21.6	-109.2	55.6	
HMC_100mg	-89.3	2.1	-99.9	22.7	-108.9	44.6	
HMC_250mg	-91.5	0.2	-99.6	27.7	-108.7	47.7	
Samples	T^1		T^2		T^3		Dc
	δ_{iso} [ppm]	*I* [%]	δ_{iso} [ppm]	*I* [%]	δ_{iso} [ppm]	*I* [%]	[%]
HMC_0mg			-55.3	7.3	-62.2	18.9	90.22
HMC_100mg	-49.2	8.7	-55.7	6.5	-62.2	16.5	80.48
HMC_250mg	-50.9	1.7	-56.2	6.5	-62.5	16.2	84.40

By looking at the chemical shifts for all Q and T species, variations were relatively unchanged for samples with different amounts of MCEs and this means the introduction of nanoparticles did not affect the condensation mechanism but only the rate of the original hybrid system.

The percentage abundance of Q^4 (55.6%) species decreased when nanoparticles were added (44.6% and 47.6%) and this was expected, as already discussed in the Chapter 5, MCEs contained calcium ions which acted as network modifier and decreased the amount of Q^4 structures in the nanoparticles and as a consequence they lower the overall Q^4 percentage abundance in the hybrid sample.

Considering the T species, the peak for T^1 was absent in HMC_0mg samples and in contrast, samples with nanoparticles both showed the presence of T^1 (8.7% and 1.7%) structures. By recalling the solid-state NMR results for MCEs in Chapter 5, the T^1 peaks in nano-hybrids were contributed by the GPTMS on particle surface. Methoxysilanes from GPTMS did not all condense into Si-O-Si bonds during the MCEs synthesis, however, in the hybrid synthesis with the presence of water and hydrochloride acid they remained un-condensed. The possible explanation for this could be those GPTMS with Q^1 structures were the ones grafted on the inner surface of the meso-pores which were then blocked, therefore, the further reaction could not occur on those GPTMS molecules. The network connectivity calculated for samples with nanoparticles (80.48% and 84.40%) were lower than the original hybrid samples without MCEs (90.22%) due to the presence of T^1 and low Q^4 structures.

6.4.5 Mechanical testing on bulk samples

After understanding the chemical composition and the network construction, it is important to investigate how MCEs affected the mechanical properties of the hybrids, which may have a great impact on the product application.

Compression tests were first conducted on hybrid samples with 0 mg, 50 mg, 100 mg, 150 mg and 250 mg MCEs added during the synthesis (Figure 6.16).

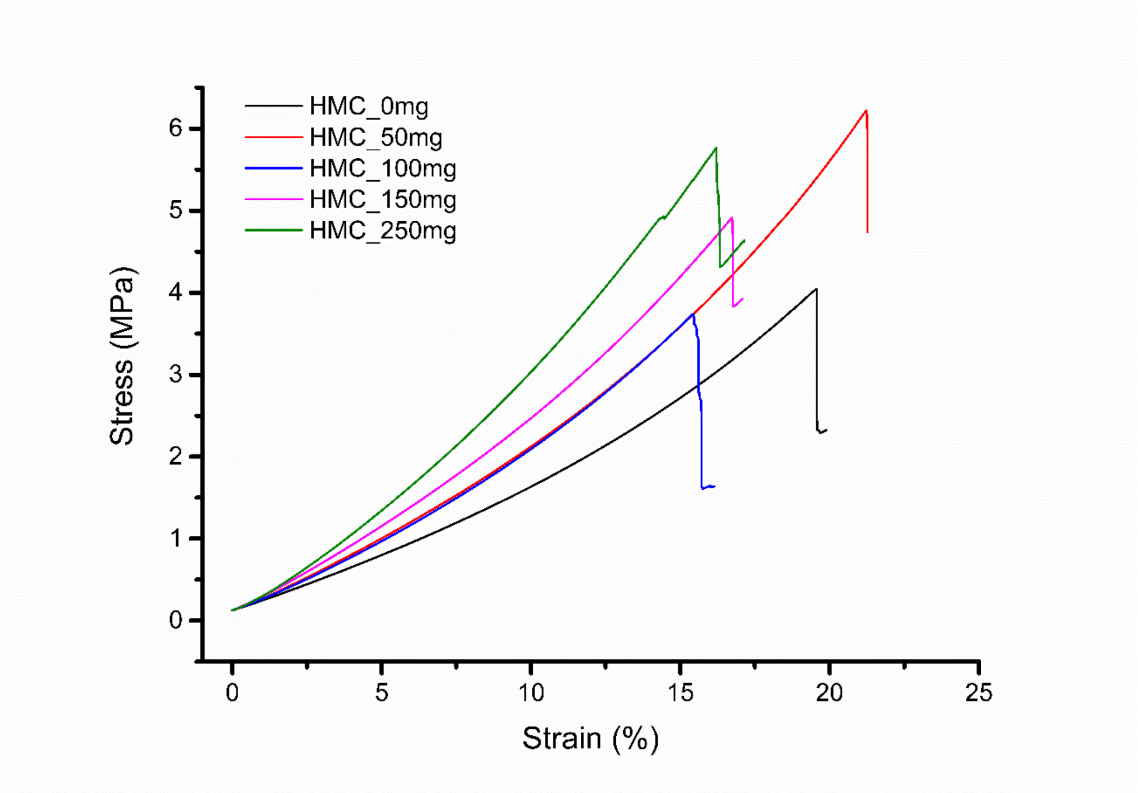
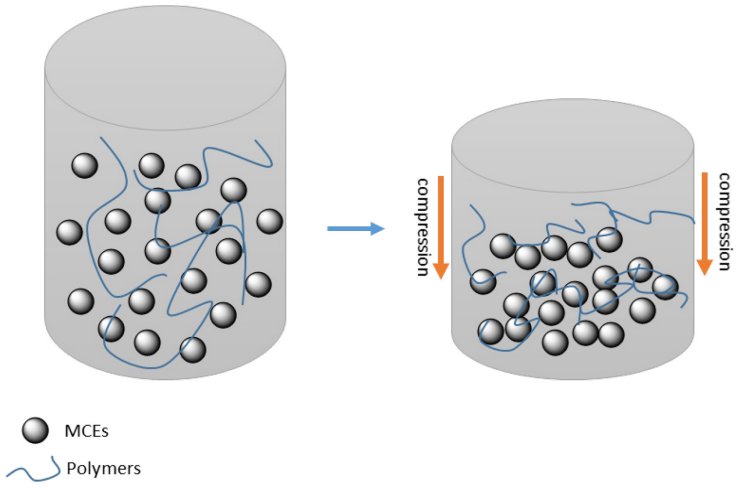


Figure 6.16 - Compression curves for samples containing MCEs from 0 mg to 250 mg. The final inorganic : organic weight ratio for all samples was around 23% : 77% and the variation was below 4%.

By comparing the compression stress at failure σ_c across samples with different amounts of MCEs, a clear trend was observed: as more nanoparticles were introduced into hybrids, σ_c increased from 4.04±1.32 MPa (0 mg MCEs) to 5.77±2.41 MPa (250 mg MCEs). However, while the material became stiffer with MCEs, the strain at failure showed a decreasing trend from 19.57±2.11% (0 mg MCEs) down to 16.18±3.31% (250 mg MCEs).



Scheme 6.2 - Scheme for showing the cylindrical bulk hybrid samples when they were under compression.

What possibly could have happened in these bulk samples was when they were under compression, MCEs were packed closer to each other and reduced the space volume that the organic components could take. As a result, while MCEs provided more resistance to the compressive force, they also limited the elasticity of the organic network (Scheme 6.2).

Cyclic loading tests in compression were then carried out (Figure 6.17) as it was also very important to know how samples behave under the continuous loading in the potential bone or cartilage applications. Unsurprisingly, the results showed a similar trend as the compression tests. Materials became stiffer when more particles were added in and the addition of MCEs did not affect the recovery capability of samples. In similar hybrid samples made with calcium methoxyethoxide (CME) as a calcium source rather than the use of MCEs [66], a significant stress loss was reported after the first cycle. The literature suggested what happened was called Mullins Effect – a mechanical softening phenomenon and give rise to hysteresis, an indication of a viscoelastic behaviour. [186]. Studied by Cantournet *et al.*, when elastomers were under stress, macromolecular chains slide over each other and cause the temporary elimination of hard domains through removal of entanglements during sliding [187]. In the cases of having MCEs in the network, this phenomenon was only significant for sample HMC_250mg as the presence of large amounts of nanoparticles disorganised the original polymer network and made it difficult to recover.

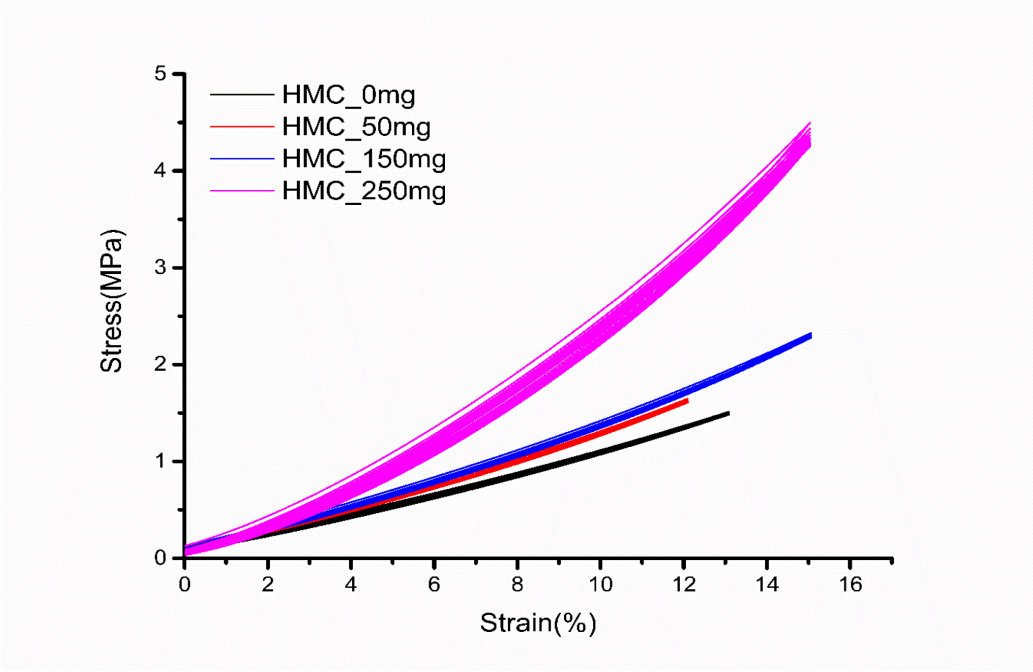


Figure 6.17 - Cyclic loading tests for hybrid samples with 0 mg, 50 mg, 150 mg and 250 mg of MCEs added during the synthesis. A total of 10 cycles were conducted.

Finally, disc samples were used to investigate how MCEs affect the mechanical behavior in tension. Before the test samples were cut into strips (Figure 6.18), compared with cylindrical bulk samples, strip samples with the exactly same composition were more flexible. The thickness of strip samples varied from 1.29 mm to 2.81 mm regardless of how much MCEs were included and this was caused by the process of aging and drying as disc moulds were wrapped with 4 layers of aluminum foil and it was hard to maintain every sample was wrapped and sealed perfectly. Consequently, only samples with thickness over 2 mm were chosen for the tests.

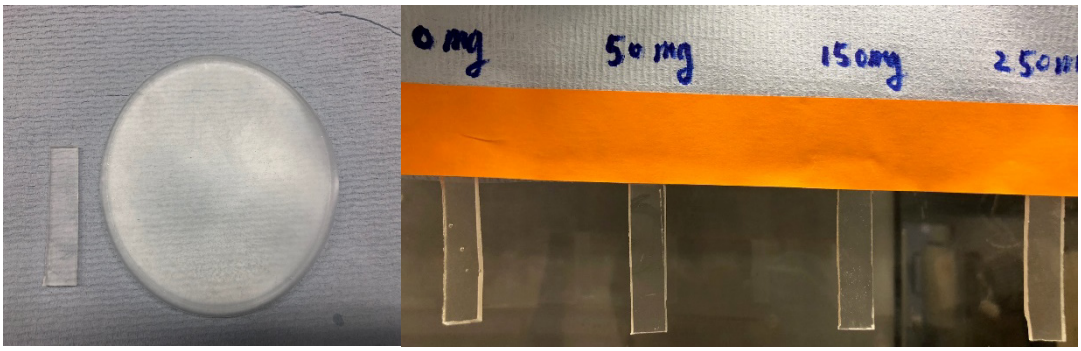


Figure 6.18 - Samples prepared for the tension test. 10 mm x 45 mm strips were cut from hybrid discs with 0 mg, 50 mg, 150 mg and 250 mg of MCEs added during the synthesis.

During the tension test, it was found that over half of samples were broken either close to the top edge or the bottom edge (Figure 6.19 a and b). Results from those samples were considered as not valid and only samples that broke at the middle position were used, which limited the overall average value calculations (n = 1 – 3). The reason for this was mainly the grips used in the tensile tests were not idea and strips were manually cut which means the width were not always 10 mm along the sample.

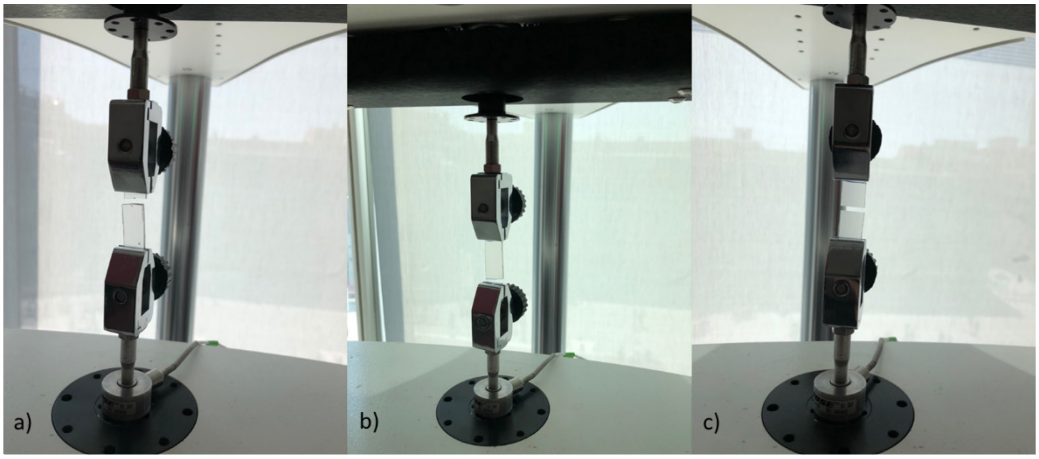


Figure 6.19 - Photographs showing samples fracturing during the tensile test at different positions : a) top, b) bottom and c) middle.

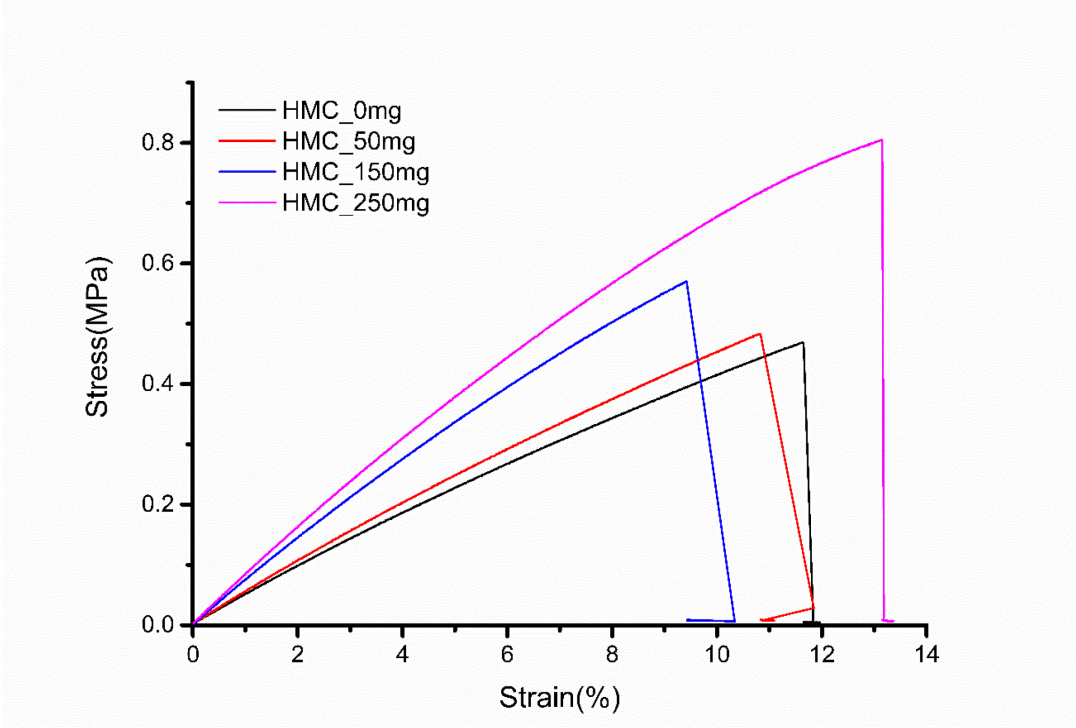
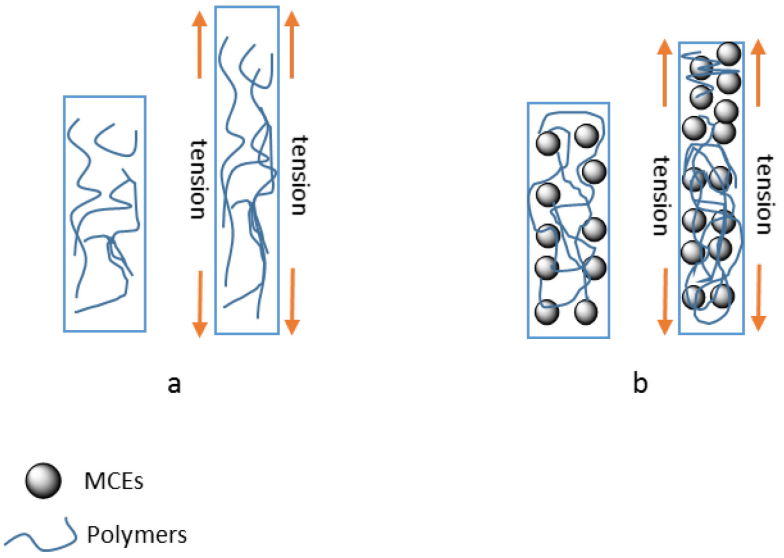


Figure 6.20 - Tensile curves for samples made with 0 mg, 50 mg, 150 mg and 250 mg of MCEs.

The tensile curves (Figure 6.20) clearly showed the tensile strength increased when samples had more nanoparticle content, while the tensile strain decreased and this result confirmed the compression results. The similar explanation can be used here that, when samples with MCEs experienced tension, MCEs were pulled closer physically with polymer chains were bonded with MCEs, as a result, the space volume for surrounding networks were limited and therefore mobility was reduced compared with samples without MCEs (Scheme 6.3).



Scheme 6.3 – Scheme showing how samples (a) with and (b) without MCEs behaved under tension.

In addition, Figure 6.20 showed an outstanding tensile strain for the HMC_250mg sample compared with all other samples. This was caused by the continuous slow loosening in the grips. Samples made with 250 mg of MCEs were more difficult to grip than other samples, which means the surface friction might also have been changed due the presence of large amounts of nanoparticles.

6.4.6 Dissolution study

A dissolution study was first conducted in tris(hydroxymethyl)aminomethane (Tris) solution. Samples used in this study had same inorganic : organic composition ratio and the same amount of MCEs (250 mg) were added in. The only difference was the amount of GPTMS added to the nanoparticles during the MCE synthesis (0 mmol/g, 1 mmol/g and 2 mmol/g). The goal of this study was to investigate if GPTMS molecules on the particle surface can affect the particle release in the hybrid system.

Considering the calcium ion release profiles (Figure 6.21 a and b), the only significant difference noticed was at the first 8 h of the study. Hybrid samples containing MCEs with no GPTMS molecules on the surface, i.e. MCEs were not covalently bonded to hybrid network, had a burst release of calcium ions in the first 30 minutes. In contrast, samples with MCEs covalently bonded to the hybrids did not release any calcium for the first 4 h and then a large amount of calcium was released in the next 4 h. At this point, results suggested that GPTMS

molecules on the particle surface did slow down the calcium release in hybrid system. However, samples prepared in this study were chunks bulk sample not powders, a plateau was reached for all the samples after 8 h until the end of the study (4 weeks). This was unexpected as theoretically chunk samples should degrade with time and MCEs in the inner part should then leave the hybrid and start releasing calcium. A continuous release of calcium was expected. Here, no more calcium was released. What could have happened was either the calcium released in the first 8 h was from the surface of the chunk samples and the PCL/PTHF/SiO_2 hybrid degraded very slowly in Tris, or the Tris was contaminated during the study, which was very unlikely.

Looking at the silicon release profiles (Figure 6.21 c), a consistent trend for all samples was found with silicon continually releasing until the end of study, although the final concentration readings on all samples were low (7.5 ppm – 15 ppm). This did suggest that hybrid degrades extremely slowly in Tris solution and confirmed that calcium release was mainly from the surface of samples. Moreover, the amount of silicon released at each time point increased when more GPTMS were grafted on the MCEs while the curve slope, releasing rate, did not change much.

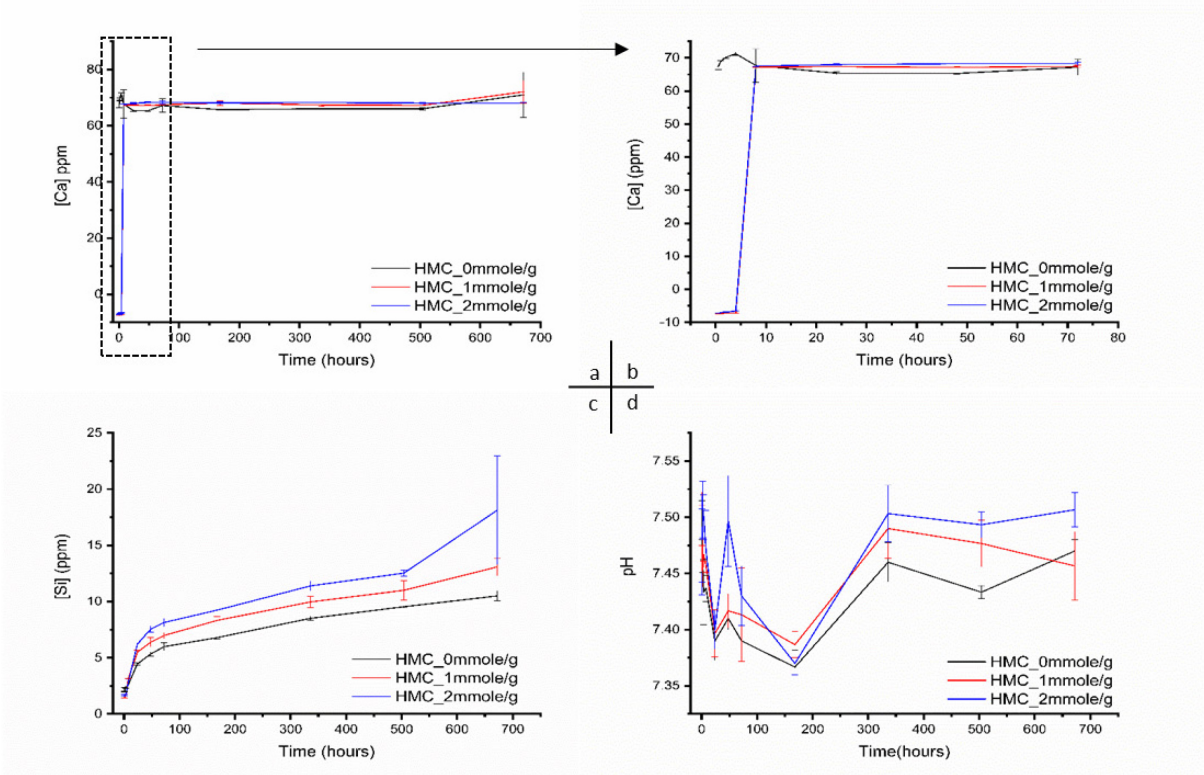


Figure 6.21 - Elemental concentration obtained from ICP-OES analysis following immersion of hybrids in Tris buffer a) calcium, b) calcium in the first 3 days, c) silicon d) the pH change.

During the Tris dissolution study, at time points of 3 days, 1 week and 4 weeks, the Tris solution containing dissolution products were removed, ultrasonicated and prepared on the TEM grids. TEM imaging under low magnification was then used to observe if there were any released MCEs from samples. Results (Figure 6.22) showed that for all samples, it was difficult to image after 4 weeks as the dissolution products polluted the TEM grid. Therefore, only images taken at 3 days and 1 week were compared.

At day 3, a large area containing mono-dispersed MCEs was discovered in HMC_0mmole/g samples, while for the other two samples containing MCEs with GPTMS grafted on and covalently bonded with the hybrid network, only some small clusters of MCEs were observed. This phenomenon was expected and suggested that with the presence of GPTMS on the particle surface, covalent bonds held the connection between particles and hybrid network until the connected polymer chains were degraded. On the other hand, MCEs in HMC_0mmole/g samples were physically trapped in the polymer chains so they left hybrid samples quicker. This confirmed the calcium release profiles which HMC_0mmole/g samples had a burst release during the first 30 minutes because particles on the sample surface were only physically attached and they were easily washed away by the Tris solution.

At week 1, all samples showed nanoparticle clusters in different areas on TEM grids. It was difficult to quantify which had more MCEs released but it could also suggest that all samples might have similar amounts of MCEs released as the calcium release profile showed a plateau at this time point.

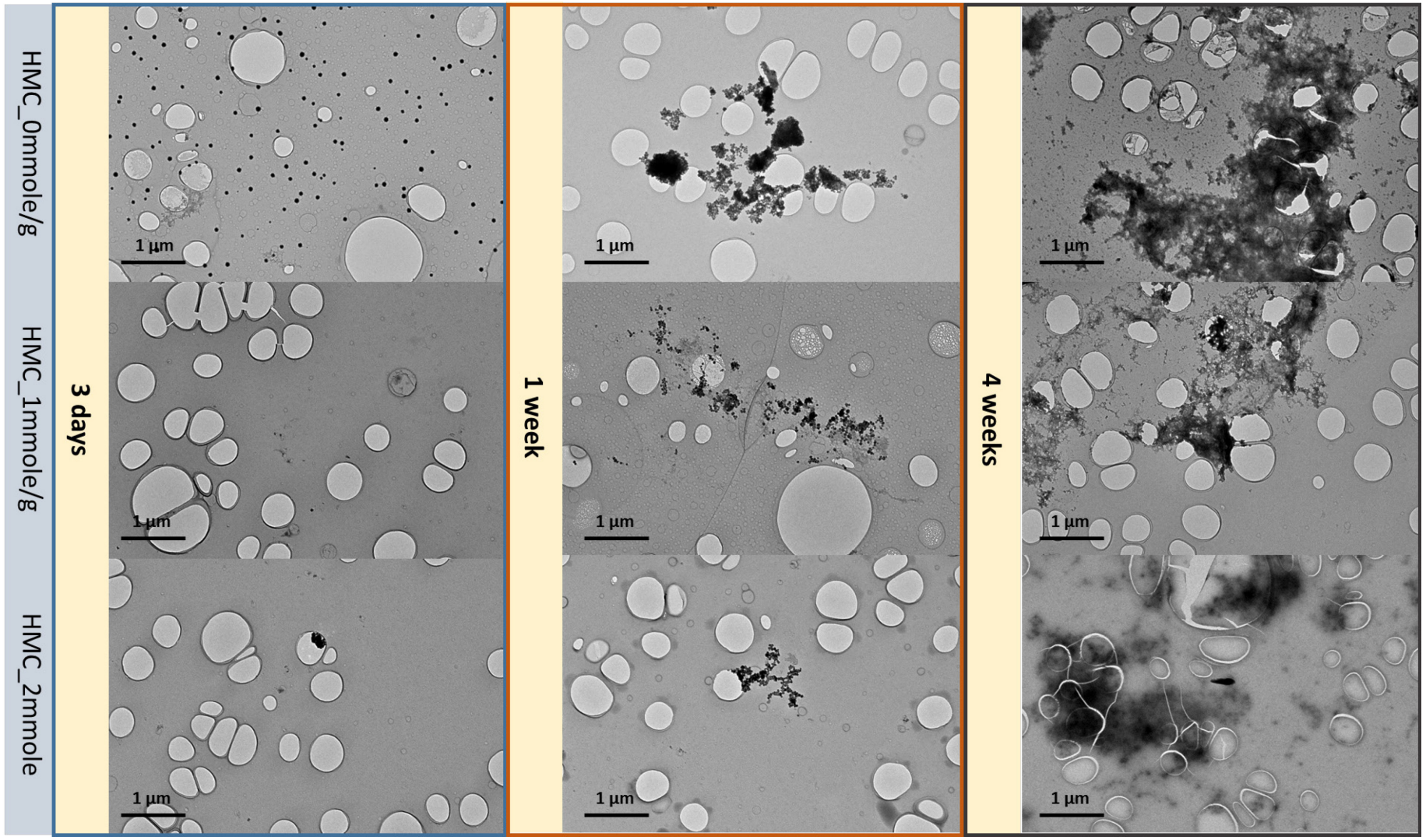


Figure 6.22 - TEM images of dissolution products in Tris solution for hybrid samples across 4 weeks. All hybrid samples had the same organic : inorganic weight ratio and the same amounts of MCEs while the GPTMS added during the MCE synthesis were different:0 mmol/g, 1 mmol/g and 2 mmol/g.

A dissolution study was also conducted in SBF to evaluate the bioactivity of the hybrid samples by assessing the formation of hydroxycarbonate apatite (HCA). Samples were made with same organic and inorganic composition weight ratio but different amounts of MCEs which were 0 mg, 50 mg, 150 mg and 250 mg. They were ground into powders and soaked in SBF for 4 weeks. Different amounts of MCEs mean different amounts of calcium would be released and therefore a different bioactivity was expected.

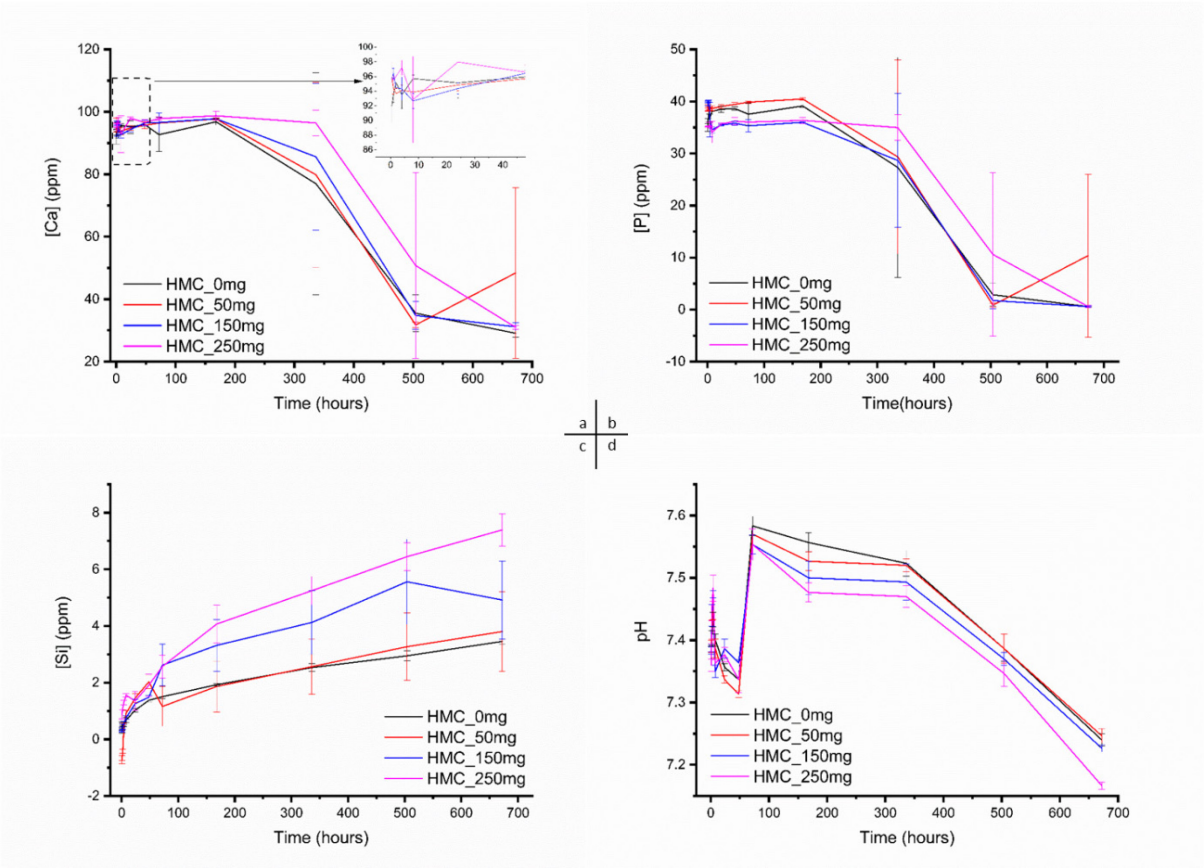


Figure 6.23 - Elemental concentration obtained from ICP-OES analysis following immersion of hybrids containing different amounts of MCEs in Tris buffer a) calcium, b) phosphorous, c) silicon d) the pH change.

Dissolution products were first analyzed by using ICP-OES to determine the ion release while the pH changes were also recorded (Figure 6.23). Looking at the silicon release profiles, samples with higher MCEs content showed a higher silicon concentration at all time points, and as expected this was given by the silica network from nanoparticles.

Considering the phosphorus and calcium concentration levels, samples with 0 mg, 50 mg and 150 mg of MCEs showed a gradually decreasing phosphorus concentration after 168 h (1 week)

and it finally dropped to 0 ppm by the end of the study. In a slightly different behavior, HMC_250mg samples showed the phosphorus concentration started to drop only after 1 week. The dropping of phosphorus concentration indicated the deposition of phosphate. By looking at the calcium concentration profile, the trends for all samples after 72 h looked very similar to the phosphorus concentration curves. HMC_250mg samples showed a delayed calcium drop after 1 week. The decreased in calcium and phosphorous was the evidence of the formation of calcium phosphate in SBF. Focusing on the first 48 h of the calcium profile, only about 2 ppm to 4 ppm of calcium was released from samples containing MCEs which was extremely low compared with the Tris dissolution profile.

Finally, the pH of SBF for all samples showed an increase after 48 h and started to drop after 72 h. The increasing of pH was caused by the calcium release and Ca^{2+} from MCEs in hybrids exchanged with H^{+} from the SBF which then increased the pH. The pH dropping towards the end of the study was possibly caused by the remaining BF_3OEt_2 from the organic sol synthesis. BF_3OEt_2 is a source of boron trifluoride (BF_3) which can be further hydrolyzed with water into fluoroboric acid, which has a high acidity [82]. The other possible explanations for the pH drop is there were some unreacted PCL-diCOOH polymers trapped in the hybrid network and when they were released during the dissolution study, carboxylic groups lower the pH of SBF. Either way, the low pH was not favorable for HCA formation because nucleation of HCA is preferential under alkaline pH [188].

FTIR was then used to capture the evidence of HCA formation on the dissolution samples at 3 days, 1 week and 4 weeks (Figure 6.24).

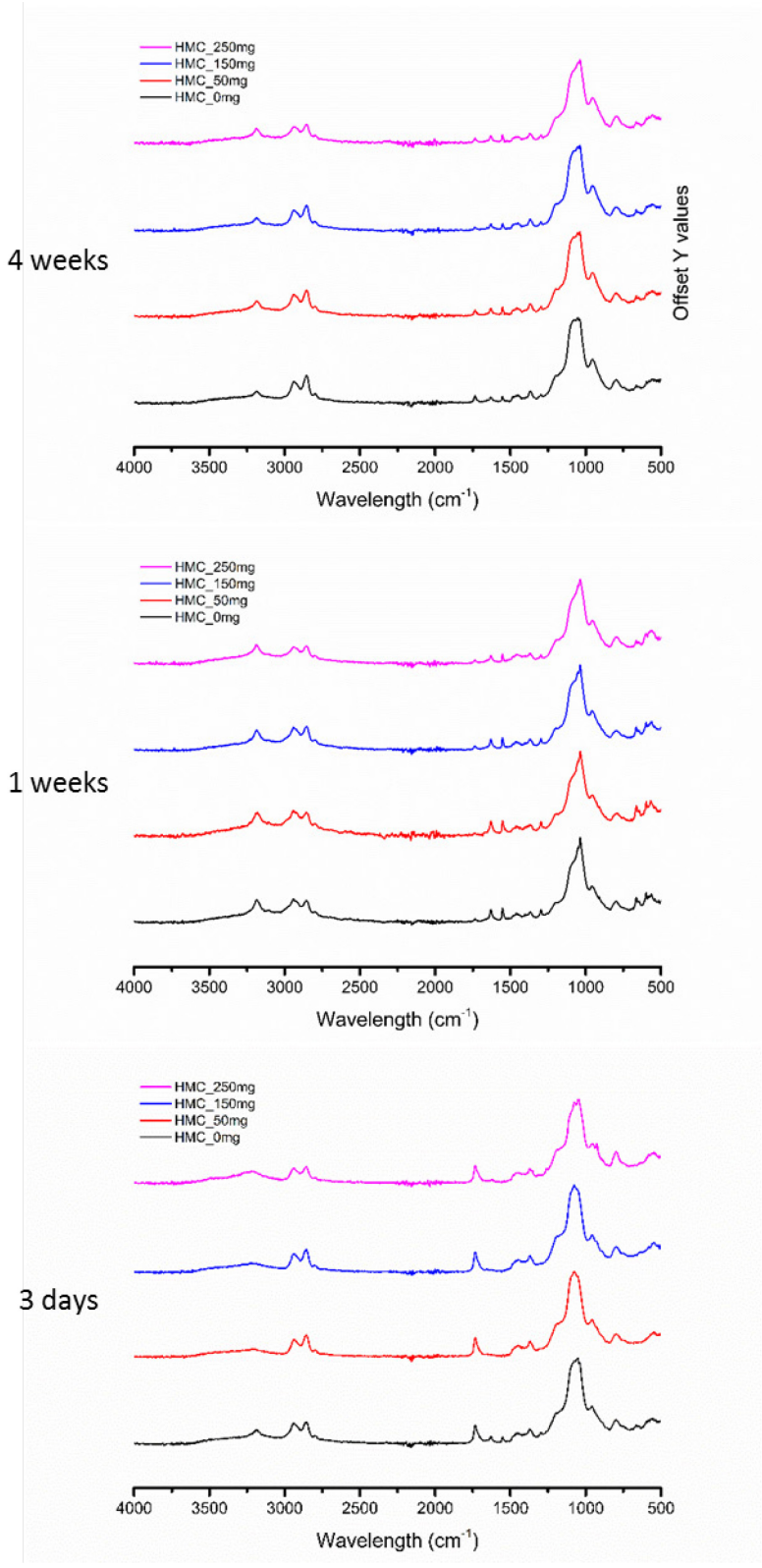


Figure 6.24 - FTIR spectra for hybrids containing different amounts of MCEs following immersion in SBF for 3 days, 1 week and 4 weeks.

For all the samples, signature bands for the silica network were found at 800 cm^{-1} attributed to Si-O-Si bending; 950 cm^{-1} attributed to Si-OH bending; 1150 cm^{-1} attributed to Si-OH stretching and 1200 cm^{-1} attributed to the Si-O-Si stretching. A small dual band around 1200 cm^{-1} was observed for sample HMC_250mg at day 3 which was caused by these samples containing more MCEs compared with others and the Si-O-Si contributed by the nanoparticles silica network was also detected.

Bands for phosphate were detected in all samples after 1 week of immersion: P-O bending at 546 cm^{-1} and 585 cm^{-1} and P-O stretching at 1010 cm^{-1}. However, it was unclear whether the formed calcium phosphate was apatite unless the presence of C-O stretching at 862 cm^{-1} and CO_3^{2-} band at 1400 cm^{-1} from HCA were confirmed [108]. Those two bands were only found in week 4 spectra for all samples but the IR absorbance values were extremely low. This suggested that in this dissolution study, only a small amount of HCA was formed.

XRD analysis on the dissolution samples was also carried out to determine the formation of apatite (Figure 6.25). Comparing samples before the dissolution study, peaks at 2θ 11.90°, 13.25°, 28.22° and 47.03° were found on hybrid samples containing MCEs and those peaks were identified as nitrocalcite [15]. During the calcium incorporation of MCEs calcium nitrate was chosen as the calcium source, when particles mixed with calcium nitrate and not fully dried before the calcination nitrocalcite might be result. By looking at the spectra for week 1, peaks for nitrocalcite were almostgone as samples were washed by the SBF. However, no peaks for HCA were observed and for HMC_50mg samples a peak at 31.37° was detected and this was the halite (mineral form of NaCl) coming from the SBF [189]. Multiple peaks were shown for all samples in week 4 which were contributed by halite and HCA respectively. Halite peaks were found on medium peaks at 27.40°, large peaks at 31.73°, small peaks at 45.47° and large peaks at 56.49° from all sample [189]. For HCA, peaks were found at 10.85°, 16.86°, 21.79° to 22.88°, 25.90°, small peaks at 31.80°, 32.22° and 32.93° and a small peak at 42.02° [15][190]. HMC_0mg samples had similar XRD patterns as samples containing MCEs at week 4 and peaks for apatite were also observed at lower relative intensity. This was because calcium phosphate can precipitate from SBF anyway at 4 weeks.

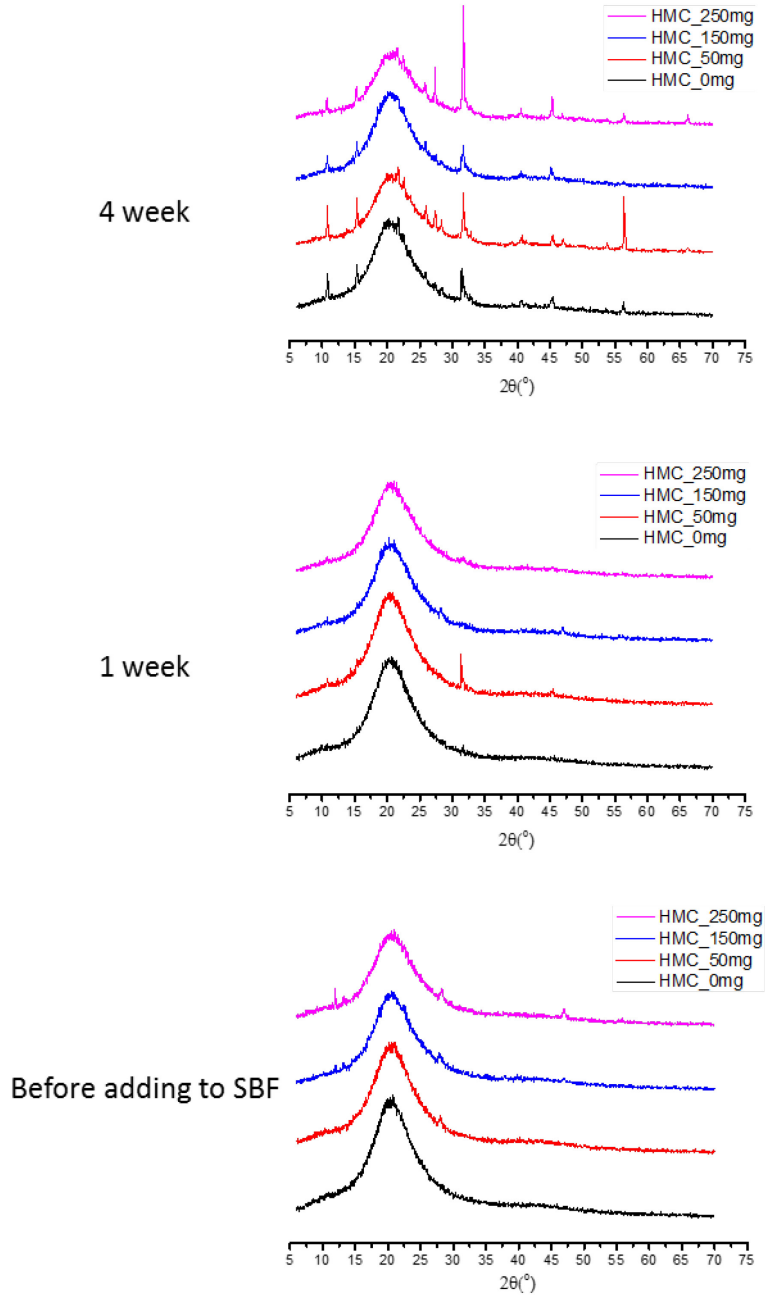


Figure 6.25 - XRD patterns of hybrid samples containing different amount of MCEs at different time points of the dissolution study in SBF.

SEM images (Figure 2.26) showed only halite crystals were found on the hybrids after 1 week and the crystals all had a needle-like morphology. At week 4, crystals resembling the morphology of HCA crystals in the literature [66] were found in some areas of all samples. It was difficult to compare the quantity of HCA formation between samples.

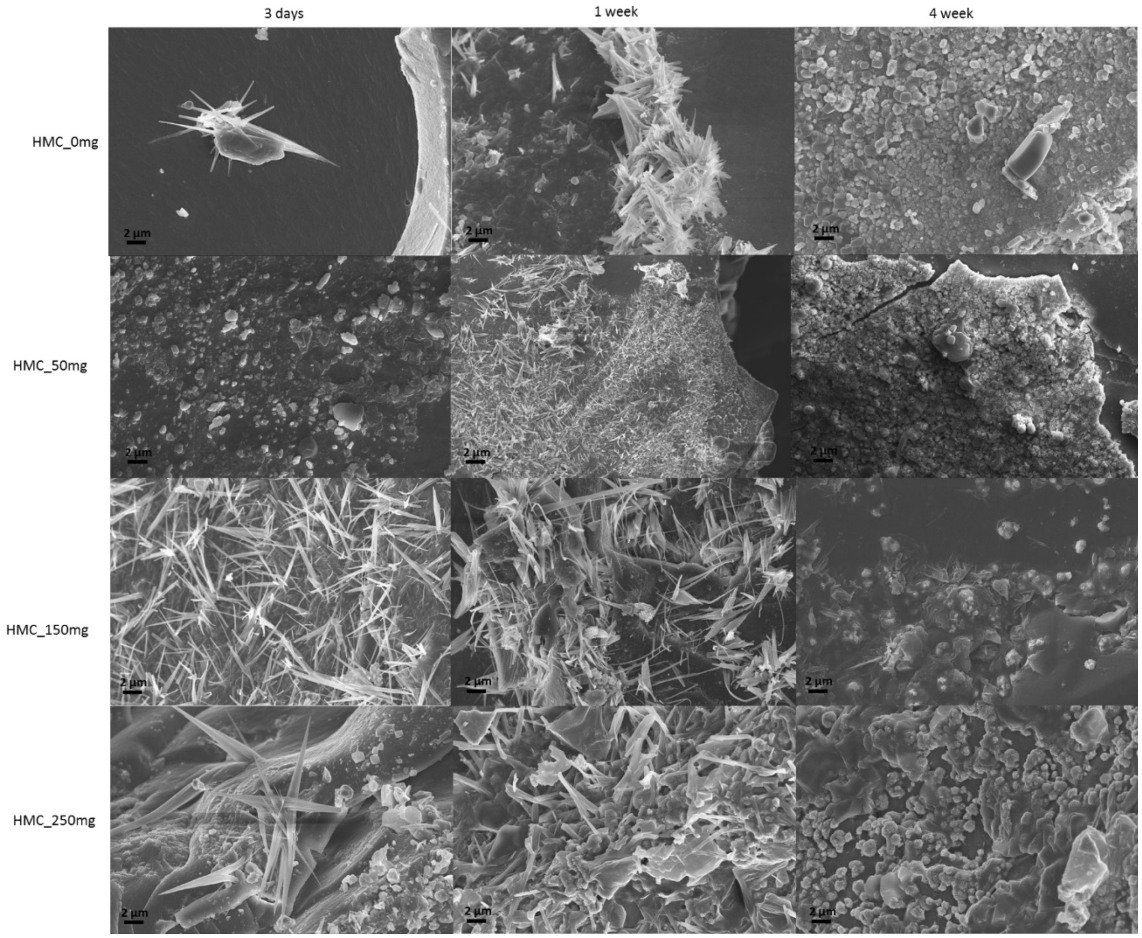


Figure 6.26 - SEM images of hybrid samples following immersion in SBF at different time points.

By the end of SBF dissolution study, results from FTIR, XRD and SEM all suggested that there was a small amount of HCA formed after 4 weeks, however, this HCA formation might be induced by the SBF itself but not by the calcium released from MCEs and it can be said that the amount of calcium in the hybrid was not enough to be considered bioactive. On the other hand, high calcium content in the hybrid can be achieved by adding more MCEs, but the failed sample HMC_500mg showed in *Section 6.3.3* suggested there was a limitation for the maximum MCEs could be put in the hybrid system.

6.4.7 Cytotoxicity test

Both ATDC5 chondrogenic and MC3T3-E1 preosteoblast cell lines were used in the cytotoxicity tests as the hybrids containing MCEs have potential application in both bone (nanoparticles incorporated with calcium) and cartilage (if nanoparticles incorporated with lithium). Samples made with fixed organic : inorganic weight ratio but different amounts of MCEs (0 mg, 50 mg, 150 mg and 250 mg) were tested. The cell viability should be great than 70% of that of the positive control to pass the ISO standard.

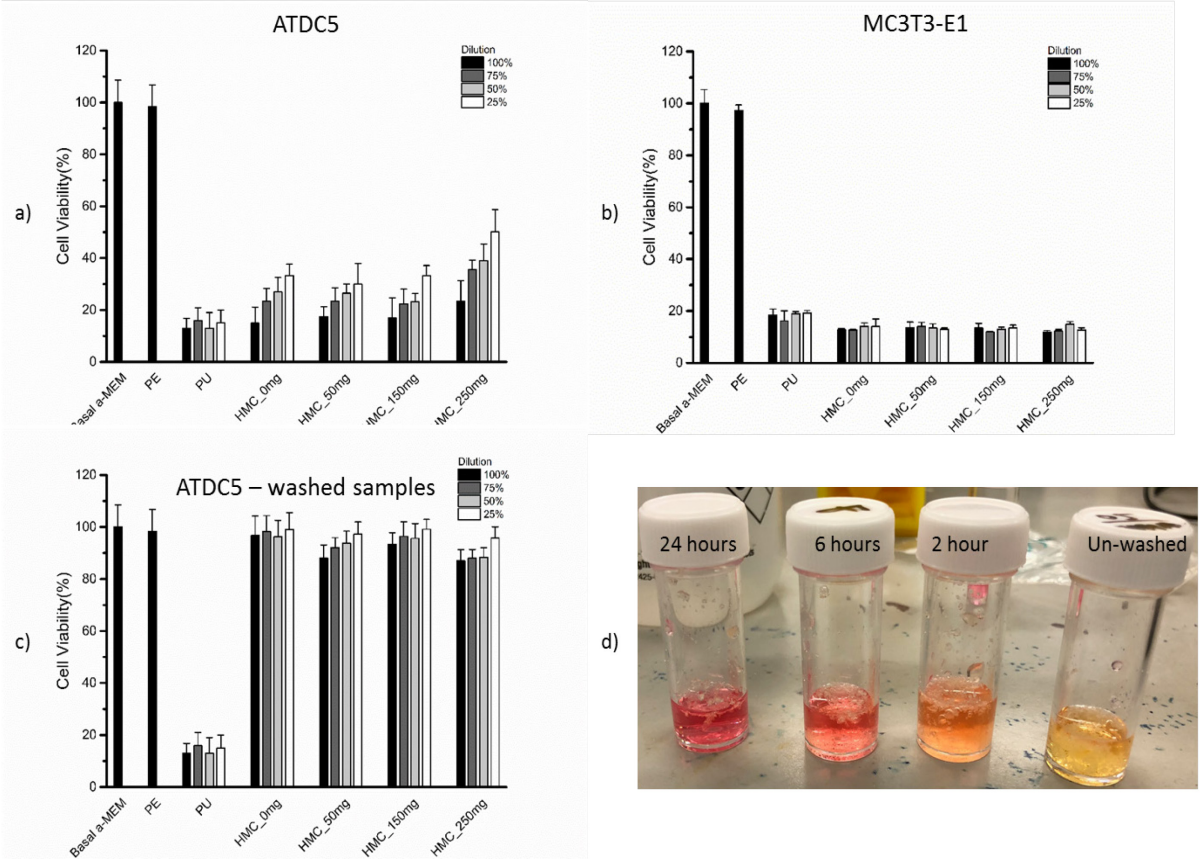


Figure 6.27 - Cell viability of the dissolution products of hybrids with different amount of MCEs with a) ATDC5 and b) MC3T3-E1 cell lines. Samples were also soaked in water for 24 h and then used for the ATDC5 tests and shown in c). Samples soaked in water for 2 h, 6 h, 24 h and un-soaked samples were put in MEM containing phenol red indicator and the colour change is shown in d).

Surprisingly, in both cell lines all samples showed extremely low cell viabilities for all dilutions (Figure 6.27 a and b). From the literature, silica, PCL and PTHF are all known to be biocompatible [67][191][41]. Possible cytotoxic products that were released could be un-reacted GPTMS if the epoxide rings were not opened and remained BF_3OEt_2.

During the cell culture study, when powdered samples were put into the α-MEM the phenol red turned light yellow in 5 minutes with shaking. Therefore, it was believed the low cell viability was caused by the drop in pH. Samples were then soaked in water for 2 h, 6 h and 24 h and then dried and put in to α-MEM (Figure 6.27 d). It was clearly seen that after samples had been soaked in water for 24 h, it stopped changing the colour of α-MEM which means the pH in α-MEM was maintained. Although the colour of α-MEM with samples soaked in water for 6 h was pink/red, it became to orange/yellow after 1 h with shaking and this did not happen when the samples were presoaked for 24 h in water. As a result, an extra ATDC5 cytotoxicity test was carried out with samples pre-treated by soaking them in water for 24 h and then dried (Figure 6.27 c). The cell viabilities for all the pre-soaked samples were over 90% and they were all passed ISO standards.

As discussed in the SBF dissolution study section, where a pH drop for all samples was also observed, the pH drop might be caused by the remained BF_3OEt_2 and the unreacted carboxylic groups from PCL-diCOOH might also lower pH values. Although the addition of MCEs did not affect the cell viability in all cases compared with non-particle samples HMC_0mg, it suggested that the organic sol synthesis procedure which used BF_3OEt_2 as a catalyst needs to be reviewed and any remaining catalyst removed before mixing with the inorganic sol.

6.4.8 3D printing of nano-hybrid scaffolds

Sol-gel ink characterisation before the printing. The rheology of prepared hybrid inks was evaluated. As reported by Gao *et al.,* a pseudoplastic shear thinning fluid behavior of the “ink” is favoured for all robotic extrusion printing [147]. Shear thinning behaviour means that the fluid viscosity decreases as the shear rate is increased. In 3D extrusion printing, this means when the force is applied to the ink, the viscosity is decreased so ink can flow through the cartridge/syringe and the printing tip nozzle smoothly and when the ink is deposited onto the printing substrate the viscosity should be restored, and the extruded filament holds its shape [142].

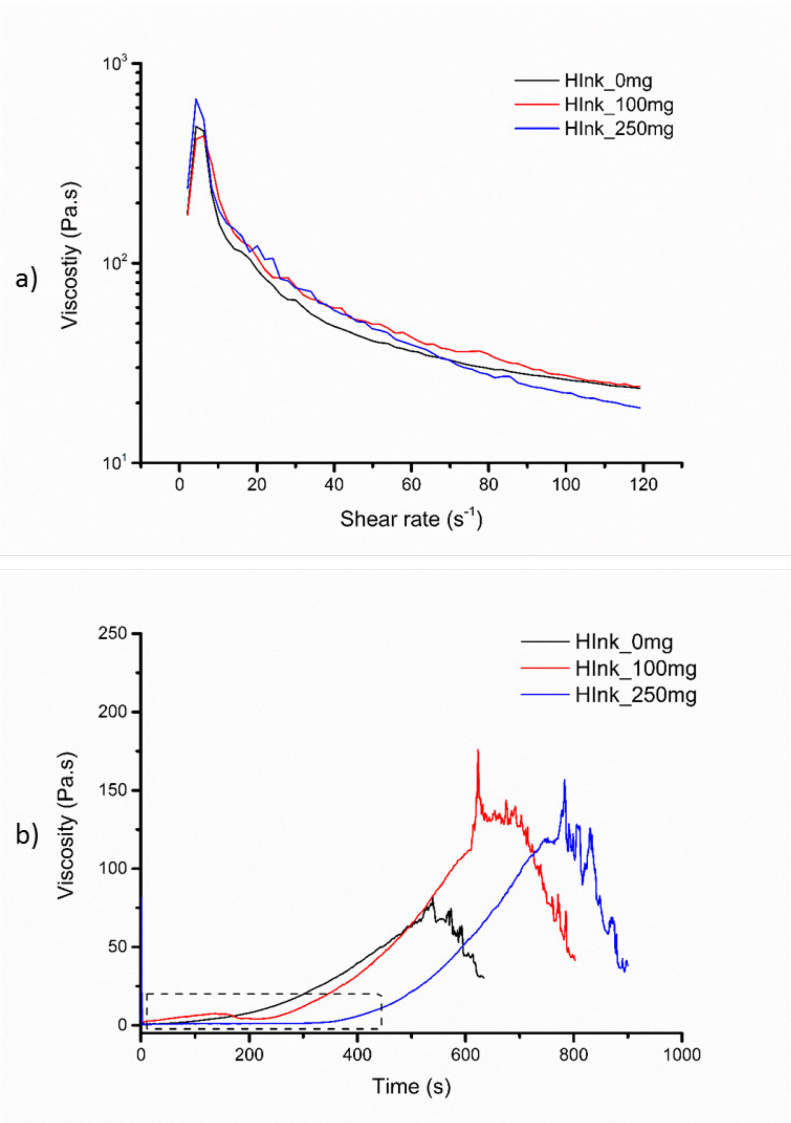


Figure 6.28 – Rheometery of the hybrid sol-gel ink with 0 mg, 100 mg and 250 mg of MCEs added during the synthesis tested using a rheometer, a), viscosities for all samples were recorded with an increase in shear rate from 1 s^{-1} to 120 s^{-1} in 60 s. In b), viscosities were recorded with a fixed shear rate of 80 s^{-1} over a time period up to 15 minutes.

The relation between viscosity and shear rate was assessed and shown in Figure 6.28 a. Hybrid ink samples were taken from the freezer and defrosted in 10 minutes and then after waiting another 10 minutes to let them back to room temperature the samples were tested. The results showed that, regardless of adding MCEs or not, all viscosities kept decreasing when the shear rate was increasing and this matched the behaviour of shear thinning.

During the hybrid bulk material synthesis discussed above, it was found that samples with MCEs introduced needed a longer time to gel, so it was believed that this property could slow the viscosity increase over time in hybrid inks and, as a consequence, lengthen the printing

window. The relation between viscosity and time was then studied and shown in Figure 6.28 b. All samples were tested 20 minutes after being taken from the freezer. From the graph, Hink_250mg samples, with the highest amounts of MCEs, showed a plateau until 400 s was reached. On the contrary, Hink_0mg samples started to build viscosity from the very beginning of the test. The difference found between samples with and without nanoparticles did suggest that the presence of MCEs slowed down material's viscosity increase rate. The fluctuation at the end of measurements was caused by the evaporation of the ink solvent, THF, and the machine lost the contact surface between samples and testing plates.

3D printing – macroscopic observation. Although the rheology tests gave information about hybrid inks, it did not mimic the actual 3D printing environment so the final 3D printing protocol was still derived from macroscopic observation by trial and error. Printing parameters of tip type, nozzle size, printing speed, deposition rate, strut spacing, layer height and printing substrate were the values reported by Tallia *et al.*[10] who printed the same hybrid material without MCEs (values stated in the Method *Section 6.2.3*). During the printing of hybrid inks Hink_100mg and Hink_250mg, those parameters were still applicable to get good shaped scaffolds so no modification was done.

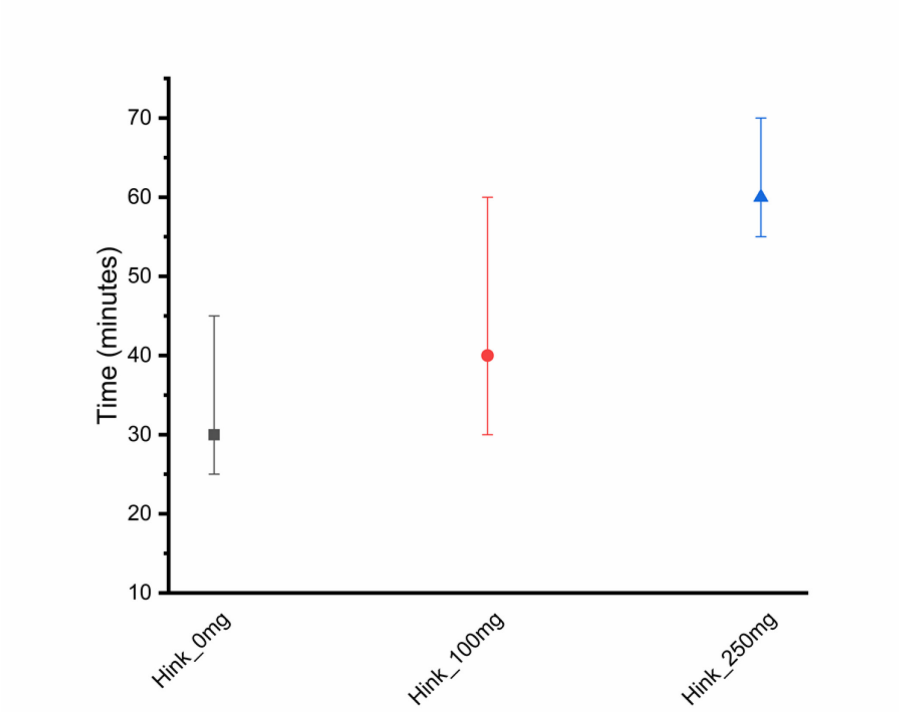


Figure 6.29 – Optimise printing time for hybrid inks with 0 mg, 100 mg and 250 mg of MCEs added during the synthesis.

The optimise printing time was then determined (Figure 6.29). The printing window in this project was defined as the time period from the beginning of the first well printed scaffold to the time when the tip nozzle was blocked because inks were fully gelled. From the graph, it shows that as more MCEs introduced into the hybrid system the longer printer window was achieved as expected. However, this printing window was limited by the ink syringe capacity, which was only 3 mL.

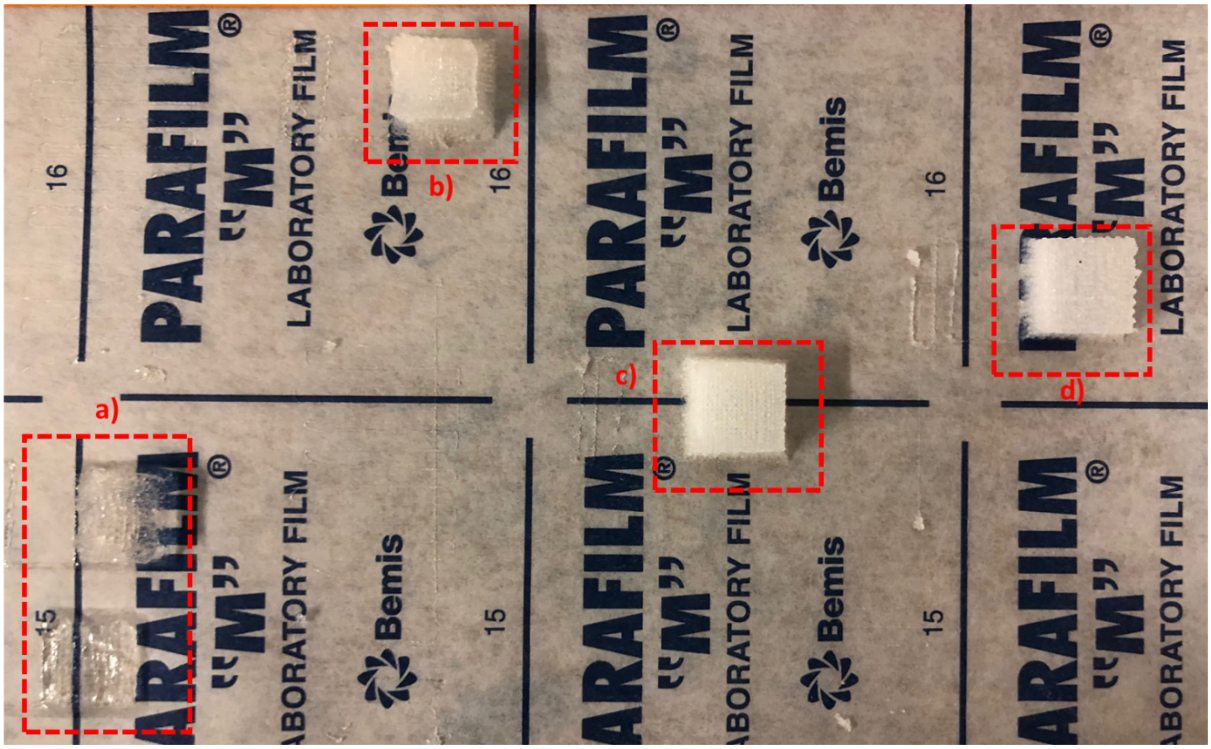


Figure 6.30 - Un-dried scaffolds printed from Hink_250mg at different printing times: a) before the printing window, b) at the beginning of the printing window, c) middle of the printing window and d) nearly the end of printing window.

Scaffolds printed in the printing window did not always have the same quality. For example, with scaffolds printed with Hink_250mg (Figure 6.30), the two scaffolds highlighted in the red rectangles were a) transparent and jelly like which means the hybrid network was not highly condensed and the polymerisation was not finished so the viscosity was not appropriate for printing, therefore, they were outside the printing window. Scaffolds highlighted in rectangular b), c) and d) were printed in the printing window.

Scaffold b was printed at the beginning of the printing window and it has irregular shape at the edge and the top surface. It was also smaller, compared with the other two, due to the solvent evaporation. Scaffolds c and d were printed at the middle and nearly the end of the printing window respectively.

Dried scaffolds observations.

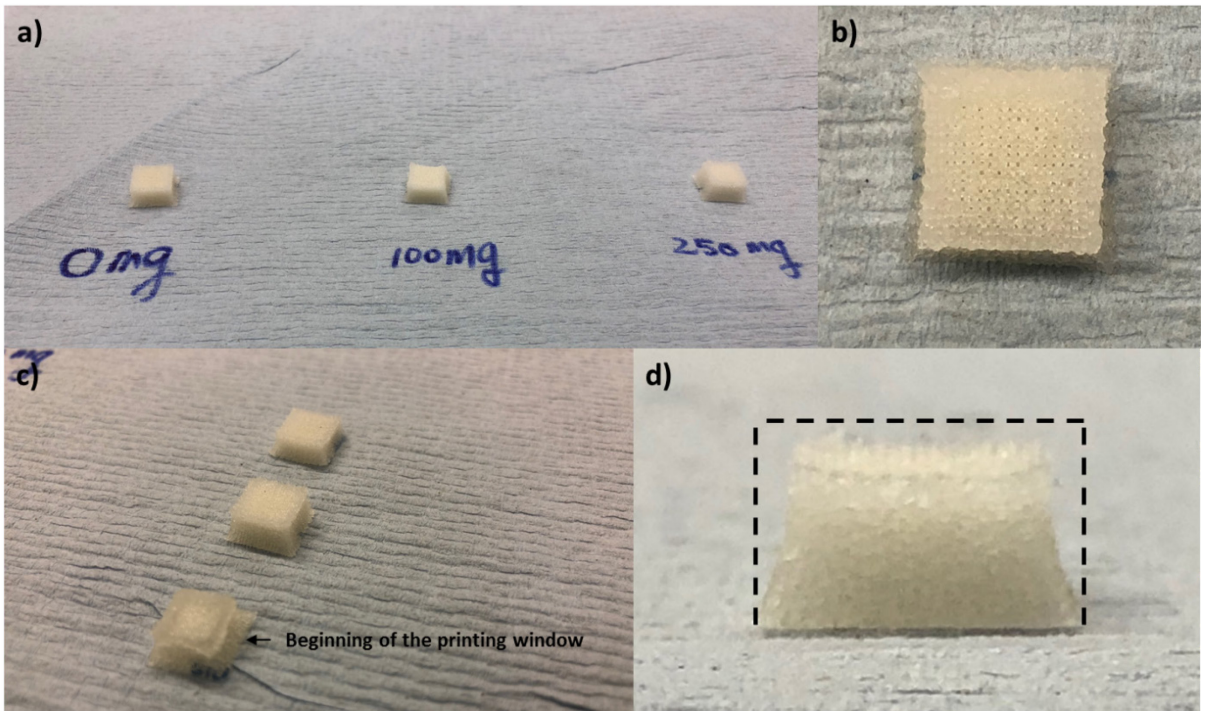


Figure 6.31 - Photographs of dried scaffolds printed from Hink_0mg, 100mg and 250mg.

After scaffolds were dried, no obvious difference was observed visually from samples containing different amounts of MCEs (Figure 6.31 a). All scaffolds had visible pores by looking at the top surface (Figure 6.31 b). Shrinkage was also noticed for all scaffolds, by measuring the length, width and height and then compared with designed dimensions (12mm x 12 mm x 6.51mm) the percentage shrinkage was calculated: 27% x 26% x 28% for Hink_0mg, 26% x 26 x 30% for Hink_100mg and 28% x 28% x 35% for Hink_250mg samples. The length and width were taken from the top surface not bottom surface because, as shown in Figure 6.31 d, the bottom layer directly contacted with printing substrate and the surface tension stopped that layer from shrinking and consequently the surface area at bottom was higher. Comparing the dried samples printed at different time points in the printing window (Figure 6.31 c), the scaffold printed at the beginning of the printing windows showed curved edges.

SEM images were taken for scaffold samples printed from Hink_0mg and Hink_250mg at different orientations (Figure 6.32). Hink_250mg samples showed a more ordered top surface structure and this was caused by scaffolds printed at different time points in the printing window. Also, during the printing of Hink_0mg samples, the quick change in viscosity made inks more gelled when it was printing the top layer and the printing tip experienced a higher pressure, depositing filaments that were curlier. Bottom surfaces for both samples looked similar and filaments looked flattened because they were in direct contact with the substrate. By looking at the vertical cross-section images, pores were smaller and some pores were closed in Hink_0mg samples. This can be explained by considering the weight experienced by the printed layers. As layers built up, previous printed layers were loaded with more weight from top layers and they were compressed, therefore, pores at vertical were closed.

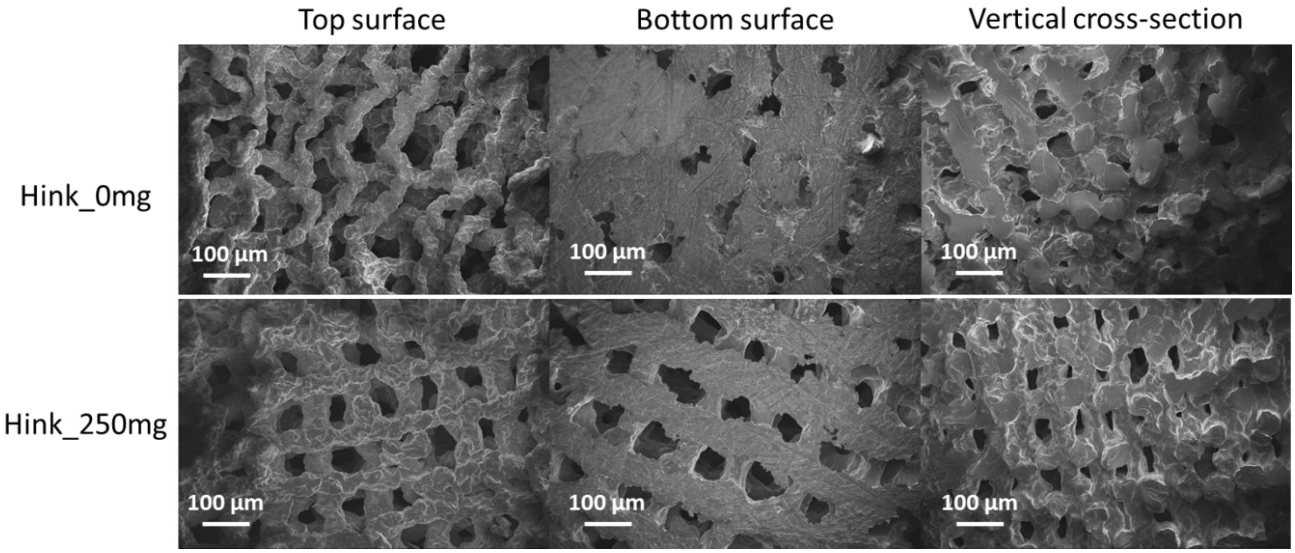


Figure 6.32 - SEM images for scaffolds printed with and without nanoparticles.

Finally, by increasing the magnification, scaffolds printed from Hink_250mg, MCEs were imaged (Figure 6.33). As highlighted in red circles in the images, both individual MCEs and particle clusters were observed. In addition, by looking at the location where struts from different layers contacted, highlighted in the blue circle, filaments were merged together instead of only being physically attached. This was given by the fact that during the printing the hybrid sol-gel inks were still reacting and condensing the network as they were not fully gelled and this would benefit scaffolds' mechanical properties.

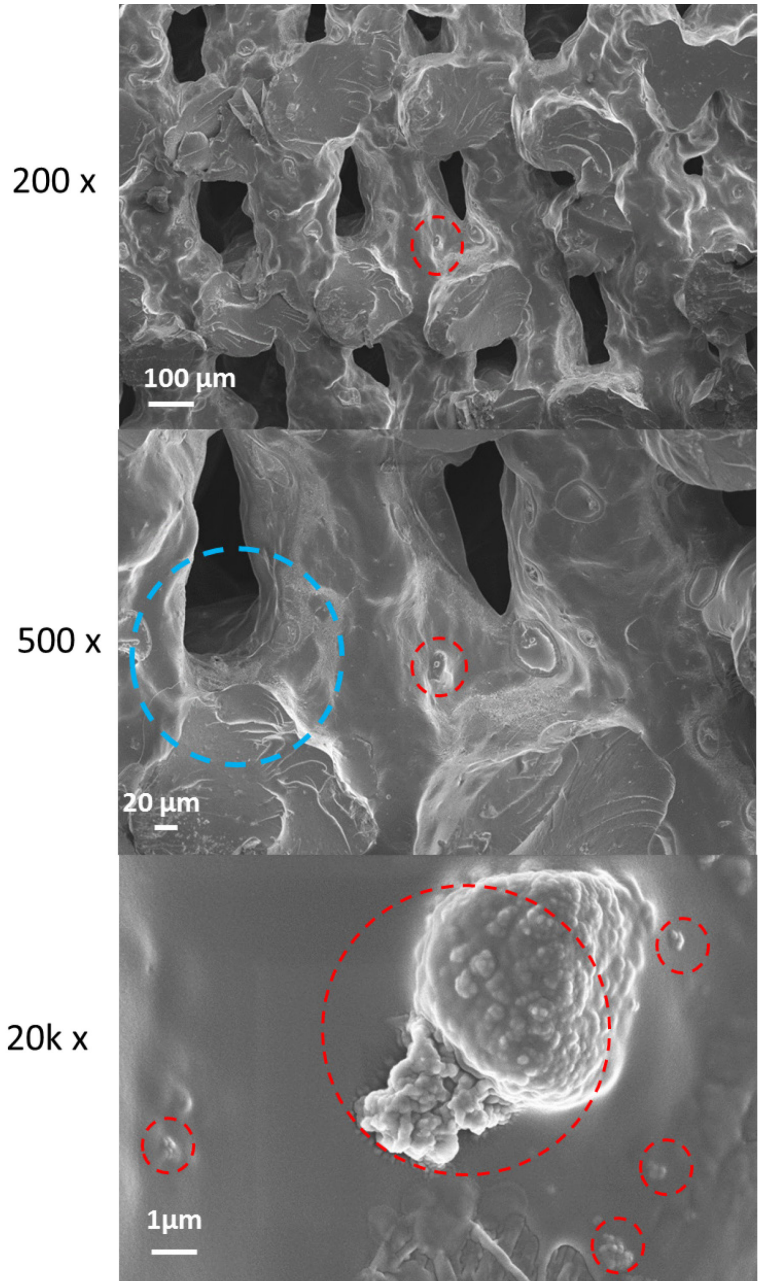


Figure 6.33 - SEM images of scaffolds printed from Hink_250mg under different magnifications. MCEs are highlighted in red dotted circles.

6.5 Conclusions

In this chapter, hybrid materials with calcium containing mesoporous nanoparticles covalently bonded with organic components were fabricated for the first time. It was found that the addition of MCEs had effects on behaviour of the original PCL/PTHF/SiO_2 hybrid in many ways.

First, the hybrid sol gelation/condensation time slowed with the presence of MCEs as mesoporous nanoparticles took over too much surface area and caused steric hindrance, in the solution which then interrupted the network formation. Maximum amounts of MCEs that could be homogeneously incorporated into the hybrids was 250 mg per 15.50 mL hybrid sol. The synthesis method was also modified by using the orbital shaker to prevent MCEs sinking to the bottom and distributed unevenly in the hybrid sol. Solid-state NMR was carried out and confirmed the structure of the hybrid network containing nanoparticles was not very different compared with the original hybrid and the presence of T^1 species in nano-hybrid samples suggested GPTMS grafted on the inner surface in the pore channels.

Both compression tests and compressive cyclic loading tests showed nano-hybrid samples were stiffer than the original hybrid samples, however, their maximum strains decreased because MCEs restricted movement of the polymer chains. Tensile tests also showed a decrease in maximum strain while the tensile strength for nano-hybrid samples was higher than original hybrid samples.

The main aim of this project was to deliver cations such as calcium to the hybrid system using functionalized mesoporous nanoparticles. Dissolution studies in Tris buffer showed that calcium release was slightly slower in samples with functionalized particles, compared to hybrids containing unfunctionalized particles. TEM images of the Tris solutions at different time points showed more particles were released at day 3 for nano-hybrid samples with un-functionalized particles. Dissolution in SBF produced only a small amount of HCA as the concentration of calcium in the nano-hybrid samples was too low as the maximum amount of MCEs can add in to the system was limited. A continuously dropping pH was also not favorable for HCA formation. The low pH was caused by remaining BF_3OEt_2, a catalyst used during the hybrid organic sol synthesis, which could be hydrolyzed in water, lowering the pH.

Because of the nano-hybrid made in this chapter lowered the pH over the time in solutions, cytotoxicity tests on both ATDC5 and MC3T3-E1 cell lines showed low cell viabilities as cells could not survive in the low pH. Samples were then soaked in water for 24 h to get rid of the remained BF_3OEt_2 and then cytotoxicity tests were carried out again on chondrogenic cells. This time cell viabilities for all washed samples were over 90%.

Finally, a 3D extrusion printing technique was used to fabricate porous scaffolds. Rheology tests were carried out on hybrid ink and found out they behaved as pseudoplastic with a shear thinning property which are favoured for robotic deposition. And also, the viscosity of inks with MCEs increased slower compared with the original hybrid inks. Longer printing windows were found for nano-hybrid samples as the hybrid sol-gel reaction was slowed by MCEs. SEM imaging showed that the overall morphology of the 3D printed scaffolds was not affected by introducing MCEs into the system. However, more characterization on the scaffolds, like the mechanical properties both in dry and wet environment, should be included in the future work.

Chapter 7 Summary and Future Works

7.1 Thesis summary

The main goal of this work was achieved in that a 3D printable and calcium containing PTHF/PCL/MCE/silica double organic and double inorganic nano-hybrid system was developed.

During this work, calcium incorporated dense silica nanoparticles (CaSNP) were functionalized with GPTMS for the first time. Results from FTIR, Raman and TGA showed that a small amount of GPMTS molecules were attached on the particles surface compared with nanoparticles without the present of calcium from literature [167]. The reason was because the high temperature used for calcination removed all the hydroxyl groups on the particle surfaces (polycondensation) and hydroxyl groups were the key element of the condensation reaction between GPTMS and nanoparticles. H_2/O_2 plasma was then applied to CaSNPs prior to the functionalization to help particles regain -OH groups on the surface. Results showed an improvement in GTPMS grafting yield by using plasma. The weight percentage of GTPMS molecules on particle surfaces of samples ESNP, CaESNP and plasma treated CaESNP were 7.82%, -0.88% and 4.05% calculated from TGA results. Acid digestion composition analysis showed only 3.51% - 4.40% of calcium was lost during the overnight reaction. Zeta potential showed a less negative charge on CaSNPs, compared to SNPs because of the loss of hydroxyl groups during calcination and the presence of Ca^{2+} ions, and the zeta potential for CaESNPs increased to +21.80 mV by grafting GPTMS molecules on the particle surfaces. Particles with increased surface area were needed.

Calcium incorporated mesoporous particles (CaMSNs) were then used and functionalized with GTPMS. CaMSNs had larger surface area compared to CaSNPs and were rich in -OH groups even after the calcination. FTIR and Raman results showed GPTMS was successfully grafted onto particle surface even without using plasma. TGA results also showed that the yield of GPTMS grafting did not increase linearly with the amount of GPTMS added in during the synthesis. Analysed by using nitrogen adsorption, small pores of MCEs were likely blocked by the addition of GPTMS. The use of solid-state NMR confirmed the success of grafting GPTMS on the particles surface and confirmed the result from TGA that GPTMS concentration on particle surface increased with the amount added during the synthesis, however, not all

hydrolyzed methoxylsilane groups from GPTMS were condensed. The dissolution profile showed GPTMS molecules on the particle surface did slow the release of calcium slightly and the formation of calcium phosphate was also slowed down.

Finally, PTHF/PCL/MCE/silica hybrid bulk samples and 3D printed scaffolds were produced. During the making of bulk samples, it was found out the introduction of MCE into the original PTHF/PCL/silica system slowed down the network condensation rate and the sol took longer time to gel. ^{29}Si solid-state NMR confirmed the nano-hybrid network formed did not change much compared with the original hybrid and the presence of T^1 species in nano-hybrid samples suggested there were GPTMS grafted on the inner surface in the pore channels and those pores were blocked eventually as the methoxysilane groups did not get hydrolyzed during synthesis. Dissolution in Tris buffer was carried out and sample supernatants were evaluated by ICP and TEM imaging, both results confirmed that when particles were covalently bonded to the hybrid network, they were released slower and a slower release on calcium consequently. Bioactivity was evaluated by using SBF dissolution study but HCA was only detected after 4 weeks were possibly given by SBF itself. The main reason of not having HCA formed earlier was: (i) the amount of calcium in nano-hybrid samples was too little and the maximum amount of MCEs that can be introduced to the hybrid was limited because if there were too much MCEs in the system hybrid condensation rate would become extremely slow; (ii) pH was decreasing continuously after 72 h, which is unfavorable for HCA formation as the concentration of OH^- in the solution became lower. This big pH dropping was also noticed during the cytotoxicity tests. The low media pH lead to all samples failed to pass the cytotoxicity tests. However, when samples were soaked in water for 24 h prior to the test, cell viabilities tested from all samples were over 90%. This suggested that a dissolution by-product was released from the sample and lower the media pH. The most possible by-product could be BF_3OEt_2 remained from the polymer sol synthesis. Samples were suggested to take a longer drying process in 40°C oven prior to use to remove all the BF_3OEt_2. Inks made from nano-hybrids were feasible for 3D extrusion printing and the introduction of MCEs enlarged the printing window.

7.2 Future work

7.2.1 Nanoparticles

Although GPTMS molecules were successfully grafted on the calcium containing dense silica particles surface by using plasma pretreatments, the average yield was still lower than bare particles. The use of H_2/O_2 plasma during this project work was limited by the machine, intentionally was designed for TEM sample surface clean, plasma could be only applied for 2 minutes each time due to the faulty machine. It was believed a longer plasma application time can help more with the regaining of hydroxyl groups. A more professional plasma treatment plan should be made and investigated.

The synthesis protocol of functionalized particles could be optimized to reach a monolayer of GPTMS by using an acidic reaction environment without opening the oxirane. If a monolayer distribution can be achieved, pore channels from mesoporous nanoparticles will have a chance not to be blocked by GPTMS.

7.2.2 Hybrid scaffolds

Investigation into the pH drop during the dissolution study and cytotoxicity is needed. A 24 h dissolution study in water and use of proton NMR to analyze the supernatant to see if there is any trace of BF_3OEt_2 release should be conducted. Mechanical tests in wet conditions is needed as the actual application will be in wet environment in body. Mechanical tests and dissolution studies should also be carried out on 3D printed scaffolds.

The amount of calcium in the nano-hybrid samples need to be increased. This can be achieved by increasing the amount of calcium incorporated into the mesoporous nanoparticles. Also, Yun *et al.*[192] reported a method to synthesis mesoporous silica nanoparticles with a SiO_2-CaO-P_2O_5 composition which can be potential used to replace the current nanoparticles in the nano-hybrids, although the detail on composition values was not reported.

The incorporation of calcium was just an example showing the possibility of this nano-hybrid system. With the diverse cation loading capability of silica nanoparticles, many other cations are possible to be introduced into the hybrid network and bring to the body, e.g. lithium for cartilage applications and strontium for bone regeneration. These are all worth to bring to the future work.

References

[1] M. Vallet-Regí, M. Colilla, and B. González, “Medical applications of organic-inorganic hybrid materials within the field of silica-based bioceramics,” *Chem. Soc. Rev.*, vol. 40, no. 2, pp. 596–607, 2011.

[2] E. Lavik and R. Langer, “Tissue engineering: current state and perspectives.,” *Appl. Microbiol. Biotechnol.*, vol. 65, pp. 1–8, 2004.

[3] L. G. Griffith, “Tissue Engineering--Current Challenges and Expanding Opportunities,” *Science (80-.).*, vol. 295, no. 5557, pp. 1009–1014, 2002.

[4] J. R. Jones, “Reprint of: Review of bioactive glass: From Hench to hybrids,” *Acta Biomaterialia*, vol. 23, no. S. Acta Materialia Inc., pp. S53–S82, Jan-2015.

[5] I. Cacciotti, M. Lombardi, A. Bianco, A. Ravaglioli, and L. Montanaro, “Sol-gel derived 45S5 bioglass: Synthesis, microstructural evolution and thermal behaviour,” *J. Mater. Sci. Mater. Med.*, vol. 23, pp. 1849–1866, 2012.

[6] T. S. Huang *et al.*, “Porous and strong bioactive glass (13-93) scaffolds fabricated by freeze extrusion technique,” *Mater. Sci. Eng. C*, vol. 31, no. 7, pp. 1482–1489, 2011.

[7] P. Gómez-Romero and C. Sanchez, Eds., *Functional Hybrid Materials*, no. 1. Wiley-VCH: Weinheim, 2004.

[8] G. Poologasundarampillai *et al.*, “Poly(γ-glutamic acid)/silica hybrids with calcium incorporated in the silica network by use of a calcium alkoxide precursor,” *Chemistry*, vol. 20, no. 26, pp. 8149–8160, 2014.

[9] W. Hui *et al.*, “Lithium protects cartilage from cytokine-mediated degradation by reducing collagen-degrading MMP production via inhibition of the p38 mitogen-activated protein kinase pathway,” *Rheumatology*, vol. 49, no. 11, pp. 2043–2053, 2010.

[10] F. Tallia *et al.*, “Bouncing and 3D printable hybrids with self-healing properties,” 2018.

[11] J. Y. Rho, L. Kuhn-Spearing, and P. Zioupos, “Mechanical properties and the hierarchical structure of bone,” *Med. Eng. Phys.*, vol. 20, no. 2, pp. 92–102, 1998.

[12] L. J. Gibson, *The mechanical behaviour of cancellous bone*, vol. 18, no. 5. 1985.

[13] R. R. D. S. S. E. Rubin, *Rubin’s Pathology: Clinicopathologic Foundations of Medicine*. 1992.

[14] S Weiner and W. Traub, “Bone structure: from angstroms to microns,” *FASEB J.*, vol. 6, no. 3, pp. 879–885, 1992.

[15] Q. Fu, *Biomedical, Therapeutic and Clinical Applications of Bioactive Glasses*. 2019.

[16] L. L. Hench and J. R. Jones, “Biomaterials, artificial organs and tissue engineering,” *Biomaterials, Artificial Organs and Tissue Engineering*. pp. 1–284, 2005.

[17] Q. Fu, E. Saiz, M. N. Rahaman, and A. P. Tomsia, “Bioactive glass scaffolds for bone tissue engineering: state of the art and future perspectives.,” *Mater. Sci. Eng. C.*

Mater. Biol. Appl., vol. 31, no. 7, pp. 1245–1256, Oct. 2011.

[18] L. Røhl, E. Larsen, F. Linde, A. Odgaard, and J. Jørgensen, "Tensile and compressive properties of cancellous bone," *J. Biomech.*, vol. 24, no. 12, pp. 1143–1149, 1991.

[19] C. Öhman *et al.*, "Compressive behaviour of child and adult cortical bone," *Bone*, vol. 49, no. 4, pp. 769–776, 2011.

[20] J. Y. Rho, M. C. Hobatho, and R. B. Ashman, "Relations of mechanical properties to density and CT numbers in human bone," *Med. Eng. Phys.*, vol. 17, no. 5, pp. 347–355, 1995.

[21] P. Zioupos and J. . Currey, "Changes in the Stiffness, Strength, and Toughness of Human Cortical Bone With Age," *Bone*, vol. 22, no. 1, pp. 57–66, 1998.

[22] M. L. Oyen, "The materials science of bone: Lessons from nature for biomimetic materials synthesis," *MRS Bull.*, vol. 33, no. 1, pp. 49–55, 2008.

[23] Q. Chen and G. Thouas, *Biomaterials: A Basic Introduction*. 2014.

[24] W. Jing *et al.*, "Reengineering autologous bone grafts with the stem cell activator WNT3A," *Biomaterials*, vol. 47, pp. 29–40, 2015.

[25] I. Marcos-Campos, D. Marolt, P. Petridis, S. Bhumiratana, D. Schmidt, and G. Vunjak-Novakovic, "Bone scaffold architecture modulates the development of mineralized bone matrix by human embryonic stem cells," *Biomaterials*, vol. 33, no. 33, pp. 8329–8342, 2012.

[26] a. J. Sophia Fox, a. Bedi, and S. a. Rodeo, "The Basic Science of Articular Cartilage: Structure, Composition, and Function," *Sport. Heal. A Multidiscip. Approach*, vol. 1, no. 6, pp. 461–468, 2009.

[27] M. H. Buckwalter JA, "Articular cartilage: degeneration and osteoarthritis, repair, regeneration and transplantation," *AAOS Inst Course Lect*, vol. 47, pp. 487–504, 1998.

[28] J. Buckwalter, V. Mow, and A. Ratcliffe, "Restoration of Injured or Degenerated Articular Cartilage.," *J. Am. Acad. Orthop. Surg.*, vol. 2, no. August 1994, pp. 192–201, 1994.

[29] K. Boettcher, S. Kienle, J. Nachtsheim, R. Burgkart, T. Hugel, and O. Lieleg, "The structure and mechanical properties of articular cartilage are highly resilient towards transient dehydration," *Acta Biomater.*, vol. 29, pp. 180–187, 2015.

[30] P. Morouço, N. Alves, and S. Amado, "The Role of Biomechanics in Tissue Engineering," *Austin J. Biomed. Eng.*, vol. 3, no. December, p. 1035, 2016.

[31] J. S. Jurvelin, M. D. Buschmann, and E. B. Hunziker, "Optical and mechanical determination of Poisson's ratio of adult bovine humeral articular cartilage," *J. Biomech.*, vol. 30, pp. 235–241, 1997.

[32] C. J. Little, N. K. Bawolin, and X. Chen, "Mechanical properties of natural cartilage and tissue-engineered constructs.," *Tissue Eng. Part B. Rev.*, vol. 17, no. 4, pp. 213–227, 2011.

[33] F. Charles, R. Jones, A. Hunt, O. Centre, and O. We, “Mechanical and biochemical properties of human articular cartilage in osteoarthritic femoral heads and in autopsy specimens,” *Clin. Biomech.*, vol. 1, no. 4, p. 233, 1986.

[34] C. Glaser and R. Putz, “Functional anatomy of articular cartilage under compressive loading quantitative aspects of global, local and zonal reactions of the collagenous network with respect to the surface integrity,” *Osteoarthr. Cartil.*, vol. 10, no. 2, pp. 83–99, 2002.

[35] B. L. Wong, W. C. Bae, J. Chun, K. R. Gratz, M. Lotz, and R. L. Sah, “Biomechanics of cartilage articulation: Effects of lubrication and degeneration on shear deformation,” *Arthritis Rheum.*, vol. 58, no. 7, pp. 2065–2074, 2008.

[36] P. R. Fortin *et al.*, “Outcomes of total hip and knee replacement: Preoperative functional status predicts outcomes at six months after surgery,” *Arthritis Rheum.*, vol. 42, no. 8, pp. 1722–1728, 1999.

[37] S. P. Nukavarapu and D. L. Dorcemus, “Osteochondral tissue engineering: Current strategies and challenges,” *Biotechnol. Adv.*, vol. 31, no. 5, pp. 706–721, 2013.

[38] E. B. Hunziker, “Articular cartilage repair: Basic science and clinical progress. A review of the current status and prospects,” *Osteoarthr. Cartil.*, vol. 10, no. 2001, pp. 432–463, 2002.

[39] S. Bose, M. Roy, and A. Bandyopadhyay, “Recent advances in bone tissue engineering scaffolds,” *Trends Biotechnol.*, vol. 30, no. 10, pp. 546–554, 2012.

[40] Q. L. Loh and C. Choong, “Three-dimensional scaffolds for tissue engineering applications: role of porosity and pore size.,” *Tissue Eng. Part B. Rev.*, vol. 19, no. 6, pp. 485–502, 2013.

[41] L. L. Hench, “Bioglass: 10 milestones from concept to commerce,” *J. Non. Cryst. Solids*, pp. 1–7, Feb. 2015.

[42] L. L. Hench, R. J. Splinter, W. C. Allen, and T. K. Greenlee, “Bonding mechanisms at the interface of ceramic prosthetic materials,” *J. Biomed. Mater. Res.*, vol. 5, no. 6, pp. 117–141, 1971.

[43] Z. Y. Wu, R. G. Hill, S. Yue, D. Nightingale, P. D. Lee, and J. R. Jones, “Melt-derived bioactive glass scaffolds produced by a gel-cast foaming technique.,” *Acta Biomater.*, vol. 7, no. 4, pp. 1807–16, Apr. 2011.

[44] R. Li, A. E. Clark, and L. L. Hench, “An investigation of bioactive glass powders by sol-gel processing.,” *J. Appl. Biomater.*, vol. 2, no. 4, pp. 231–239, 1991.

[45] L. L. Hench and J. K. West, “The sol-gel process,” *Chem. Rev.*, vol. 90, no. 1, pp. 33–72, Jan. 1990.

[46] E. M. Valliant and J. R. Jones, “Softening bioactive glass for bone regeneration: sol–gel hybrid materials,” *Soft Matter*, vol. 7, no. 11, p. 5083, 2011.

[47] J. R. Jones and A. G. Clare, *Bio-Glasses: An Introduction*. 2012.

[48] F. Hench LL, Jones JR and MB, *New materials and technologies for healthcare*.

Singapore: World Scientific, 2011.

[49] A. E. CLARK, C. G. PANTANO, and L. L. HENCH, “Auger Spectroscopic Analysis of Bioglass Corrosion Films,” *J. Am. Ceram. Soc.*, vol. 59, no. 1–2, pp. 37–39, 1976.

[50] L. L. Hench, “Bioceramics: From Concept to Clinic,” *J. Am. Ceram. Soc.*, vol. 74, no. 7, pp. 1487–1510, 1991.

[51] A. El-Ghannam, P. Ducheyne, and I. M. Shapiro, “Effect of serum proteins on osteoblast adhesion to surface-modified bioactive glass and hydroxyapatite,” *J. Orthop. Res.*, vol. 17, no. 3, pp. 340–345, 1999.

[52] I. D. Xynos, A. J. Edgar, L. D. K. Buttery, L. L. Hench, and J. M. Polak, “Gene-expression profiling of human osteoblasts following treatment with the ionic products of Bioglass® 45S5 dissolution,” *J. Biomed. Mater. Res.*, vol. 55, no. 2, pp. 151–157, 2001.

[53] B. M. Novak, “Hybrid nanocomposite materials - Between inorganic glasses and organic polymers,” *Adv. Mater.*, vol. 5, no. 6, pp. 422–433, 1993.

[54] T. Yoshioka, K. Tsuru, S. Hayakawa, and A. Osaka, “Preparation of alginic acid layers on stainless-steel substrates for biomedical applications,” *Biomaterials*, vol. 24, no. 17, pp. 2889–2894, 2003.

[55] A. L. B. Maçon *et al.*, “A structural and physical study of sol-gel methacrylate-silica hybrids: intermolecular spacing dictates the mechanical properties,” *Phys. Chem. Chem. Phys.*, vol. 17, no. 43, pp. 29124–29133, 2015.

[56] R. Ravarian, H. Wei, A. Rawal, J. Hook, W. Chrzanowski, and F. Dehghani, “Molecular interactions in coupled PMMA-bioglass hybrid networks,” *J. Mater. Chem. B*, vol. 1, no. 13, pp. 1835–1845, 2013.

[57] O. Mahony *et al.*, “Silica-Gelatin Hybrids with Tailorable Degradation and Mechanical Properties for Tissue Regeneration,” *Adv. Funct. Mater.*, vol. 20, no. 22, pp. 3835–3845, Nov. 2010.

[58] A. Helminen, H. Korhonen, and J. V. Seppälä, “Biodegradable crosslinked polymers based on triethoxysilane terminated polylactide oligomers,” *Polymer (Guildf).*, vol. 42, no. 8, pp. 3345–3353, 2001.

[59] J. Zarzycki, M. Prassas, and J. Phalippou, “Synthesis of glasses from gels: the problem of monolithic gels,” *J. Mater. Sci.*, vol. 17, no. 11, pp. 3371–3379, 1982.

[60] S. Lin, C. Ionescu, K. J. Pike, M. E. Smith, and J. R. Jones, “Nanostructure evolution and calcium distribution in sol-gel derived bioactive glass,” pp. 1276–1282, 2009.

[61] G. Poologasundarampillai *et al.*, “Synthesis of bioactive class II poly(γ-glutamic acid)/silica hybrids for bone regeneration,” *J. Mater. Chem.*, vol. 20, no. 40, p. 8952, 2010.

[62] G. Poologasundarampillai *et al.*, “Bioactive silica-poly(γ-glutamic acid) hybrids for bone regeneration: Effect of covalent coupling on dissolution and mechanical properties and fabrication of porous scaffolds,” *Soft Matter*, vol. 8, no. 17, pp. 4822–4832, 2012.

[63] M. M. Pereira, A. E. Clark, and L. L. Hench, “Calcium phosphate formation on sol-gel-derived bioactive glasses in vitro,” *J. Biomed. Mater. Res.*, vol. 28, no. 6, pp. 693–698, 1994.

[64] A. Rámila, F. Balas, and M. Vallet-Regí, “Synthesis routes for bioactive sol-gel glasses: Alkoxides versus nitrates,” *Chem. Mater.*, vol. 14, no. 2, pp. 542–548, 2002.

[65] G. Poologasundarampillai, B. Yu, J. R. Jones, and T. Kasuga, “Electrospun silica/PLLA hybrid materials for skeletal regeneration,” *Soft Matter*, vol. 7, no. 21, pp. 10241–10251, 2011.

[66] H. Ting, “PhD Thesis Role of phosphate and calcium in sol-gel bioactive glasses and silica / poly (caprolactone) hybrids,” 2016.

[67] M. A. Woodruff and D. W. Hutmacher, “The return of a forgotten polymer - Polycaprolactone in the 21st century,” *Prog. Polym. Sci.*, vol. 35, no. 10, pp. 1217–1256, 2010.

[68] V. Thomas, M. V. Jose, S. Chowdhury, J. F. Sullivan, D. R. Dean, and Y. K. Vohra, “Mechano-morphological studies of aligned nanofibrous scaffolds of polycaprolactone fabricated by electrospinning,” *J. Biomater. Sci. Polym. Ed.*, vol. 17, no. 9, pp. 969–984, 2006.

[69] J. S. Choi, S. J. Lee, G. J. Christ, A. Atala, and J. J. Yoo, “The influence of electrospun aligned poly(ε-caprolactone)/collagen nanofiber meshes on the formation of self-aligned skeletal muscle myotubes,” *Biomaterials*, vol. 29, no. 19, pp. 2899–2906, 2008.

[70] A. A. Sawyer *et al.*, “The stimulation of healing within a rat calvarial defect by mPCL-TCP/collagen scaffolds loaded with rhBMP-2,” *Biomaterials*, vol. 30, no. 13, pp. 2479–2488, 2009.

[71] C. X. Lam, Swee Hin Teoh, and D. W. Hutmacher, “Comparison of the degradation ofpolycaprolactone and polycaprolactone–(β-tricalcium phosphate) scaffolds in alkalinemedium,” *Polym. Int.*, vol. 56, no. 6, pp. 718–728, 2007.

[72] S. A. Abbah, C. X. L. Lam, D. W. Hutmacher, J. C. H. Goh, and H. K. Wong, “Biological performance of a polycaprolactone-based scaffold used as fusion cage device in a large animal model of spinal reconstructive surgery,” *Biomaterials*, vol. 30, no. 28, pp. 5086–5093, 2009.

[73] Q. Huang, J. C. H. Goh, D. W. Hutmacher, and E. H. Lee, “*In Vivo* Mesenchymal Cell Recruitment by a Scaffold Loaded with Transforming Growth Factor *β* 1 and the Potential for *in Situ* Chondrogenesis,” *Tissue Eng.*, vol. 8, no. 3, pp. 469–482, 2002.

[74] W. J. Li, K. G. Danielson, P. G. Alexander, and R. S. Tuan, “Biological response of chondrocytes cultured in three-dimensional nanofibrous poly(ε-caprolactone) scaffolds,” *J. Biomed. Mater. Res. - Part A*, vol. 67, no. 4, pp. 1105–1114, 2003.

[75] C. Chiari *et al.*, “A tissue engineering approach to meniscus regeneration in a sheep model,” *Osteoarthr. Cartil.*, vol. 14, no. 10, pp. 1056–1065, 2006.

[76] J. R. Jones, “New trends in bioactive scaffolds: The importance of nanostructure,” *J.*

Eur. Ceram. Soc., vol. 29, no. 7, pp. 1275–1281, 2009.

[77] D. Tian, S. Blacher, J. Pirard, and R. Je, "Biodegradable and Biocompatible Inorganic - Organic Hybrid Materials . 3 . A Valuable Route to the Control of the Silica Porosity," vol. 35, no. 11, pp. 1905–1910, 1998.

[78] D. Tian *et al.*, "A novel biodegradable and biocompatible ceramer prepared by the sol-gel process," *Chem. Mater.*, vol. 9, no. 4, pp. 871–874, 1997.

[79] S. H. Rhee, J. Y. Choi, and H. M. Kim, "Preparation of a bioactive and degradable poly(ε-caprolactone)/silica hybrid through a sol-gel method," *Biomaterials*, vol. 23, no. 24, pp. 4915–4921, 2002.

[80] S. H. Rhee, "Bone-like apatite-forming ability and mechanical properties of poly(ε-caprolactone)/silica hybrid as a function of poly(ε- caprolactone) content," *Biomaterials*, vol. 25, no. 7–8, pp. 1167–1175, 2004.

[81] T. Sang, S. Li, H. K. Ting, M. M. Stevens, C. R. Becer, and J. R. Jones, "Hybrids of Silica/Poly(caprolactone coglycidoxypropyl trimethoxysilane) as Biomaterials," *Chem. Mater.*, vol. 30, no. 11, pp. 3743–3751, 2018.

[82] C. A. Wamser, "Equilibria in the System Boron Trifluoride-Water at 25°," *J. Am. Chem. Soc.*, vol. 73, no. 1, pp. 409–416, 1951.

[83] L. Gabrielli *et al.*, "Exploring GPTMS reactivity against simple nucleophiles: chemistry beyond hybrid materials fabrication," *RSC Adv.*, vol. 4, p. 1841, 2014.

[84] O. Nuyken and S. D. Pask, "Ring-opening polymerization-An introductory review," *Polymers (Basel).*, vol. 5, no. 2, pp. 361–403, 2013.

[85] J. K. and R. D. B. Ko¨hler, W. Ebert, K. Horn, W. S. Scha¨fer, "US Pat.5633339," 1997.

[86] L. P. Singh *et al.*, "Sol-Gel processing of silica nanoparticles and their applications," *Adv. Colloid Interface Sci.*, vol. 214, pp. 17–37, 2014.

[87] A. CE *et al.*, "The targeted delivery of multicomponent cargos to cancer cells by nanoporous particle-supported lipid bilayers," *Nat. Mater.*, vol. 10, no. 5, pp. 389–397, 2011.

[88] P. Naruphontjirakul, A. E. Porter, and J. R. Jones, "In vitro osteogenesis by intracellular uptake of strontium containing bioactive glass nanoparticles," *Acta Biomater.*, vol. 66, pp. 67–80, 2018.

[89] S. L. Greasley *et al.*, "Controlling particle size in the St??ber process and incorporation of calcium," *J. Colloid Interface Sci.*, vol. 469, pp. 213–223, 2016.

[90] W. Stöber, A. Fink, and E. Bohn, "Controlled growth of monodisperse silica spheres in the micron size range," *J. Colloid Interface Sci.*, vol. 26, pp. 62–69, 1968.

[91] I. A. Rahman and V. Padavettan, *Synthesis of Silica Nanoparticles by Sol-Gel: Size-Dependent Properties, Surface Modification, and Applications in Silica-Polymer Nanocomposites—A Review*, vol. 2012, no. May 2015. 2012.

[92] C. J. Brinker and G. W. Scherer, *Sol-Gel Science*. 2013.

[93] K. Lee, A. N. Sathyagal, and A. V. McCormick, “A closer look at an aggregation model of the Stöber process,” *Colloids Surfaces A Physicochem. Eng. Asp.*, vol. 144, no. 1–3, pp. 115–125, 1998.

[94] G. H. Bogush and C. F. Zukoski IV, “Uniform silica particle precipitation: An aggregative growth model,” *J. Colloid Interface Sci.*, vol. 142, no. 1, pp. 19–34, 1991.

[95] V. K. Lamer and R. H. Dinegar, “Theory, Production and Mechanism of Formation of Monodispersed Hydrosols,” *J. Am. Chem. Soc.*, vol. 72, no. 11, pp. 4847–4854, 1950.

[96] S. K. Park, K. Do Kim, and H. T. Kim, “Preparation of silica nanoparticles: Determination of the optimal synthesis conditions for small and uniform particles,” *Colloids Surfaces A Physicochem. Eng. Asp.*, vol. 197, no. 1–3, pp. 7–17, 2002.

[97] M. Vallet-Regi, A. Rámila, R. P. Del Real, and J. Pérez-Pariente, “A new property of MCM-41: Drug delivery system,” *Chem. Mater.*, vol. 13, no. 2, pp. 308–311, 2001.

[98] F. Tang, L. Li, and D. Chen, “Mesoporous silica nanoparticles: Synthesis, biocompatibility and drug delivery,” *Adv. Mater.*, vol. 24, no. 12, pp. 1504–1534, 2012.

[99] D. Peer, J. M. Karp, S. Hong, O. C. Farokhzad, R. Margalit, and R. Langer, “Nanocarriers as an emerging platform for cancer therapy,” *Nat. Nanotechnol.*, vol. 2, no. 12, pp. 751–760, 2007.

[100] M. Vallet-Regí, “Ordered mesoporous materials in the context of drug delivery systems and bone tissue engineering,” *Chem. - A Eur. J.*, vol. 12, no. 23, pp. 5934–5943, 2006.

[101] P. Naruphontjirakul, “Strontium containing bioactive glass nanoparticles Department of Materials degree of Doctor of Philosophy (PhD),” no. April, 2018.

[102] B. Chang *et al.*, “Bioresponsive controlled drug release based on mesoporous silica nanoparticles coated with reductively sheddable polymer shell,” *Chem. Mater.*, vol. 25, no. 4, pp. 574–585, 2013.

[103] I. I. Slowing, J. L. Vivero-Escoto, C.-W. Wu, and V. S. Y. Lin, “Mesoporous silica nanoparticles as controlled release drug delivery and gene transfection carriers,” *Adv. Drug Deliv. Rev.*, vol. 60, no. 11, pp. 1278–1288, 2008.

[104] Y. S. Lin *et al.*, “Well-ordered mesoporous silica nanoparticles as cell markers,” *Chem. Mater.*, vol. 17, no. 18, pp. 4570–4573, 2005.

[105] H. Y. Lin and Y. W. Chen, “Preparation of spherical hexagonal mesoporous silica,” *J. Porous Mater.*, vol. 12, no. 2, pp. 95–105, 2005.

[106] H. Fan and J. Brinker, “Evaporation-induced nanostructures to functional,” 2004.

[107] S. Lin, C. Ionescu, K. J. Pike, M. E. Smith, and J. R. Jones, “Nanostructure evolution and calcium distribution in sol-gel derived bioactive glass,” *J. Mater. Chem.*, vol. 19, no. 9, pp. 1276–1282, 2009.

[108] B. Yu *et al.*, “Effect of calcium source on structure and properties of sol-gel derived bioactive glasses,” *Langmuir*, vol. 28, no. 50, pp. 17465–17476, 2012.

[109] O. Tsigkou, S. Labbaf, M. M. Stevens, A. E. Porter, and J. R. Jones, “Monodispersed bioactive glass submicron particles and their effect on bone marrow and adipose tissue-derived stem cells,” *Adv. Healthc. Mater.*, vol. 3, no. 1, pp. 115–125, 2014.

[110] G. Kickelbick and E. Corporation, *Hybrid materials: synthesis, characterization, and applications*. Wiley-VCH: Weinheim, 2007.

[111] H. Zou, S. Wu, and J. Shen, “Hybrid Materials: Synthesis, Characterization, and Applications,” 2008, pp. 3893–3957.

[112] B. Dorj, J. H. Park, and H. W. Kim, “Robocasting chitosan/nanobioactive glass dual-pore structured scaffolds for bone engineering,” *Mater. Lett.*, vol. 73, pp. 119–122, 2012.

[113] L. Ji, W. Wang, D. Jin, S. Zhou, and X. Song, “In vitro bioactivity and mechanical properties of bioactive glass nanoparticles/polycaprolactone composites,” *Mater. Sci. Eng. C*, vol. 46, pp. 1–9, 2015.

[114] A. M. El-Kady, R. A. Rizk, B. M. Abd El-Hady, M. W. Shafaa, and M. M. Ahmed, “Characterization, and antibacterial properties of novel silver releasing nanocomposite scaffolds fabricated by the gas foaming/salt-leaching technique,” *J. Genet. Eng. Biotechnol.*, vol. 10, no. 2, pp. 229–238, 2012.

[115] Z. Hong, R. L. Reis, and J. F. Mano, “Preparation and in vitro characterization of scaffolds of poly(l-lactic acid) containing bioactive glass ceramic nanoparticles,” *Acta Biomater.*, vol. 4, no. 5, pp. 1297–1306, 2008.

[116] S. Loher *et al.*, “Improved degradation and bioactivity of amorphous aerosol derived tricalcium phosphate nanoparticles in poly(lactide-co-glycolide),” *Nanotechnology*, vol. 17, no. 8. pp. 2054–2061, 2006.

[117] A. Liu *et al.*, “Surface modification of bioactive glass nanoparticles and the mechanical and biological properties of poly(l-lactide) composites,” *Acta Biomater.*, vol. 4, no. 4, pp. 1005–1015, 2008.

[118] A. El-Fiqi, J. H. Lee, E. J. Lee, and H. W. Kim, “Collagen hydrogels incorporated with surface-aminated mesoporous nanobioactive glass: Improvement of physicochemical stability and mechanical properties is effective for hard tissue engineering,” *Acta Biomater.*, vol. 9, no. 12, pp. 9508–9521, 2013.

[119] L. Deliang, C. Zhixian, and Z. Zhijun, “The surface modification of silica with GPTMS,” *Prog. Chem.*, vol. 20, no. 7–8, 2008.

[120] B. Alonso *et al.*, “Structural control in germania hybrid organic-inorganic materials,” *Chem. Mater.*, vol. 17, no. 12, pp. 3172–3180, 2005.

[121] D. Allen and Z. El Rassi, “Capillary electrochromatography with monolithic silica columns: III. Preparation of hydrophilic silica monoliths having surface-bound cyano groups: Chromatographic characterization and application to the separation of carbohydrates, nucleosides, nucleic a,” *J. Chromatogr. A*, vol. 1029, no. 1–2, pp. 239–247, 2004.

[122] W. He *et al.*, “Surface modification of colloidal silica nanoparticles: Controlling the

size and grafting process," *Bull. Korean Chem. Soc.*, vol. 34, no. 9, pp. 2747–2752, 2013.

[123] M. Iijima, M. Tsukada, and H. Kamiya, "Effect of particle size on surface modification of silica nanoparticles by using silane coupling agents and their dispersion stability in methylethylketone," *J. Colloid Interface Sci.*, vol. 307, no. 2, pp. 418–424, 2007.

[124] L. S. Kasten, V. N. Balbyshev, and M. S. Donley, "Surface analytical study of self-assembled nanophase particle (SNAP) surface treatments," *Prog. Org. Coatings*, vol. 47, no. 3–4, pp. 214–224, 2003.

[125] J. a. a. Sales and C. Airoldi, "Calorimetric investigation of metal ion adsorption on 3-glycidoxypropyltrimethylsiloxane + propane-1,3-diamine immobilized on silica gel," *Thermochim. Acta*, vol. 427, pp. 77–83, 2005.

[126] S. R. Davis, A. R. Brough, and A. Atkinson, "Formation of silica/epoxy hybrid network polymers," *J. Non. Cryst. Solids*, vol. 315, no. 1–2, pp. 197–205, 2003.

[127] A. G. Mitsak, J. M. Kemppainen, M. T. Harris, and S. J. Hollister, "Effect of Polycaprolactone Scaffold Permeability on Bone Regeneration *In Vivo*," *Tissue Eng. Part A*, vol. 17, no. 13–14, pp. 1831–1839, 2011.

[128] S. H. Huang, P. Liu, A. Mokasdar, and L. Hou, "Additive manufacturing and its societal impact: A literature review," *Int. J. Adv. Manuf. Technol.*, vol. 67, no. 5–8, pp. 1191–1203, 2013.

[129] P.-C. Chang *et al.*, "Bone tissue engineering with novel rhBMP2-PLLA composite scaffolds.," *J. Biomed. Mater. Res. A*, vol. 81, pp. 771–780, 2007.

[130] M. L. Harris, a. Doraiswamy, R. J. Narayan, T. M. Patz, and D. B. Chrisey, "Recent progress in CAD/CAM laser direct-writing of biomaterials," *Mater. Sci. Eng. C*, vol. 28, pp. 359–365, 2008.

[131] B. Guillotin *et al.*, "Laser assisted bioprinting of engineered tissue with high cell density and microscale organization," *Biomaterials*, vol. 31, no. 28, pp. 7250–7256, 2010.

[132] J. M. Williams *et al.*, "Bone tissue engineering using polycaprolactone scaffolds fabricated via selective laser sintering," *Biomaterials*, vol. 26, pp. 4817–4827, 2005.

[133] B. Duan, M. Wang, W. Y. Zhou, W. L. Cheung, Z. Y. Li, and W. W. Lu, "Three-dimensional nanocomposite scaffolds fabricated via selective laser sintering for bone tissue engineering," *Acta Biomater.*, vol. 6, no. 12, pp. 4495–4505, 2010.

[134] T. F. Pereira *et al.*, "Effect of process parameters on the properties of selective laser sintered Poly(3-hydroxybutyrate) scaffolds for bone tissue engineering," *Virtual Phys. Prototyp.*, vol. 7, no. June 2015, pp. 275–285, 2012.

[135] P. X. Lan, J. W. Lee, Y. J. Seol, and D. W. Cho, "Development of 3D PPF/DEF scaffolds using micro-stereolithography and surface modification," *J. Mater. Sci. Mater. Med.*, vol. 20, pp. 271–279, 2009.

[136] J. W. Lee, G. Ahn, D. S. Kim, and D. W. Cho, "Development of nano- and microscale

composite 3D scaffolds using PPF/DEF-HA and micro-stereolithography," *Microelectron. Eng.*, vol. 86, no. 4–6, pp. 1465–1467, 2009.

[137] a. Ronca, L. Ambrosio, and D. W. Grijpma, "Preparation of designed poly(d,l-lactide)/nanosized hydroxyapatite composite structures by stereolithography," *Acta Biomater.*, vol. 9, no. 4, pp. 5989–5996, 2013.

[138] J. M. Sobral, S. G. Caridade, R. a. Sousa, J. F. Mano, and R. L. Reis, "Three-dimensional plotted scaffolds with controlled pore size gradients: Effect of scaffold geometry on mechanical performance and cell seeding efficiency," *Acta Biomater.*, vol. 7, no. 3, pp. 1009–1018, 2011.

[139] R. Detsch, F. Uhl, U. Deisinger, and G. Ziegler, "3D-Cultivation of bone marrow stromal cells on hydroxyapatite scaffolds fabricated by dispense-plotting and negative mould technique," *J. Mater. Sci. Mater. Med.*, vol. 19, pp. 1491–1496, 2008.

[140] C. Wu, Y. Luo, G. Cuniberti, Y. Xiao, and M. Gelinsky, "Three-dimensional printing of hierarchical and tough mesoporous bioactive glass scaffolds with a controllable pore architecture, excellent mechanical strength and mineralization ability," *Acta Biomater.*, vol. 7, no. 6, pp. 2644–2650, 2011.

[141] T. Serra, J. a. Planell, and M. Navarro, "High-resolution PLA-based composite scaffolds via 3-D printing technology," *Acta Biomater.*, vol. 9, no. 3, pp. 5521–5530, 2013.

[142] Q. Fu, E. Saiz, and A. P. Tomsia, "Direct ink writing of highly porous and strong glass scaffolds for load-bearing bone defects repair and regeneration," *Acta Biomater.*, vol. 7, no. 10, pp. 3547–3554, 2011.

[143] K. Mithoefer *et al.*, "The microfracture technique for the treatment of articular cartilage lesions in the knee. A prospective cohort study.," *J. Bone Joint Surg. Am.*, vol. 87, pp. 1911–1920, 2005.

[144] Y. Chen, Z. Xu, C. Smith, and J. Sankar, "Recent advances on the development of magnesium alloys for biodegradable implants.," *Acta Biomater.*, vol. 10, no. 11, pp. 4561–4573, Jul. 2014.

[145] J. a. Lewis, "Direct Ink Writing of 3D Functional Materials," *Adv. Funct. Mater.*, vol. 16, no. 17, pp. 2193–2204, Nov. 2006.

[146] J. Franco, P. Hunger, M. E. Launey, a. P. Tomsia, and E. Saiz, "Direct write assembly of calcium phosphate scaffolds using a water-based hydrogel," *Acta Biomater.*, vol. 6, no. 1, pp. 218–228, 2010.

[147] C. Gao, M. N. Rahaman, Q. Gao, A. Teramoto, and K. Abe, "Robotic deposition and in vitro characterization of 3D gelatin-bioactive glass hybrid scaffolds for biomedical applications.," *J. Biomed. Mater. Res. A*, vol. 101, no. 7, pp. 2027–37, Jul. 2013.

[148] M. Nelson, "3D Silica-Gelatin Hybrid Scaffolds for Tissue Regeneration," pp. 1–222, 2016.

[149] D. K. Carpenter, "Dynamic Light Scattering with Applications to Chemistry, Biology, and Physics (Berne, Bruce J.; Pecora, Robert)," *J. Chem. Educ.*, vol. 54, no. 10, p. 430, 1977.

[150] J. P. Meyburg and D. Diesing, “Teaching the Growth, Ripening, and Agglomeration of Nanostructures in Computer Experiments,” *J. Chem. Educ.*, vol. 94, no. 9, pp. 1225–1231, 2017.

[151] R. W. O’Brien, B. R. Midmore, A. Lamb, and R. J. Hunter, “Electroacoustic studies of moderately concentrated colloidal suspensions,” *Faraday Discuss. Chem. Soc.*, vol. 90, pp. 301–312, 1990.

[152] F. Booth, “Theory of electrokinetic effects,” *Nature*, vol. 161, no. 4081, pp. 83–86, 1948.

[153] K. S. W. Sing, “Reporting physisorption data for gas/solid systems with special reference to the determination of surface area and porosity (Provisional),” *Pure Appl. Chem.*, vol. 54, no. 11, 1982.

[154] S. Brunauer, P. H. Emmett, and E. Teller, “Adsorption of Gases in Multimolecular Layers,” *J. Am. Chem. Soc.*, vol. 60, no. 2, pp. 309–319, 1938.

[155] P. Tarazona, U. Marconi, and R. Evans, “Phase equilibria of fluid interfaces and confined fluids: non-local versus local density functionals,” *Molecular Physics*, vol. 60, no. 3. pp. 573–595, 1987.

[156] N. a. Seaton, J. P. R. B. Walton, and N. Quirke, “A new analysis method for the determination of the pore size distribution of porous carbons from nitrogen adsorption measurements,” *Carbon N. Y.*, vol. 27, no. 6, pp. 853–861, 1989.

[157] Peter R. Griffiths, *Fourier transform infrared spectrometry*. 2007.

[158] “Background and Theory Page of Nuclear Magnetic Resonance Facility,” *Mark Wainwright Analytical Centre - University of Southern Wales Sydney*, 2011. [Online]. Available: http://www.nmr.unsw.edu.au/usercorner/nmrhistory.htm.

[159] “Inductively coupled plasma optical emission spectroscopy (ICP-OES),” *EAG Laboratories*. [Online]. Available: http://www.eag.com/inductively-coupled-plasma-icp-oes/.

[160] H. M. Rosenberg, “The Solid State: An Introduction to the Physics of Crystals for Students of Physics,” *Materials Science, and Engineering, 3rd ed.(Oxford University Press, Oxford, New York, 1988)*. p. 326, 1979.

[161] M. Bohner and J. Lemaitre, “Can bioactivity be tested in vitro with SBF solution?,” *Biomaterials*, vol. 30, no. 12, pp. 2175–2179, 2009.

[162] A. L. B. Maçon *et al.*, “A unified in vitro evaluation for apatite-forming ability of bioactive glasses and their variants,” *J. Mater. Sci. Mater. Med.*, vol. 26, 2015.

[163] T. Kokubo, H. Kushitani, S. Sakka, T. Kitsugi, and T. Yamamuro, “Solutions able to reproducein vivo surface-structure changes in bioactive glass-ceramic A-W3,” *J. Biomed. Mater. Res.*, vol. 24, no. 6, pp. 721–734, 1990.

[164] A. Hoppe, N. S. Güldal, and A. R. Boccaccini, “A review of the biological response to ionic dissolution products from bioactive glasses and glass-ceramics,” *Biomaterials*, vol. 32, no. 11, pp. 2757–2774, 2011.

[165] M. Chen and A. Von Mikecz, “Formation of nucleoplasmic protein aggregates impairs nuclear function in response to SiO2nanoparticles,” *Exp. Cell Res.*, vol. 305, no. 1, pp. 51–62, 2005.

[166] R. P. Bagwe, L. R. Hilliard, and W. Tan, “Surface Modification of Silica Nanoparticles to Reduce Aggregation and Nonspecific Binding Surface Modification of Silica Nanoparticles to Reduce Aggregation and Nonspecific Binding,” no. 2, pp. 4357–4362, 2006.

[167] Q. Zhang, R. F. Huang, and L. H. Guo, “One-step and high-density protein immobilization on epoxysilane-modified silica nanoparticles,” *Chinese Sci. Bull.*, vol. 54, no. 2006, pp. 2620–2626, 2009.

[168] S. L. Greasley, “Bioactive glass nanoparticles for therapeutic applications,” no. September, pp. 1–171, 2015.

[169] P. Saravanapavan and L. L. Hench, “Mesoporous calcium silicate glasses. I. Synthesis,” *J. Non. Cryst. Solids*, vol. 318, pp. 1–13, 2003.

[170] S. Bonollo, D. Lanari, and L. Vaccaro, “Ring-opening of epoxides in water,” *European J. Org. Chem.*, no. 14, pp. 2587–2598, 2011.

[171] M. W. Ambrogio, C. R. Thomas, Y. L. Zhao, J. I. Zink, and J. F. Stoddart, “Mechanized silica nanoparticles: A new frontier in theranostic nanomedicine,” *Acc. Chem. Res.*, vol. 44, no. 10, pp. 903–913, 2011.

[172] Z. Tao, “Mesoporous silica-based nanodevices for biological applications,” *RSC Adv. Biol. Appl.*, vol. 4, pp. 18961–18980, 2014.

[173] X. Lv, L. Zhang, F. Xing, and H. Lin, “Controlled synthesis of monodispersed mesoporous silica nanoparticles: Particle size tuning and formation mechanism investigation,” *Microporous Mesoporous Mater.*, vol. 225, no. January, pp. 238–244, 2016.

[174] S. Ek, A. Root, M. Peussa, and L. Niinistö, “Determination of the hydroxyl group content in silica by thermogravimetry and a comparison with1H MAS NMR results,” *Thermochim. Acta*, vol. 379, no. 1–2, pp. 201–212, 2001.

[175] H. Hu *et al.*, “Mesoporous silica nanoparticles functionalized with fluorescent and MRI reporters for the visualization of murine tumors overexpressing αvβ3receptors,” *Nanoscale*, vol. 8, no. 13, pp. 7094–7104, 2016.

[176] L. L. H. Pilar Sepulveda, Julian R. Jones, “Dose-Dependent Behavior of Bioactive Glass Dissolution Julian,” *J. Biomed. Mater. Res.*, no. July, pp. 564–569, 2001.

[177] I. Luzinov, D. Julthongpiput, A. Liebmann-Vinson, T. Cregger, M. D. Foster, and V. V. Tsukruk, “Epoxy-terminated self-assembled monolayers: Molecular glues for polymer layers,” *Langmuir*, vol. 16, no. 8, pp. 504–516, 2000.

[178] Y. Wan and D. Zhao, “On the controllable soft-templating approach to mesoporous silicates,” *Chem. Rev.*, vol. 107, no. 7, pp. 2821–2860, 2007.

[179] M. C. Eckersley, P. H. Gaskell, A. C. Barnes, and P. Chieux, “Structural ordering in a

calcium silicate glass," *Nature*, vol. 335, no. 6190. pp. 525–527, 1988.

[180] J. F. Stebbins, J. V. Oglesby, and Z. Xu, "Disorder among network-modifier in silicate glasses : cations New constraints from triple-quantum 17O NMR," *Am. Mineral.*, vol. 82, pp. 1116–1124, 1997.

[181] P. L. Anelli, C. Biffi, F. Montanari, and S. Quici, "Fast and Selective Oxidation of Primary Alcohols to Aldehydes or to Carboxylic-Acids and of Secondary Alcohols to Ketones Mediated by Oxoammonium Salts under 2-Phase Conditions," *J. Org. Chem.*, vol. 52, no. 12, pp. 2559–2562, 1987.

[182] G. Tojo and M. Fernández, "Oxidation of primary alcohols to carboxylic acids: a guide to current common practice," *Basic reations in organic synthesis CN - QD281.O9 T654 2007*. p. 115, 2007.

[183] "Biological evaluation of medical devices. Tests for in vitro cytotoxicity," *Ch, BS EN ISO 10993- 5 2009*, 2009.

[184] "Biological evaluation of medical devices. Sample preparation and reference materials," *Ch, BS EN ISO 10993- 12 2012*, 2012.

[185] F. Tallia, "3-D printed flexible hybrids for tissue regeneration," no. November, 2016.

[186] P. M. Visakh, S. Thomas, A. K. Chandra, and A. P. Mathew, *Advances in Elastomers I: Blends and Interpenetrating Networks*. 2013.

[187] S. Cantournet, R. Desmorat, and J. Besson, "Mullins effect and cyclic stress softening of filled elastomers by internal sliding and friction thermodynamics model," *Int. J. Solids Struct.*, vol. 46, no. 11–12, pp. 2255–2264, 2009.

[188] E. M. Valliant, C. A. Turdean-Ionescu, J. V. Hanna, M. E. Smith, and J. R. Jones, "Role of pH and temperature on silica network formation and calcium incorporation into sol-gel derived bioactive glasses," *J. Mater. Chem.*, vol. 22, no. 4, pp. 1613–1619, 2012.

[189] A. Williams-Jones, "Theoretical estimation of halite solubility in the system NaCl-CaCl2-H2O: Applications to fluid inclusions," *Can. Mineral.*, vol. 28, no. January, pp. 299–304, 1990.

[190] M. I. Kay, R. A. Young, and A. S. Posner, "Crystal structure of hydroxyapatite," *Nature*, vol. 204, no. 4963, pp. 1050–1052, 1964.

[191] B. J. M. Pol, P. B. Van Wachem, M. J. A. Van Luyn, Z. L. Van Der Does, and A. Bantjes, "In vivo testing of crosslinked polyethers. I. Tissue reactions and biodegradation," *J. Biomed. Mater. Res.*, vol. 32, no. 3, pp. 307–320, 1996.

[192] H. suk Yun, S. hyun Kim, S. Lee, and I. hyuck Song, "Synthesis of high surface area mesoporous bioactive glass nanospheres," *Mater. Lett.*, vol. 64, no. 16, pp. 1850–1853, 2010.

[193] A. C. M. Renno, P. S. Bossini, M. C. Crovace, A. C. M. Rodrigues, E. D. Zanotto, and N. A. Parizotto, "Characterization and in vivo biological performance of biosilicate," *Biomed Res. Int.*, vol. 2013, no. Figure 1, 2013.

[194] F. Hoffmann, M. Cornelius, J. Morell, and M. Fröba, "Silica-based mesoporous

organic-inorganic hybrid materials," *Angew. Chemie - Int. Ed.*, vol. 45, no. 20, pp. 3216–3251, 2006.

[195] B. Derby, "Review: Printing and Prototyping of Tissues and Scaffolds," *Science (80-.).*, vol. 338, no. November, pp. 921–926, 2012.

[196] D. B. Williams and C. B. Carter, *Transmission Electron Microscopy*. Plenum, 1996.

Appendix

Permissions for using images from publications:

This is not an invoice

Order Details

Chemical Society reviews

Billing Status: **N/A**

Order detail ID:	71781199	**Permission Status:**	**Granted**
ISSN:	1460-4744	**Permission type:**	Republish or display content
Publication Type:	e-Journal	**Type of use:**	Thesis/Dissertation
Volume:		**Order License Id:**	4516000812908
Issue:		**Order ref number:**	1
Start page:			
Publisher:	ROYAL SOCIETY OF CHEMISTRY		
Author/Editor:	Royal Society of Chemistry (Great Britain)	⊞ View details	

Note: This item was invoiced separately through our **RightsLink service.** More info **$ 0.00**

ELSEVIER LICENSE
TERMS AND CONDITIONS

Jan 25, 2019

This Agreement between Imperial college london -- ZHENLUN Li ("You") and Elsevier ("Elsevier") consists of your license details and the terms and conditions provided by Elsevier and Copyright Clearance Center.

License Number	4516001222413
License date	Jan 25, 2019
Licensed Content Publisher	Elsevier
Licensed Content Publication	Medical Engineering & Physics
Licensed Content Title	Mechanical properties and the hierarchical structure of bone
Licensed Content Author	Jae-Young Rho,Liisa Kuhn-Spearing,Peter Zioupos
Licensed Content Date	Mar 1, 1998
Licensed Content Volume	20
Licensed Content Issue	2
Licensed Content Pages	11
Start Page	92
End Page	102
Type of Use	reuse in a thesis/dissertation
Intended publisher of new work	other
Portion	figures/tables/illustrations
Number of figures/tables/illustrations	1
Format	electronic
Are you the author of this Elsevier article?	No
Will you be translating?	No
Order reference number	1
Original figure numbers	Figure 1
Title of your thesis/dissertation	Bioactive nanoparticle incorporation into inorganic/organic hybrids
Publisher of new work	Imperial college London
Expected completion date	Feb 2019
Estimated size (number of pages)	1
Requestor Location	Imperial college london flat 43 ehtelburga tower london

WOLTERS KLUWER HEALTH, INC. LICENSE TERMS AND CONDITIONS

Jan 25, 2019

This Agreement between Imperial college london -- ZHENLUN Li ("You") and Wolters Kluwer Health, Inc. ("Wolters Kluwer Health, Inc.") consists of your license details and the terms and conditions provided by Wolters Kluwer Health, Inc. and Copyright Clearance Center.

License Number	4516001374047
License date	Jan 25, 2019
Licensed Content Publisher	Wolters Kluwer Health, Inc.
Licensed Content Publication	Journal of the American Academy of Orthopaedic Surgeons
Licensed Content Title	Restoration of Injured or Degenerated Articular Cartilage
Licensed Content Author	Joseph Buckwalter, Van Mow, and Anthony Ratcliffe
Licensed Content Date	Jul 1, 1994
Licensed Content Volume	2
Licensed Content Issue	4
Type of Use	Dissertation/Thesis
Requestor type	Individual
STM publisher name	
Portion	Figures/table/illustration
Number of figures/tables/illustrations	1
Figures/tables/illustrations used	Fig 1
Author of this Wolters Kluwer article	No
Title of your thesis / dissertation	Bioactive nanoparticle incorporation into inorganic/organic hybrids
Expected completion date	Feb 2019
Estimated size(pages)	1
Requestor Location	Imperial college london flat 43 ehtelburga tower london London, other United Kingdom Attn: Imperial college london
Publisher Tax ID	EU826013006
Billing Type	Invoice
Billing Address	Imperial college london flat 43 ehtelburga tower london

Order Completed

Thank you for your order.

This Agreement between Imperial college london -- ZHENLUN Li ("You") and Elsevier ("Elsevier") consists of your license details and the terms and conditions provided by Elsevier and Copyright Clearance Center.

Your confirmation email will contain your order number for future reference.

printable details

License Number	4516010013425
License date	Jan 25, 2019
Licensed Content Publisher	Elsevier
Licensed Content Publication	Acta Biomaterialia
Licensed Content Title	Reprint of: Review of bioactive glass: From Hench to hybrids
Licensed Content Author	Julian R. Jones
Licensed Content Date	Sep 1, 2015
Licensed Content Volume	23
Licensed Content Issue	n/a
Licensed Content Pages	30
Type of Use	reuse in a thesis/dissertation
Portion	figures/tables/illustrations
Number of figures/tables/illustrations	1
Format	electronic
Are you the author of this Elsevier article?	No
Will you be translating?	No
Original figure numbers	Fig 8
Title of your thesis/dissertation	Bioactive nanoparticle incorporation into inorganic/organic hybrids
Publisher of new work	Imperial college London
Expected completion date	Feb 2019
Estimated size (number of pages)	1
Requestor Location	Imperial college london flat 43 ehtelburga tower london London, other United Kingdom Attn: Imperial college london

Confirmation Number: 11785846
Order Date: 01/25/2019

Print citation information (What's this?)

Customer Information

Customer: ZHENLUN Li
Account Number: 3001397812
Organization: Imperial college london
Email: viewtiful.akira@gmail.com
Phone: +44 7792724991

Search order details by: Choose One Go

This is not an invoice

Order Details

Materials Horizons

Billing Status: **N/A**

Order detail ID: 71781233

ISSN: 2051-6355
Publication Type: e-Journal
Volume:
Issue:
Start page:
Publisher: Royal Society of Chemistry
Author/Editor: Royal Society of Chemistry (Great Britain)

Permission Status: **Granted**

Permission type: Republish or display content
Type of use: Thesis/Dissertation
Order License Id: 4516010414187
Order ref number: 1

⊞ View details

Note: This item was invoiced separately through our **RightsLink service.** More info **$ 0.00**

Order Completed

Thank you for your order.

This Agreement between Imperial college london -- ZHENLUN Li ("You") and Elsevier ("Elsevier") consists of your license details and the terms and conditions provided by Elsevier and Copyright Clearance Center.

Your confirmation email will contain your order number for future reference.

printable details

License Number	4516010541567
License date	Jan 25, 2019
Licensed Content Publisher	Elsevier
Licensed Content Publication	Advances in Colloid and Interface Science
Licensed Content Title	Sol-Gel processing of silica nanoparticles and their applications
Licensed Content Author	Lok P. Singh,Sriman K. Bhattacharyya,Rahul Kumar,Geetika Mishra,Usha Sharma,Garima Singh,Saurabh Ahalawat
Licensed Content Date	Dec 1, 2014
Licensed Content Volume	214
Licensed Content Issue	n/a
Licensed Content Pages	21
Type of Use	reuse in a thesis/dissertation
Portion	figures/tables/illustrations
Number of figures/tables/illustrations	1
Format	electronic
Are you the author of this Elsevier article?	No
Will you be translating?	No
Original figure numbers	fig 1
Title of your thesis/dissertation	Bioactive nanoparticle incorporation into inorganic/organic hybrids
Publisher of new work	Imperial college London
Expected completion date	Feb 2019
Estimated size (number of pages)	1
Requestor Location	Imperial college london flat 43 ehtelburga tower london London, other United Kingdom Attn: Imperial college london

Order Completed

Thank you for your order.

This Agreement between Imperial college london -- ZHENLUN Li ("You") and John Wiley and Sons ("John Wiley and Sons") consists of your license details and the terms and conditions provided by John Wiley and Sons and Copyright Clearance Center.

Your confirmation email will contain your order number for future reference.

printable details

License Number	4516010907757
License date	Jan 25, 2019
Licensed Content Publisher	John Wiley and Sons
Licensed Content Publication	Angewandte Chemie International Edition
Licensed Content Title	Silica-Based Mesoporous Organic–Inorganic Hybrid Materials
Licensed Content Author	Frank Hoffmann, Maximilian Cornelius, Jürgen Morell, et al
Licensed Content Date	May 5, 2006
Licensed Content Volume	45
Licensed Content Issue	20
Licensed Content Pages	36
Type of use	Dissertation/Thesis
Requestor type	University/Academic
Format	Electronic
Portion	Figure/table
Number of figures/tables	1
Original Wiley figure/table number(s)	Fig 1
Will you be translating?	No
Title of your thesis / dissertation	Bioactive nanoparticle incorporation into inorganic/organic hybrids
Expected completion date	Feb 2019
Expected size (number of pages)	1
Requestor Location	Imperial college london flat 43 ehtelburga tower london